INSTYTUT FIZYKI JĄDROWEJ
IM. HENRYKA NIEWODNICZAŃSKIEGO
POLSKIEJ AKADEMII NAUK

Ill-posed inverse problems in the controlled nuclear fusion neutron measurements

Thesis submitted to obtain the degree of
Doctor of Philosophy
by

Katarzyna Mikszuta-Michalik

Prepared under the supervision of
dr hab. Jakub Bielecki (IFJ PAN)

Thesis co-supervisor
dr Ewa Łaszyńska (IFPiLM)

Kraków, 2023

This thesis has been published as part of the international project co-financed by the Polish Ministry of Science and Higher Education within the programme called 'PMW' for 2021 under the contract No 5220/HEU-Euratom/2022/2.
This work has been carried out within the framework of the EUROfusion Consortium, funded by the European Union via the Euratom Research and Training Programme (Grant Agreement No 101052200 — EUROfusion). Views and opinions expressed are however those of the author(s) only and do not necessarily reflect those of the European Union or the European Commission. Neither the European Union nor the European Commission can be held responsible for them.

The work leading to this thesis has been funded partially by Fusion for Energy under the Contract F4E-FPA-327. This publication reflects the views only of the author and Fusion for Energy cannot be held responsible for any use which may be made of the information contained therein.
This thesis has been published as part of the international project called 'PMW'. co-financed by the Polish Ministry of Science and Higher Education within the framework of the scientific financial resources for 2020-2024 under the contract no 5111/ITER/2020/0

Abstract

The thesis presents mathematical methods' potential to solve inverse problems related to the measurement by neutron diagnostics on fusion devices. Similar algorithms can be used to reconstruct the neutron emissivity spatial distribution and neutron energy spectrum.

The main subject of this thesis is the tomography reconstruction of the neutron emissivity as the tool for studying plasma temperature and density or interactions and transport of the ions during the tokamak operation. An algorithm based on the Minimum Fisher Information Regularisation (MFR) has been implemented to analyse the data obtained by neutron cameras on ITER and JET tokamaks. The MFR algorithm was applied to optimise the Radial Neutron Camera for ITER architecture and detectors type during its design. Investigation of various operation regimes and issues that can appear during the experiment allows for preparing the efficient tool for thermal plasma analysis during ITER operation. The total neutron yield was applied to the MFR algorithm as the additional constraint and improved the tomography reconstruction precision. The developed method was used to analyse the experimental data from the neutron camera on JET tokamak collected during the deuterium-tritium campaign in 2021. The interpretation of th neutron emissivity for two scenarios, baseline and hybrid, considered for ITER is described. The tomography calculations provide information about fuel isotopes ratio influence on the plasma stability and MHD activity impact on neutron production. The total neutron yield constraint does not improve the absolute values of the neutron emissivity distribution for JET tokamak. The problem is the different threshold energies for neutron camera detectors and neutron rate monitors.

The combination of Tikhonov Regularization, Minimum Fisher Information, Maximum Entropy, and Maximum Likelihood methods was applied to analyse the energy spectra emitted by two kinds of the 14 MeV portable neutron generators based on deuterium-tritium reaction. The activities induced in the Al, Zn, Fe, Ni, Zr, Au by Gradel-Fusion NSD 35 2-DT-C-W gas-plasma target neutron generator were measured by the BrilLanCe 380 scintillator with the lowest uncertainty equal to 10%. The reconstruction results show the domination of the 14 MeV neutrons in the energy spectrum. The impact of the deuterium-deuterium and tritium-tritium reactions is not demonstrated. The lowest energy spectrum reconstruction uncertainty, equal to 18%, was obtained by calculating the mean spectrum from all the considered methods. The neutron emission from the sealed tube neutron generator Genie 16C manufactured by Sodern was monitored by Al, Fe, Ni, Zr, Au, Mg, and Nb foils. The HPGe spectrometer measured their activity with a precision of better than 12%. The best spectrum reconstruction uncertainty was obtained for mean energy spectra and varied from 11% to 15%. A significant impact from the scattered neutrons on the measured neutron intensity makes it impossible to distinguish the presence of the deuterium-deuterium reaction. It is planned to implement the developed methodology on fusion devices like tokamaks.

Streszczenie

Fuzja termojądrowa to obiecująca reakcja jądrowa dla bezpiecznej i przyjaznej dla środowiska produkcji energii. Zrozumienie fizyki plazmy jest kluczowe dla opracowania reaktora termojądrowego, który zostanie wykorzystany do budowy komercyjnej elektrowni. Głównymi produktami fuzji jądrowej są neutrony, które wydostają się z plazmy bez interakcji dzięki czemu niosą niezaburzoną informację na temat swojego źródła. Celem pracy jest interpretacja rozkładu przestrzennego oraz energetycznego emisji neutronów. Rozkłady te są wynikiem rozwiązania źle postawionych problemów odwrotnych, które pozwalają na zrozumienie zjawisk zachodzących w plazmie. W rozprawie przedstawiono opracowane procedury matematyczne użyte do rozwiązywania problemów odwrotnych związanych z pomiarem diagnostykami neutronowymi na urządzeniach fuzyjnych. Algorytmy oparte na różnych metodach zostały wykorzystane do rekonstrukcji przestrzennego rozkładu emisyjności oraz widma energetycznego neutronów.

Podstawowym przedmiotem rozprawy jest rekonstrukcja rozkładu emisyjności neutronów użyta jako narzędzie do badania temperatury i gęstości plazmy lub oddziaływań oraz transportu jonów podczas pracy tokamaka. Autorka rozprawy zaimplementowała kod komputerowy oparty na regularyzacji poprzez minimalizację Informacji Fishera (MFR) do tomografii neutronowej, która w rozprawie definiowana jest jako rekonstrukcja dwu-wymiarowego rozkładu wielkości fizycznej. Opracowana metoda została wykorzystana do analizy danych syntetycznych w przypadku tokamaka ITER oraz eksperymentalnych dla tokamaka JET. Rekonstrukcja tomograficzna profili emisji neutronów umożliwia badanie temperatury jonów paliwa i kontrolę stabilności plazmy. Algorytm MFR został wykorzystany do optymalizacji architektury i wyboru rodzaju detektorów Radialnej Kamery Neutronowej (RNC – ang. Radial Neutron Camera) projektowanej dla tokamaka ITER. Analiza wyników otrzymanych z symulacji przy różnych trybach pracy tokamaka wykazała, że zmiana w architekturze kamery nie spowoduje znaczących zmian w jakości rekonstrukcji emisyjności neutronów w plazmie. Zastosowanie dodatkowego ograniczenia w postaci całkowitej emisji neutronów zmierzonej za pomocą niezależnego monitora neutronów znacząco poprawia wyniki tomografii. Dodatkowo zbadano wpływ zaburzeń w danych wejściowych, które mogą pojawić się podczas eksperymentu, na wyniki obliczeń. Opracowana metoda została wykorzystana również do analizy danych eksperymentalnych z kamery neutronowej na tokamaku JET, uzyskanych podczas kampanii deuterowo-trytowej w 2021 roku. Badanie zaburzeń w rozkładzie emisyjności neutronów dostarcza informacji niezbędnych do optymalizacji parametrów pracy pozwalających na wydłużenie czasu wyładowania plazmy. Zinterpretowano wyniki rekonstrukcji rozkładu emisyjności neutronów w przypadku dwóch scenariuszy pracy; bazowego i hybrydowego. Obliczenia tomograficzne dostarczają informacji o wpływie stosunku izotopów paliwa na stabilność plazmy oraz wpływie aktywności MHD na produkcję neutronów. W wyładowaniach zawierających małe ilości trytu zaobserwowano wiele odstępstw od standardowych rozkładów symetrycznych z maksymalną emisyjnością neutronów w centrum. W przypadku zaburzeń magnetohydrodynamicznych przeprowadzona analiza nie pozwoliła powiązać niestabilności emisji neutronów z badanymi zjawiskami. Ograniczenie w postaci całkowitej emisyjności neutronów nie poprawia bezwzględnych wartości rozkładu emisyjności neutronów dla tokamaka JET. Problemem są różne energie progowe dla detektorów kamer neutronowych i monitorów neutronów.

Kolejnym przykładem źle postawionego problemu odwrotnego w pomiarach neutronów na urządzeniach fuzyjnych jest rekonstrukcja widma energetycznego z wykorzystaniem metody aktywacyjnej. Autorka rozprawy przygotowała kody komputerowe oparte na regularyzacji Tichonowa, minimalizacji informacji Fishera, zasadzie maksymalnej entropii i zasadzie maksymalnego prawdopodobieństwa. Nowatorskie podejście dotyczy łączenia różnych technik poprzez obliczanie średniego widma energetycznego ze wszystkich otrzymanych rezultatów. Opracowana metoda zastosowana została do analizy widm energetycznych neutronów

emitowanych przez dwa rodzaje przenośnych generatorów neutronów 14 MeV opartych na reakcji deuter-tryt. Analiza widma energetycznego emitowanego przez plazmowy generator neutronów została wykonana z użyciem folii dozymetrycznych Al, Zn, Fe, Ni, Zr, oraz Au. Obliczenia pokazały, że reakcje deuter-deuter i tryt-tryt mogące zachodzić w urządzeniu mają pomijalnie mały wpływ na rozkład energii neutronów emitowanych w tym urządzeniu. Ze względu na dużą niepewność pomiarową aktywności folii dozymetrycznych najniższy błąd rekonstrukcji wynosił 18% dla widma otrzymanego z uśredniania po wszystkich metodach. Pomiar aktywności próbek Al, Fe, Ni, Zr, Au, Mg i Nb naświetlonych neutronami z generatora opartego na reakcji wiązka-tarcza został wykonany za pomocą innego spektrometru z większą dokładnością. Pozwoliło to na zrekonstruowanie energetycznego widma neutronów dla którego otrzymano zgodność aktywności symulowanej i eksperymentalnej na poziomie 10%. Ustawienie próbek w odległości 21 cm od generatora spowodowało, że zarejestrowano wiele neutronów rozproszonych, które uniemożliwiają rozstrzygniecie czy w generatorze występują reakcje związane z adsorpcja jonów wiązki na tarczy. Opracowane metody zostaną w przyszłości zastosowane w analizie energetycznych widm neutronów na tokamakach.

Table of content

Aim of the thesis

Understanding plasma physics is essential for developing new reliable energy sources related to growing energy needs. Thermonuclear fusion is a promising phenomenon for safe and environmentally friendly energy production. Neutrons are the major fusion reaction products that escape from the plasma without interactions. The neutron measurements are essential for understanding plasma physics because they provide information about fusion power generation, ion temperature and transport. The knowledge about neutron emission is necessary to understand plasma phenomena and helps extend plasma confinement time. The reconstruction of the neutron emission profiles allows for interpreting plasma physics and ion behaviour. The neutron spectrum measurement provides information about ions' velocity distributions, isotopes amount and particle interactions. The analysis of neutron emissivity and its energy spectrum requires solving the ill-posed and ill-conditioned inverse problems by applying a sophisticated method.

The aim of the thesis is an interpretation of the reconstructed neutron emissivity distribution in tokamaks and an evaluation of the developed method precision. The author implemented the code based on the Minimum Fisher Information Regularization with smoothing along toroidal magnetic field lines for neutron analysis. The implementation required analysis of the neutron interactions with matter, neutron source physics and geometry of the neutron cameras. The novel approach includes adding the total neutron yield constraint from an independent measurement to improve the absolute values of the reconstruction. The capability of the tomographic reconstruction by the prepared tools was validated with the simulation data for ITER tokamak. In ITER, the thermonuclear reactions will dominate. The tomography reconstruction of the neutron emission profiles will allow studies of the temperature of the fuel ions and control the plasma stability. The interpretation of the neutron emissivity requires reconstruction with an uncertainty below 10% in the plasma core. The prepared code was used to optimize the Radial Neutron Camera (RNC) design to obtain high precision in reconstructing the neutron emission profiles during ITER operation. The author also implemented the code to the neutron camera installed on JET tokamak. The analyzed data was collected during the deuterium-tritium (DT) campaign, which took place in 2021. In JET, the primary source of the neutrons are interactions of the accelerated ions related to the heating systems. The neutron emission profiles provide information about the interactions of ions, transport of the injected particles and disruptions that influence fusion reactions and plasma termination. Investigation of the instabilities in the neutron emissivity distribution provides the information necessary for optimizing the operation parameters, allowing for the plasma discharge duration prolongation. The plasma scenarios analyzed during the DT campaign on JET will be further investigated during ITER operation with the conditions allowing to achieve self-sustained plasma.

The same mathematical methods were applied to another inverse problem related to a neutron diagnostic. The Minimum Fisher Information technique was applied to reconstruct the neutron energy spectrum from the activation measurement. The characterization of a portable DT neutron generator provides information about neutron flux and the energy spectrum required for neutron diagnostics calibration and application to the experiments. The neutron spectrum can change in time due to decreasing tritium amount and other physical phenomena like beam adsorption on the target. The analysis of the emitted neutrons' energy allows for evaluating the generator exploitation and chemical effects (e.g. molecules presence). Algorithms prepared by the author based on Tikhonov Regularization, Minimum Fisher Information, Maximum Entropy, and Maximum Likelihood were used to reconstruct the neutron energy spectrum from activation measurement. Additionally, the mean spectrum reconstructed by the different methods was provided. The reconstruction of the neutron spectra emitted by the two kinds of portable 14-MeV neutron generators was performed. The developed methods

can be implemented on JET or ITER to interpret the neutron energy spectrum from the measurement not disturbed by the tokamak environment.

State of the art

Inverse problems are common in experimental plasma physics. Different methods have been developed and applied to the analysis, which takes into account phenomena related to the particular diagnostic and measured physical quantity. The approaches differ due to their application to continuous or discrete problems. The continuous problems can be solved by the methods developed for medical purposes. This thesis concern the discrete problems with a strongly limited number of measurement data.

Tomography is a non-invasive imaging technique used in science, industry, and medicine [Bat2011]. This term in fusion physics usually relates to reconstructing the two-dimensional physical quantity distribution. The tomography described in this thesis concerns the spatial profile of radiation emissivity in the single poloidal cross-section of the tokamak. It requires observation of the plasma from several positions. The diagnostics allow tomography calculations involving cameras with fan-shaped lines of sight (LOSs) geometry in one toroidal position in a plasma device. The ability of the reconstruction depends on the plasma coverage by the LOSs, the measurement description's precision, and the method itself. The application of the tomography method to the camera looking from a single direction is usually not practised due to the very low number of experimental data and the impossibility of providing asymmetric images.

The basic technique applied to different diagnostics is the Tikhonov regularisation [Ing1998, Jac2016, Ods2016]. It is widely used to solve one and two-dimensional problems. An example of the application in tomography is an analysis of the neutron emissivity in JET tokamak [Bie2015]. It is also used to reconstruct the neutron energy spectrum from different sources, tokamak, and Am-Be, based on the activation method [Mly2013, Liu2021]. The published analysis concerns measurement by Bonner Spheres like in [Her1985].

The first use of the Minimum Fisher Information method on the tokamak was described in [Ant1996] and concerned the soft X-ray tomography. Most of the subsequent papers are based on this description. The method is widely applied on different tokamaks to analyse the bolometric and soft X-ray data [Mly2015, Jar2016]. It was also used in neutron tomography at JET tokamak [Bon2006]. The lines describe the camera's geometry, and each detector's contribution to the measurement is the line's length.

The Maximum Entropy method was found as the ultimate for reconstructing the distribution of the physical quantity from incomplete and noisy measurement data [Lin1995]. Therefore, it was adapted for plasma diagnostics data processing [Den1998]. It was used in the tomography of soft X-ray at JET tokamak [Ing1998] and W7-X stellarator [Ert1996], and fast ion velocity on ASDEX-Upgrade tokamak [Jac2016]. The Maximum Entropy method was widely applied to the neutron energy spectrum reconstruction from the measurement by scintillators [Reg2008, Mer2010] and the activation method [Tri2007]. The most prevalent code is MAXED [Reg1999], which was developed for spectrometry based on the Bonner Spheres. It combines the Maximum Entropy with a simulated annealing algorithm [Reg1999]. The application of this code to the neutron energy spectrum reconstruction from the activation measurement was described in [Jo2018, Las2020].

The last method described in this thesis is Maximum Likelihood. It was applied to gamma and neutron tomography on JET tokamak [Cra2016] and reconstruction of the neutron spectrum from measurement by scintillators [Peh2013]. The use of this method with the multifoil activation method is also reported [Mae2013].

The algorithms based on deep learning [Mat2017] and neural networks [Jar2019] have become popular, but they are not the subject of this thesis.

There are many methods to solve the inverse ill-posed problems. They are widely used in the processing of data from plasma diagnostics. An algorithm based on the neural networks was the only one previously applied to reconstruct the neutron emissivity in ITER tokamak. In this

thesis, the Minimum Fisher Information method was applied to the analysis of the synthetic data by ITER Radial Neutron Camera (RNC). The used code evolved from the algorithm presented in [Ods2012]. The calculations were modified by changing the definition of the plasma observed by the detectors. The fields of view substituted the lines of sight. The examples of measurement geometry described by the areas with solid angles for JET or ITER were not found in the literature. Additionally, the total neutron yield was added as the new constraint. The Minimum Fisher Information method was not used before for the tomography reconstructions for camera observing plasma from a single direction like in the case of ITER RNC. The calculations are based on the assumption that reactions in plasma have thermonuclear character and plasma shape is symmetric to the core centre. The modified code was applied to the JET neutron camera for the first time. The experimental data from the second deuterium-tritium campaign have been analysed. The mixture of the hydrogen isotopes was used for the first time during the operation of the JET tokamak with the ITER-like first wall [Pam2007].

Due to insensitivity to gamma radiation, magnetic field, and temperature, the activation method is applied to the total neutron yield determination for fusion devices. It can also be used for the reconstruction of the neutron energy spectrum. A wide variety of methods is used for this purpose. For each method, many mathematical approaches to calculation exist. Additionally, different methods for a regularisation parameter selection are available. Usually, the codes include a combination of various techniques. The algorithms prepared by the thesis author are different from those previously published, e.g. the regularisation equations are solved by the lower–upper factorisation, not by generalised singular value decomposition. The new approach is to reconstruct the neutron spectra by different methods and present the mean results from all of them. Adapting the FISPACT-II inventory code [Sub2017] to evaluate the reconstruction precision is also an innovative methodology.

List of abbreviations

CFC – carbon fibre composite
CXRS – Charge Exchange Recombination Spectroscopy
DD – deuterium-deuterium plasma/reaction
DT – deuterium-tritium plasma/reaction
DTE1 – the first deuterium-tritium experimental campaign on JET tokamak performed in 1997
DTE2 – the second deuterium-tritium experimental campaign on JET tokamak performed in 2021
ECRH - Electron Cyclotron Resonance Heating
FWHM – the full-width at half maximum
HRNS – High-Resolution Neutron Spectrometer
ICRH – Ion Cyclotron Resonance Heating
ISA - Intermediate System Architecture
ITER – 'the way to new energy', the world's largest fusion experiment (tokamak)
JET – Joint European Torus
LOS – Line of Sight
NG – neutron generator
RF – radio frequency
RGRS - Radial Gamma-Ray Spectrometer
RMS – root mean square of accuracy
RNC – Radial Neutron Camera
SVD – Singular Value Decomposition

List of symbols

a – minor radius of tokamak
A – radioactivity induced by neutron flux
A_c – area of the detector's channel
A_p – area of the pinhole
A_R – radioactivity simulated for reconstructed spectrum
A_S – synthetic radioactivity induced by neutron flux
b – impact parameter of collision
B – magnetic field
$B_{\varphi 0}$ - toroidal magnetic field in mid-plane
B_φ – toroidal magnetic field
$B_{//}$ – operator describing first derivative in radial, horizontal and diagonal directions parallel to magnetic field lines
$B_\perp$ – operator describing first derivative perpendicular to the magnetic flux surfaces
C - heat capacity
C_R – ratio between $accuracy_s$ and $accuracy_a$
d – data vector
D – thermal diffusivity
d' – vector of data divided by the uncertainty
D_p – poloidal dimension of the channel
D_p – poloidal dimension of the pinhole
E – kinetic energy
$\bar{E}$ – mean energy of reacting particles
e – the elementary charge
E_g – bandgap energy
E_n – neutron energy
E_{ph} – the energy of the incident photon
et – etendue
E_α – the energy carried by the alpha particle
f – collimator diameter
F – collimator length
G – geometry matrix
g – kernel function
G' – geometry matrix divided by the uncertainty
Gf – geometry factor including solid angle influence on the measurement
h – distance from the pixel to the end of collimator
I – neutron emission intensity
I_F – Fisher Information function
I_S - signal current
j – plasma current density
J_l – Bessel function of the first kind
K – relative kinetic energy of reacting particles
k_B – Boltzmann's constant
k_{ij} - constant of the reaction in reaction rate per particle pair
L – convex functional, regularisation operator/matrix
l – harmonic line number
$L(m'|d)$ – likelihood function of model parameters m' for given data d
I_p – plasma current
L_p – the distance between the pinhole and channel in the poloidal plane
m – particle mass

m' – model of the measured parameters, solution of the regularisation problem
m'_0 - default model used for the first iteration in the reconstruction
N – degrees of freedom equal to the number of measurements
$n_{i/e}$ – ion/electron plasma density
N_0 - number of target nuclei
N_g – number of eigenvalues corresponding to data with the reliable signal-to-noise ratio
N_i – density of particle species "i"
N_N – number of radioactive nuclei
NY_n – the total neutron yield normalised to the highest value for the particular discharge
NRY_n – the reconstructed total neutron yield normalized to the highest value for the particular discharge
o – number of the elements in the solution of the regularisation problem
p – plasma pressure
$p(d)$ – probability corresponding to the discrete values obtained in the measurement
$p(d|m')$ – a conditional probability distribution that model parameters m' let for measurement data d
$p(x)$ – probability density function for noise
P_{AH} – auxiliary heating power
P_H – heating power
P_{LOS} – total radiation loss
P_{trans} – energy lost through transport processes
P_α – power produced in fusion reactions carried by alpha particles
Q – gain factor
q – safety factor
Q_F – energy released in reaction
R – distance from the major tokamak axis to the position of the interest
r – radial tokamak coordinate
R_0 – major radius of tokamak
R_C – radius of the cone in the defined distance from the collimator
R_{d0} – detector resistance
R_I - current spectral responsivity
r_N – neutron radius
r_r – reaction rate in cross-section unit
r_T – radius of target nuclei
R_V – voltage spectral responsivity
R_y – Rydberg's constant
RY_n – the reconstructed total neutron yield from the tomography calculations
S – entropy
$S(\Omega)$ – logistic sigmoid function
s_i – singular values
Sm – neutron emission profile obtained in the simulation
S_v – diagonal matrix with singular values
T – temperature
t_c – cooling time
t_i – irradiation time
t_m – measurement time
U - the orthogonal matrix consisting of unit basis vectors spanning the data space
V – centre-of-mass velocity in the laboratory frame
V_p – plasma volume
V_s – the orthogonal matrix with columns consisting of the basis vectors spanning the model space
W – weight matrix in Minimum Fisher Information method

x – the distance between detector and pixel
Y_n – the total neutron yield measured by the fission chambers
Z – atomic number
α_R – temperature coefficient of resistance
β – the ratio of plasma pressure to magnetic pressure
β_N – the normalised ratio of plasma pressure to magnetic pressure
δ_{ij} – Kronecker delta function
ε – noise/error of the measurement
η_{ij} - constant characterising reaction in reaction rate per particle pair
Λ – eigenvalues of the least square matrix
λ – regularisation parameter ($\in R_+$)
λ_T - decay constant
μ – reduced mass
μ_0 – vacuum permeability
ξ – angle describing the orientation of the channel concerning the pinhole
σ – reaction cross-section
σ_i – singular value
σ_s – standard deviation
τ – plasma confinement time
τ_{00} - time constant of the fundamental mode of Fourier expansion.
τ_c - cooling time constant
υ – ions velocity
$\langle \upsilon\sigma \rangle$ – reaction rate per particle pair
$\phi\ (l,x,y)$ – Trubnikov function
Φs – spectral radiant incident power
X^2 – Pearson chi-squared
Ψ – poloidal magnetic flux
ω – frequency of radiated electromagnetic waves
Ω – smoothing parameter in the MFR method
ω_L – relativistic Larmor frequency/gyrotron frequency of particle moving in uniform magnetic field
ω_p – plasma frequency
γ – Lorentz factor
ζ – the angle between velocity in the lab frame and particle velocity in the center-of-mass frame

List of figures

Figure 8.50. RMS for different values of smoothing parameter Ω for scenario (c) and different types of the detectors in the ex-port camera part.

Figure 8.51. The comparison of the 2D accuracy profiles obtained with different values of smoothing parameter for scenario (c) and the sCD detectors in the ex-port system.

Figure 8.52. The comparison of the 1D accuracy profiles horizontal (left) and vertical (right) obtained with different values of smoothing parameter for scenario (c) and the sCD detectors in the ex-port system.

Figure 8.53. RMS for different values of smoothing parameter Ω for scenario (d) and different types of the detectors in the ex-port camera part.

Figure 8.54. The comparison of the 2D accuracy profiles obtained with different values of smoothing parameter for scenario (d) and the ^{4}He scintillators in the ex-port system.

Figure 8.55. The comparison of the 1D accuracy profiles horizontal (left) and vertical (right) obtained with different values of smoothing parameter for scenario (d) and the ^{4}He scintillators in the ex-port system.

Figure 8.56. RMS for different values of smoothing parameter Ω for scenario (e) and different types of the detectors in the ex-port camera part.

Figure 8.57. The comparison of the 2D accuracy profiles obtained with different values of smoothing parameter for scenario (e) and the plastic scintillators in the ex-port system.

Figure 8.58. The comparison of the 1D accuracy profiles horizontal (left) and vertical (right) obtained with different values of smoothing parameter for scenario (e) and the plastic scintillators in the ex-port system.

Figure 8.59. RMS for magnetic field displacement in R positive direction for scenario (c) and different types of the detectors in the ex-port camera part.

Figure 8.60. The comparison of the 2D accuracy profiles obtained with magnetic field shift along R-axis in the positive direction for scenario (c) and the ^{4}He scintillators in the ex-port system.

Figure 8.61. The comparison of the 1D accuracy profiles obtained with magnetic field shift along R-axis in the positive direction for scenario (c) and the ^{4}He scintillators in the ex-port system.

Figure 8.62. RMS for magnetic field displacement in R negative direction for scenario (c) and different types of the detectors in the ex-port camera part.

Figure 8.63. The comparison of the 2D accuracy profiles obtained with magnetic field shift along R-axis in the negative direction for scenario (c) and the ^{4}He scintillators in the ex-port system.

Figure 8.64. The comparison of the 1D accuracy profiles obtained with magnetic field shift along R-axis in the negative direction for scenario (c) and the ^{4}He scintillators in the ex-port system.

Figure 8.65. RMS for magnetic field displacement in Z positive direction for scenario (c) and different types of the detectors in the ex-port camera part.

Figure 8.66. The comparison of the 2D accuracy profiles obtained with magnetic field shift along Z-axis in the positive direction for scenario (c) and the sCD detectors in the ex-port system.

Figure 8.67. The comparison of the 1D accuracy profiles obtained with magnetic field shift along Z-axis in the positive direction for scenario (c) and the sCD detectors in the ex-port system.

Figure 8.68. RMS for magnetic field displacement in Z negative direction for scenario (c) and different types of the detectors in the ex-port camera part.

Figure 8.69. The comparison of the 2D accuracy profiles obtained with magnetic field shift along Z-axis in the negative direction for scenario (c) and the sCD detectors in the ex-port system.

Figure 8.70. The comparison of the 1D accuracy profiles obtained with magnetic field shift along Z-axis in the negative direction for scenario (c) and the sCD detectors in the ex-port system.

Figure 8.71. RMS comparison for magnetic field displacement in R direction with constant Z shift (positive – top, negative – bottom) for scenario (c) and the plastic scintillators in the ex-port camera part.

Figure 8.72. RMS comparison for magnetic field displacement in Z direction with constant R shift (positive – top, negative – bottom) for scenario (c) and the plastic scintillators in the ex-port camera part.

Figure 8.73. The comparison of the 2D accuracy profiles obtained with magnetic field shift along R and Z axis for scenario (c) and the plastic scintillators in the ex-port system.

Figure 8.74. The comparison of the 1D accuracy profiles obtained with magnetic field shift along R and Z axis for scenario (c) and the plastic scintillators in the ex-port system.

Figure 8.75. RMS for magnetic field displacement in R positive direction for scenario (d) and different types of the detectors in the ex-port camera part.

Figure 8.76. The comparison of the 2D accuracy profiles obtained with magnetic field shift along R-axis in the positive direction for scenario (d) and the plastic scintillators in the ex-port system.

Figure 8.77. The comparison of the 1D accuracy profiles obtained with magnetic field shift along R-axis in the positive direction for scenario (d) and the plastic scintillators in the ex-port system.

Figure 8.78. RMS for magnetic field displacement in R negative direction for scenario (d) and different types of the detectors in the ex-port camera part.

Figure 8.79. The comparison of the 2D accuracy profiles obtained with magnetic field shift along R-axis in the negative direction for scenario (d) and the plastic scintillators in the ex-port system.

Figure 8.80. The comparison of the 1D accuracy profiles obtained with magnetic field shift along R-axis in the negative direction for scenario (d) and the plastic scintillators in the ex-port system.

Figure 8.81. RMS for magnetic field displacement in Z positive direction for scenario (d) and different types of the detectors in the ex-port camera part.

Figure 8.82. The comparison of the 2D accuracy profiles obtained with magnetic field shift along Z-axis in the positive direction for scenario (d) and the ^{4}He scintillators in the ex-port system.

Figure 8.83. The comparison of the 1D accuracy profiles obtained with magnetic field shift along Z-axis in the positive direction for scenario (d) and the ^{4}He scintillators in the ex-port system.

Figure 8.84. RMS for magnetic field displacement in Z negative direction for scenario (d) and different types of the detectors in the ex-port camera part.

Figure 8.85. The comparison of the 2D accuracy profiles obtained with magnetic field shift along Z-axis in the negative direction for the scenario (d) and the ^{4}He scintillators in the ex-port system.

Figure 8.86. The comparison of the 1D accuracy profiles obtained with magnetic field shift along Z-axis in the negative direction for scenario (d) and the ^{4}He scintillators in the ex-port system.

Figure 8.87. The comparison of the 2D accuracy profiles obtained with magnetic field shift along R and Z axis for scenario (d) and the plastic scintillators in the ex-port system.

Figure 8.88. The comparison of the 1D accuracy profiles obtained with magnetic field shift along R and Z axis for scenario (d) and the plastic scintillators in the ex-port system.

Figure 8.89. RMS for magnetic field displacement in R positive direction for scenario (e) and different types of the detectors in the ex-port camera part.

Figure 8.90. The comparison of the 2D accuracy profiles obtained with magnetic field shift along R-axis in the positive direction for scenario (e) and the ^{4}He scintillators in the ex-port system.

Figure 8.91. The comparison of the 1D accuracy profiles obtained with magnetic field shift along R-axis in the positive direction for scenario (e) and the ^{4}He scintillators in the ex-port system.

Figure 8.92. RMS for magnetic field displacement in R negative direction for scenario (e) and different types of the detectors in the ex-port camera part.

Figure 8.93. The comparison of the 2D accuracy profiles obtained with magnetic field shift along R-axis in the negative direction for scenario (e) and the ^{4}He scintillators in the ex-port system.

Figure 8.94. The comparison of the 1D accuracy profiles obtained with magnetic field shift along R-axis in the negative direction for scenario (e) and the ^{4}He scintillators in the ex-port system.

Figure 8.95. RMS for magnetic field displacement in Z positive direction for scenario (e) and different types of the detectors in the ex-port camera part.

Figure 8.96. The comparison of the 2D accuracy profiles obtained with magnetic field shift along Z-axis in the positive direction for scenario (e) and the sCD detectors in the ex-port system.

Figure 8.97. The comparison of the 1D accuracy profiles obtained with magnetic field shift along Z-axis in the positive direction for scenario (e) and the sCD detectors in the ex-port system.

Figure 8.98. RMS for magnetic field displacement in Z negative direction for scenario (e) and different types of the detectors in the ex-port camera part.

Figure 8.99. The comparison of the 2D accuracy profiles obtained with magnetic field shift along Z-axis in the negative direction for scenario (e) and the sCD detectors in the ex-port system.

Figure 8.100. The comparison of the 1D accuracy profiles obtained with magnetic field shift along Z-axis in the negative direction for scenario (e) and the sCD detectors in the ex-port system.

Figure 8.101. The comparison of the 2D accuracy profiles obtained with magnetic field shift along R and Z axis for scenario (e) and the plastic scintillators in the ex-port system.

Figure 9.8. Comparison of the reconstructed total neutron yield obtained in calculations with and without the additional constraint for discharge #99949 with values measured by the fission chambers (left side – comparison of the absolute values, right side – comparison of the changes dynamics).

Figure 9.9. The comparison of the ion temperature measured by CXRS, normalised reactivity, and reconstructed neutron emission profile with count rates registered by the camera for time 48.81 s in discharge #99423.

Figure 9.10. The comparison of the ion temperature measured by CXRS, normalised reactivity, and reconstructed neutron emission profile with count rates registered by the camera for time 47.85 s in discharge #99522.

Figure 9.11. The comparison of the ion temperature measured by CXRS, normalised reactivity, and reconstructed neutron emission profile with count rates registered by the camera for time 47.79 s in discharge #99916.

Figure 9.12. The comparison of the ion temperature measured by CXRS, normalised reactivity, and reconstructed neutron emission profile with count rates registered by the camera for time 51.92 s in discharge #99520.

Figure 9.13. The comparison of the ion temperature measured by CXRS, normalised reactivity, and reconstructed neutron emission profile with count rates registered by the camera for time 50.08 s in discharge #99866.

Figure 9.14. Comparison of the tritium amount in the plasma during the different discharges of the experiment with the hybrid scenario.

Figure 9.15. Comparison of the normalised NBI power and the total neutron yield from FC functions in time for discharge #99423.

Figure 9.16. The neutron emission profiles reconstructed for time 52.10 s, 52.49 s, and 52.61 s in discharge #99423.

Figure 9.17. The total neutron yield measured by FC (left), NBI power (centre), and ICRH power (right) functions in time for discharge #99510.

Figure 9.18. The neutron emission profiles reconstructed for time 45.35 s, 45.65 s, and 46.36 s in discharge #99510.

Figure 9.19. The neutron emission profiles reconstructed for time 48.72 s, 48.85 s, and 48.97 s in discharge #99510.

Figure 9.20. The total neutron yield measured by FC (left), NBI power (centre), and ICRH power (right) functions in time for discharge #99448.

Figure 9.21. The neutron emission profiles reconstructed for time 47.39 s, 47.50 s, and 47.78 s in discharge #99448.

Figure 9.22. The neutron emission profiles reconstructed for time 48.59 s, 48.77 s, and 48.80 s in discharge #99448.

Figure 9.23. The total neutron yield measured by FC (left), NBI power (centre), and ICRH power (right) functions in time for discharge #99914.

Figure 9.24. The neutron emission profiles reconstructed for time 48.48 s, 50.09 s, and 51.31 s in discharge #99914.

Figure 9.25. The total neutron yield measured by FC (left), NBI power (centre), and ICRH power (right) functions in time for discharge #99949.

Figure 9.26. The neutron emission profiles reconstructed for time 48.01 s, 49.25 s, and 51.14 s in discharge #99949.

Figure 9.27. The total neutron yield measured by FC (left), NBI power (centre), and ICRH power (right) functions in time for discharge #99868.

Figure 9.28. The neutron emission profiles reconstructed for time 48.03 s, 49.05 s, and 50.01 s in discharge #99868.

Figure 9.29. The total neutron yield measured by FC (left), NBI power (centre), and ICRH power (right) functions in time for discharge #99866.

Figure 9.30. The neutron emission profiles reconstructed for time 47.68 s, 48.04 s, and 49.28 s in discharge #99866.

Figure 9.31. The total neutron yield measured by FC (left), NBI power (centre), and ICRH power (right) functions in time for discharges #96994 (top), #99512 (centre), and #99513 (bottom).

Figure 9.32. The neutron emission profiles reconstructed for time 48.67 s, 49.54 s, and 50.62 s in discharge #96994.

Figure 9.33. The neutron emission profiles reconstructed for time 49.26 s, 49.27 s, and 53.00 s in discharge #99512.

Figure 9.34. The neutron emission profiles reconstructed for time 49.57 s, 50.39 s, and 50.72 s in discharge #99513.

Figure 9.35. The total neutron yield measured by FC (left), NBI power (centre), and ICRH power (right) functions in time for discharges #97995.

Figure 9.36. The neutron emission profiles reconstructed for time 50.20 s, 50.32 s, and 50.43 s in discharge #97995.

Figure 9.37. The total neutron yield measured by FC (left), NBI power (centre), and ICRH power (right) functions in time for discharges #99460.

Figure 9.38. The neutron emission profiles reconstructed for time 47.91 s, 48.61 s, and 48.65 s in discharge #99460.

Figure 9.39. Ion density (left) and temperature (right) profiles measured during discharge #99460.

Figure 9.40. The total neutron yield measured by FC (left), NBI power (centre), and ICRH power (right) functions in time for discharges #99520.

Figure 9.41. The neutron emission profiles reconstructed for time 48.79 s, 48.84 s, and 48.86 s in discharge #99520.

Figure 9.42. Ion density (left) and temperature (right) profiles measured during discharge #99520.

Figure 9.43. The total neutron yield measured by FC (left), NBI power (centre), and ICRH power (right) functions in time for discharges #99522.

Figure 9.44. The neutron emission profiles reconstructed for time 48.69 s, 48.76 s, and 48.77 s in discharge #99522.

Figure 9.45. Ion density (left) and temperature (right) profiles measured during discharge #99522.

Figure 9.46. The total neutron yield measured by FC (left), NBI power (centre), and ICRH power (right) functions in time for discharges #99523.

Figure 9.47. The neutron emission profiles reconstructed for time 49.72 s, 49.73 s, and 49.74 s in discharge #99523.

Figure 9.48. Ion density (left) and temperature (right) profiles measured during discharge #99523.

Figure 9.49. The total neutron yield measured by FC (left), NBI power (centre), and ICRH power (right) functions in time for discharges #99797.

Figure 9.50. The neutron emission profiles reconstructed for time 50.08 s, 50.09 s, and 50.11 s in discharge #99797.

Figure 9.51. Ion density (left) and temperature (right) profiles measured during discharge #99797.

Figure 9.52. The total neutron yield measured by FC (left), NBI power (centre), and ICRH power (right) functions in time for discharges #99799.

Figure 9.53. The neutron emission profiles reconstructed for time 49.52 s, 49.57 s, and 49.63 s in discharge #99799.

Figure 9.54. Ion density (left) and temperature (right) profiles measured during discharge #99799.

Figure 9.55. The total neutron yield measured by FC (left), NBI power (centre), and ICRH power (right) functions in time for discharges #99861.

Figure 9.56. The neutron emission profiles reconstructed for time 49.89 s, 49.90 s, and 49.91 s in discharge #99861.

Figure 9.57. Ion density (left) and temperature (right) profiles measured during discharge #99861.

Figure 9.58. The total neutron yield measured by FC (left), NBI power (centre), and ICRH power (right) functions in time for discharges #99863.

Figure 9.59. The neutron emission profiles reconstructed for time 48.91 s, 50.07 s, and 50.46 s in discharge #99863.

Figure 9.60. Ion density (left) and temperature (right) profiles measured during discharge #99863.

Figure 10.7. The $accuracy_s$ (9 bins) for the reconstruction results obtained by different methods with the synthetic activity originated from spectrum I (9 bins) simulated for Gradel-Fusion NSD 35 2-DT-C-W (TR and MFI – top left, ML – top right, MaxEnt – bottom).

Figure 10.8. $Accuracy_a$ for the reconstruction results obtained by different methods with the synthetic activity originated from spectrum I (9 bins) simulated for Gradel-Fusion NSD 35 2-DT-C-W.

Figure 10.9. The reconstructed spectra (16 bins) obtained with the synthetic data simulated for Gradel-Fusion NSD 35 2-DT-C-W by different methods (TR and MFI – top left, ML – top right, MaxEnt – bottom).

Figure 10.10. $Accurcay_s$ (16 bins) for the reconstruction results obtained by different methods with the synthetic activity originated from spectrum I (16 bins) simulated for Gradel-Fusion NSD 35 2-DT-C-W (TR and MFI – top left, ML – top right, MaxEnt – bottom).

Figure 10.11. $Accuracy_a$ for the reconstruction results obtained by different methods with the synthetic activity originated from spectrum I (16 bins) simulated for Gradel-Fusion NSD 35 2-DT-C-W.

Figure 10.12. The spectra (51 bins) reconstructed by the TR and MFI methods using the synthetic data simulated for Gradel-Fusion NSD 35 2-DT-C-W.

Figure 10.13. The spectra (51 bins) reconstructed by the ML method using the synthetic data simulated for Gradel-Fusion NSD 35 2-DT-C-W.

Figure 10.14. The spectra (51 bins) reconstructed by the MaxEnt method using the synthetic data simulated for Gradel-Fusion NSD 35 2-DT-C-W.

Figure 10.15. $Accuracy_a$ for the reconstruction results obtained by different methods with the synthetic activity originated from spectrum I (51 bins) simulated for Gradel-Fusion NSD 35 2-DT-C-W.

Figure 10.16. The average spectrum (51 bins) from the TR, MFI, ML, and MaxEnt results obtained using the synthetic data simulated for Gradel-Fusion NSD 35 2-DT-C-W.

Figure 10.17. The spectra (71 bins) reconstructed by the TR and MFI methods using the synthetic data simulated for Gradel-Fusion NSD 35 2-DT-C-W.

Figure 10.18. The spectra (71 bins) reconstructed by the ML method using the synthetic data simulated for Gradel-Fusion NSD 35 2-DT-C-W.

Figure 10.19. The spectra (71 bins) reconstructed by the MaxEnt method using the synthetic data simulated for Gradel-Fusion NSD 35 2-DT-C-W.

Figure 10.20. $Accuracy_a$ for the reconstruction results obtained by different methods with the synthetic activity originated from spectrum I (71 bins) simulated for Gradel-Fusion NSD 35 2-DT-C-W.

Figure 10.21. The average spectrum (71 bins) from the MFI, ML, and MaxEnt results obtained using the synthetic data simulated for Gradel-Fusion NSD 35 2-DT-C-W.

Figure 10.58. The average spectrum (76 bins) from the MFI, ML, and MaxEnt results obtained using the experimental data from foils irradiation by Sodern Genie 16C.

List of tables

Table 10.2. The results of the neutron activation measurement of Gradel-Fusion NSD 35 2-DT-C-W measured by the BrilLanCe scintillation detector.

Table 10.3. The synthetic specific activity calculated by the FISPACT-II inventory code with spectrum I for Gradel-Fusion NSD 35 2-DT-C-W analysis.

Table 10.4. Comparison of C_R for 9 bin spectra obtained with the synthetic data simulated for Gradel-Fusion NSD 35 2-DT-C-W by different methods.

Table 10.5. Comparison of C_R for 16 bin spectra obtained with the synthetic data simulated for Gradel-Fusion NSD 35 2-DT-C-W by different methods.

Table 10.6. The accuracies$_s$, accuracies$_a$, and C_R obtained for the synthetic data simulated for Gradel-Fusion NSD 35 2-DT-C-W and 51 bin structure by different methods.

Table 10.7. The accuracies$_s$, accuracies$_a$, and C_R obtained for the synthetic data simulated for Gradel-Fusion NSD 35 2-DT-C-W and 71 bin structure by different methods.

Table 10.8. Results of the neutron activation measurement of Sodern Genie 16C measured by the HPGe detector.

Table 10.9. Synthetic specific activity obtained by the FISPACT-II inventory code with spectrum I for Sodern Genie 16C analysis.

Table 10.10. The accuracies$_s$, accuracies$_a$, and C_R obtained for the synthetic data simulated for Sodern Genie 16C and 51 bin structure by different methods.

Table 10.11. The accuracies$_s$, accuracies$_a$, and C_R obtained for the synthetic data simulated for Sodern Genie 16C and 76 bin structure by different methods.

Part I: Introduction

Chapter 1: Nuclear fusion

Increasing demand for environment-friendly energy production began the growth of interest in nuclear fusion. Compared to conventional energy sources, fusion has inviting features in terms of safety and fuel reserves [Fre2010].

The binding energy of an atomic nucleus varies with atomic number and mass. For elements lighter than iron, the binding energy increase with the atomic mass. Consequently, the merging of two light nuclei causes a release of energy. Energy production by nuclear reactions naturally takes place in stars. It is achieved in an environment with a very high temperature (above 10^6 K), and the process is called thermonuclear fusion [Kra1988].

At this specific temperature, the matter is in a plasma state. The plasma is ionised and decomposed for negatively charged electrons and positively charged ions but remains electrically neutral. Particles behave collectively. It means that plasma is controlled by long-range electromagnetic interactions and resembles a fluid [Miy2006]. The appearance of the fusion reactions also depends on the plasma density and frequency of the ions' collisions. In stars, gravitational forces prevent the escape of particles and radiation from plasma [Rol1988].

1.1 Thermonuclear reactions

The primary reaction in the stars is the fusion of hydrogen to helium. In a laboratory, the fusion of the hydrogen isotopes is most promising because of the high energy released in this reaction and high cross-section for relatively low temperature compared to other ones. These properties make reactions of deuterium-deuterium (DD) and deuterium-tritium (DT) most commonly used in fusion devices. The main reactions between hydrogen isotopes are [Atz2004]:

$$D + D \rightarrow T + p + 4.0\ \text{MeV}, \tag{1.1.1}$$

$$D + D \rightarrow {}^3He + n + 3.3\ \text{MeV}, \tag{1.1.2}$$

$$D + T \rightarrow {}^4He + n + 17.6\ \text{MeV}, \tag{1.1.3}$$

$$T + T \rightarrow {}^4He + 2n + 11.3\ \text{MeV}. \tag{1.1.4}$$

The second DT reaction, omitted from this list, produces an excited ^{5}He nucleus which relaxes to the ground state or the 1st excited state via emission of 16.8 MeV or 13.5 MeV gamma-rays, respectively. However, the gamma-to-neutron branching ratio for DT fusion is about 10^{-5}. Therefore, the influence of this reaction on the plasma is negligible. The branching ratio of two possible DD reactions is 50% [Kim2012].

The probability of the reaction is described by a cross-section σ. It strongly depends on the energy of incident particles. Classically, the cross-section is a geometrical probability of the particle contact. Quantum mechanics allows a situation when a particle with insufficient energy to overcome the Coulomb barrier passes it. It is called the tunnelling effect. The overall cross-section needs to consider incident particle wavelength and tunnelling probability through the potential barrier. The cross-sections of the thermonuclear reactions are lower than 10 b [Sas2008].

The cross-sections for the mentioned processes are shown in figure 1.1 [Atz2004]. The figure also contains other reactions that are of interest to controlled fusion but are not the subject of this thesis.

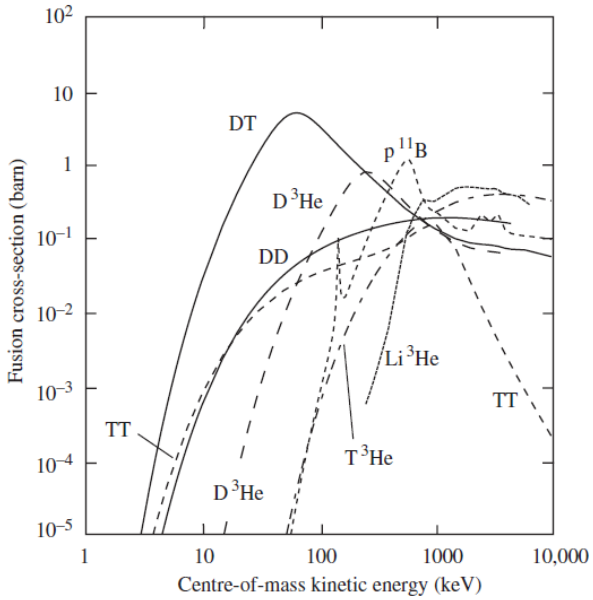

Figure 1.1 Cross-sections of fusion reactions (DD represents the sum of the two possible reactions) [Atz2004].

The DT reaction has the highest cross-section with the maximum for the lowest ion temperature and releases the most significant amount of energy. Radioactivity of tritium with a half-life of about 12 years limits the efficient collection of this isotope and reduces the safety of the plasma device. Scientists have been working on breeding systems for future reactors to solve the tritium retention problem. Deuterium is stable and has a natural abundance in the Earth's ocean and seawater. The DD fusion is more difficult to achieve. Present devices commonly use the DD plasma due to safety and economic reasons.

Number of reactions per cubic centimetre per second, i.e. reaction rate is equal to [Rol1988]:

$$r_r = N_j N_i \upsilon\sigma(\upsilon), \tag{1.1.5}$$

where $N_{i/j}$ is the density of particles species *i/j*.
The velocity of the ions in the plasma varies over a wide range of values and depends on a temperature. In thermal equilibrium, the probability that the ion has velocity $\vec{v}$ is described by the Maxwell-Boltzmann distribution:

$$f(\vec{v}) = \left(\frac{m}{2\pi k_B T}\right)^{3/2} e^{-\frac{m\vec{v}^2}{2k_B T}}, \tag{1.1.6}$$

where k_B is the Boltzmann constant, *T* is the temperature, and *m* is the particle mass.
The $\upsilon\sigma(\upsilon)$ should be replaced by average over the velocity distribution $\langle\upsilon\sigma\rangle$, which is called reaction rate per particle pair, to obtain the total reaction rate. The reaction rate per particle per reaction of two different nuclei is defined by the double integral over two velocities distributions where particle mass can be replaced by the reduced mass:

$$\mu = \frac{m_i m_j}{(m_i + m_j)}, \tag{1.1.7}$$

and the velocity represents relative value. The reaction rate per particle pair is equal to [Rol1988]:

$$\langle \upsilon\sigma \rangle = \left(\frac{8}{\pi\mu}\right)^{1/2} \frac{1}{(k_B T)^{3/2}} \int_0^\infty E\sigma(E)\, e^{-\frac{E}{k_B T}} dE, \quad (1.1.8)$$

where *E* represents the kinetic energy.
The reaction rate per particle pair can be parametrised by experimental data in dependence on the temperature. In the low-temperature plasma approximation, the fusion reaction rate per particle pair can be calculated by:

$$\langle \upsilon\sigma \rangle = k_{ij}\sqrt{T} e^{-3\eta_{ij} T^{-1/3}}, \quad (1.1.9)$$

where k_{ij} and η_{ij} are constants characterising the reaction [Wol1999].
The total reaction rate for fusion reactions is:

$$r_r = \frac{N_j N_i}{1+\delta_{ij}} \langle \upsilon\sigma \rangle, \quad (1.1.10)$$

where δ_{ij} is the Kronecker delta that prevents counting twice if identical particles react.
The maximum of the Maxwell-Boltzmann distribution is at energy equal to $k_B T$, and the tunnelling probability increases with the energy. In consequence of these effects, fusion reactions occur in a relatively narrow energy window [Rol1988]. The DT reaction has a resonance at about 100 keV. The probability of the reaction at this energy is the highest.

Neutrons produced in fusion reactions escape from the plasma without interactions, but charged alpha particles transfer their energy by collisions to the plasma [Nis2000].

High temperature and plasma radiation emission make the controlled fusion a demanding challenge. The main problem in achieving controlled fusion is the confinement of the high-temperature plasma.

1.2 Plasma confinement

The controlled thermonuclear fusion aims to provide a self-sustained plasma that produces energy. The state of plasma, when the self-heating by alpha particles is sufficient to maintain the temperature that allows fusion reactions, is called ignition. For energy generation, plasma heat needs to be higher than radiation losses. The Lawson criterion describes the plasma ignition conditions. It defines the minimum value of the plasma density (n) and confinement time (τ) product for a given temperature [Nis2013]. The fusion reactor design requires a configuration that ensures the fulfilment of thermonuclear fusion conditions and separates plasma from reactor walls [Wes2004]. There are two basic confinement types:

- magnetic – relatively low-density plasma ($n \approx 10^{20}$ m^{-3}) confined by a magnetic field with relatively long confinement time (≈ s),
- inertial – driven by lasers, extremely dense plasma ($n \approx 10^{31}$ m^{-3}) with short confinement time (≈ ns) [Nis2013].

This thesis focuses on the magnetic confinement.

A strong magnetic field confines the charged particles inside the defined area away from a device's walls. Trapped ions move spiral along the magnetic field because of the Lorentz force. Different kinds of devices can be distinguished based on the magnetic field configuration:

- open systems – magnetic mirrors are linear machines with axial magnetic field and converging fields at the ends,
- pinch devices – cylindrical devices consist of coaxial electrodes and induce plasma compression by the magnetic field produced by an electric current discharge,
- toroidal systems – closed systems that have been developed to avoid particle loss along magnetic field lines. Toroidal bending of the solenoid results in a non-uniform magnetic field

with higher values at the inner side of the torus (HFS – High-Field Side) and lower on the outer side where solenoid coils are further to each other (LFS – Low-Field Side). The most commonly used toroidal device is a tokamak. More complicated torus shape machines are stellarators. Magnetic coils produce a closed helical magnetic field, which confines the particles away from the device walls [Bit2013]. The confinement is restricted by radiation losses, convection processes and heat conduction. It is also dependent on Coulomb collisions. In these devices, ohmic heating is used to increase the temperature of the gas, but it is not enough for the ignition. Auxiliary heating is required to overcome radiation losses. One option of heating is neutral beam injection (NBI). High-energy neutrals are injected into the plasma and transfer their energy by the collisions with the plasma particles. Another auxiliary heating method is electron (ECRH) or ion (ICRH) cyclotron heating, where radio-frequency waves are used. The electromagnetic waves are launched into the plasma, where resonant absorption takes place. The auxiliary heating power needs to be higher than the losses caused by plasma radiation [Fre2010].

The particles in the external magnetic field responsible for plasma confinement behave collectively. Macroscopically, plasma can be described as a quasi-neutral fluid. In the most advanced model, plasma is treated as two fluids; electrons and positively charged ions with different velocities. The difference in electric charge causes the possibility of phenomena that cannot be seen in a neutral fluid. The simple approximation of plasma by the fluid model is called magnetohydrodynamics (MHD). The MHD is based on the Maxwell equations coupled with hydrodynamics. These equations describe the fluid, electric and magnetic fields that vary on the exact length and time scale. The motion of the fluid is characterised by elements of volume small enough that variation of macroscopic quantities across its dimension is negligible, and the number of particles in this element is relatively large to justify the use of statistical physics [Boy2003]. The MHD effects can occur when fluid dynamics are strongly related to the magnetic field, and the thermal diffusion impact is smaller than convection. These conditions raise the most significant feature of MHD that the magnetic field is “frozen in” plasma [Fri2004].

In the plasma, many phenomena cause changes in the kinetic energy of particles and its destabilisation. The MHD theory can describe the processes that act to destroy the plasma equilibrium. The different approach to describing the plasma is a kinetic theory that includes information about interactions between particles [Fri2004].

1.3 Plasma radiation

The source of energy in the plasma is fusion reactions. The energy carriers are different types of radiation. The fusion reactions produce neutrons and high energetic ions. Most of the neutrons escape from the plasma without interactions [Sas2008]. The fusion reactions themselves, as well as interactions between fast ions produced in reactions or connected with the external heating, are the origin of the gamma-ray emission [Sas2008]. The plasma is an ionised gas and the source of the full spectrum of electromagnetic radiation. The astrophysical plasma emits the black body spectrum. The plasma in the fusion devices has a more complicated energy spectrum because the degrees of ionisation depends on various operating parameters. The radiation sources are fuel ions (hydrogen isotopes) and impurities originating from plasma interactions with the device walls' [Str2008]. The radiation production is due to atomic processes (line and recombination radiation) and charged particles' motion (bremsstrahlung, cyclotron and synchrotron radiation) [Coo1966]. The plasma in the fusion devices is not fully ionised, and neutral atoms can be the product of recombination [Sta1981]. Neutral particle analysers measure the escaping particles to study the plasma ion characteristics [Kar2006]. The radiation type, energy and yield depend mainly on the plasma composition, temperature, and density [Sun2013].

1.3.1 Neutron radiation

The fusion reactions in plasma are the primary source of neutrons. The DD and DT reactions produce 2.5-MeV and 14.1-MeV neutrons, respectively. Continuous neutron energy spectrum up to 8.8 MeV is produced in TT reactions. Tritons with the energy of 1 MeV produced in the second DD reaction can react with the plasma. By this reaction, 14.1-MeV neutrons are produced (triton burn-up) in the pure deuterium plasma. Non-fusion neutrons are also observed in the plasma. The sources are interactions of protons, deuterons and helium ions with impurities and photoinduced reactions. In the plasma, there are thermal ions and ions accelerated by auxiliary heating. Therefore, three components: thermonuclear, beam-thermal and beam-beam reactions, contribute to the total reaction rate. The beam-thermal reaction plays a dominant role in the DD plasma because of the increasing cross-section with the energy [Sas2008].

The energy of neutrons depends on the kinetic energy of reacting ions and the energy released in the process. The conservation of momentum law requires that in D(D,n)^{3}He reaction discussed in the centre-of-mass frame, the velocity ($\vec{u}$) of helium is equal to [Mun2016]:

$$m_n\overrightarrow{u_n} + m_{He}\overrightarrow{u_{He}} = 0 \underset{\overrightarrow{u_{He}}}{\Longrightarrow} \overrightarrow{u_{He}} = -\frac{m_n\overrightarrow{u_n}}{m_{He}}. \tag{1.3.1.1}$$

The conservation of energy law indicates that [Mun2016]:

$$Q_F + K = \frac{m_n\overrightarrow{u_n}^2}{2} + \frac{m_{He}\overrightarrow{u_{He}}^2}{2} \underset{u_n}{\Rightarrow} |u_n| = \sqrt{\frac{2(Q_F+K)}{m_n}\frac{m_{He}}{m_n+m_{He}}}, \tag{1.3.1.2}$$

where *K* is the relative kinetic energy of reacting particles, and Q_F is the energy released in the reaction.

If the centre-of-mass have $\vec{V}$ velocity in the lab frame, the neutron velocity is [Mun2016]:

$$\overrightarrow{v_n} = \vec{V} - \overrightarrow{u_n}, \tag{1.3.1.3}$$

Consequently, the kinetic energy of the neutron is:

$$E_n = \frac{m_n}{2}\left(\vec{V}^2 + \overrightarrow{u_n}^2 + 2\vec{V}\cdot\overrightarrow{u_n}\right) = \frac{m_n}{2}\vec{V}^2 + (Q_F+K)\left(\frac{m_{He}}{m_n+m_{He}}\right) + V\sqrt{(Q_F+K)\frac{2m_nm_{He}}{m_n+m_{He}}}\cos\zeta, \tag{1.3.1.4}$$

where ζ is the angle between velocity in the lab frame and the neutron velocity in the centre-of-mass frame [Mun2016].

The mean energy of the emitted neutrons in the DD reaction is 2.5 MeV and $\vec{V}^2$ and *K* are related to its small shifts. The angle ζ is a random variable. For thermonuclear reactions, neutron emission can be assumed as isotropic. Therefore, the mean value, of all possible directions, of the ζ angle is zero. The mean energy of neutrons is higher than the fraction from the fusion Q-value, which corresponds to the cold plasma approximation when *V*=0 and *K*=0. The mean energy of reacting particles can be calculated by implementing neutron energy to the equation for reaction rate per particle pair and integration over *V* [Hut2002]:

$$\bar{E} = \frac{7}{6}T + \frac{\eta_{DD}}{2}T^{2/3}. \tag{1.3.1.5}$$

The general equation for the neutron spectrum of defined emission direction is defined as [Wol1999]:

$$\frac{d^2N}{d\Omega_{lab}d\bar{E}} = \frac{n_i n_j}{1+\delta_{ij}} \iint f_A(v_A) f_B(v_B) \frac{d^2\sigma}{d\Omega_{lab}dE} \delta(E - E_n)|v_A - v_B|\, dv_A dv_B, \quad (1.3.1.6)$$

The average neutron energy over the emission angle is equal to:

$$\bar{E}_n = \frac{m_n}{2}\vec{V}^2 + (Q_F + \bar{K})\left(\frac{m_{He}}{m_n + m_{He}}\right), \quad (1.3.1.7)$$

After substitution to the equation (1.3.1.6), the Maxwellian distributions and expansion of the differential cross-section *dσ/dΩ* in the Legendre polynomials, the energy distribution of the neuron emission is approximately Gaussian [Wol1999]:

$$\frac{d^2N}{d\Omega_{lab}d\bar{E}} = \frac{1}{\sqrt{2\pi}\sigma_s} e^{-(E_n - \overline{E_n})^2/2{\sigma_s}^2}, \quad (1.3.1.8)$$

where the standard deviation of the distribution is equal to:

$$\sigma_s = \sqrt{\frac{4kT\bar{E}m_n}{m_n + m_{He}}}. \quad (1.3.1.9)$$

The plasma temperature determines the full width at half maximum (FWHM) of the neutron spectrum equal to $2\sigma_s\sqrt{ln2}$. The beam-target mechanism causes the deviation from isotropic emission. The neutron emission direction depends on the reacting particles' movement pathway [Wol1999].

1.3.2 Electromagnetic radiation

Atomic processes in an ionised matter are the primary source of electromagnetic radiation. In the tokamak plasma, radiation above plasma frequency propagates, and its spectrum might be modified by collective effects connected with the ion and electrons interactions. In fusion devices, the reabsorption of the radiation energy is usually very low [Coo1966]. The main processes responsible for electromagnetic radiation emission are described below.

In the plasma, electron transitions from an excited bound state to another lower state occur. The emitted energy is characteristic of a given element. Emission of the line radiation covers a range from infrared to X-rays. The significant radiation sources are impurities like oxygen and carbon produced in the detachment effects of molecules absorbed in the plasma-facing components. The damage to the device's internal structures by sputtering or arcing produces intermediate-Z impurities like iron and more heavy ions like tungsten. The content of the impurities depends on the materials used to build the plasma-facing components. The intensity of the line radiation is determined locally by electron density and its temperature, ions concentration, and coefficient of populating the excited states. Origins of the excited states are: ionisation, collisional excitation, charge exchange and recombination [Isl1984].

The capture of a free electron to the bound state is another source of electromagnetic radiation. The electron's kinetic energy plus the difference between the ionisation energy of the ion and its final state is emitted through recombination radiation. Free electrons' possible energy levels are continuous; therefore, emitted radiation has a continuous spectrum. Recombination radiation power can be found as integration over energy in Maxwellian distribution. Plasma emissivity contains the recombination radiation only if the photon energy is higher than the ionisation energy of the involved quantum state [Boy2003].

Another radiation source is a fast electron slowing down in the electromagnetic field of the ions. This free-free transition is called Bremsstrahlung. The range of the emitted radiation spectrum is broad, from microwave to X-ray. The deceleration effect is connected with the electron interaction with the Coulomb field of other particles. During the deflection of the motion trajectory, the particle loses part of its energy. The electron energy loss is emitted as a photon. If the electron is completely stopped, the emitted energy equals its kinetic energy before the collision. The spectrum of Bremsstrahlung radiation is continuous, and the intensity of higher frequencies increases with the braking electron's energy [Zoh2017].

The electron moving in a uniform magnetic field is a source of cyclotron radiation. The spectrum of the cyclotron radiation is discrete, and the magnitude of emissivity depends strongly on the motion direction. The relative emission intensity depends on the temperature of the electrons. Synchrotron radiation refers to electrons with energy about tens of keV and ultra-relativistic particles. The radiation can be divided into two modes with an electric field parallel or perpendicular to the magnetic field. Synchrotron radiation for ultra-relativistic electrons is significant only for cosmic plasma [Boy2003].

1.3.3 Neutral particles

Plasma usually is not fully ionised. Neutral atoms are continuously formed in plasma in the charge-exchange process and plasma interactions with device walls. At the plasma's edge, the dominant process of producing the neutral particles is a dissociation of hydrogen released from vessel walls induced by electrons. The produced neutrals can move across the magnetic field without collision and escape from the plasma or interact with other particles. The collision may result in charge-exchange or ionisation. The charge-exchange process is repeated until the new neutrals are ionised or escaped. The charge-exchange is more probable than ionisation at low energies, and its cross-section increases with decreasing energy. If the time when the neutral atom and ion are close to each other increases, the possibility of electron transfer is higher. The density of neutral atoms is much higher on the plasma edge than in the core. The flux of escaping particles depends on their density, velocity, probability of collision and strongly on the plasma temperature [Hut2002, Wes2004].

1.4 Power balance

Total radiation losses significantly impact the power balance in the fusion devices. The power losses need to be compensated by the heating power of alpha particles (P_α) and external sources (P_{AH}) to achieve the steady-state. The energy produced in the steady-state fusion is described by a gain factor Q. The gain factor is the ratio of fusion power to auxiliary supplied input power. If $Q=1$, the break-even state is reached. Plasma is self-sustained if Q is much higher than 1.

The overall heating power P_H required to reach the steady-state is:

$$P_H = P_\alpha + P_{AH} - P_{LOS}, \tag{1.4.1}$$

where P_{LOS} is the total radiation loss [Kik2012].
Power transferred to the plasma by alpha particles depends on the plasma volume V_p and is given by the following formula:

$$P_\alpha = {n_e}^2 \langle \sigma v \rangle E_\alpha \frac{V_p}{2}, \tag{1.4.2}$$

where E_α is the energy carried by the alpha particle [Kik2012].
The bremsstrahlung radiation has the highest contribution to the radiation loss.

Another way to define the required heating power is:

$$P_H = P_{trans} + \frac{dE}{dt}, \tag{1.4.3}$$

where P_{trans} is the energy lost through all transport processes, and *dE/dt* is equal to the power required to increase the plasma kinetic energy [Kik2012]:

$$K = 3n_e kT_e V_p. \tag{1.4.4}$$

The power balance represented in the confinement time dependence leads to the Lawson criterion [Kik2012].

Chapter 2: Plasma devices

The most popular and prospective plasma devices intended for research in plasma physics and thermonuclear fusion are toroidal magnetic confinement machines, i.e. tokamak and stellarator. This thesis focuses on the studies of the physics phenomena in tokamaks. Another device included in the analysis is a portable neutron generator based on the DT reaction. The portable neutron generators are commonly used in research for calibration and tests of neutron diagnostics and data acquisition systems before their application to tokamaks.

2.1 Tokamak

The magnetic confinement plasma device's leading idea is a tokamak, designed in the Soviet Union by Sakharov and Tamm [Pie2010]. The name tokamak is an acronym from Russian words that means toroidal chamber with magnetic field coils. The scheme of the tokamak is presented in figure 2.1. The ring-like coils around the torus produce a toroidal field (TF). The curvature of the field lines creates charge separation by opposite particles' drifts, and the electric field causes plasma loss. The poloidal field (PF) component is needed to cancel the drifts. The central solenoid (CS) induces a plasma current, which flows in the toroidal field direction to form the PF. The superposition of two magnetic field components produces helical lines that confine the plasma inside the torus. The formed magnetic field creates loops in the poloidal plane. The nested toroidal lines produce closed magnetic flux surfaces. The toroidal currents induced by the poloidal magnetic field coils control the shape of the plasma [Kik2012].

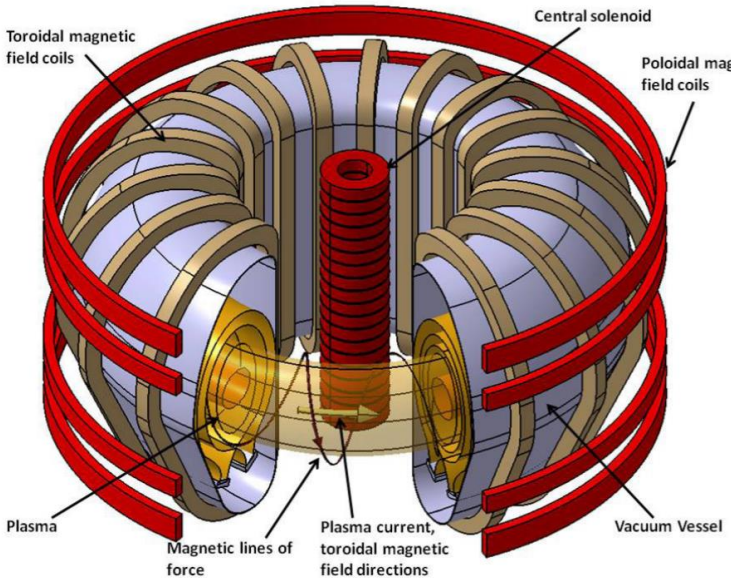

Figure 2.1. The coils configuration in a tokamak [Kik2012].

The strength of the magnetic field determines the plasma stability and pressure. High pressure is required for the fusion reactions. The technological limitations restrict the pressure magnitude. The energy confinement time decreases with pressure but increases with the plasma current [Wes2004].

The tokamak plasma density is typically around $10^{19} – 10^{20}$ m^{-3}. The presence of impurities causes the growth of the radiation losses and also dilutes the fuel gas. The impurities content can be reduced by good plasma separation from the vessel walls achieved by a material limiter or divertor [Wes2004]. The limiter is a solid surface typically made from carbon, molybdenum or tungsten. It defines the edge of the plasma and decreases toroidal asymmetry. The divertor is the bottom or top structure of tokamak with toroidal conductors that produce an additional

magnetic field with a separatrix. The separatrix divides confined plasma into closed and open magnetic field lines that terminate on the divertor walls [Kik2012].

The equilibrium state of the tokamak is defined by the internal balance between forces exerted by the magnetic field and pressure. The total magnetic field results from the superimposition of the internal field induced by the currents and the field created by the coils. Ampere's law describes the basic shape of the toroidal magnetic field (B_φ), and its magnitude can be calculated from:

$$B_\varphi = \frac{\mu_0 I_p}{2\pi R_0}, \tag{2.1.1}$$

where μ_0 is the vacuum permeability, I_p is the plasma current, and R_0 equals the major tokamak radius.

The radial variation of the magnetic field across the plasma can be estimated as:

$$\Delta B_\varphi \approx B_{\varphi 0} \frac{2a}{R_0}, \tag{2.1.2}$$

where a is the minor torus radius, $B_{\varphi 0}$ is the magnetic field in the mid-plane where the distance from the major axis of the torus is equal to the major radius R_0 [Wes2004].

The toroidal current profile influences the distribution of the poloidal magnetic field. The electrical conductivity determines the steady-state current of the plasma and increases with the electron temperature. Therefore, the current has a maximum in the centre, where the temperature is the highest. The combination of radial gradients of the temperature, density and configuration of the magnetic field causes the rise of an additional part of the current called bootstrap current [Wes2004].

The total magnetic field creates an infinite set of nested magnetic surfaces in the poloidal plane. The magnetic field lines follow a helical path around the torus. The direction of the magnetic field is different on each surface. The magnetic shear influences plasma stability and is described by a radial change of the safety factor parameter. The main part of the particle motion is gyration along helical orbits along the magnetic field. In low temperatures (≈ 1 keV), particles collide frequently and can be described as fluid. At high temperatures (a few keV), collisions are less frequent, and orbits are affected by a toroidal magnetic field [Fre2010].

A tokamak equilibrium can be described by the pressure and forces related to the magnetic field. The axisymmetric equilibrium is independent of toroidal angle. The primary condition of the equilibrium is the compensation of all forces at every point. The balance between magnetic force and plasma pressure gradient ($\vec{\nabla} p$) can be described as:

$$\vec{j} \times \vec{B} = \vec{\nabla} p\,, \tag{2.1.3}$$

where $\vec{j}$ is the plasma current density.

The equation (2.1.3) implies that the pressure gradient along the magnetic lines is zero, and pressure is constant on the magnetic surfaces. A flux function Ψ represents a poloidal magnetic flux inside the magnetic surface, which are called flux surfaces because they are described by the constant values of Ψ [Dha2012].

The toroidal currents heat the plasma by ohmic phenomena, but it does not provide the ignition temperature. The auxiliary heating methods are essential for the fusion reactions. Neutral Beam Injection heating (NBI) is the insertion of the high-energy hydrogen isotopes through the plasma across the magnetic field [Nis2013]. The beam passes freely through the plasma because the magnetic field does not affect neutral atoms. The plasma traps the injected nuclei after reionisation with electrons or charge exchange with ions [Tel1981]. The injected atoms are ionised, slowed and thermalised. The energy is transferred by Coulomb

collisions. Collisions with electrons do not change the isotopes' trajectory because of the small scattering angles. The slowing down electrons transfer the energy to the plasma and heat fuel ions. Velocities of the particles from the beam are principally perpendicular to the primary beam trajectory after collision with the fuel ions [Wes2004]. Another way to heat plasma is to act by radio frequency (RF) waves. The electric field of a wave propagating in the plasma accelerates ions and electrons, which heat the plasma by collisions. This mechanism is not efficient in high-temperature plasma. The waves' energy can be transferred through a collisionless phenomenon of resonant absorption. The plasma has a couple of resonant frequencies, dependent on the density and magnetic field, for which strong absorption or reflection occurs. The power from the RF generator is transported by a transmission line and antenna that launches electromagnetic waves into the plasma. The wave propagates through the edge into the absorption zone and is converted into the resonant particles' kinetic energy. Then, the current is driven, or resonant particles collide with others. There are two types of frequency ranges used for heating. The Ion Cyclotron Resonance Heating (ICRH) uses frequency in the lower range (MHz). The ICRH provides a significant fraction of the heating into bulk plasma. It asymmetrically heats the minority of ions with low efficiency, but it produces localised current by interaction with electrons. The Electron Cyclotron Resonance Heating (ECRH) is based on a higher frequency range (GHz). The electron resonance waves transfer their energy in a localised area with good efficiency [Kee2012]. The NBI, ICRH, and ECRH are sources of high-energy ions with a higher cross-section for the fusion reactions. In present tokamaks, where plasma ions distributions are not Maxwellian, neutrons are produced dominantly in beam-thermal reactions connected with the heating [Wes2004].

The stable equilibrium state is a condition for achieving a self-sustain thermonuclear plasma. In tokamaks, the plasma confinement is destroyed by perturbative forces. The stability of the equilibrium depends on perturbations that can grow, oscillate or elapse. Scientists sought advanced regimes allowing for operation with depreciated impact from instabilities and improved confinement [Zoh2017]. The most popular are L- (low confinement) and H-mode (high-energy confinement). The MHD instability called the Edge Localised Mode (ELM) is the problem in the H-mode. These periodic heat transfer and particle ejections from the plasma core cause particles loss on the plasma edge. The way to reduce the ELMs is by operating in the quiescent H-mode (QH). The ELMs are stabilised by the result of the increased edge particle transport [Gar2011]. Another regime is the improved mode (I-mode), which is characterised by stationary pedestal temperature and the ELMs' absence [Why2010]. There is also the Enhanced D-Alpha mode (EDA-mode), where particle transport results in good confinement without impurity accumulation [Gre2000]. The advanced modes are difficult to achieve on the existing tokamaks.

The perturbations in the magnetic field are the source of the particle orbits modification and perturbation in currents [Tel1981]. The MHD instabilities obstruct the creation of satisfactory magnetic configurations, energy confinement and steady-state operation in the H-mode. An understanding of their nature is essential for plasma control. Most of the instabilities cause characteristic oscillations in the measurable parameters and energy loss, especially in the divertor region. Persistent magnetic islands in the plasma core are connected with issues limiting the performance of the standard and advanced operating modes. The MHD instabilities can be controlled by a localised current drive and fast ion generation. Many experiments aim to avoid or mitigate the influence of the MHD instabilities and minimise the disruptions [Hen2007]. The thermal instabilities can trigger sawtooth oscillations. It is quasi-periodical relaxation in the plasma centre that causes sharp collapses in the temperature and density. The fluctuations are observed in the characteristic X-ray emission. The instability leads to plasma current collapse and discharge termination [Wes2004].

The example of the measured plasma parameters in function of time during DT discharge on JET tokamak is presented in figure 2.2. There are many experiments with tokamaks around

the world. The research aims to develop the tokamak that achieves the ignition and produces more power than is supplied for operation. The international collaboration focuses on the project of the largest device called ITER tokamak, which will accomplish a relatively long time operation with a high gain factor. During this thesis preparation, the largest operating tokamak is JET (Joint European Torus). At this time, the experiments on JET are aimed at testing the operation scenarios considered for ITER.

In the tokamak, the toroidal current production required for plasma confinement is technologically limited in time. Therefore, a continuous operation is not possible. Another type of researched toroidal device is called a stellarator. The stellarator consists of a vacuum vessel of isomorphic shape. The coils produce a helically twisted magnetic field. There is no plasma current, and the magnetic field is produced only by the external coils. If the magnetic field is twisted, the magnetic forces eliminate the plasma drift. It makes a stellarator suitable for continuous operation [Zoh2017, Bei1990].

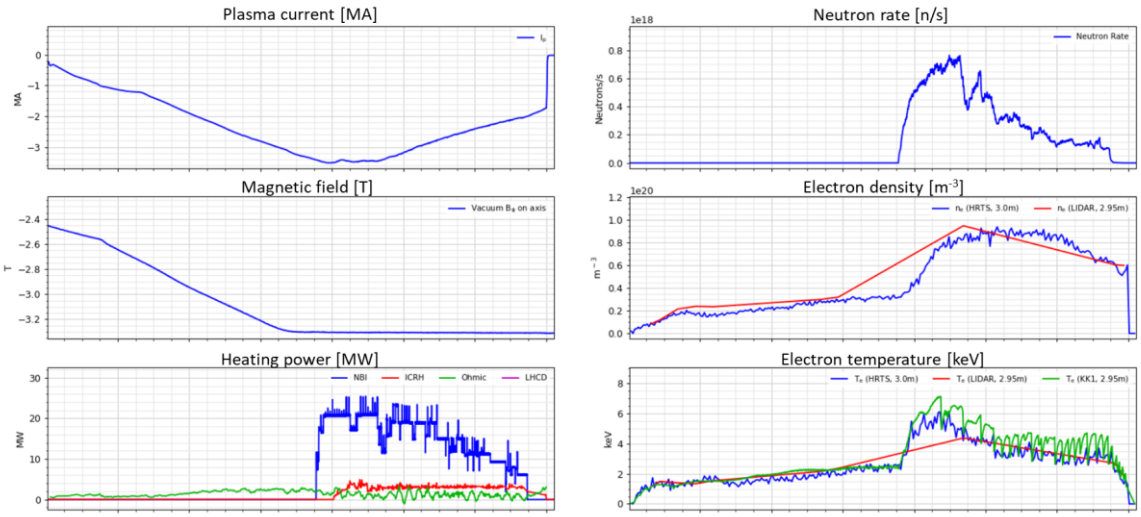

Figure 2.2. The example of plasma parameters (plasma current, neutron rate, magnetic field, electron density, NBI and ICRH power, electron temperature) time evolution during #99522 discharge on JET tokamak.

2.1.1 ITER

The ITER project began in 1985. Name ITER means “the way” in Latin, way to carbon-free energy. The European Union, Russia, the USA, Japan, India, China, and Korea collaborate on developing the tokamak fusion reactor. ITER will be the experimental machine that leads to building the fusion reactor. It will produce up to 500 MW output fusion power with a *Q* factor of power amplification equal to 10. The overview of ITER parameters is presented in table 2.1. In ITER, the deuterium-tritium mixture is planned to be used as the fuel. The planned discharge duration will be 400 s to 600 s [Hor2015]. The fusion power production in ITER will be derived from thermonuclear reactions. In the burning plasma, the velocity of the ions has Maxwellian distribution. Therefore, neutron production in ITER will be dominated by thermonuclear reactions. The total neutron yield during the full DT operation will be about 10^{20} n/s [Sas2010].

The scientific priorities of ITER are:

- Achievement of the ratio of fusion power to heating power at least 10, and discharge duration satisfactory for stationary conditions of the timescales characteristic of plasma processes,
- Achievement of the ratio of fusion power to heating power at least 5 for steady-state operation with a non-inductive current drive.

ITER tokamak will be a testbed for future reactors. It will explore new operation regimes and research plasma physic's supplementary aspects. This project leads to understanding, controlling and optimising the plasma. The new materials and components will be examined there. It helps to demonstrate the economic attractiveness of the tokamak [Sip2005].

This thesis was written when ITER tokamak was in the construction stage. The methods prepared for this project were developed based on synthetic data analysis. The validation and verification should be made with the experimental data from other devices.

Table 2.1. The design parameters of ITER tokamak [Hor2015].

Major radius	6.2	[m]
Minor radius	2	[m]
Elongation	1.7	
Plasma volume	840	[m^3]
Magnetic field on-axis	5.3	[T]
Plasma current	16	[MA]
NBI heating power	33 - 55	[MW]
ICRH heating power	20 - 40	[MW]
ECRH heating power	20 - 40	[MW]
Current drive	15	[MA]
Central density	10^{20}	[m^{-3}]
Electron temperature	21	[keV]
Ion temperature	18	[keV]
Fusion energy	120	[GJ in 200s]

2.1.2 JET

The Joint European Torus (JET) project started in 1972 and has aimed at plasma studies in conditions and dimensions approaching the needs of thermonuclear reactors. The scientific purposes of the project are the studies of:

- plasma confinement and its properties,
- alpha particles behaviour,
- plasma heating methods,
- plasma interaction with tokamak walls [Gib1990].

JET tokamak was built in Culham (United Kingdom) and started operation in 1983 [Wes2000]. The construction demanded the application of the most advanced engineering techniques and new technologies available at that time. JET basic parameters are presented in table 2.2 [Ber1990]. Over the years, the tokamak has been modified to improve plasma performance. The project assumed construction of the tokamak in limiter configuration with good control of the currents and a long discharge duration (≈ 20s). The plasma confinement requires a power supply of up to 800 MW. The achieved confinement time with ohmic heating only was 0.6 s. Added auxiliary heating, the NBI and ECRH, allows for prolonging this time up to 2 s. It was connected with the ion temperature rise from 1 keV to 30 keV [Wes2000]. The allocation of the heating systems in the tokamak is presented in figure 2.3. [May2014]. The vacuum chamber consists of eight sections accessible only by remote handling because of the radioactivity connected with the strong neutron yield of up to $6 \cdot 10^{18}$ n/s. The energy and yield of the emitted neutrons depend on the used fuel [Joh2008]. JET performance has been tested with the DD, DT, and TT plasmas. In the beginning, the first wall was made of carbon fibre composite (CFC). Later, plasma-facing components were coated with beryllium, which provided a lower impurity level. The use of low-Z materials might reduce the radiation losses. There was also a decision to add

the divertor on the vacuum vessel bottom. It changed the plasma shape, reduced the heat flux on the walls and allowed for removing the impurities [Wes2000]. Currently, JET is a machine with a full tungsten divertor and ITER-like wall, which means that the plasma-facing components consist of tungsten-coated CFC and Be-coated Inconel tiles [Mat2007].

Activities on JET have focused on the issues connected with ITER design and operation. The physics studies concentrate on the impurity control during the operation and advanced regimes development [Pam2003].

Table 2.2. The basic parameters of JET tokamak [Ber1990].

Major radius	2.96	[m]
Minor radius	2.1 (vertical) 1.25 (horizontal)	[m]
Elongation	1.68	
Plasma volume	80	[m^3]
Toroidal magnetic field	3.45	[T]
Plasma current	3.2 (circular shape) 4.8 (D-shape)	[MA]
NBI	20	[MW]
ICRH	15	[MW]
Plasma density	$5 - 10 \cdot 10^{19}$	[m^{-3}]
Pulse length	20	[s]

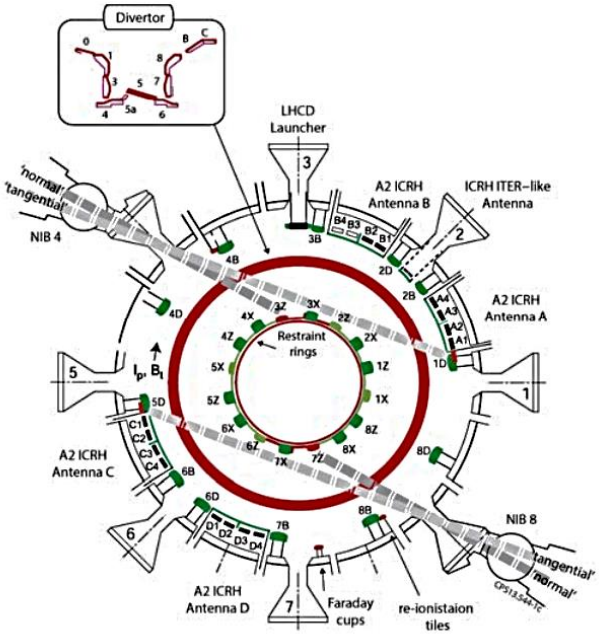

Figure 2.3. Allocation of the heating systems in JET tokamak chamber [May2014].

2.3 Neutron generators

Neutron generators (NGs) are devices based on the DD and DT fusion reactions. The NGs are used in industry for activation and material analysis, nuclear medicine and science for nuclear physics research. Commercial machines can emit 10^{11} n/s from the DT reaction and 10^9 n/s from the DD reaction. Among the producers of portable generators are Thermo Electron, Schlumberger, Sodern [Sod] and NSD-Gradel [Gra].

The most commonly used portable generators are seal-tube devices. These NGs consist of a radiation source, an acceleration tube and a target. The ion source is usually of the Penning type. The generator consists of one or two acceleration sections. Usually, it includes tritium target and deuterium ion source, less often a mixture of the DT. The target is a thin foil of metal (titanium, zirconium or scandium) deposited on a substrate, e.g. cooper. The metal target constitutes hydrates with hydrogen isotopes. The product is a stable compound with a high density of hydrogen. Atoms that are displaced from the target can be accelerated back. The general scheme of the neutron generator design is presented in figure 2.4 [Val2015].

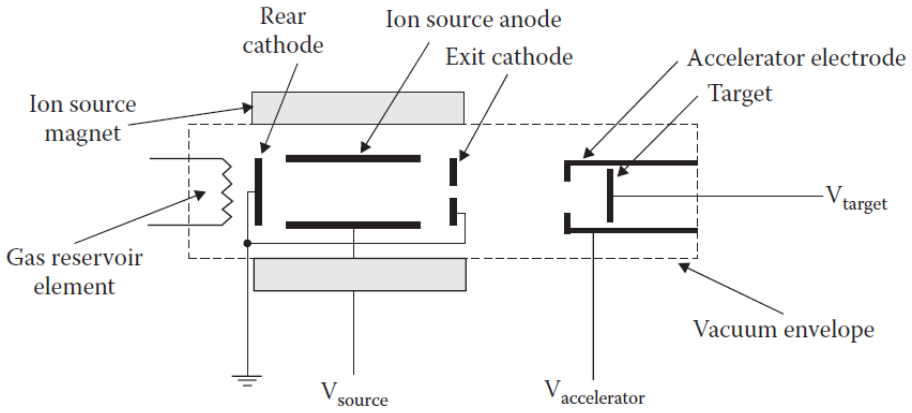

Figure 2.4. Schematic design of the seal-tube neutron generator [Val2015].

The performance of the neutron generator can vary in time and with input parameters. Besides the neutrons, the generator produces gamma radiation. The neutrons can scatter or react with the materials surrounding the generator and its elements. These phenomena disturb the angular and energy distribution of the neutron emission. The produced radiation needs to be controlled during the operation [Rom2011]. The lifetime of the generators is limited and depends on the output determined by working conditions like high voltage level and temperature [Val2015].

2.3.1 Sodern Genie 16C

Sodern is a French company specialising in optronic and neutron technology which manufactures sealed-tube neutron generators based on the DD or DT reactions [Val2015].

One of the Sodern products is the Genie 16C neutron generator (see figure 2.5), which was used in the experiment described in this thesis (see chapter 9.2). It predominantly emits the 14.1-MeV neutrons. This NG can operate in two modes: pulse and continuous. The pulse time is less than 1.5 µs. The neutron flux is typically about $2 \cdot 10^8$ n/s. The Genie 16C is very mobile because it weighs only 8 kg. During operation, the vacuum pressure in the sealed tube varies from 10^{-5} to 10^{-3} mbar. The neutron generator consists of a tube with a target containing a mixture of deuterium and tritium. The tube has a diameter of 11.5 cm and a length of 71.5 cm. The maximal beam current is 60 µA, and the acceleration voltage is 110 kV. The neutron generator is controlled by computer software. The pulse repetition frequency can be set from 56 mHz to 10 MHz [Ros2009].

Figure 2.5. The neutron generator Genie 16C manufactured by Sodern [Sodman].

2.3.2 Gradel-Fusion NSD 35 2-DT-C-W

A neutron generator NSD 35 2-DT-C-W produced by the Gradel-Fusion has a different principle of operation. There is no solid target or accelerator. The generator consists of a cylindrical reaction chamber, spherical electrode and cooling system. The central hollow cathode and outer electrode produce a symmetric electrostatic field. The schematic design of this kind of neutron generator is presented in figure 2.6. The reaction chamber is filled with a mixture of deuterium and tritium gases. The gas in the case of model 35 2-DT-C-W is under low pressure. The neutrons are produced by applying a very high voltage (120 kV) and 15 mA maximum to the gas. The pulsed, high voltage induces glow discharges in the reaction chamber. Positively charged ions (D^+, T^+) are accelerated in the trajectory toward the cathode. Molecule ions (DD^+, DT^+, TT^+) are also present in the gas, influencing the emitted neutron spectrum. The cathode has a structure with aligned radial vane elements. The ions can flow through it without a collision. During a discharge, the vacuum chamber is filled with a gas-plasma mixture where ions collide, and fusion reactions occur. The neutron emission zone is placed along the electrode. The neutron emission is continuous and pulsed mode is not available. The generator's walls need to be cooled down because of the heating by plasma radiation [Gra2010].

The Gradel-Fusion NSD 35 2-DC-C-W neutron generator used in the experiment described in chapter 9.1 has an aluminium reaction chamber of 81.5 cm in length and 13.5 cm in diameter. The pressure in the chamber is about $3 \cdot 10^{-2}$ mbar. The neutron yield declared by the manufacturer is 10^7 – 10^8 n/s for DD reaction and 10^8 – 10^{10} n/s for DT reaction. The spectrum of emitted neutrons also contains neutrons from TT reaction with energy from 0.5 to 8.8 MeV [Gra2015].

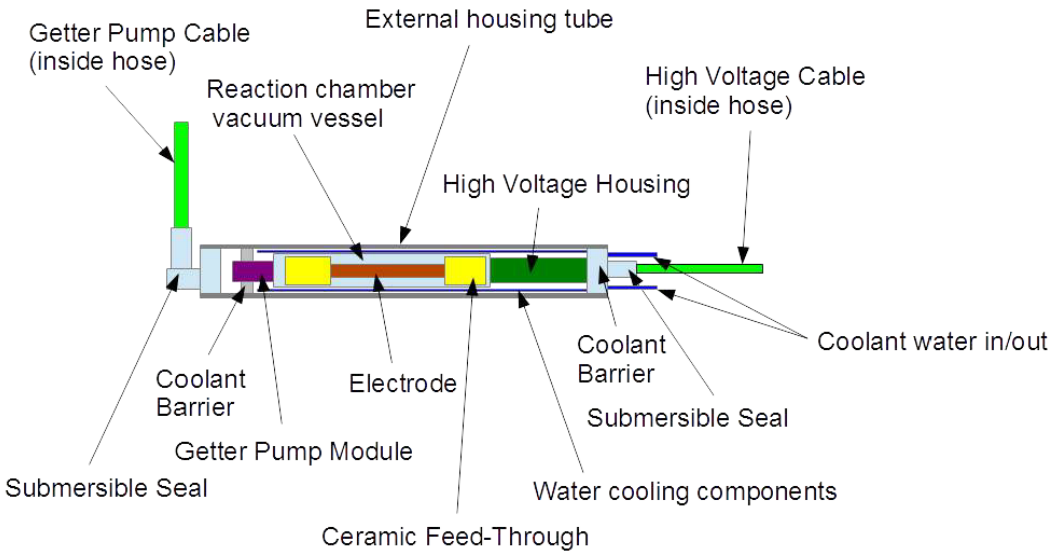

Figure 2.6. Schematic design of the Gradel NSD 35 2-DT-C-W neutron generator [Gra2015].

Chapter 3: Plasma diagnostics

The measurement of plasma parameters is required for control, device protection and evaluation of plasma physics. The developed measurement techniques are known as plasma diagnostics. They are generally designed for study:

- Methods of obtaining stable plasma,
- Neutron yield and achieved fusion power,
- MHD instabilities,
- Plasma impurities,
- Supplementary plasma heating methods,
- Plasma fluctuations [Wes2004].

Diagnostics aim to deduce information about operation parameters from observations of physical processes and their effects. In plasma physics, it is usually connected with well understanding of physical phenomena [Hut2002]. The plasma diagnostics operate in an extremely difficult environment near the plasma, where the strong magnetic field, high temperature and radiation fluxes are present. They need to be suitable for requirements defined for the specific device [Don2007].

Often, more than one diagnostic is used to measure each physical quantity. The measured parameters and related diagnostics are:

- Magnetic field – The local magnetic field is measured by the magnetic coils or probes placed in the vacuum vessel. The placement inside the vacuum vessel reduces the influence of the screening by the metal walls [Wes2004]. The coils are small solenoids where magnetic fluctuations cause voltage induction. This measurement informs about the plasma position, the poloidal field outside the plasma, and poloidal and toroidal fluxes. These measurements can be used to calculate safety factor (q), a ratio of plasma pressure to magnetic pressure (β), ohmic heating power, energy confinement time and plasma magnetic energy [Equ1978, Orl1988].
- Current profile – The coils are also used for the plasma current and loop voltage measurement. The plasma current is usually measured by the Rogowski coil. It is a long solenoid where plasma current induces a voltage proportional to the current change in time [Rai2014].
- Electron density – Two main methods for electron density profile measurement are interferometry and Thomson scattering. Both techniques are based on electromagnetic wave interactions with electrons. The interferometry measures the variation of the plasma refractive index by comparing the laser wave propagation along two paths through the plasma and vacuum. Far-infrared lasers are used to avoid refraction effects [Equ1978].
- Electron temperature – The primary diagnostics used for electron temperature measurement is Thomson scattering. It is based on incoherent scattering of the laser beam on free charges in plasma [Men2003]. Multiple monochromatic laser beams intersect the plasma volume, and the optical elements collect the scattered light. The high-resolution spectrometers measure the modified spectrum in comparison to the input beam. The electron temperature is determined based on wavelength-shift and spectrum shape [Pas2004]. The electron temperature can also be deduced from Electron Cyclotron Emission (ECE) diagnostic or Charge Exchange Recombination Spectroscopy (CXRS). Both techniques obtain parameters from the electromagnetic spectrum analysis [Equ1978].
- Neutral particle density - Neutral atoms of working gas emit alpha and beta radiation that can be measured. A spectroscopy measurement of the D_α spectrum is made by conventional polarimetry [Don2007]. The neutral particles can escape from the plasma and may be detected directly [Equ1978].
- Ion temperature – The ion temperature can be measured indirectly by fast-neutrals, Doppler broadening, neutron radiation analysis or Thomson scattering measurement [Fro2006]. The thermal motion of the radiating ions causes a Doppler shift of the emitted lines.

Therefore, the ion temperature can be deduced from the broadening of the measured electromagnetic radiation profile [Equ1978]. It can also be determined from neutron spectroscopy according to equation 1.3.1.9.

- Impurity concentration – The density and temperature of the impurities can be measured by spectroscopy. Passive spectroscopy methods measure the plasma self-radiation of various spectral ranges. Active measurement is based on fluorescence or recombination spectroscopy [Equ1978].
- Runaway electrons – Relativistic electrons escape from the plasma and cause energy loss. The loss can be through direct energy transport to the walls, synchrotron radiation emission or increased transport induced by plasma waves. The high-energy electrons can be detected indirectly by a hard X-ray monitor and spectroscopy or Cherenkov detector [Kno1979].
- Neutrons – neutron diagnostics are described in subchapter 3.1.
- Radiated power – Radiation power emitted by the plasma in fusion devices consists of electromagnetic radiation from infrared to several tens of keV and neutral particles. Plasma is generally optically thin for this radiation range, and the whole plasma volume is the emitter. The measurement along a defined line of sight (LOS) is an integral of the emissivity over the viewed area. The emission distribution in the plasma can be measured by detectors of multiple views in the plasma cross-section and be reconstructed by inversion methods. The bolometers or AXUV diodes are suitable detectors for thermal losses measurements and MHD activities monitoring. The operation of bolometers is based on the mechanism that changes some of the material properties after radiation absorption and connected rise of temperature [Kru2001].

Many types of diagnostics can be used to calculate more than one parameter. This thesis is focused on the neutron diagnostics.

The diagnostics require a control system that includes data acquisition (DAQ) and post-processing. Some of the plasma and vacuum vessel parameters are controlled in real-time. The diagnostics are triggered at the beginning of the discharge. The DAQ records data with high time resolution. A massive amount of data is collected in a common database and available for further analysis [Bos2013].

3.1 Neutron diagnostics

The neutron diagnostics provide knowledge that is crucial for solving the fundamental problems of plasma physics, device protection and plasma control. Neutrons, as products of fusion reactions, are primary objects to observe. Most electrically uncharged neutrons escape freely from the plasma with unperturbed information about their source. They are difficult to measure because they do not ionise a matter. The neutron diagnostics are based on indirect detection. The neutrons can pass through a material without interactions. There is some probability of the event occurring between a neutron and nuclei in the material. This probability is described by the cross-section, σ. The cross-section has a dimension of the area (barn = 10^{-28} m^2). The geometrical cross-section describes the chance that a single neutron hits one of the nuclei in the material, and it is equal to the effective area:

$$\sigma = \pi(r_N + r_T)^2, \tag{3.1.1}$$

where r_N is the neutron radius, and r_T is the radius of the nucleus in the target.
The reaction cross-section also includes nuclear forces and strongly depends on the incident neutron energy and interaction type. The neutrons interactions can be divided into:

- Elastic scattering – Neutrons transfer kinetic energy to a material. The nucleus from the material gets recoil velocity. The total kinetic energy in the centre-of-mass frame is constant.

- Inelastic scattering – The scattered neutron transfers the energy and excites the nucleus in the material. Excitation radiation is released from the nucleus with a delay and can be detected.
- Absorption or capturing – The incident neutron combines with the nucleus. The effect of the merger can be prompt or delayed gamma radiation, particle emission or fission. All products of the neutron absorption can be registered. The absorption with particle emission is called nuclear reaction [Rin1991].

The cross-section of the fusion reaction depends steeply on the energy of the interacting particles and consequently on the plasma temperature. The theoretical spectrum of neutrons from the DT plasma in the equilibrium state is presented in figure 3.1 [Fan2012]. The actual spectrum observed in the fusion devices has a more complicated shape because of the interactions of the particles in the plasma. The neutron emission spectrum and its distribution in space can be calculated by simulating the neutron source and interactions with the matter by sophisticated transport codes like MCNPX [Car1975] or TRANSP [Gri2018]. These codes allow predicting the measurement results or calculation of the plasma parameters from experimental data.

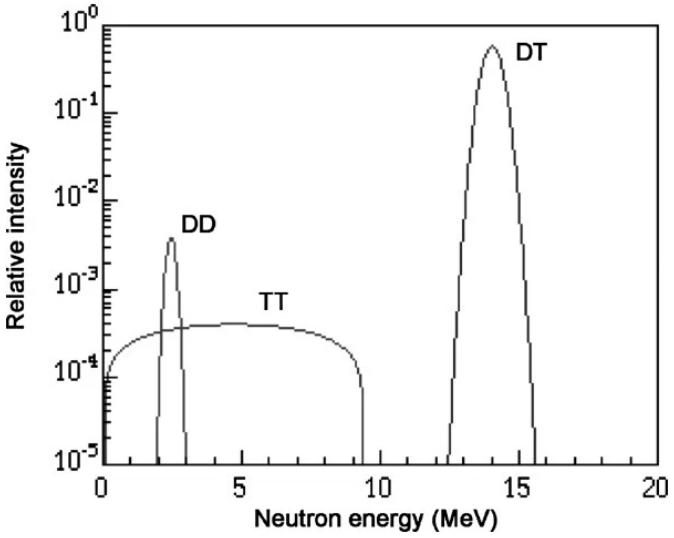

Figure 3.1. Theoretical neutron spectrum for the DT plasma including fusion reactions DD, DT and TT [Fan2012].

The neutron diagnostics allow the evaluation of:

- the total neutron yield that brings the information about the fusion power and its density, which is an essential parameter in the case of device protection and reactor optimisation,
- neutron emission distribution in time and space that influences the damage of plasma-facing components (PFCs) and other device elements,
- alpha source distribution, which is responsible for self-heating fundamental to achieving sustainable fusion plasma [Bre2012],
- fuel ratio for deuterium-tritium plasma,
- ions temperature.

The ion temperature can be deduced from neutron spectrometry or neutron rate measurement if the ions density is known. If the ions velocity distribution is Maxwellian, the neutron spectrum is expected to have a Gaussian shape. Therefore, the ion temperature can be calculated from the spectrum shape by the value of the FWHM [Jar1994].

The simplest time-integrated neutron measurement can be performed by a neutron activation system. Samples of different materials, usually metal disks, are irradiated in neutron flux. After a defined time (cooling time, t_c), their activity is measured by a high-precision gamma-ray detector. The radioactive nuclei production is calculated from:

$$\frac{dN_N}{dt} = \sigma\varphi N_0 - \lambda_T N_N, \tag{3.1.2}$$

where N_N is the number of radioactive nuclei, ϕ is the neutron flux, N_0 is the number of the target nuclei, and λ_T is the decay constant.
Therefore, the activity induced in the activation foils measured by the gamma spectrometer is:

$$A = \sigma\varphi N_0\left(1 - e^{-\lambda_T t_i}\right)e^{-\lambda_T t_c}\left(1 - e^{-\lambda_T t_m}\right), \tag{3.1.3}$$

where t_i is the irradiation time, and t_m is the measurement time [Gre2011].

The materials that will be the subject of the irradiation are selected based on the parameters of nuclear reaction occurring in the sample (cross-section, threshold energy) as well as the reaction products parameters, i.e. respectively long half-life time of the produced nuclei and detectable energy of the product decay. The different materials are used to the monitoring of the 2.5-MeV neutrons from the DD reaction and 14.1-MeV from the DT reaction. The multifoil activation technique allows for estimation of the neutron spectrum and determination of the fuel ratio in the case of the DT plasma or triton burn-up ratio for the DD plasma [Bie2019].

The most conventional neutron diagnostics are counters. They are fast and resistant to radiation and temperature. The counters are gas proportional detectors with an active target. A gas like helium or boron trifluoride acts as a target and reacts with neutrons. An example is the helium counter (filled by ^{3}He). The neutron capturing by the helium nucleus produces proton and triton. The charged products deposit their energy in the counter, and a neutron is detected [Deb2011].

Another type of counter is a fission chamber (FC). The FC is a gas ionisation chamber with the electrodes coated by a thin layer of fission material. The chamber is filled with argon or/and nitrogen [Ave1954]. The ^{238}U and ^{235}U coatings are used for fast and slow neutrons detection, respectively. Applied voltage creates a symmetric electric field. After neutron capture, two fission fragments with an energy of about 160 MeV travel in the opposite directions and transfer their energy to the gas. Produced free electrons induce a current in electrodes. The current is proportional to the number of fission events in the detector [Cob2016]. The high energy of the fission fragments allows for easy gamma-ray radiation discrimination from the measured neutrons [End1982].

Another counting detector is a scintillator. Its response time is in the range of nanoseconds. The scintillators contain many carbon or hydrogen atoms having a high cross-section for elastic neutron scattering. Due to interaction, the neutron transfers its energy to the proton or carbon nucleus. The kinetic energy of the recoiling particle is absorbed by the scintillator and converted into light and then to an electric pulse with a magnitude proportional to the deposited energy. The neutron spectrum can be deduced from the registered signals by an unfolding method [Kas2002]. Examples of neutron scintillators are NE102A (plastic) and NE213 (liquid). The scintillators have better efficiency than the gas counters because of the higher nuclei density. The disadvantage of the scintillators is the sensitivity to gamma radiation. The problem can be solved by the pulse-shape discrimination (PSD) method. The signal from gamma rays has a faster decay time than one from neutron. The measurement of the time-dependence of the signal allows for removing the counts produced by photons [Cra1991]. The comparison of the signal's shape produced by gamma rays and neutrons is presented in figure 3.2.

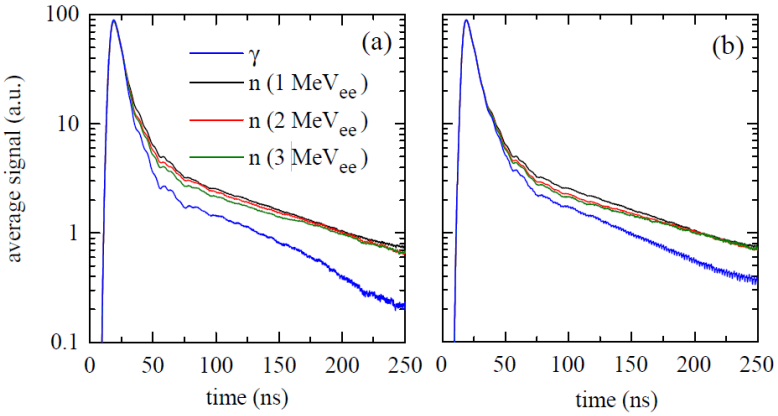

Figure 3.2. Comparison of the signals sourced by neutron and gamma radiation in the plastic scintillators (a) EJ301 and (b) EJ299-33 [Ces2014].

Another type of neutron detector rich in carbon nuclei is a diamond detector. Diamond is a semiconductor with a wide bandgap and good resistivity. Neutrons with ^{12}C can react and scatter elastically or inelastically [Sin2014]. The neutrons with energy higher than 6 MeV interact through different reactions: (n,n'), (n,α), (n,p), and (n,d). The most important reaction, $^{12}C(n,\alpha)^{9}Be$, has the threshold energy equal to 6.2 MeV and produces 9-MeV alpha particles. The charged particle is detected as a peaked structure in the measured pulse high spectrum that can be converted to the neutron energy spectrum or the total number of neutrons. The energy resolution for this kind of detector is about 1%. The diamond detectors are more commercially available since a chemical vapour deposition of diamond (CVD) is commonly used for crystal production [Zim2010]. The signals produced by neutrons in the natural diamond detector (NDD) and CVD are slightly different (see figure 3.3). The CVD sensitivity is not uniform on the surface due to the polycrystalline structure. The measurement efficiency is lower than in the NDD, and slight polarisation decreases pulse amplitude by reducing the electric field in the detector. Despite this, the CVDs are used as high-resolution spectrometers. The electric signal produced by charged particles has a very low amplitude due to the 5.3 eV bandgap. Fast carriers mobility allows for quick (~ps) response [Ang2011]. The signal shape depends on the energy of neutrons (see figure 3.4.). This property allows for reconstructing the neutron spectrum from the measured pulse-high spectrum.

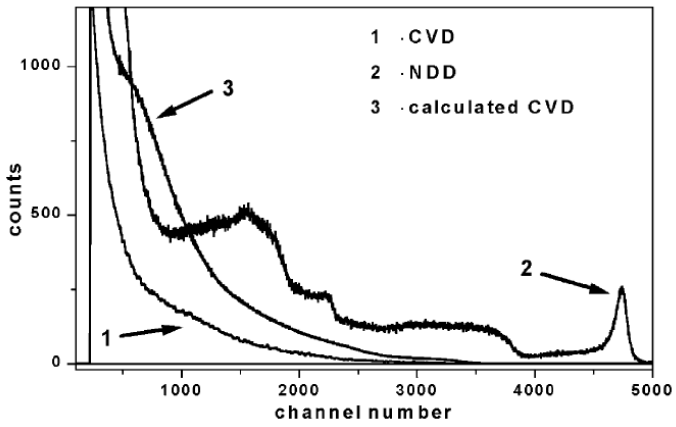

Figure 3.3. The difference between the signal (pulse high spectra) produced by 14-MeV neutrons in the NDD, the CVD, and the CVD response calculated with the assumption that it has a uniform spectrum shape with the energy of incident particles [Fou2002].

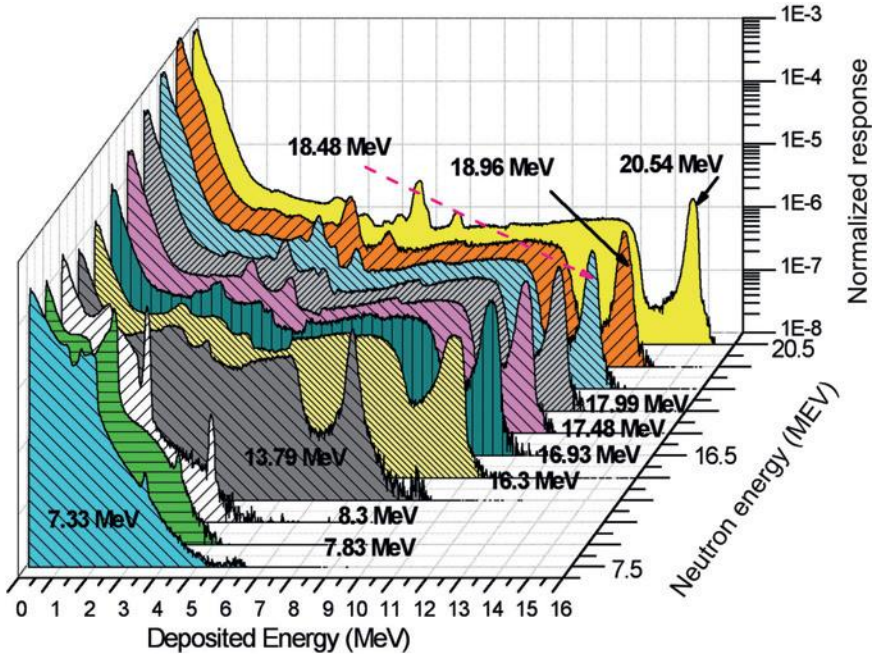

Figure 3.4. The shape of the signal induced in the CVD by neutrons of different energies [Pil2011].

The neutron emission spectrum can be measured by a Time of Flight spectrometer (ToF) without applying the unfolding methods as for the previously described detectors. The ToF spectrometer consists of scintillators that record the recoil protons resulting from interaction with neutrons in the detector material. The schematic view of the ToF system installed at JET tokamak is presented in figure 3.5. The first scintillator (*S1*) is placed after the collimator and used as a neutron scattering target and recoil proton detector. The scattered neutrons are detected in one of the *S2* scintillators located on a ring-shaped array. The angles and distances of the detectors' positions are well known. The measurement uses the coincidence method; the delay between the signals from detectors *S1* and *S2* gives information about the time of flight of scattered neutrons that can be used to calculate the energy of the incident neutron [Hja2003].

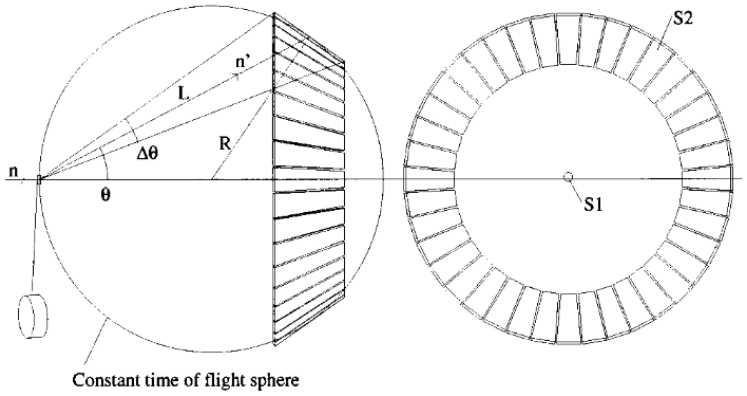

Figure 3.5. Scheme of the TOFOR – time of flight spectrometer with an optimised rate which is installed at JET tokamak ($S_{1/2}$ – scintillators, ϑ – scattering angle, L – distance between scintillators/neutron flight path, R – radius of the time-of-flight sphere, n - incident neutron, n'- scattered neutron) [Hja2003].

The neutron detectors described above can be used for spatially resolved measurement. The neutron intensity monitoring by many detectors from different directions allows tomographic

reconstruction of emission profiles. Neutron cameras consist of fun-shaped collimators equipped with detectors. Each detector views the plasma along a line of sight (LOS) defined by the collimator geometry. The LOSs should be uniformly distributed in the poloidal cross-section of one toroidal position. The camera's resolution increases with the number of detectors and viewing directions [Jar1994]. Its primary function is the determination of the local neutron emissivity in a complete poloidal cross-section. A secondary purpose is the alpha birth profile or fusion power determination. The neutron cameras are installed at tokamaks, for example, JET [Ron2010] and MAST-U [Cec2018]. A new diagnostic is designed for ITER based on the experience from existing ones. The main topic of this thesis is tomography analysis of the neutron cameras' measurement, including the development of the inversion method that allows for optimisation of the Radial Neutron Camera for ITER [Mar2012] design (experimental data analysis in future) and interpretation of the tomography analysis of the neutron measurement during the DT campaign on JET. The detailed description of the Radial Neutron Camera for ITER and JET Neutron Camera are in chapters 8 and 9, respectively.

Chapter 4: Inverse problems

All physical measurements can be described as a collection of observations resulting from the appearing phenomena. The measurement (*d(x)*) can be a function of time, space or energy. The measurement itself is a forward problem that can be described by the Fredholm equation of the first kind:

$$\int_a^b g(x,\xi)m'(\xi)d\xi = d(x), \tag{4.1}$$

where *g* is the operator called kernel function, and *m'* is the model that describes the distribution of the measured physical quantity by the *ξ* factors [Pre2007].
The inverse problem is to find the model which describes the physical quantity. If the problem is well-posed, according to Hadamard's definition, it has a unique solution continuously dependent on the input data, and it is possible to find it by a straightforward inversion [Sam2008]. The well-posed problem can be ill-conditioned, which means that the inversion result is very sensitive to changes in the experimental data related to the measurement error. Therefore, the solution obtained by straightforward methods is not stable and reliable. If the kernel function is symmetric, continuous, and derivative with respect to ξ is discontinuous, the problem can be presented as a convolution equation [Pre2007]:

$$\int_{-\infty}^{+\infty} g(x-\xi)m'(\xi)d\xi = d(x). \tag{4.2}$$

The deconvolution of the presented equation can be calculated by the Fourier transform [Arf1999]:

$$m'(\xi) = \frac{1}{\sqrt{2\pi}}\int_{-\infty}^{+\infty} e^{-ix\xi}d(x)dx. \tag{4.3}$$

The inverse problems which describe neutron measurements are often ill-posed and ill-conditioned. Therefore, it cannot be solved by the Fourier transform. The ill-posedness is connected with the high number of unknown parameters compared to the input data. It is the source of the issue with the existence of an infinite number of solutions and their discontinuous dependence on the input data. The random noise in the experimental data makes the inverse problem ill-conditioned. The small changes in the measured values influence the inversion. The consequence is a non-unique and unstable solution [Ast2018].

The number of degrees of freedom in the integral representation of the inverse problem is infinite. It can be reduced by discretisation of the physical quantity distribution, and the undetermined system of integrals can be transformed into a system of algebraic equations [Ant1996]:

$$\sum G_{ij}m'_j = d_i, \tag{4.4}$$

where G_{ij} is the element of the contribution matrix, if ***G*** is rank deficient direct inversion is not possible.

The discretisation is a finite-dimensional approximation of the physical quantity distribution by expanding into an orthogonal basis function. The basis function can have different forms. It can predetermine the geometrical requirements. In this thesis, tomography is defined as the reconstruction of the two-dimensional spatial distribution of the physical quantity equivalent to an image. The image can be expanded into Zernike polynomials connected with the radial coordinates or projections of the Chebyshev functions of the second kind [Mly2010]. A special

example of discretisation is dividing the image into the pixels (two-dimensional problem) or the energy spectrum into a finite number of energy bins (one-dimensional problem).

The basic method for solving the system of equations produced after data discretization is the least square analysis. The goal is to find $\vec{m}'$ that minimize the residual $\|\boldsymbol{G}\vec{m}'-\vec{d}\|_2$. The $\| \|_2$ denotes Euclidean norm. The least-square solution is equal to [Cho2004]:

$$\vec{m}' = (\boldsymbol{G}^T\boldsymbol{G})^{-1}\boldsymbol{G}^T\vec{d}. \tag{4.5}$$

The measurement errors make data points inconsistent. The problem usually is rank-deficient and ill-conditioned. Therefore, the least square method gives an extremely unstable solution. The characteristics of the problem can be examined by the singular value decomposition (SVD). In the SVD, the matrix ***G*** is factored into:

$$\boldsymbol{G} = \boldsymbol{U}\boldsymbol{S}_V\boldsymbol{V}_s^T, \tag{4.6}$$

where ***U*** is the orthogonal matrix consisting of the unit basis vectors spanning the data space ($\vec{U}_i$), $\boldsymbol{S_v}$ is the diagonal matrix with the singular values s_i, and $\boldsymbol{V_s}$ is the orthogonal matrix with columns consisting of the basis vectors spanning the model space ($\vec{V}_{Si}$).
The inverse problem solution can be written as:

$$\vec{m}' = \sum \frac{\vec{U}_i^T\vec{d}}{s_i}\overrightarrow{V_{Si}}. \tag{4.7}$$

The singular values decrease along the diagonal. The elements of vectors $\vec{U}_i$ and $\vec{V}_{Si}$ change sign more frequently with this decrease. Small singular values imply that the contribution matrix is rank deficient, and model space basis vectors related to these values are numerically null-vectors [Han1994]. The vectors $\vec{V}_{Si}$ dominate the solution for very small or equal zero s_i values. It amplifies the noise influence on the data and the results instability. The instability measure is the condition number of kernel operator, which is the ratio of the largest to smallest singular value. If ***G*** is not full rank, the condition number is infinite. The instability increases with the condition number. It is related to the discrete Picard condition. This condition is satisfied if $\vec{U}_i^T\vec{d}$ decay to zero faster than singular values. Therefore, the instabilities due to small singular values are not visible. The equation (4.7) represents a solution of the Moore-Penrose pseudoinverse. This generalised inverse solution relates to a minimum length least squares solution. The least-square method applied to the ill-posed problem leads to over-fitting the input data and the model domination by the noise. The model space basis vectors connected with the large singular values filer the solution but those related to smaller values cause strong oscillations. The solution is more stable if the model space vectors related to the smallest singular values are eliminated [Ast2018].

The reconstruction of neutron emission profiles or neutron energy spectrum are ill-posed and ill-conditioned problems. The ill-posedness is connected with the ***G*** matrix's nontrivial null space and an infinite number of solutions. The selection of the one solution requires supplementary constraints. The sophisticated regularisation methods stabilise the inversion and provide a reliable, unbiased solution because of the additional assumptions [Ast2018]. A detailed description of the regularisation methods that can be applied to discrete inverse problems is described in chapter 5.

Part II: Numerical codes

Chapter 5: Reconstruction methods

The inverse problems occur in the analysis of the data from neutron diagnostics. The two-dimensional neutron emissivity spatial distribution in a tokamak can be reconstructed from the neutron camera measurement. Different neutron detection techniques allow for neutron energy spectrum determination. This thesis describes the reconstruction of the one-dimensional distribution of the neutron emission intensity related to energy from neutron activation measurement. Both problems, before the calculations, are discretised and thus can be described by equation 4.4. The inverse problems require sophisticated methods to reconstruct the unknown physical quantity distribution. The numerical regularisation techniques with proper side constraints provide an efficient and stable solution, which will be a good approximation of the unknown model [Han1994]. The same approaches can be extended to reconstruct the physical quantity distribution in two dimensions. The Tikhonov regularisation, Minimum Fisher Information, Maximum Entropy and Maximum Likelihood methods and algorithms developed by the thesis author are described in the following subchapters.

5.1 Tikhonov regularisation

The most popular and simple deconvolution method is the linear regularisation method, also called Tikhonov Regularisation (TR). The linear least-squares problem may have an infinite number of solutions. A solution is not unique, especially if data contain the noise [Ast2018]. Regularisation is required to filter out the influence of measurement errors. The TR method is based on the looking for a regularised solution $\vec{m}'$, which minimises the weighted combination of the residual norm and the side constraint:

$$\vec{m}' = \min \left(\left\| \boldsymbol{G}\vec{m}' - \vec{d} \right\|_2 + \lambda^2 \|\boldsymbol{L}\vec{m}'\|_2 \right), \tag{5.1.1}$$

where λ is the regularisation parameter ($\in R_+$), and $\boldsymbol{L}$ is the convex functional, called the regularisation operator [Ble2015].
The regularisation parameter controls the weight given to the side constraint. A large value of λ supports a small solution norm (second term in the minimisation) and a significant residual norm. A low λ value gives the opposite effect. The parameter λ also controls the sensitivity of a solution to perturbations in input data [Han1994].

The residual norm measures the agreement between the model and data or is related to the "sharpness" of the mapping between a solution and underlying function. Minimising the residual norm provides good agreement with data, but the solution is very unstable. The result values widely oscillates and can represent not physical quantities, e.g. contain negative values. The first term of the equation (5.1.1) corresponds to the least squares method. The second term represents the smoothness of the solution and is related to the quantity that describes stability concerning the input data variations. The operator $\boldsymbol{L}$ reflects a prior judgment about the likelihood of the solution. Figure 5.1 shows the trade-off curve between these two parts for various regularisation parameter values [Pre2007].

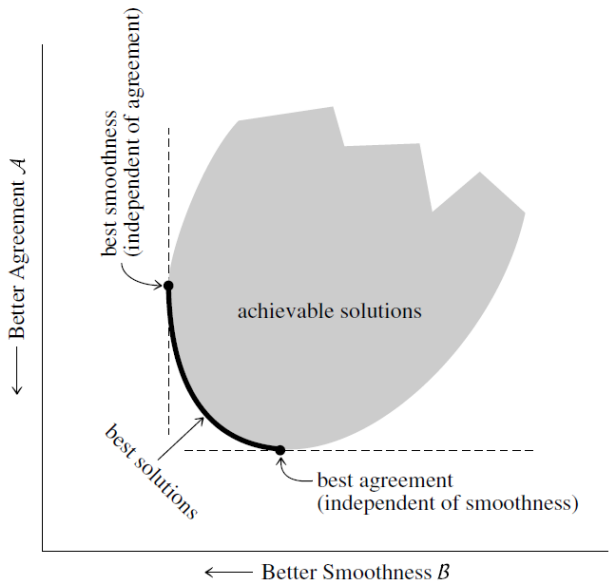

Figure 5.1. Trade-off curve (L-curve) for regularisation problems (*A* – logarithm of residual norm, *B* – logarithm of side constraint) [Pre2007].

The regularisation parameter controls the balance between residual norm and side constraint and filters out the noise without losing information about the solution. The value of λ needs to be carefully chosen. Examples of methods for optimising the regularisation parameter are generalised cross-validation [Gol1979] or U-curve [Kra2007]. The most commonly used method, the L-curve, has been found to give the most stable results [Mik2018]. The L-curve is the parametric plot equivalent to the trade-off curve named from its shape. It is derived from the asymptotic theory of filtering. The selection of the regularisation parameter includes information about the solution and residual. The curve corner represents the change from the over-smoothing to errors domination in the solution. This point corresponds to the optimal parameter λ with a good balance between smoothness and agreement between reconstructed and input data represented by the residual norm. The L-curve shape with the flat part of regularised solution domination and vertical part with the domination of the error requires fulfilment of the assumptions [Han1993]:

- Picard condition satisfaction ($\vec{U}_i^T \vec{d}$ decay to zero faster than singular values *s*),
- The errors need to be samples of the same probability distribution for uncorrelated measurement data,
- The signal-to-noise ratio needs to be relatively large.

The corner of the L-curve can be found by the curvature calculations. The sought-for point corresponds to the curvature maximum [Han1993].

The regularisation operator ***L*** is the side constraint of the problem. It can be defined in various ways. The simplest operator form is a first- or second-order derivative matrix.

$$L\,(1^{st}\ order\ derivative) = \begin{bmatrix} -1 & 1 & 0 & & 0 & 0 & 0 \\ 0 & -1 & 1 & \cdots & 0 & 0 & 0 \\ 0 & 0 & -1 & & 0 & 0 & 0 \\ & \vdots & & \ddots & & \vdots & \\ 0 & 0 & 0 & & -1 & 1 & 0 \\ 0 & 0 & 0 & \cdots & 0 & -1 & 1 \end{bmatrix}. \tag{5.1.2}$$

For defined regularisation parameter and operator, the minimisation can be done by solving the system of equations:

$$(\boldsymbol{G}^T\boldsymbol{G} + \lambda\boldsymbol{L}) \cdot \vec{m}' = \boldsymbol{G}^T\vec{d}. \quad (5.1.3)$$

This equation is not ill-posed because of the regularisation parameters influence. It can be solved by standard techniques like LU decomposition (factorisation into lower and upper triangular matrices) [Pre2007].

Figure 5.2 presents the flowchart of the TR code. The algorithms for all described methods have been implemented in Python programming language with an application of the standard libraries [Ros1995].

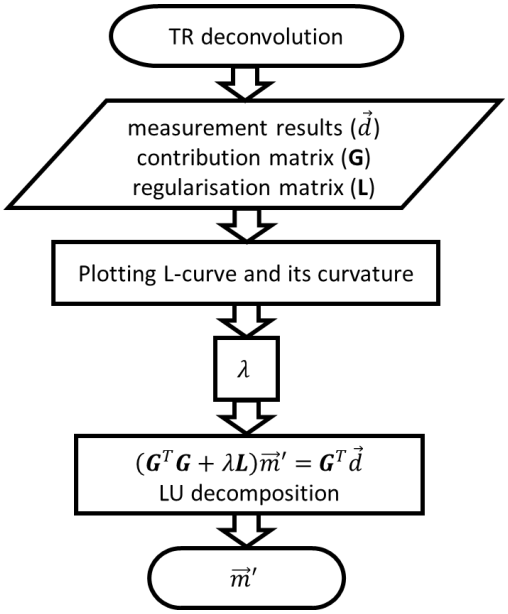

Figure 5.2. The flowchart of the TR code developed by the thesis author.

5.2 Minimum Fisher Information

Fisher Information has two roles in statistics theory:

- measures the capability to estimate a parameter,
- measures the state of system disorder,

which means it contains information about variations of the data. It estimates the smoothness of the probability function [Fri2000].

Fisher Information function comes from the classical measurement theory. The information arises as a degree of the expected error in the measurement. The mean-square error (ε^2) of parameter estimation is described by Cramer-Rao inequality [Fri2007]:

$$\varepsilon^2 I_F \geq 1, \quad (5.2.1)$$

where I_F is Fisher Information which becomes:

$$I_F = \int dx \left(\frac{dp}{dx}\right)^2 \frac{1}{p(x)}, \quad (5.2.2)$$

where *p(x)* is the probability density function for noise *x*.

If the Gaussian statistics describes the uncertainty of the data, I_F is related to $1/\sigma_s^2$. Fisher Information determines the magnitude of mean-square error. The Cramer-Rao inequality shows that estimation quality grows with increasing I_F. Therefore, Fisher Information is a quality unit of the estimation procedure. Inequality (5.2.1) also implies that minimising Fisher Information increases the variance limit of the probability distribution. The definition of I_F as a measure of

a disorder indicates that a high Fisher Information value corresponds to a lack of predictability. Broad and smooth probability distributions correlate to small I_F values [Fri2000]. Frieden proved that the minimum Fisher Information value with appropriate constraints corresponds to the best probability distribution [Fri1988].

The Minimum Fisher Information method (MFI) is based on equations (5.1.1) and (5.1.3). Fisher Information can be represented by the operator. This operator in the calculations replaces the regularisation operator $\boldsymbol{L}$. The application of I_F to regularisation is also called Minimum Fisher Regularisation (MFR) [Mly2012].

The Fisher Information operator is a combination of the weight matrix with a side constraint. The weight matrix is defined as follows:

$$W_{ij} = \frac{1}{m'_i}\delta_{ij} \qquad for\ \ m'_i > 0, \tag{5.2.3}$$

$$W_{ij} = W_{max}\delta_{ij} \qquad for\ \ m'_i \leq 0,$$

where W_{max} is the upper bound of weights [Ant1996].
The dependency of the weight matrix on the solution makes regularisation non-linear, and equation (5.1.3) needs to be solved iteratively [Ods2012]. The division by the model values causes stronger smoothing of the elements with lower values. It reduces the probability that peaked emissivity areas will be over-smoothed. The side constraint expression depends on the specified problem [Mly2012].

The MFI algorithm is similar to the TR. The main difference is in the side constraint. The stopping criterion is based on χ^2 tending to 1:

$$\chi^2 = \frac{1}{N}\sum_i^N \left(\frac{\sum G_{ij}m'_j - d_i}{\sigma_{s\,i}}\right)^2, \tag{5.2.4}$$

where N is the number of measurements.
The initial guess called default distribution, $\vec{m}'^0$, is required in the first iteration. The good choice for the default model is a simulated distribution. In the subsequent iterations, the weight matrix depends on the previous solution. In this thesis, two codes based on the MFI method have been used. The algorithm developed by the thesis author uses the LU decomposition to obtain the result. The regularisation parameter λ for a given iteration is sought by the L-curve method. The cycle repeats as long the χ^2 value is very close to one. The MFI code's flowchart is presented in figure 5.3. The second code, called the MFR, is based on the Cholesky factorisation, which is decomposition into the lower triangular matrix and its conjugate transpose [Hig2009]. The parameter λ is optimised iteratively to satisfy the condition of χ^2 close to 1 [Mly2012].

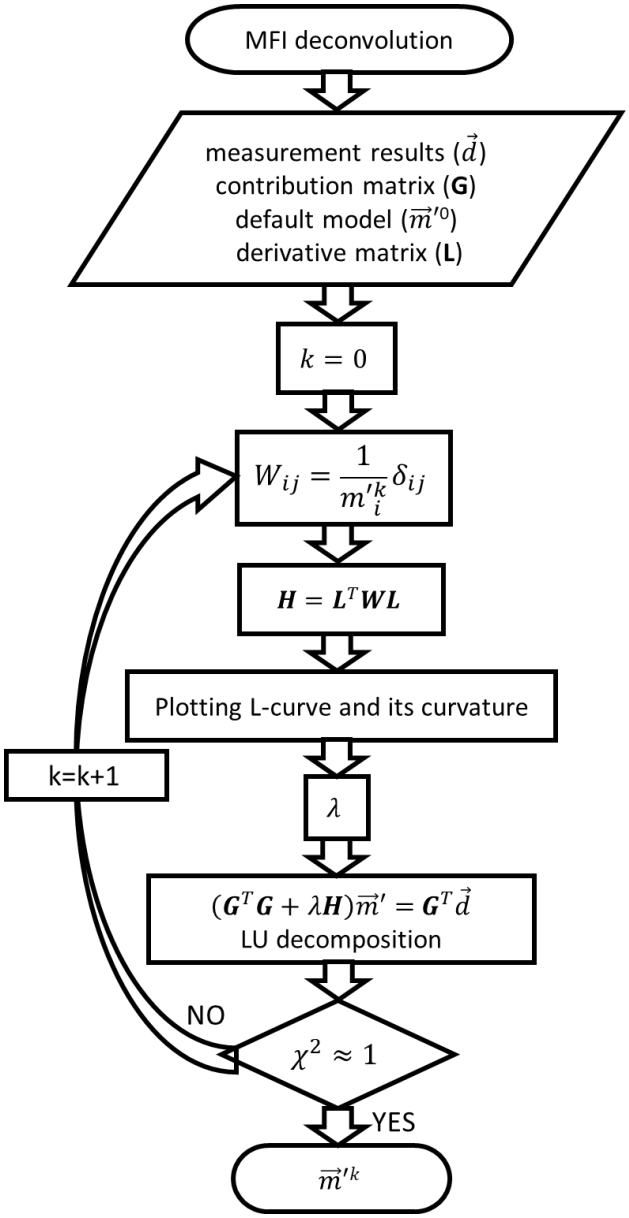

Figure 5.3. The flowchart of the MFI code developed by the thesis author.

5.3 Maximum Entropy

Another widely used method to solve an inverse problem is Maximum Entropy (MaxEnt). It is a powerful technique for reconstructing parameter distributions from noisy and incomplete data. There are many different algorithms developed based on Maximum Entropy theory [Ski1984].

In physics, an isolated system's entropy (S) is the logarithmic number of microscopically distinct configurations that all result in the one system observed macroscopically [Mut1998]. In the information theory and statistical mechanics, entropy measures the amount of information needed to reconstruct the unknown parameter distribution and can be described by the same concept:

$$S = -\sum_i p(d_i) \ln p(d_i), \tag{5.3.1}$$

where $p(\vec{d})$ is the probability corresponding to the discrete values obtained in the measurement [Jay1957].
The specification of the probabilities is demanding if only the expectation function value is known. In information theory, the probabilities can be described by the uncertainty represented by a discrete probability distribution. Shannon proved that entropy:

- is a continuous probability function,
- increase with growing uncertainty,
- is additive for independent sources of uncertainty.

Shannon entropy is represented by a similar equation to (5.3.1) with the constant value *k* before the sum. The equation for thermodynamic entropy is similar to Shannon entropy with Boltzmann constant [Pre2013].

Laplace's principle of insufficient reason leads to the maximisation of entropy. The entropy theory supplies the criterion of choice needed to remove the apparent arbitrariness of the principle of insufficient reason [Jay1957]. The method's key is that solution requires minimum knowledge about the inverse problem. Maximum entropy principle states that a particular parameter distribution has the best representation for probability corresponding with the greatest possible entropy. It is connected with Boltzmann argument that the most probable distribution can be produced in the largest number of ways. Another motivation was derived by Shannon, who states that maximum uncertainty is related to the probability distribution, which maximises the entropy [Pre2013]. The disadvantage of the MaxEnt method is the lack of a physics basis [Jay1957]. The advantage is the requirement of the solution's positivity defined values automatically applied to MaxEnt because the entropy does not exist for negative parameters [Ski1984].

For positive and additive physical quantity distributions, the most popular entropy definition is [Lin1995]:

$$S = \sum_i \left(m'_i - m'^0_i - m'_i \ln\left(\frac{m\prime_i}{m\prime^0_i}\right)\right). \tag{5.3.2}$$

Entropy can also be defined with excluded default model and probability represented by [Pre2013]:

$$p = \frac{m\prime_i}{\sum m\prime_i} \tag{5.3.3}$$

applied to equation (5.3.1).
The solution of the MaxEnt method can be obtained as a minimum of the regularisation equation, which is the posterior probability:

$$\overrightarrow{m'} = min\left(\lambda S - \frac{1}{2}\chi^2\right). \tag{5.3.4}$$

There are many approaches to calculating this non-linear problem [Lin1995]. The non-linear nature of the problem forces the method to be iterative. The regularisation parameter controls the solution's change compared to the default model [Gul1989]. The χ^2 value can be arbitrarily chosen as equal to the number of measurements, and these assumptions can lead to finding the regularisation parameter. This criterion can strongly underestimate the solution. Another way to find λ is probabilistic treatment. This approach leads to the following requirement:

$$N_g = \sum_j^{N_g} \frac{\Lambda_j}{\lambda + \Lambda_j}, \tag{5.3.5}$$

where Λ are the eigenvalues of the least square solution matrix, and N_g is the number of eigenvalues corresponding to the data with a reliable signal-to-noise ratio.
The experimental data are only information about the quantity under consideration. If χ^2 is equal to the number of degrees of freedom controlled by entropy, which means: N-N_g, the data points should be totally reproduced by the reconstructed profile. The detailed calculations are presented in [Lin1995] and [Gul1989]. Another approach is solving an integral equation [Ski1984]. The maximum entropy can be found by the conjugate gradient method. The technique is based on calculating the conjugate vectors of the changes in the default model established with derivatives of equation (5.3.4) [Cho2004].

The MaxEnt code has a structure similar to the TR algorithm. MaxEnt combines the Bayesian method and standard approach [Reg2008]. The L-curve technique of the λ parameter selection was modified to fulfil the assumptions of maximum entropy. The entropy operator is determined based on equation (5.3.3) as the matrix with the diagonal elements equal to the components of the sum from (5.3.1):

$$\boldsymbol{S} = \begin{bmatrix} \frac{m\prime_1}{\sum m\prime_i} \ln \frac{m\prime_1}{\sum m\prime_i} & 0 & 0 \\ 0 & \frac{m\prime_2}{\sum m\prime_i} \ln \frac{m\prime_2}{\sum m\prime_i} & 0 \\ 0 & 0 & \ddots \end{bmatrix}. \tag{5.3.6}$$

A default spectrum is used only in the first iteration. The solutions are calculated based on the Singular Value Decomposition [Gul1994]. The regularisation parameter is sought in the supplementary module, where solutions with different values of λ are determined for the defined entropy. The results with χ^2 closest to 1 are selected, and the one with maximal entropy is found optimal. The iterations are continued if χ^2 is not proximate to 1, or the set maximal value of iterations is not reached. The flowchart for the MaxEnt code is presented in figure 5.4. Other methods were tested but did not give satisfactory results.

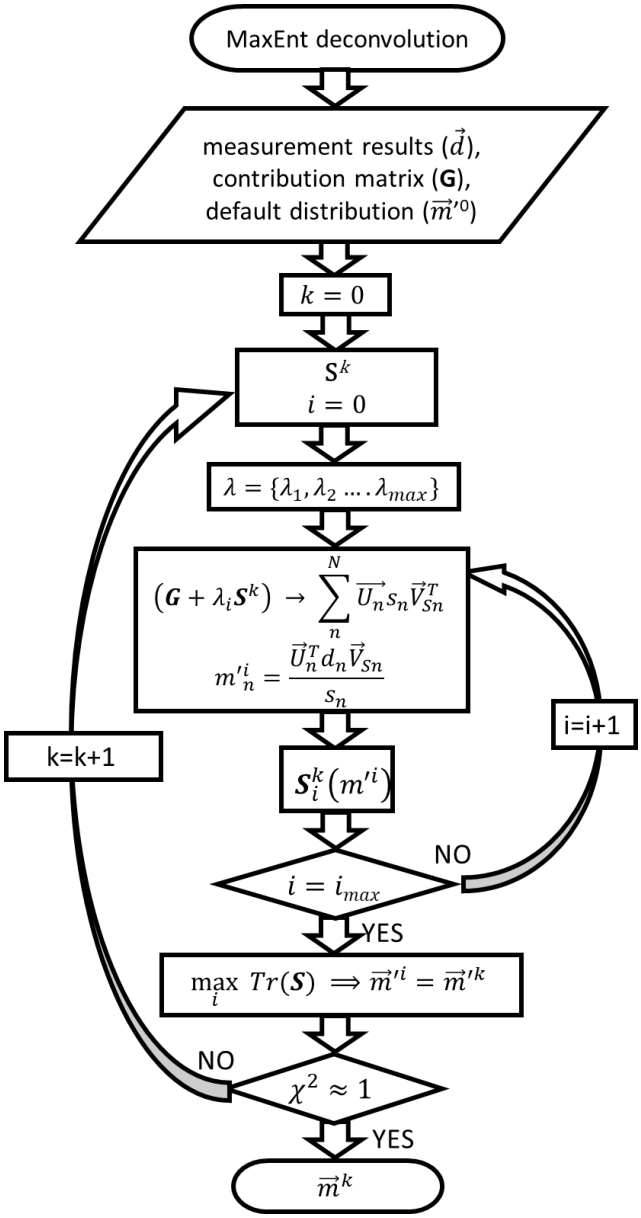

Figure 5.4. The flowchart for the MaxEnt code developed by the thesis author.

5.4 Maximum Likelihood

The last approach described in this thesis is the Maximum Likelihood method (ML). The Likelihood principle states that all the information about quantity under consideration obtained from measurement is contained in the likelihood function of the physical quantity for the given data:

$$\mathcal{L}(\vec{m}'|\vec{d}) = p(\vec{d}|\vec{m}'), \tag{5.4.1}$$

where $p(\vec{d}|\vec{m}')$ is the conditional probability distribution that the particular model distribution $\vec{m}'$ give the measurement data $\vec{d}$ [Ber1988].
The Likelihood function indicates how likely the model's values generate the measurement data. It does not describe a probability but relative uncertainty of the reliability of physical quantity $\vec{m}'$ [Kas2014]. The Likelihood Principle also states that if some data points result in the proportional likelihood function, they contain the equivalent information about the unknown

values. ML is a popular method of parameter estimation. The likelihood function for *N* measurements can be defined as [Cas2002]:

$$\mathcal{L}\left(\vec{m}'\middle|\vec{d}\right) = \prod_i^N p(d_i|\vec{m}'). \tag{5.4.2}$$

The ML method leads to the determination of physical quantity distribution with the highest probability [Kas2014]. The Poisson distribution can describe the problem concerning neutron emission probability:

$$p(d_i|\vec{m}') = e^{-\sum_j G_{ij} m'_j} \frac{\left(\sum_j G_{ij} m'_j\right)^{d_i}}{d_i!}. \tag{5.4.3}$$

The mathematical calculations are facilitated by using a logarithm of the likelihood function. This approach does not influence the solution. Maximum Likelihood in this form leads to the iterative algorithm developed by Shepp and Vardi. The algorithm is based on the equation, which derivation is described in detail in [She1982]:

$$m'^{k+1}_i = \frac{m'^k_i}{\sum_n G_{ni}} \sum_n \frac{d_n}{\sum_j G_{nj} m'^k_j} G_{ni}. \tag{5.4.4}$$

The equation is widely used in tomography and other reconstruction methods.

The ML code is a simple loop that iteratively calculates the new solutions from equation (5.4.4) until the difference between solutions is lower than the defined precision. The change in the solution decreases with the number of iterations.

Chapter 6: Problems with one-dimensional physical quantity distribution

All reconstruction methods described in chapter 5 have been implemented for the one-dimensional distributions reconstruction. In this thesis, two inverse problems related to the neutron measurement have been described.

The measurement by neutron camera provides the neutron emissivity in a single plasma poloidal cross-section. The desired reconstructed distribution has two dimensions. The simplification of the problem to 1D requires strong assumptions. The ion temperature and density have to be constant on the magnetic flux surfaces. Therefore, the neutron emissivity depends only on the poloidal magnetic flux, Ψ. The neutron emission needs to be isotropic on the whole surface. The assumptions are fulfilled only for thermal plasma in an equilibrium state [Mly2007]. The contribution matrix describes the overall impact of each flux surface on the measurement. The elements of matrix $\boldsymbol{G}$ contain the sum of the areas of fields of view intersecting with flux surfaces on both tokamak sides, LFS and HFS, or bottom and top. Therefore, it is not possible to reconstruct asymmetries. The result of the reconstruction is the neutron emissivity in the function of normalised poloidal flux. The simplification was applied to the data analysis for ITER RNC, and the results were described in subchapter 8.3.1.

Another example of the one-dimensional problem is the reconstruction of a neutron energy spectrum based on the activation measurement (see chapter 10). The input data are results of the activation measurements of multiple dosimetry foils. The neutron energy spectrum after discretisation is divided into a finite number of bins. The width of a single bin determines the resolution for which the intensity of neutron emission is reconstructed. The response matrix $\boldsymbol{G}$ consists of the activity per neutron defined as:

$$G_{kj} = \frac{A_{kj}}{I_j} = \sigma_k(E_j) N_0 \left(1 - e^{-\lambda_{Tk} t_i}\right), \tag{6.1}$$

where j is the index of bin in the spectrum, A is activity related to reaction k, I is the number of emitted neutrons, and $\sigma_k(E)$ is cross-section of reaction k for defined energy.

The regularisation operator in TR and MFI methods is a derivative matrix for neutron emissivity in the function of the normalised poloidal flux and neutron spectrum reconstructions. The order of the derivative is chosen separately for particular measurement data. The synthetic data simulated for the defined experiment are used for the test of the reconstruction performance with various derivative operators. The regularisation matrix related to the result of the lowest discrepancy between solution and simulated data is used in the reconstruction based on the experimental data.

Chapter 7: Problems with two-dimensional physical quantity distribution

Tomography is imaging by analysis of the object slices [Kak2001]. In this thesis, tomography refers to reconstructing a single projection for a particular time slice, a two-dimensional physical quantity distribution, from integrated measurement. The measurement for tomography requires many detectors viewing the plasma from different directions. The performance of the reconstruction is bounded by the limited number of directions, irregular sampling, finite view, and noisy measurement data connected with a harsh environment near the plasma device [Ing2008]. The neutron camera measurement aims to determine the neutron emissivity distribution in the whole plasma poloidal cross-section. The number of detectors is limited, and tomography requires the reduction of the unknown values and application of the additional constraints. The problem is highly ill-posed and depends strongly on the discretisation. The poloidal plasma cross-section is divided into pixels. The pixels can have a variety of shapes. They need to be sufficiently small to assume the constant emissivity in their area. This thesis considers rectangular pixels due to the absence of the prior assumptions and straightforward transformation from integral equations [Ant1996]. The pixel grid definition controls the resolution of the reconstructed cross-section. The cartesian coordinates system is used to simplify the mathematical calculations [Mly1995].

The tomography is based on integrated measurement along the line of sight (LOS) or field of view (FOV). LOS and FOV are defined by the position of the detector, viewing direction and type of collimation. The basic description of the space seen by detectors is based on lines. This assumption is valid only for highly collimated measurements, e.g. soft X-ray pinhole cameras where the slit size is small compared to the channel area. The contribution matrix for neutrons requires an extension of the geometry description into FOVs and taking into account solid angles. The collimation of the neutrons is more difficult because of the low probability of the interaction with matter. The thick shielding is required to reduce the influence of neutrons produced in the plasma area other than defined by LOS. Therefore, the collimator is long, and FOV has the shape of a truncated cone. The collimating aperture needs to reduce the area seen by the detector, but registered radiation should be sufficiently high to provide a good signal-to-noise ratio. The radius of the collimator and neutron detector is usually very similar. The contribution matrix contained the length of LOSs intersecting the pixel usually is strongly ill-defined. The LOSs pass through only a few pixels, and the contribution matrix contains a small number of nonzero values. The consequence is that eigenvalues are close to zero, which is the source of numerical instabilities. The same effect is caused by reducing the number of detectors or decreasing pixels area. The sensitivity to measurement noise is high, and reconstruction is strongly unstable. The solution is an application of the regularisation method. Nevertheless, tomography results can differ from the actual physical quantity distribution. The consideration of FOV improves the definition of the contribution matrix. There are fewer zero elements because viewing cones pass through more pixels. It is crucial for cameras with a low density of LOSs [Wei2015].

The basic code [Ods2012] used in this thesis for plasma emissivity reconstruction is based on the MFR method. The algorithm has been initially developed in EPFL Lausanne for soft X-ray tomography [Ant1996]. The basic assumptions are isotropic emission and optically thin plasma for electromagnetic radiation. The significant simplification is a hypothesis that radiation emission is independent of toroidal direction. It is related to plasma volume coverage with negligible bending of the torus. The fusion plasma is roughly toroidally symmetric. The soft X-ray emissivity is determined by temperature, density, and impurities content. Therefore, the emissivity profile should be smooth with low radiation outside the plasma [Ing1998]. The probability of the neutron interaction with matter is minimal, which is equivalent to the optical thickness for electromagnetic radiation. In the thermal plasma, ion velocity is described by the Maxwell-Boltzmann distribution (equation (1.1.6)), which is the function of temperature. The reaction rate for neutron production (1.1.10) depends directly on ion density. The plasma parameters are constant on

magnetic flux surfaces for an approximation of the equilibrium state. Therefore, the constant emissivity along magnetic field lines and isotropic emission assumption can be applied to neutron emissivity reconstruction. In non-thermal plasma, the neutron energy and direction depend on the pitch angle between the magnetic field and ion velocity. The plasma rotation also influences the emitted neutron energy spectrum. In the current tokamaks, the heating systems cause strong anisotropy in the neutron emission. The assumption of the constant emission in all directions can be applied only to sufficiently small pixels. In non-thermal plasma, the assumption about the fixed plasma parameters on the magnetic flux surface is not valid. The impossibility of neutron emission outside the plasma, and emission decrease on the edges, is always actual.

The discretisation of the continuous emissivity profile by the pixel grid changes the problem of the tomography reconstruction to the system of the equations (equation (4.4)). The contribution matrix ***G***, also called the geometry matrix, describes the geometrical contribution of the emissivity to the measurement. The definition of the matrix ***G*** depends on the type of collimation and the measured type of radiation because it influences the emission direction and the way of spreading out in plasma.

The side constraint in the MFR method for tokamaks is related to the plasma density and temperature gradients. The gradients are low along the magnetic field lines but may rise in the perpendicular direction. It is the consequence of the assumption that parameters are linked to the magnetic field surfaces but are not demanded to be constant. The regularisation matrix smooths the reconstructed emissivity along magnetic field lines and is given as [Ods2012]:

$$\boldsymbol{L} = S(\Omega)\boldsymbol{B}_{||}^{T}\boldsymbol{W}\boldsymbol{B}_{||} + S(-\Omega)\boldsymbol{B}_{\perp}^{T}\boldsymbol{W}\boldsymbol{B}_{\perp}, \tag{7.1}$$

where $\boldsymbol{B}_{//}$ is the derivative acting parallel to the magnetic field lines, $\boldsymbol{B}_{\perp}$ is the derivative perpendicular to the magnetic flux surfaces, *S(Ω)* is the logistic sigmoid function that controls the anisotropy amplitude, and *Ω* is the scalar parameter called the smoothing parameter later in this thesis.

High values of *Ω* are related to the strong smoothing along the magnetic field lines compared to other directions. If the smoothing parameter is equal to 0, the smoothing is isotropic. A sigmoid function has horizontal asymptotes in y=0 and 1. The function is close to 1 for all values greater than 10. Therefore, increasing *Ω* above 10 changes negligibly the derivatives combination.

The first-order derivative operators are implemented as matrices with smoothing directions determined for each pixel. The operator $\boldsymbol{B}_{//}$ contains derivatives in two directions, parallel and diagonal, as presented in figure 7.1. The elements of derivative $\boldsymbol{B}_{\perp}$ act in the toroidal direction (*a*, *b* and *c* values depend on the magnetic field for a particular tokamak) [Ods2012]:

$$\boldsymbol{B}_{\perp} = \begin{bmatrix} -a & b & 0 & & & & & & \\ 0 & -a & b & & \cdots & & & 0 & \\ 0 & 0 & -a & & & & & & \\ & & & -c & 0 & 0 & & & \\ & \vdots & & 0 & -c & 0 & & \vdots & \\ & & & 0 & 0 & -c & & & \\ & & & & & & -a & b & 0 \\ & 0 & & & \ldots & & 0 & -a & b \\ & & & & & & 0 & 0 & \ddots \end{bmatrix}. \tag{7.2}$$

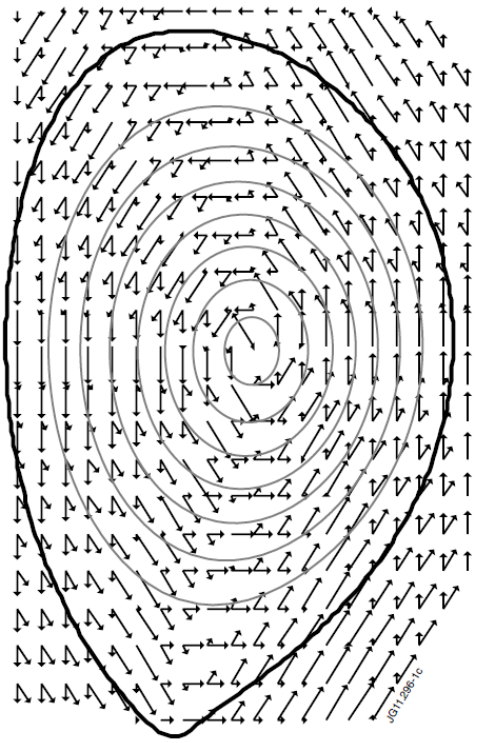

Figure 7.1. The vector representation of the derivatives in diagonal and parallel directions to the magnetic flux surfaces [Ods2012].

The elements of matrix and vector in equation (5.1.3) are modified before the tomography calculations as follows:

$$G'_{ij} = \frac{G_{ij}}{\sigma_{s\,i}} \tag{7.3}$$

$$d'_i = \frac{d_i}{\sigma_{s\,i}} \tag{7.4}$$

to take into account the uncertainty of the measurement represented by standard deviations.
The residual norm in the tomography code is defined as χ^2 (equation (5.2.4)), also called the goodness-of-fit parameter. The algorithm consists of two nested cycles. The regularisation parameter is selected in the inner loop by testing the results for different values. The condition for optimal λ is χ^2 close to 1. The solution of the regularisation problem is obtained based on the Cholesky decomposition. The outer cycle optimises the weighting matrix. The previous solution is used for weight matrix calculation and impacts the regularisation operator. Typically three iterations per reconstruction are sufficient to obtain the proper solution [Ods2012].

The original tomography code has been written in Python programming language for soft X-ray measurements on JET and used on COMPASS tokamak. Only the basic Python libraries were used in the first version, and the code structure was complicated. Afterwards, the code was improved by replacing many functions with advanced Python modules. The code version implemented for neutron tomography was initially incompatible with Windows operating system. The author of the thesis adjusted the code and replaced part of the algorithm based on the standard libraries. All changes are connected with improving the time of calculations. The modification of the code's structure makes it more flexible and understandable. Description of the technical details is omitted in this thesis as it is not relevant to physics. The other version of the same code is available on GitHub [Svo2021]. The changes related to the neutron measurement are described in following subchapter. The primary goal was to apply the tomography code to

analyse the data from the Radial Neutron Camera (RNC) for ITER concerning the thermal plasma. Additionally, the prepared tools have been applied to interpret the neutron emissivity profiles measured during the DT campaign on JET.

7.1 Optimisation of the code for neutron tomography

The neutron emissivity has been assumed as constant and isotropic in the very small pixel compared to the poloidal tokamak cross-section. The regularisation is based on the assumption that gradients of plasma parameters (temperature, density, neutron emission) are close to zero on magnetic field lines and increase perpendicular to the magnetic field. This problem simplification has been applied to both types of plasma, thermal and with non-Maxwellian ion velocity distribution.

The implementation of the tomography code to the neutron emissivity reconstruction includes programming the new module for a particular tokamak. The prepared part of the code loads input data, measurement data and magnetic field configuration for particular discharge. The module for ITER recalculates the count rates to the total number of neutrons that reached the detectors with included noise. The MCNP simulation of the measurement by RNC includes the detection efficiency and background level [Mar2011]. The random noise with Poisson character is considered. There is also the possibility of analysing the influence of the measurement error with the Gaussian distribution of different amplitudes on the reconstruction performance. The module loads poloidal flux values and projects them into the defined coordinate system. The reconstruction is performed many times for the same data set with a slightly different noise, and the final result is the mean value from all reconstructions. This approach improves the precision of the reconstruction and makes the method more stable. The final solution is not sensitive to the changes in the data connected to the randomly distributed noise. The module for JET loads the input data and prepares it for analysis in a particular time range. The possibility of time resolution modification is also implemented. The thesis author wrote the program which prepares the magnetic field calculated by EFIT [Lao1990] to be compatible with tomography code. The reconstruction of the neutron emissivity for JET is performed for the whole time range, which means the normalisation of the inputs is related to the complete data set, and error calculations include the variations of the count rates in time.

Initially, the geometry matrix included lengths of the line of sights crossing the pixels. The contribution matrix for the neutron tomography was specially prepared for the collimating system and based on the knowledge about neutron production and interactions with plasma. The comparison of the geometry matrices computed by two methods is presented in figure 7.2. The example concerns the metallic bolometers layout designed by the thesis author for COMPASS-Upgrade tokamak. The reconstruction results for the small number of detectors are better with the contribution matrix described by areas. In the case of very dense LOSs distribution in poloidal cross-section combined with a small separation between channels in one camera, the better solution is obtained with the geometry defined as lines [Mik2021].

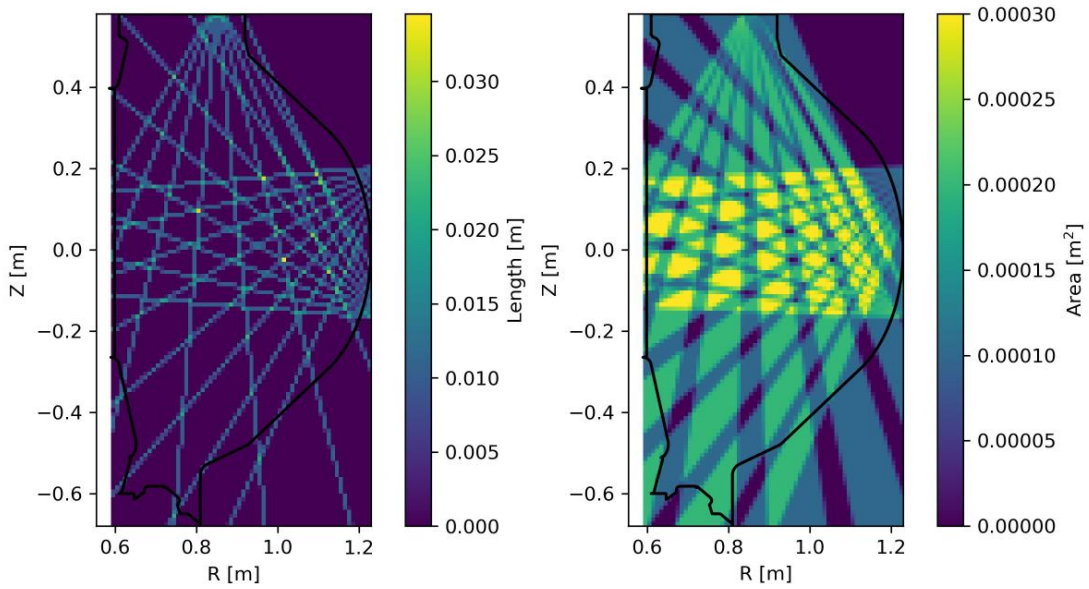

Figure 7.2. Comparison of the geometry matrix for the metallic bolometers diagnostic for tokamak COMPASS-Upgrade with lines length (left side) and areas (right side) [Mik2021].

The neutron cameras consist of long collimators with detectors at the ends. The area of the plasma that is seen by the detectors has a truncated cone shape. The schematic drawing of FOV is presented in figure 7.3.

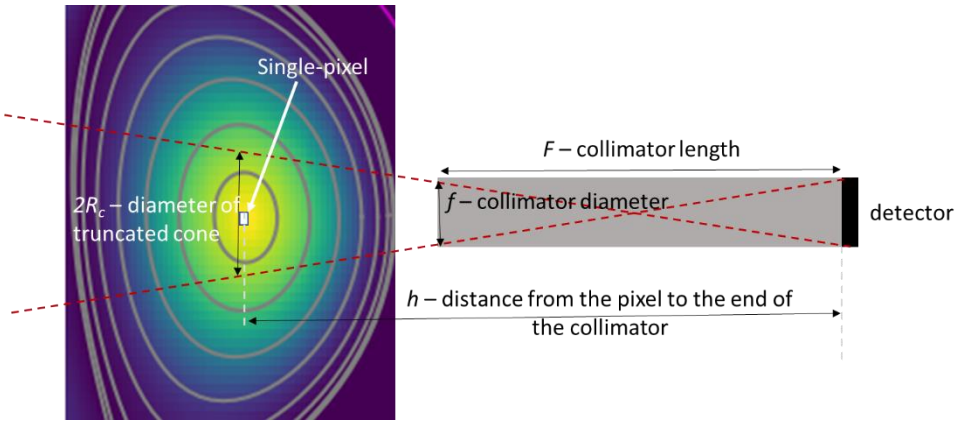

Figure 7.3. Schematic representation of the neutron detector field of view.

The radius of the truncated cone in distance *h* from the collimator end is equal to the following equation resulting from the neutron transport calculations:

$$R_C = \frac{f}{2}\left(1.1 + \frac{2h}{F}\right), \tag{7.2.1}$$

where *f* is the collimator diameter, and *F* is the collimator length [DDD2017].
The basic elements of the geometry matrix are areas of pixels covered by neutron detectors' fields of view. The contribution matrix for ITER RNC and JET neutron camera are presented in figures 7.4 and 7.5, respectively. The pixels can be estimated as isotropic, point neutron sources for thermal plasma. The assumption increases the reconstruction's uncertainty for the emissivity related to the non-Maxwellian ion velocity distribution. The nonthermal neutrons originate from collisions with accelerated ions, which are highly dependent on the moving direction. The assumption is more realistic for ITER RNC and thermal plasma. The neutron camera at JET relative position to the NBI beam allows for a rough estimation that the probability of emission in all directions in

a single pixel is nearly constant. The contribution matrix takes into consideration solid angles. The elements of the geometry matrix are multiplied by geometry factors (*Gf*) for the single pixels related to the solid angle, which is inversely proportional to the distance between detector and pixel (x_i). The value of x_i is an integral over coordinates correlated with the pixel. The geometry factor (Gf_{ip}) for a single pixel is equal to:

$$Gf_{ip} = \frac{{D_p}^2}{4}\frac{1}{x_i}, \tag{7.2.2}$$

where D_p is the detector diameter.
The truncated cones concern three-dimensional measurement. Therefore, the reconstructed emissivity unit is neutrons/time/volume.

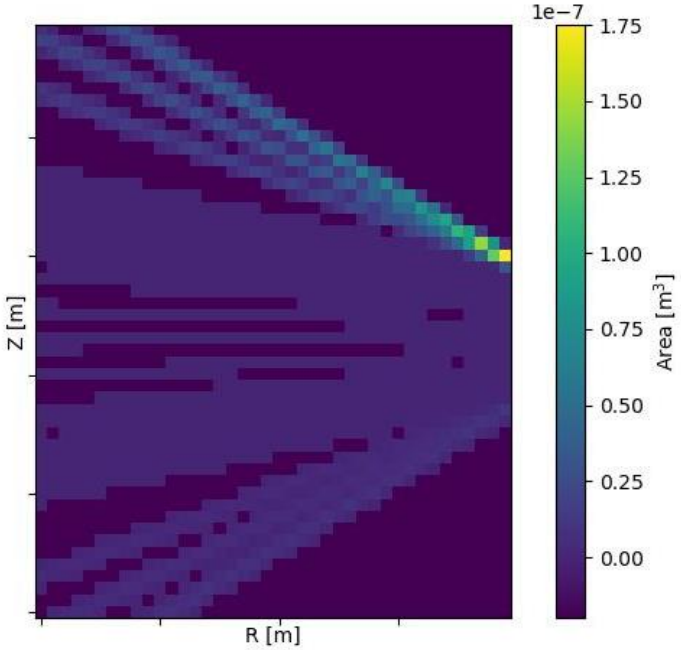

Figure 7.4. The graphical representation of the contribution matrix for ITER RNC.

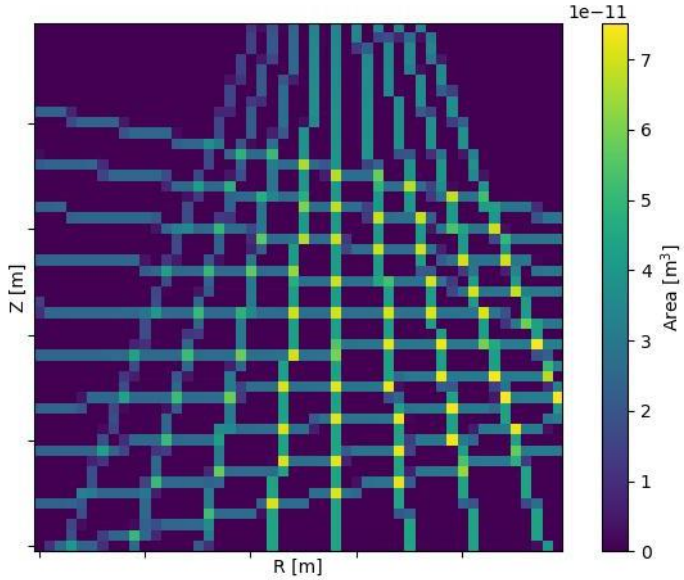

Figure 7.5. The graphical representation of the contribution matrix for JET neutron camera.

The number of measurement data is low for neutron cameras. Therefore, tomography reconstruction is complex, even for sophisticated regularisation methods. Supplementary information about the experiment's physics can be implemented in the calculations. A priori assumptions in the form of additional constraints help improve the tomography accuracy. It is possible to add data to the measurement vector and contribution matrix. The basic boundary condition is no emission outside the plasma (last closed flux surface). The zero data point is added to the measurement set. The geometry matrix gains an additional row. In this part, all matrix elements outside plasma are equal to the pixel area, and those inside plasma are equal to zero. This condition agrees with the observation that only neutrons produced in the plasma can originate in the fusion reactions. The secondary neutrons may originate from the wall and other device components, but the neutron emission analysis should not include them. The constraint is valuable in reconstructing the plasma boundary and helps avoid artefacts outside the plasma. The second constraint is the total neutron yield measured by independent diagnostics. The data from a neutron monitor like a fission chamber can be added to the input. The part of the geometry matrix corresponding to the total neutron yield constraint is equal to the pixel area for pixels contained in the plasma. The zero elements are everywhere outside the last closed flux surface. There is an option of adding the total neutron yield to the reconstruction in the code. The contribution matrix and measurement vector with side constraints are represented by:

$$G = \begin{bmatrix} \cdots & G_{1\,i} & G_{1\,i+1} & G_{1\,i+2} & G_{1\,i+3} & \cdots \\ \cdots & G_{2\,i} & G_{2\,i+1} & G_{2\,i+2} & G_{2\,i+3} & \cdots \\ & & & \vdots & & \\ \cdots & G_{n-1\,i} & 0 & 0 & G_{n-1\,i+3} & \cdots \\ \cdots & 0 & G_{n\,i+1} & G_{n\,i+2} & 0 & \cdots \end{bmatrix} \leftrightarrow \vec{d} = \begin{bmatrix} d_1 \\ d_2 \\ \vdots \\ 0 \\ total\ neutron\ yield \end{bmatrix}. \quad (7.2.3)$$

The last additional constraint that can be added to the calculations concerns the ion temperature measurement. The neutron emission is highly correlated with the ions' parameters. Therefore, the result of the reconstruction should be consistent with temperature measurement. The reaction rate calculated based on the temperature profile can be implemented in the geometry matrix. The estimated values in each pixel are calculated by equation (1.1.9) with the parameters defined by Bosch and Hale [Bos1992].

The application of the additional constraint and optimisation of the parameter that controls smoothing along magnetic field lines, pixel grid size and contribution matrix need to be analysed for the particular problem. The results of the reconstruction of the neutron emissivity in ITER based on RNC measurement simulation are described in chapter 8. The analysis of the neutron tomography for JET is presented in chapter 9.

Part III: Data analysis

In this part of the thesis, the Radial Neutron Camera for ITER and its tomography ability is described. Chapter 8 focuses on the neutron emissivity spatial distribution reconstruction for different diagnostic configurations. The analysis includes the comparison of the results with the implemented additional constraint in the form of the total neutron yield. The tomography code performance was verified with experimental data from the neutron camera measurement on JET during the DT Campaign in 2021. The results of the reconstruction are presented in chapter 9. The application of another inverse method is neutron energy spectrum reconstruction. It can be accomplished if the dependence of the measured values on energy distribution is well known. The results of the activation method implementation to the neutron spectrum deconvolution are described in chapter 10.

Chapter 8: Tomography performance of Radial Neutron Camera for ITER

The Radial Neutron Camera (RNC) is diagnostic for ITER tokamak devoted to the 14-MeV and 2.5-MeV line-integrated neutron measurement in one toroidal position. During the writing of this thesis, the diagnostic design was prepared for the final review. RNC consists of collimators equipped with neutron flux monitors or compact spectrometers. The flux reaching the detectors along collimated lines includes neutrons originating directly in observed plasma and neutrons scattered in the surrounding structures. The measured flux is proportional to the line integral of the neutron emissivity along the collimator view if the scattered component is kept negligible. The primary purpose of RNC is a time-resolved measurement of the neutron and alpha source profile for real-time plasma burn control. The line-integrated measurement allows the neutron emissivity profile evaluation using inversion techniques. The 1D distribution in flux surfaces is highly correlated with an assumption about low parameters gradients along the magnetic field lines. The 2D reconstruction is based on the same assumption due to only one direction of the plasma observation. The tomography requires a more sophisticated method and additional side constraints connected with the physics understanding.

The time resolution of the neutron emissivity measurement should be in the range of 1 – 100 ms, which allows for obtaining 10% accuracy of 1D and 2D reconstruction. The predicted neutron yield is in the range of $2 \cdot 10^{17} – 2.6 \cdot 10^{20}$ n/s. LOSs cover the full poloidal cross-section with spatial resolution from $a/10$ to $a/30$ (a - minor tokamak radius) [DDD2017].

The tomography performance analysis aims to optimise the diagnostic configuration to fulfil the required accuracy. The ability of the reconstruction has been analysed on the different levels of the design progress. Chapter 8.3 contains the analysis of the tomography performance for the preliminary design. The analysis includes the study of the total neutron yield constraint influence and robustness tests for changes in the input data that can occur in the experimental environment. In chapter 8.4, the comparison of the tomography results for different types of detectors is described.

8.1 Diagnostic description

RNC is located in ITER equatorial port #1 together with the Radial Gamma-Ray Spectrometer (RGRS) and the High-Resolution Neutron Spectrometer (HRNS) (see figure 8.1). RNC consists of two fan-shaped collimating sub-systems: in-port and ex-port, which view the plasma radially by slots in the diagnostic shielding in the port plug. The Intermediate System Architecture (ISA) concerns parameters of three diagnostics defining LOSs distribution. The RNC baseline architecture solves the minimalization of the detectors number issues and optimization of the collimator geometry. The collimator's length, diameter, and position define the region of the plasma seen by the detector. The parameters of collimators should be optimized to reduce

the background and provide the measured radiation level with a reliable uncertainty. The CAD model of the RNC layout that includes interfering diagnostics is presented in figure 8.2 [DDD2020].

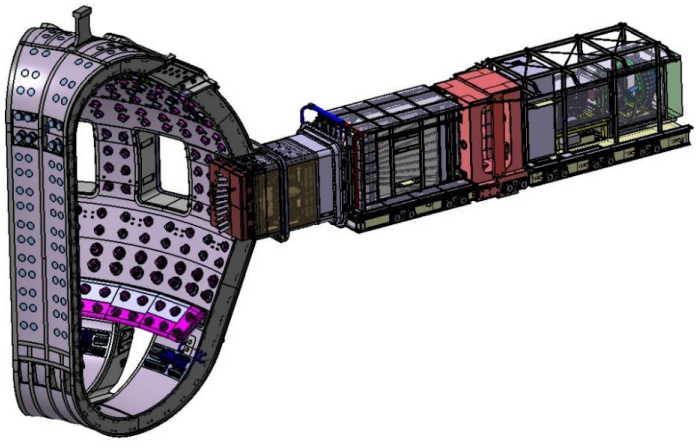

Figure 8.1. The location of RNC in ITER tokamak poloidal plane [DDD2017].

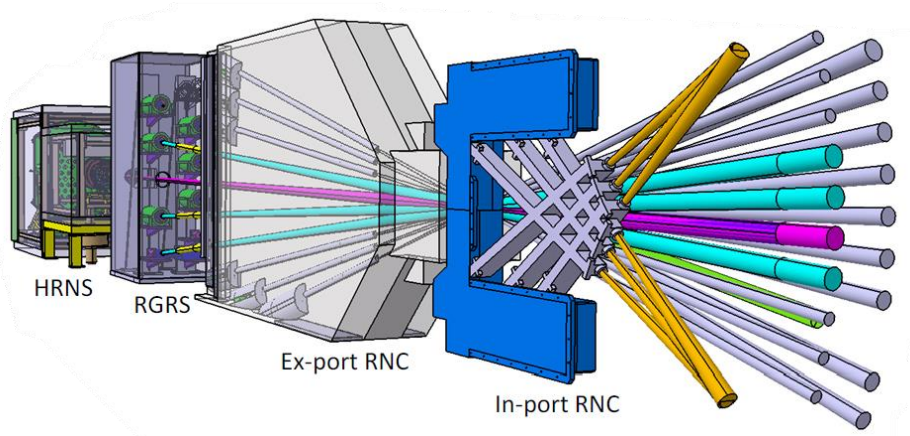

Figure 8.2. The RNC layout (grey and yellow lines are optical paths) including RGRS (magenta lines) and HRNS (cyan lines) systems position [DDD2020].

Introduced architecture is the result of a sequence of optimisations. In the preliminary design activities, the general structure of the collimator layout has been chosen from the options presented in figure 8.3. The performance analysis shows that LOSs viewing the plasma edge are relevant for the emissivity profile reconstruction [Mar2016]. The in-port detectors need to be directed to the plasma edges. More than three LOS per in-port cassette are not beneficial because of the poor quality of signals correlated with weak neutron fluxes for the detectors located on the furthest upper or lower edge (not shown in figure 8.3). The six collimators of the in-port part are found to be optimal. Considered crossings of LOSs (MAXCROSS/AVECROSS in figure 8.3) do not improve the ability of the emissivity profile reconstruction. The dense distribution of the ex-port LOSs in the plasma core provides the data with satisfying accuracy, but their number should be limited because of technical requirements. The structure of the collimator is the same for both systems. A shielding block with drilled voids serves as a flight tube. The two stainless steel collimators are mounted on the front and rear sides. The shielding along the flight tube is made of boron carbide. The geometry of the collimators has been optimised for detectors to handle strong neutron fluxes [DDD2020].

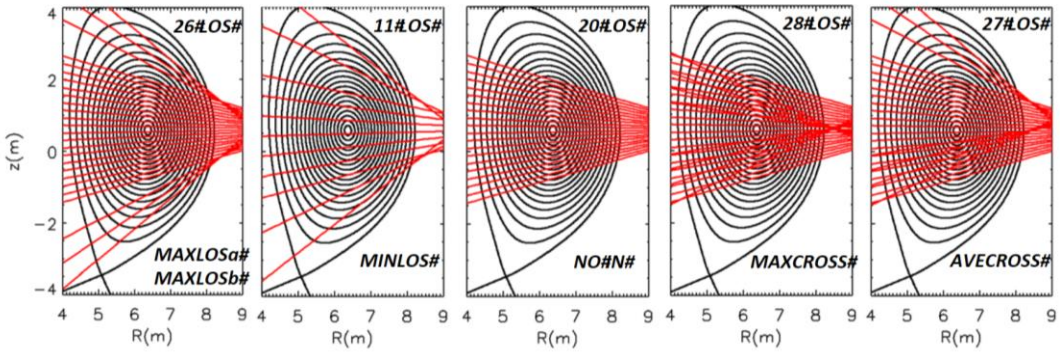

Figure 8.3. Possible options of the RNC layout considered in the preliminary analysis [DDD2020].

The ex-port part of the system consists of detector modules, flight tubes with collimation units and beam dumps, and a shielding block placed in the port interspace. Metallic double windows and optical paths are located in the port plug. The ex-port part of the system is distributed in two radial planes separated by a 1.42° angle. Each plane contains 10 LOSs. RNC ex-port part has substantial interference with HRNS and RGRS. These two diagnostics, to feature sufficient performance, require to have separated collimators. Therefore, the number of RNC detectors has been reduced to 16. One position is shared between RNC and RGRS. The ISA architecture concerns the diagnostic version with the complete number of LOSs and is presented in figure 8.4. The baseline architecture includes the shared collimator (#8), but #11, #12, #15, and #17 are excluded from the layout. The tomography performance ability for both layouts is analysed in this thesis. The in-port part of RNC is located in the port plug. It consists of the upper cassette assembly with three detector modules guided to the bottom edge of the plasma and the lower cassette assembly with three detectors directed to the opposite side. Two cassettes are located in parallel planes, thus not intersecting the tokamak axis. The conical-shaped optical paths cross the diagnostic shielding module and reach the first wall of ITER. The positioning close to the plasma requires the application of a cooling system. Active water cooling sustains the temperature below 150°C around the detectors. The geometrical parameters of all RNC LOSs are presented in table 8.1 [DDD2020].

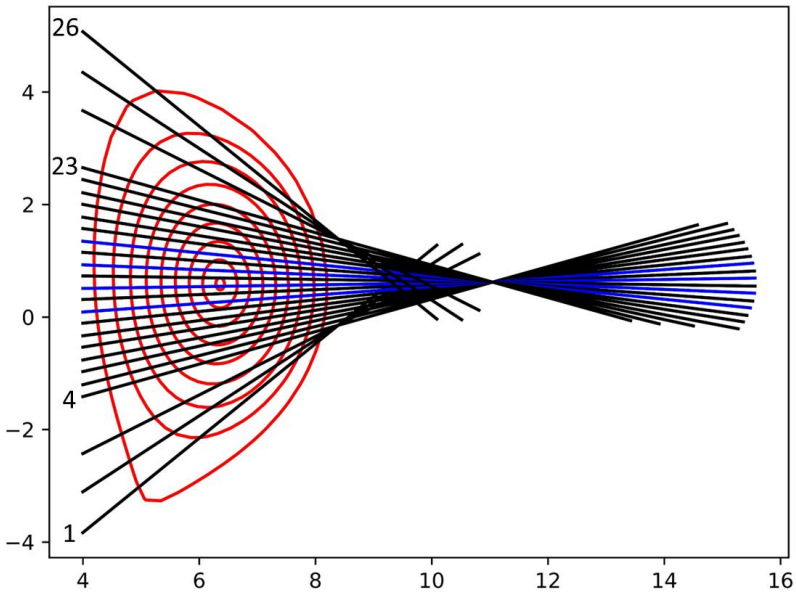

Figure 8.4. The Intermediate System Architecture of RNC & RGBS & HRNS diagnostics (black lines – LOSs, red lines – magnetic field, blue lines – LOSs excluded from baseline architecture).

Table 8.1 Geometrical parameters of RNC ISA architecture (the collimators excluded from the baseline layout are highlighted in grey) [DDD2020].

Number	Position	Angle [degrees] (clockwise from vertical)	Collimator diameter [mm]	Length [m]
1	in-port upper cassette	50	32	0.9
2	in-port upper cassette	56	32	1.3
3	in-port upper cassette	62.5	32	1.5
4	ex-port	73.9	11	2.6
5	ex-port	75.5	11	3.0
6	ex-port	77.3	11	3.0
7	ex-port	78.9	11	3.0
8	ex-port (+ RGRS)	80.7	11	3.0
9	ex-port	82.3	11	3.0
10	ex-port	84.1	11	3.0
11	RGRS	85.7	11	3.0
12	ex-port	87.5	11	3.0
13	HRNS	89.1	11	3.0
14	ex-port	90.9	11	3.0
15	RGRS	92.5	11	3.0
16	ex-port	94.3	11	3.0
17	RGRS	95.9	11	3.0
18	ex-port	97.7	11	3.0
19	ex-port	99.3	11	3.0
20	ex-port	101.1	11	3.0
21	ex-port	102.7	11	2.3
22	ex-port	104.5	11	1.8
23	ex-port	106.1	8	1.4
24	in-port lower cassette	117.5	32	1.5
25	in-port lower cassette	124	32	1.3
26	in-port lower cassette	130	32	0.9

The detectors considered to be used in RNC are scintillators (plastic EJ-276G or gas ^{4}He Arktis), single-crystal diamond detectors (sCD), and ^{238}U fission chambers. The scintillators are widely used for neutron measurement because they have fast response, high efficiency, good energy resolution, and pulse shape discrimination possibility. The light produced in the scintillator is proportional to the neutron energy. Therefore, the spectrum can be deduced from pulse-high distribution, and the background can be separated from fusion neutrons. The sCD can measure the neutron flux and energy spectrum. The analysis of the neutron reactions with diamond atoms provides information about neutron energy. The background radiation can be easily separated in fission chambers by signal threshold setup. The use of high purity ^{238}U enables the detection of fast neutrons in count mode. The measurement efficiency can be increased by increasing the surfaces of the electrodes [Del2020].

In the in-port system, two in-line detectors will be placed inside the port plug. Therefore, the detector module must be prepared for operation in higher temperatures and strong radiation fluxes. The detectors require a strong support structure, active cooling and magnetic field shielding. The in-port module is presented in figure 8.5. The sCD detector is located in front of

the fission chamber containing ^{238}U prepared for fast neutrons measurement. The parameters of the selected detectors are presented in table 8.2 [Del2020].

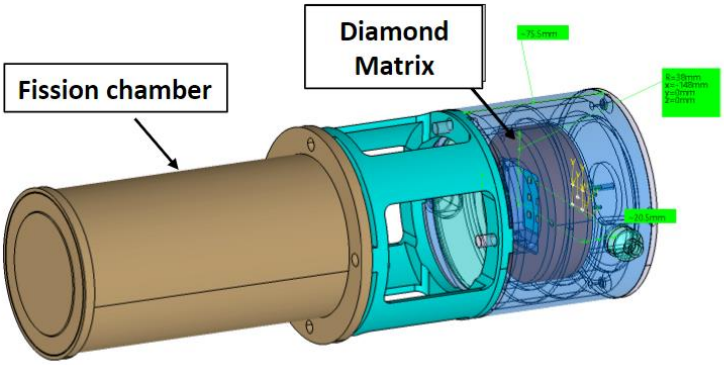

Figure 8.5. The in-port RNC detector module [Del2020].

Table 8.2. Properties of the detectors selected for the in-port part of RNC [Del2020].

Type	Diameter of sensitive area [mm]	Form	Efficiency of 14.1 MeV neutrons measurement [counts/ neutron]
^{238}U fission chamber	32	145 mg in 0.5 mg/cm^2 coating	$5.4 \cdot 10^{-5}$
sCD	30	30 pixels (4.5 x 4.5 mm) thickness 50 m	$5.4 \cdot 10^{-5}$

The ex-port module is located at a longer distance from the plasma in the port interspace. The environment in this position is connected with the maximal temperature of 100°C, and the magnetic field equals 0.2 T. The first choice for the ex-port was two in-line plastic scintillators: 1 cm thick for full power DT operation and 10 cm thick for lower power and DD operation (those detectors are considered in the tomography analysis in chapter 8.3). The detectors are able to detect neutrons of energy equal to 2.5 MeV and 14.1 MeV with discrimination possibility. The ability to separate gammas and background is also required. The statistical error of measured counts resulting from Poisson distribution should be about 1% in 10 ms. The design of the ex-port system has been not finalised during this thesis preparation. The detectors considered for this system are plastic scintillators EJ-276G, sCD, and ^4He Arktis scintillators. Table 8.3 shows a comparison of the properties of detectors. The considered options differ in size and form. The main dissimilarities concern the efficiency of measurement and background influence on the signal [Del2020]. The analysis of the influence of the detector type on tomography performance is described in chapter 8.4.

Table 8.3. Properties of the detectors selected for the ex-port part of RNC [Del2020].

Detector type	Size [mm]	Efficiency of 14.1 MeV neutrons measurement [counts/neutron]	Background [%]
plastic scintillator EJ-276G	10 thickness 11 diameter	$7.7 \cdot 10^{-3}$	0.6 - 1.7
sCD (4 pixels)	4 x 4 x 0.1	$1.3 \cdot 10^{-3}$	2.7 - 7.1
^4He Arktis scintillator (150 bar)	30 thickness 44 diameter	$2.8 \cdot 10^{-3}$	1.4 - 3.6

Total neutron yield from an external flux monitor can be used as an additional constraint in the reconstruction. The independent diagnostics that can provide the data for tomography are fission chambers. ITER neutron flux monitors (NFM) will be placed in two toroidal locations (the equatorial port #1 and #7): inside and outside the vessel. Adjusted content of ^{238}U and ^{235}U allows for the measurement of DD or DT neutrons. Combinations of detectors in different locations and with varying uranium content supply the measurement of the neutron strength and will be used to estimate the relative fusion power [Ber2019]. The time resolution of the detection will be 1 ms. Expected neutron fluxes are in the range of 10^4 – 10^{14} n/(s·cm^2). This dynamic range allows reaching 10% of the accuracy [Jin2008].

8.2 Simulations

The simulations of ITER operational scenarios include only symmetric neutron emission profiles with maximal intensity in the core centre. The disruptions and more complicated shapes are not expected due to the Maxwellian ion velocity distribution in the predicted plasma. ITER Organisation provided the simulations of the operational scenarios. The equilibria containing magnetic field configuration, plasma temperature and density distributions were calculated by ASTRA and PRETOR codes. The determination of plasma configuration is based on the Grad-Shafranov equilibrium equation [Pol2002].

First simulations are based on the ITER baseline scenario II of inductive operation. It concerns full power DT tokamak operation in H-mode. This scenario established 400 MW fusion power without heating during the current ramp-up to 15 MA. The power multiplication is predicted as 10 with a burn time of 400 s [How2007]. A component from non-thermal neutrons is small (below 3%), and toroidal asymmetries are not expected for this scenario. The plasma properties are constant on the magnetic flux surfaces and can be presented as symmetric 1D profiles dependent on the poloidal magnetic flux, Ψ. The thermal neutron emission is calculated based on the ion temperature and density profiles. A detailed description of the simulation is presented in [Mar2011]. Two versions of the emissivity distribution were prepared for a pedestal temperature scenario (a) and a peaked density scenario (b). The 1D neutron emissivity profiles prepared based on the temperature and density distribution for the considered scenarios are presented in figure 8.6. Figure 8.7 shows corresponding 2D profiles. The 1D profiles obtained from tomography are horizontal cuts through the plasma centre (Z=0.6 m).

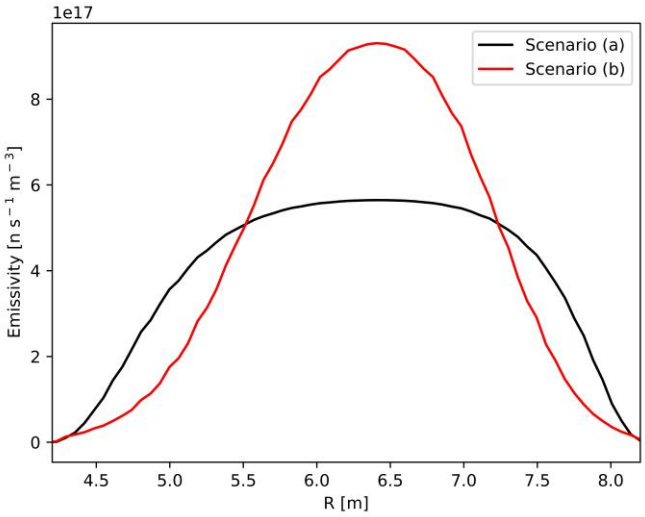

Figure 8.6. The 1D emissivity profiles for the pedestal temperature scenario (a - black) and the peaked density scenario (b - red).

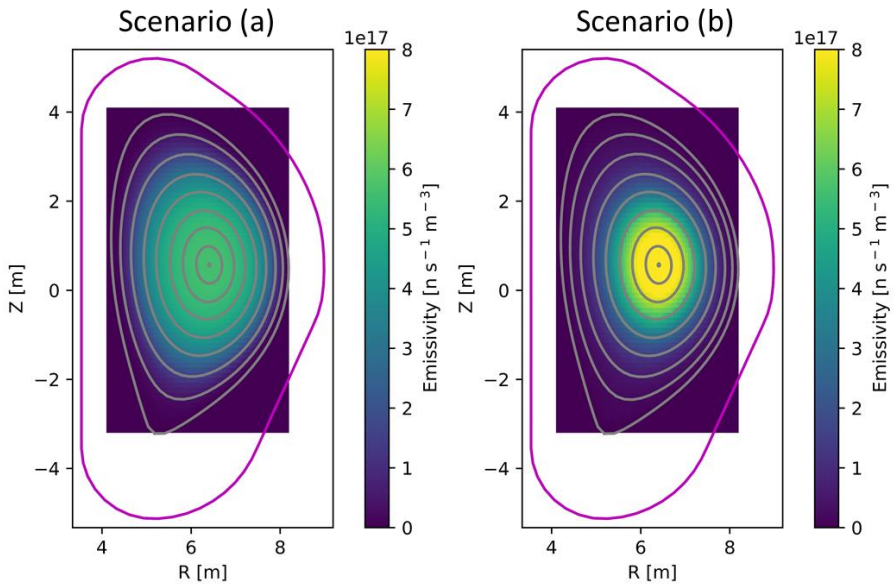

Figure 8.7. The 2D emissivity profiles for the pedestal temperature scenario (a - left) and the peaked density scenario (b - right).

Three different scenarios from RNC PA Annex B [IPA] have also been used for the tomography tests. Scenario (c) is based on the H-mode operation with a 15 MA current with a flat top duration over 400 s. Scenario (d) is connected with a hybrid operation with a stable 12.5 MA current for the 1300 s. Its equilibrium is the most similar to the baseline configuration. Scenario (e) is related to the steady-state operation with 9 MA current with 3000 s flat top duration. The neutron emissivity distributions in plasma for these scenarios are shown in figure 8.8. Presented scenarios differ not only by emissivity distribution but also in the magnetic field configuration. The differences between scenarios (c) and (d) are not clearly visible in the figures. The variations are connected to the positions of the magnetic field lines relative to the tokamak vessel.

The precision of the magnetic flux surfaces used in the tomography code depends on the resolution of the magnetic configuration grid calculated by ASTRA and PRETOR [Pol2002], which is different for various scenarios. The equilibria calculated for the baseline scenario have precisely defined magnetic field configuration (513x257 resolution). Scenario (c) is defined on the grid with 257x129 elements. Scenarios (d) and (e) have resolutions equal to 129x65. The approximation of the magnetic field lines from low-resolution equilibrium can be the source of the unphysical artefacts, for example, intersecting poloidal magnetic flux surfaces. Therefore, the loss of accuracy in tomography calculations can be observed.

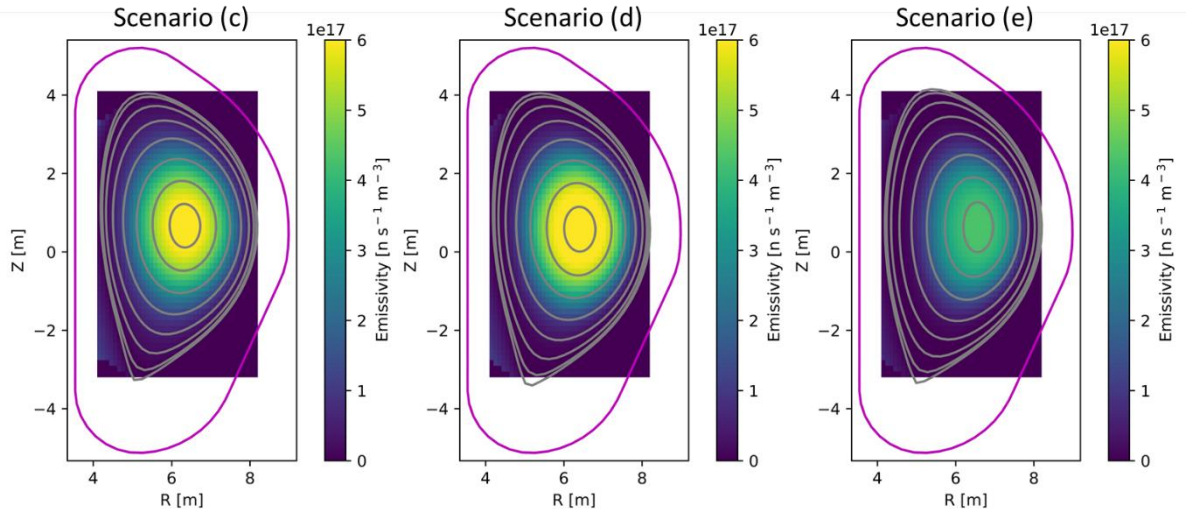

Figure 8.8. The 2D neutron emissivity profiles for H-mode (left), hybrid (centre), and steady-state (right) scenarios.

The simulation of the count rates registered by the defined kind of detector has been done by the following procedure. The MCNP [MCNP] calculations have been performed to obtain the neutron spectra and flux at the locations of the detectors. The simulations include the contribution from particles origin directly in the plasma volume defined by the line of sights and scattered neutrons [Mor2009]. The pulse height spectra from direct and scattered neutrons have been obtained by folding the neutron spectrum with the response function (RF) of the detector. RF for scintillators is generated by NRESP code [SG03-15A]. It takes into account the scintillator material, size, and temperature. RF for sCD detectors was obtained in the experiment presented in [Pil2011]. The calculation of RF for fission chambers includes the thickness of the coating layer and isotopes composition with relative abundance. The detector sensitivity is based on the cross-section of the fission reactions taken from [NDS]. The generated pulse heigh spectra were used to calculate the count rates registered by the detectors. The impact of scattered neutrons is defined as the background of the measurement [Mar2016]. RFs have been calculated for constant temperature because of the prediction of its low fluctuations. The influence of the magnetic field is not included and will be analysed experimentally in the further stage of the project. The impact of the gamma radiation on the background will be reduced by pulse shape discrimination and energy threshold setup.

Analysis of the reconstruction takes into account possible measurement errors. Poisson distribution describes the noise in the measurement connected with the count rate statistics. The measurement simulation includes adding random noise to the synthetic data. The measurement error is the difference between the count rates and values produced by the random number generator. The noise with different characters, e.g. Gaussian distribution, can be produced. The Poisson distribution describes the basic considered error, but the influence of the error with a Gaussian shape of different amplitude was also analysed.

The simulated count rates for scenarios (a) and (b) are presented in table 8.4. After the analysis of scenario (a), the decision about camera design was made due to the small differences in obtained tomography performance. Therefore, the simulation for ISA architecture was not done in the case of scenario (b). Additionally, the total neutron yield value can be added to the data vector. The total neutron yield corresponding to scenarios (a) and (b) equals $1.76 \cdot 10^{20}$ n/s and $1.83 \cdot 10^{20}$ n/s, respectively. The total neutron yield uncertainty is expected to be about 10% (related to the Gaussian distribution), and this value was used in the tomography analysis [Jin2008].

Table 8.4. The simulated count rate and background for ITER RNC and scenarios (a) and (b) (simulation for scenario (b) was not performed for the detectors excluded from the baseline architecture, the estimated background level is the same for both scenarios).

Detector Number	Count rates scenario (a) (s^{-1})	Count rates scenario (b) (s^{-1})	Background (%)
1	$4.90 \cdot 10^5$	$3.71 \cdot 10^5$	3.3
2	$5.83 \cdot 10^5$	$4.02 \cdot 10^5$	3.3
3	$7.38 \cdot 10^5$	$5.26 \cdot 10^5$	3.3
4	$7.54 \cdot 10^5$	$6.42 \cdot 10^5$	1.5
5	$6.25 \cdot 10^5$	$5.70 \cdot 10^5$	1.5
6	$6.82 \cdot 10^5$	$6.67 \cdot 10^5$	1.5
7	$7.24 \cdot 10^5$	$7.49 \cdot 10^5$	1.5
8	$7.63 \cdot 10^5$	$8.32 \cdot 10^5$	1.5
9	$7.91 \cdot 10^5$	$8.96 \cdot 10^5$	1.5
10	$8.15 \cdot 10^5$	$9.55 \cdot 10^5$	1.5
11	$8.30 \cdot 10^5$		1.5
12	$8.42 \cdot 10^5$	$1.02 \cdot 10^6$	1.5
13	$8.47 \cdot 10^5$		1.5
14	$8.47 \cdot 10^5$	$1.03 \cdot 10^6$	1.5
15	$8.41 \cdot 10^5$		1.5
16	$8.29 \cdot 10^5$	$9.74 \cdot 10^5$	1.5
17	$8.12 \cdot 10^5$		1.5
18	$7.86 \cdot 10^5$	$8.59 \cdot 10^5$	1.5
19	$7.56 \cdot 10^5$	$7.88 \cdot 10^5$	1.5
20	$7.13 \cdot 10^5$	$6.97 \cdot 10^5$	1.5
21	$1.13 \cdot 10^5$	$1.04 \cdot 10^6$	1.5
22	$1.68 \cdot 10^6$	$1.41 \cdot 10^6$	1.5
23	$6.93 \cdot 10^5$	$5.40 \cdot 10^5$	1.5
24	$6.45 \cdot 10^5$	$4.16 \cdot 10^5$	3.3
25	$4.61 \cdot 10^5$	$2.92 \cdot 10^5$	3.3
26	$3.28 \cdot 10^5$	$2.38 \cdot 10^5$	3.3

8.3 Neutron profile reconstruction for preliminary design

In this chapter, the ability of the tomography reconstruction for two RNC architectures has been analysed. The RNC measurement aims to obtain the neutron emissivity distribution with an accuracy of at least 10% in the plasma core. The analysis was performed to verify that the current architecture design allows for fulfilling the requirements. The results was described in [Mik2020]. The synthetic data described in chapter 8.2 was used in the reconstruction for the precision evaluation.

The final solution is the mean value from 100 reconstructions of the synthetic data with a slightly different noise. The error bars presented in the figures are standard deviations for the full set of reconstructions. The quality of the reconstruction is evaluated by comparison of the accuracy, which is defined as the relative difference between the solution ($\vec{m}'$ for the one-dimensional problem or ***m'*** for the tomography) and the profile called original, which was used to obtain the input data ($\overrightarrow{Sm}$ or ***Sm***):

$$Accuracy_j = \frac{(m'_j - Sm_j)}{Sm_j}, \quad (8.3.1)$$

where *j* is the index describing the elements in the reconstructed distribution that can be one or two dimensional.
Additionally, for the global assessment Root Mean Square (RMS) is used:

$$RMS = \sqrt{\frac{1}{o}(Accuracy_1^2 + Accuracy_2^2 + \cdots + Accuracy_o^2)}, \quad (8.3.2)$$

where *o* is the number of the elements in the calculated distribution.

The reference scenarios and modelled data descriptions are presented in chapter 8.2. At first, the reconstruction of the 1D dependence of the emissivity on poloidal flux, which is more suitable for real-time analysis due to the computation time, has been done by different methods and described in chapter 8.3.1. This analysis has been performed with the algorithms written by the thesis author and presented in chapters 5 and 6. The consideration of the two-dimensional neutron emissivity distribution that allows for detailed physical phenomena studies is described in chapter 8.3.2. The tomography calculations have been performed by the MFR code presented in chapter 7. The analysis includes a comparison of the results for different architectural options. Additionally, the evaluation of the tomography robustness has been done. Chapter 8.3.3 includes the analysis of the error level influence on the results. Chapter 8.3.4 describes the effects of different LOS exclusion from calculations.

8.3.1 One-dimensional neutron profile reconstruction

The data sets for two scenarios and two camera architectures have been used for the 1D reconstruction. The calculation is based on the assumption that neutron emission is constant on the magnetic flux surfaces. The simplification leads to the distribution of the neutron intensity dependent on the normalised poloidal flux Ψ. The contribution matrix for deconvolution contains the areas of fields of view intersections with flux surfaces. Each element includes the sum of the areas on the tokamak's low and high field sides. The number of unknown parameters is close to the measurement data, making reconstruction more stable and less sensitive to measurement errors. Tokamak plasma can be subject to derogations from the isotropy of parameters on the poloidal flux surfaces. The results of the one-dimensional problem are perfectly symmetric, which is not valid if disruptions are presented in the plasma. The assumption can be applied for the neutron emissivity profiles analysis for ITER because asymmetries are not expected. The codes presented in Part II of this thesis were used to reconstruct the one-dimensional distribution of neutron emissivity in ITER. The presented analysis was used to characterise the quality of the different reconstruction techniques and guide the selection of the most suitable method for the real-time application. Two options for the number of reconstructed data points were tested. First is a symmetric problem with a flux surfaces number equal to the number of detectors, 26 for ISA and 22 for the baseline architecture. The second considered case has a much higher number of unknown elements in profile (40) than measured values. Figure 8.9 presents the 1D profile of scenarios (a), (b), and the linear profile used only as an initial guess in the reconstructions. The last distribution does not result from any simulation and is a randomly chosen line. The emissivity is presented as a function of Ψ. All emissivity profiles have been used as the default distribution to compare the influence on the results.

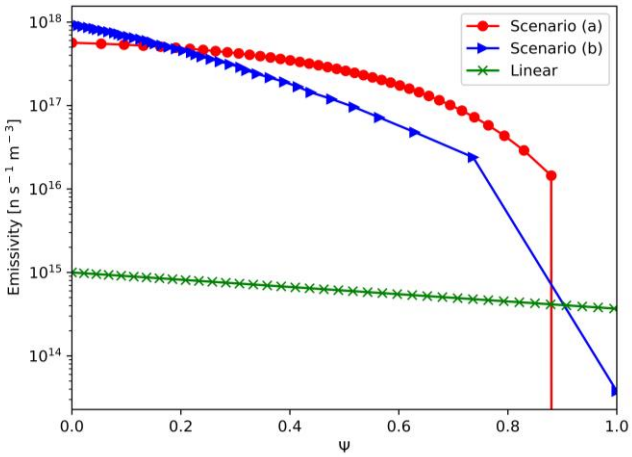

Figure 8.9. The 1D emissivity profiles used as default distribution in the analysis of the reconstruction ability from measurement by RNC (40 flux surfaces).

The one-dimensional neutron emissivity distribution analysis for scenario (a) has been done for two architectures. The comparison of the results obtained for the ISA and baseline layouts by the TR method is presented in figure 8.10. It includes both options of the number of unknown parameters. The reconstruction accuracy of all results is better than 10% for Ψ up to 0.8. The reconstruction error rises only on the plasma edges. The error bars, which are standard deviation from all 100 results, indicate that the reconstruction is unstable due to the noise influence. RMS for the ISA layout is below 0.01. The value for the baseline architecture is higher (about 0.03) but still allows fulfilling the accuracy requirement.

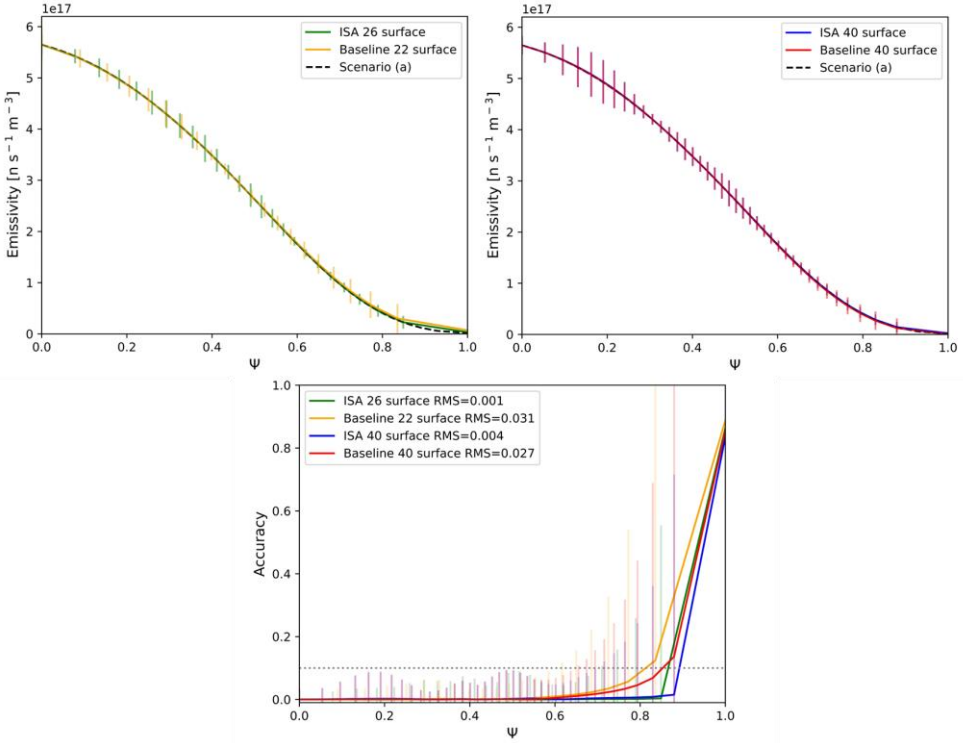

Figure 8.10. The results of neutron emissivity reconstruction for the ISA and baseline architectures data by the TR method for scenario (a) for different numbers of flux surfaces (top) and their accuracy (bottom).

The following results concern the ISA layout and iterative reconstruction techniques. The outcomes from the MFI and ML methods for scenario (a) in the function of 26 flux surfaces and different initial distributions are presented in figure 8.11. The results obtained by the MFI technique are very similar for all initial guesses. The reconstruction accuracy is better than 10% for Ψ about 0.8. The lowest RMS is for reconstruction with scenario (b) as the initial distribution (RMS=0.074). The influence of the default spectra is stronger for the ML method. RMSs obtained in calculations with scenarios (a) and (b) as default profiles are below 0.005. The higher discrepancy has been achieved with linear distribution with about three orders of magnitude lower neutron intensity than in simulated scenarios. Nonetheless, every result fulfils the requirement of the accuracy better than 10% in the plasma core. The results obtained by the same methods for 40 flux surfaces are shown in figure 8.12. The solutions from the MFI algorithm are similar to the lower number of the considered poloidal flux surfaces. RMS is 0.072 for scenario (b) as the initial guess and equal to 0.084 for scenario (a) and linear. The results obtained by ML are less stable. The approach with 100 reconstructions with slightly different errors added to the data allows for obtaining the mean result with accuracy close to 1% in the plasma core. The discrepancy increases on the plasma edges due to the precision of the calculations and noise influence. The reconstruction by the MFI and ML methods with simulated profiles as default determines the neutron emissivity distribution with RMS below 0.1. The MaxEnt algorithm does not provide the reconstruction results with the required accuracy. The entropy as the side constraint causes too strong regularisation with respect to the low ratio of the unknowns to the amount of measurement data. The solution with automatically selected λ from a wide range of values gave an over-smoothed solution similar to a straight line. The approach presented in figure 8.13 using extremely small regularisation parameters ($< 10^{-15}$) provides an unstable solution with strong variations of the neutron emissivity values. The ompensation of the impact from the regularisation matrix by λ is not possible in this case.

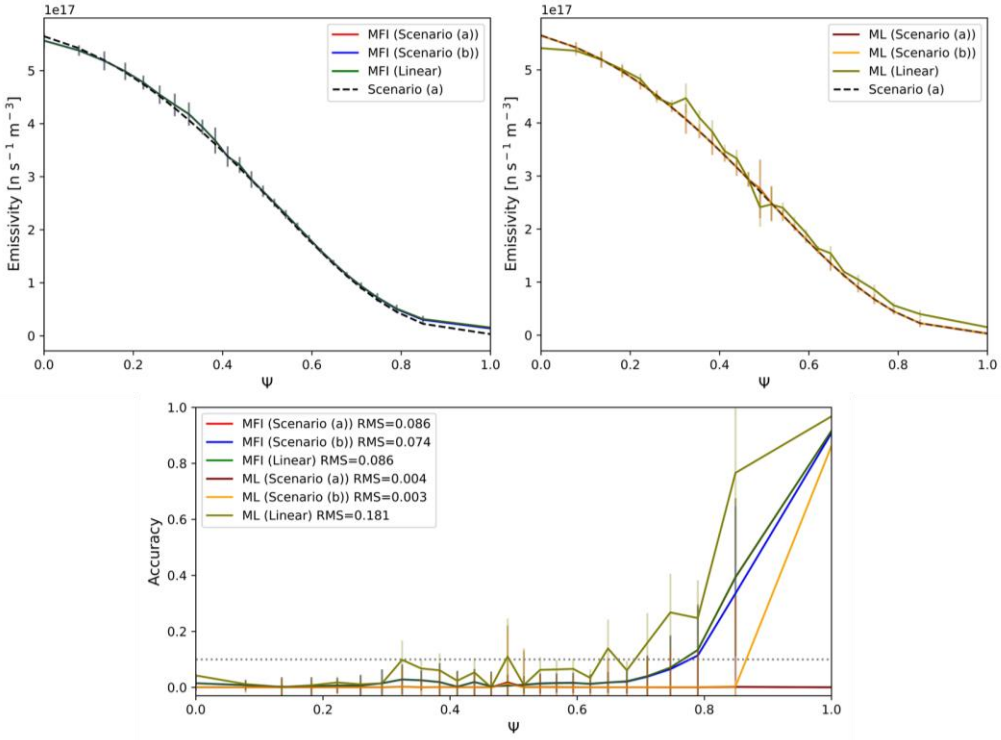

Figure 8.11. The results of neutron emissivity reconstruction for the ISA architecture data obtained for scenario (a) (26 flux surfaces) by the MFI (left upper side) and ML (right upper side) methods with different initial distributions indicated in the parenthesis in legend, and their accuracy (bottom).

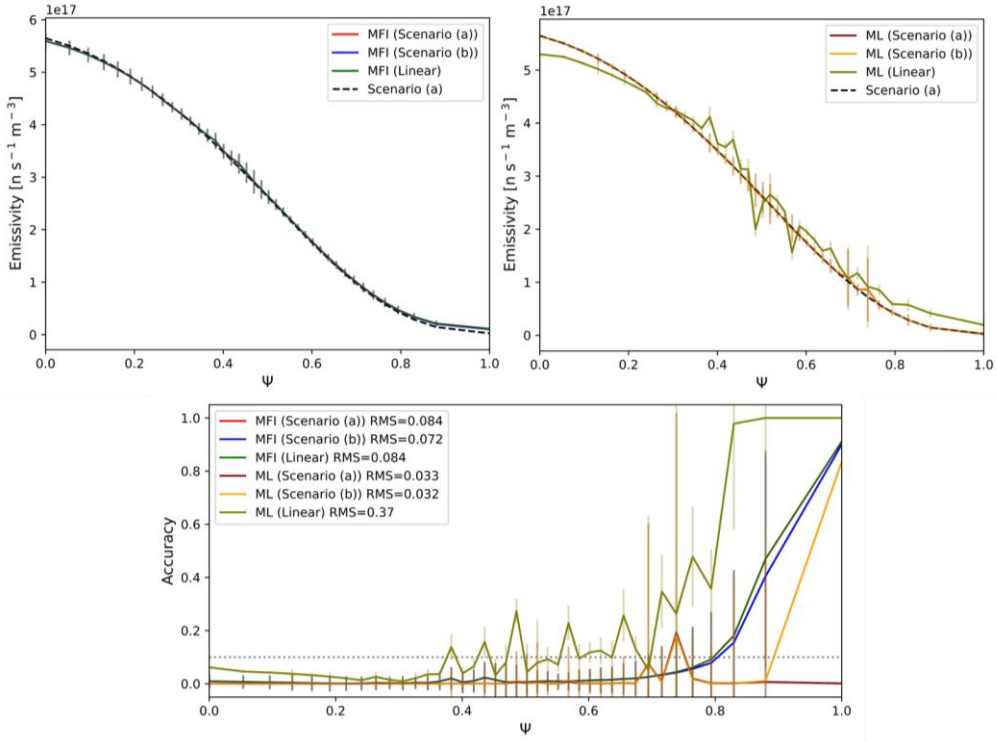

Figure 8.12. The results of neutron emissivity reconstruction for the ISA architecture data obtained for scenario (a) (40 flux surfaces) by the MFI (left upper side) and ML (right upper side) methods with different initial distributions indicated in the parenthesis in legend, and their accuracy (bottom).

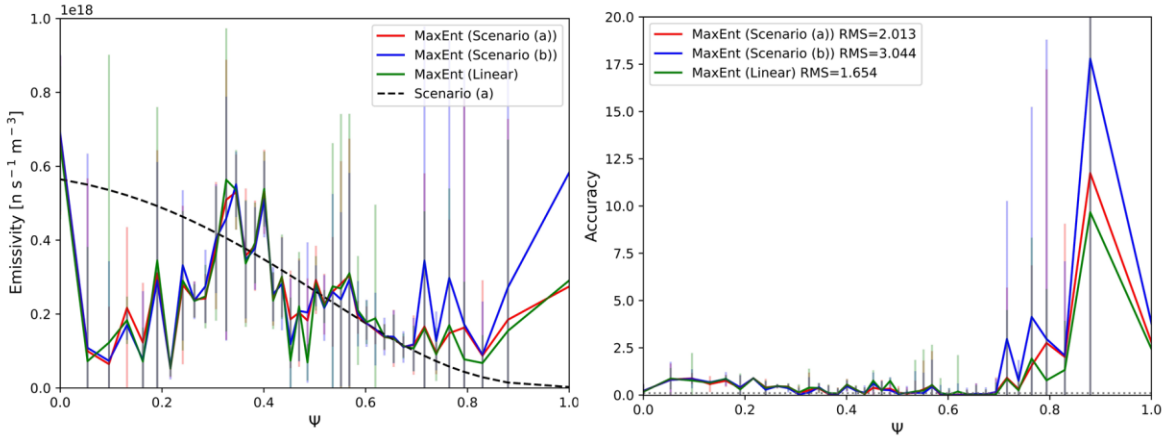

Figure 8.13. The results of neutron emissivity reconstruction (left) for the ISA architecture data obtained for scenario (a) (40 flux surfaces) by the MaxEnt method with different initial distributions indicated in the parenthesis in legend, and their accuracy (right).

The following analysis includes only results with a default profile unidentical to the original, which is a more realistic situation. The comparison of the results for various methods with data for the baseline layout and scenario (a) distributed in 22 flux surfaces is presented in figure 8.14. RMS is the lowest for the TR technique and equals 0.031. The accuracy obtained by the MFI method is better than 10% up to the normalised poloidal flux equal to 0.75. The difference between results obtained for various initial guesses is not visible in the figure. RMS equals 0.121 and 0.132 for default distribution defined as scenario (b) and linear, respectively. The ML method with scenario (b) provides a stable solution with accuracy better than 10% for Ψ up to 0.8. RMS is

higher for the linear profile. The results for the MaxEnt method were not shown. The problems with too strong regularisation and a very unstable solution occur in all cases. The reconstructed one-dimensional neutron emissivity profiles with 40 flux surfaces are presented in figure 8.15. The results are very similar to the symmetric problem. RMS for the TR method is even lower than for 22 flux surfaces and equals 0.027. Both MFR solutions fulfil the accuracy requirement for poloidal flux values of about 0.8. Stronger variations characterise the ML reconstructions with more elements in the distribution, but RMS obtained for scenario (b) is lower and equals 0.02. Outcomes for scenario (b) and the baseline architecture are presented in figures 8.16 and 8.17 for 22 and 40 flux surfaces, respectively. The results for scenario (b) were expected to be worse than reconstructions for scenario (a) because of the abrupt changes in the neutron emissivity in the plasma core. The lowest RMS equals 0.095 characterises the profiles with 40 flux surfaces obtained by the MFI algorithm. The results are the same for both initial guesses (figure 8.17) or differ slightly only on the plasma edge (see figure 8.16). The reconstruction by ML method with scenario (a) gave precision better than 10% up to 0.8 - 0.9 Ψ. The results obtained with linear default distribution fulfil the accuracy requirement only in the poloidal flux of about 0.3.

The TR, MFI and ML methods were successfully applied to the 1D neutron emissivity reconstruction, allowing for real-time burn control during ITER operation. The TR algorithm provides the best results, but the MFI code is the fastest [Mik2022].

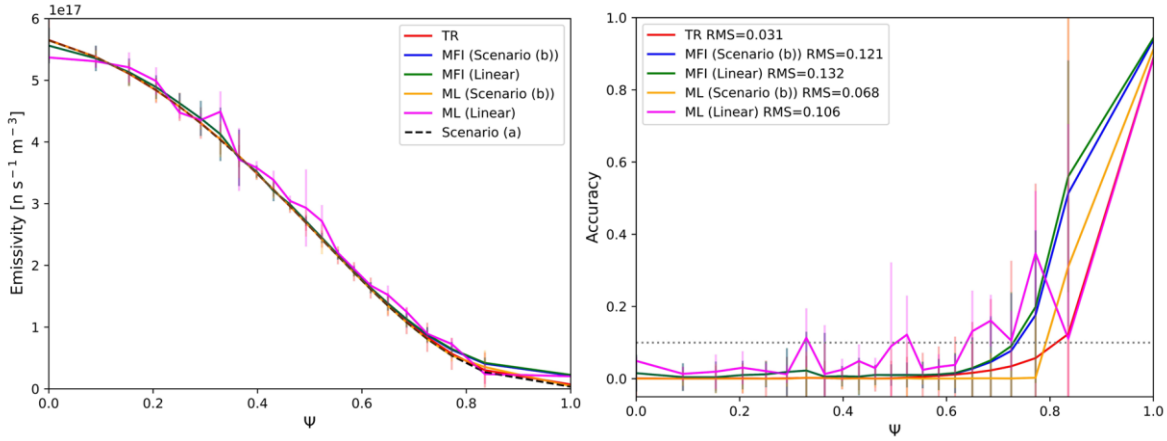

Figure 8.14. The results of neutron emissivity reconstruction (left) for the baseline architecture data obtained for scenario (a) (22 flux surfaces) by the TR, MFI, and ML methods with different initial distributions indicated in the parenthesis in legend, and their accuracy (right).

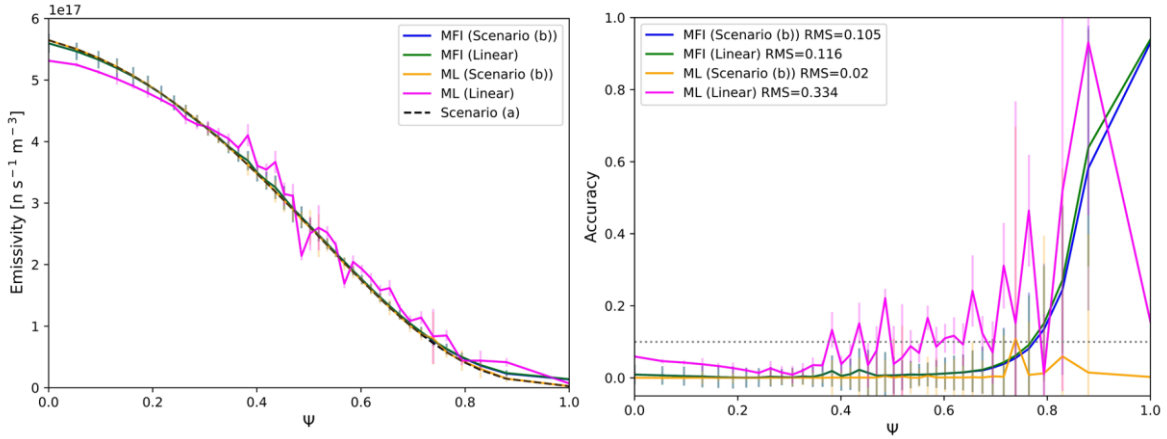

Figure 8.15. The results of neutron emissivity reconstruction (left) for the baseline architecture data obtained for scenario (a) (40 flux surfaces) by the TR, MFI, and ML methods with different initial distributions indicated in the parenthesis in legend, and their accuracy (right).

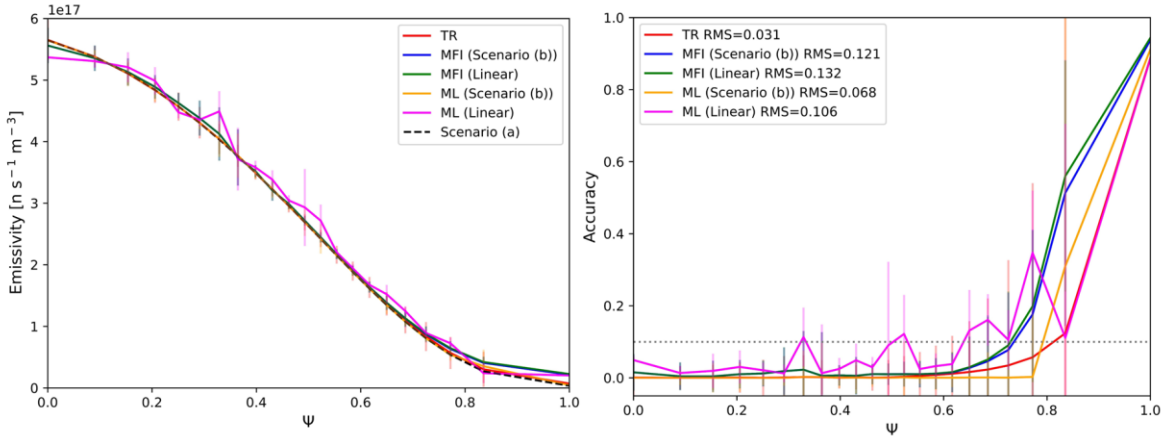

Figure 8.16. The results of neutron emissivity reconstruction (left) for the baseline architecture data obtained for scenario (b) (22 flux surfaces) by the TR, MFI, and ML methods with different initial distributions indicated in the parenthesis in legend, and their accuracy (right).

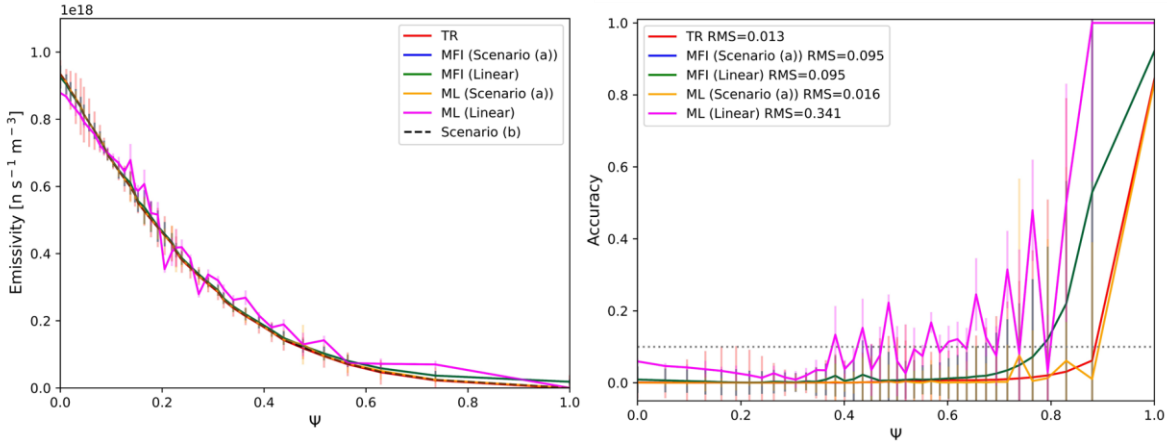

Figure 8.17. The results of neutron emissivity reconstruction (left) for the baseline architecture data obtained for scenario (b) (40 flux surfaces) by the by the TR, MFI, and ML methods with different initial distributions indicated in the parenthesis in legend, and their accuracy (right).

8.3.2 Tomography performance tests for baseline and ISA architecture

The basic tomography performance test includes the comparison of the quality of the results for the ISA and baseline architectures. The input data used for the calculations are described in chapter 8.2.

The reconstructed pixel grid contains 65 pixels in the x-direction and 65 in the y-direction. The 1D profiles were obtained by cutting 2D accuracy maps through the plasma centre (Z=0.6 m). The right part of the 1D profiles corresponds to the low field side (LFS) and, consequently, the left edge to the high field side (HFS) of the tokamak.

The influence of excluding four detectors from the ex-port system corresponding to the architecture change from ISA to baseline has been analysed with simulation data for scenario (a). Figure 8.18 presents the tomography result and its accuracy for the ISA layout. The 10% reconstruction accuracy requirement is fulfilled in the wide plasma area. RMS for the whole plasma cross-section equals 0.51 with 0.11 standard deviation. A significant discrepancy between simulation and reconstruction is observed on the plasma edges due to the low emission level. Overlapping the fields of view and very dense distribution of the magnetic field lines on the LFS is the source of the calculation difficulties. In the pixels containing many flux surfaces, the derivative matrix corresponding to the smoothing along magnetic field lines is defined with

a significant error because the algorithm considers only one of them. The plasma region on the HFS has a small impact on the geometry matrix because factors connected with the solid angles are inversely proportional to the long distance between the pixels and detectors. The combination of these properties is the reason for low accuracy on the plasma edges. The tomography result for the baseline architecture is presented in figure 8.19. RMS equals 0.51 ± 13%. The standard deviation for the layout with excluded detectors is higher than for ISA results. The mean accuracy in the plasma core differs only by about 1%. There is no visible loss of accuracy after excluding the LOSs dedicated to RGRS and HRNS. Design change from the ISA to baseline layout has a negligible impact on tomography ability, and the camera can still fulfil requirements. The conclusion from tomography analysis was one of the reasons for the decision about the camera architecture. The baseline architecture will be the final shape of RNC, and all further simulations have been done with excluded detectors corresponding to other diagnostics.

The tomography result for scenario (b) is presented in figure 8.20. The peaked density corresponds to the steep neutron emissivity change that is more difficult to reconstruct. RMS equals 0.55 with 0.06 standard deviation. The accuracy in the core centre is up to 20%. Therefore, the requirement of RNC measurement is not accomplished. The methodology that can improve the result has been investigated. An analysis of the influence of the additional constraint applied to the tomography calculation is described in the following subchapter.

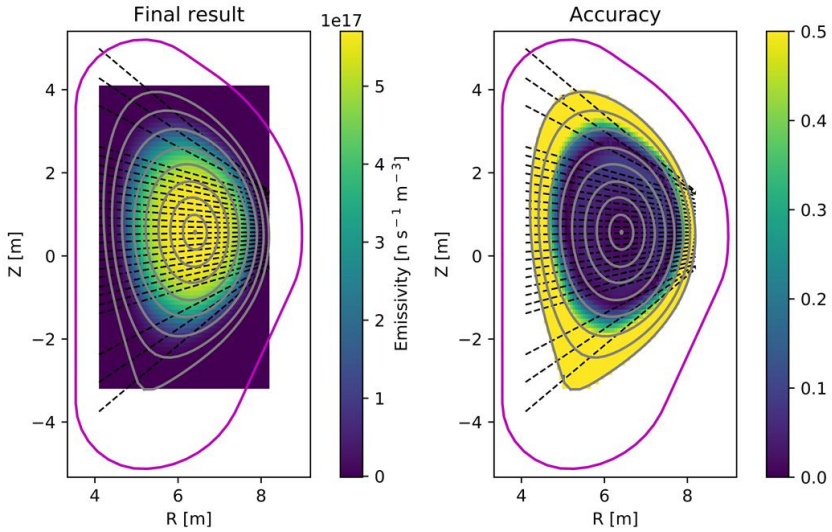

Figure 8.18. Result of the tomography (left) and its accuracy (right) for the ISA layout and scenario (a).

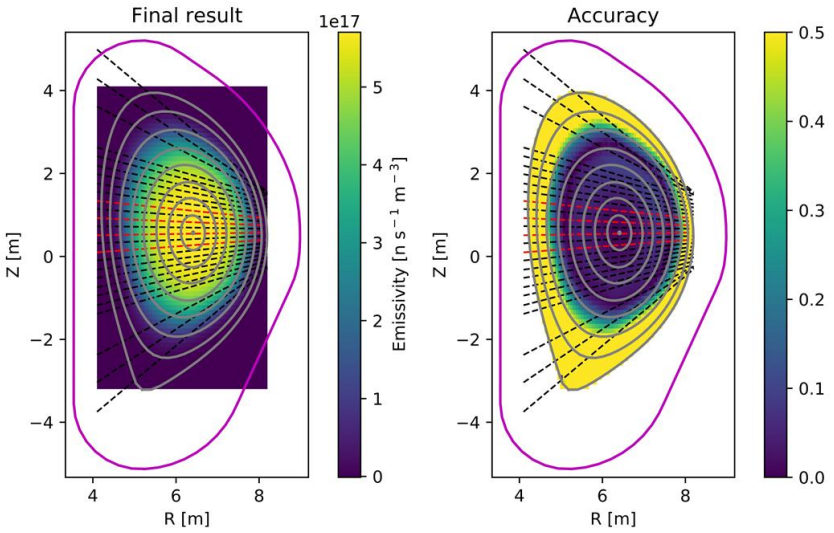

Figure 8.19. Result of the tomography (left) and its accuracy (right) for the baseline layout and scenario (a).

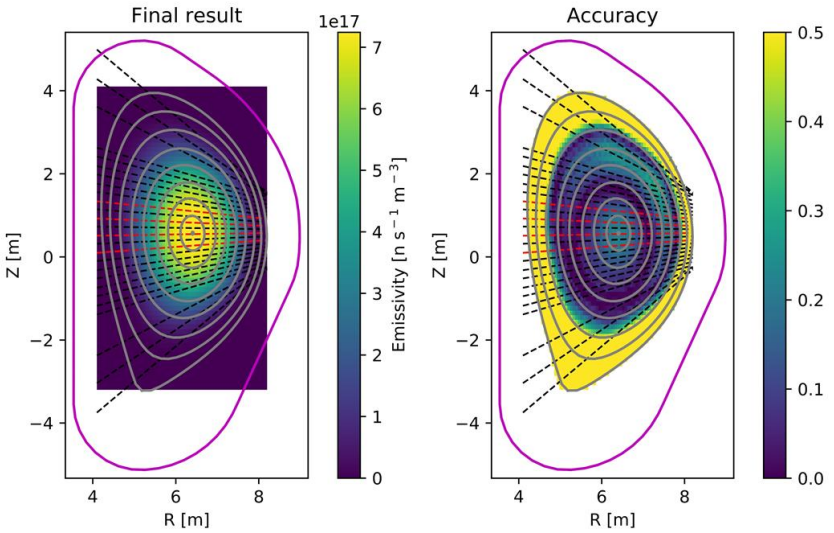

Figure 8.20. Result of the tomography (left) and its accuracy (right) for the baseline layout and scenario (b).

8.3.3 Evaluation of the influence of the additional constraint on tomography

The goal of the analysis was to study a possibility of the tomography results improvement by adding the additional constraint. The total neutron yield from an external neutron monitor (NFM, chapter 8.1) has been added to the dataset, and its influence on the calculations result has been analysed. The considered measurement error is random Gaussian noise of 10% amplitude. The total neutron yield is orders of magnitude higher than the count rates simulated for detectors. Therefore, the constraint and its part of the contribution matrix need to be re-scaled. A similar order of magnitude as for the count rates prevents perturbations in the tomography related to the finite precision of the values used in the calculations.

The results obtained with the additional constraint for scenario (a) are presented in figures 8.21 and 8.22 for the ISA and baseline architecture, respectively. Again, the difference between the neutron emissivity profiles for the two layouts is negligible. Figure 8.23 shows the comparison of the 1D accuracy profiles. The lines related to the two architectures overlap. The accuracy obtained with the total neutron yield constraint is better than 10% in the broader

range on HFS. There is a small peak ($R \approx 8$ m) of the discrepancy between simulation and reconstruction in the area of the dense magnetic field lines distribution due to the smoothing disruption. The comparison of RMS is shown in table 8.5. The accuracy improvement after applying the additional constraint to the tomography is significant.

The result obtained with the additional constraint for scenario (b) is presented in figure 8.24. The accuracy in the plasma core centre is significantly improved. The 1D accuracy profiles obtained with and without the total neutron yield constraint are shown in figure 8.25. The accuracy in the core changed from about 20% to 5%. The improvement of RMS in the whole poloidal cross-section is equal to 0.11.

Applying the total neutron yield as the additional constraint to the tomography analysis improves the results significantly. RMS change is on the level of 0.1 with reduction of standard deviation. The constraint influence on the reconstruction is stronger for the more complicated cases. According to the ITER Organisation, the 10% accuracy requirement fulfilment is important from the point of view of the interpretation of the plasma physics (e.g. burn control, fusion power calculations) based on the reconstructed neutron emissivity distributions.

Table 8.5. RMS for the tomography reconstruction results obtained with and without the additional constraint for scenario (a) and (b).

Scenario	Architecture	Standard tomography		Application of the total neutron yield	
		RMS	σ_s	RMS	σ_s
(a)	ISA	0.51	0.11	0.41	0.03
	Baseline	0.51	0.13	0.41	0.11
(b)	Baseline	0.55	0.06	0.44	0.04

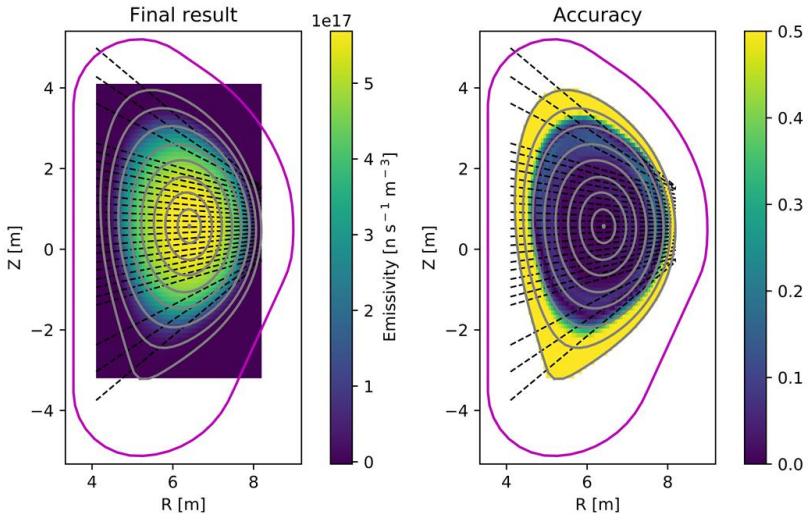

Figure 8.21. Result of the tomography (left) and its accuracy (right) for the ISA layout and scenario (a) with the total neutron yield constraint.

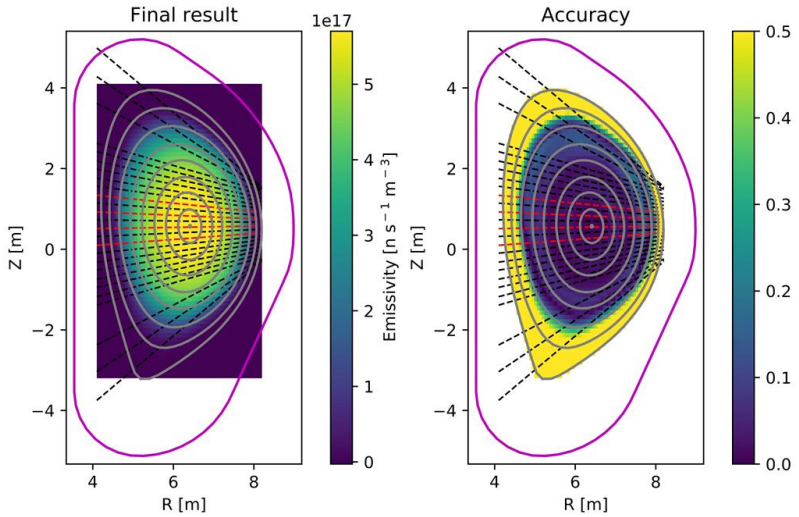

Figure 8.22. Result of the tomography (left) and its accuracy (right) for the baseline layout and scenario (a) with the total neutron yield constraint.

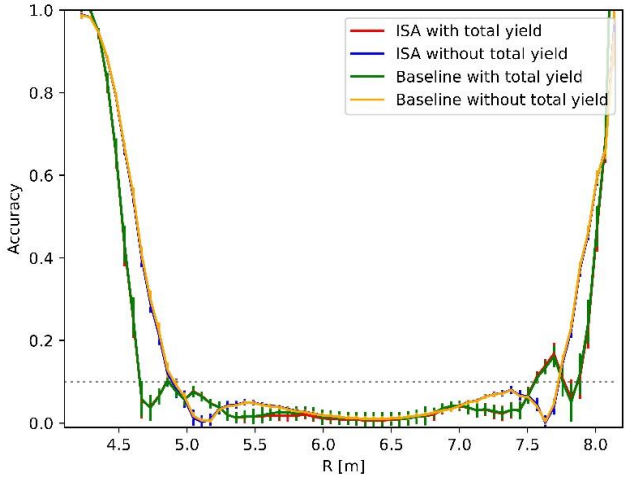

Figure 8.23. The comparison of the tomography accuracy 1D profiles for results obtained with and without the additional constraint for scenario (a).

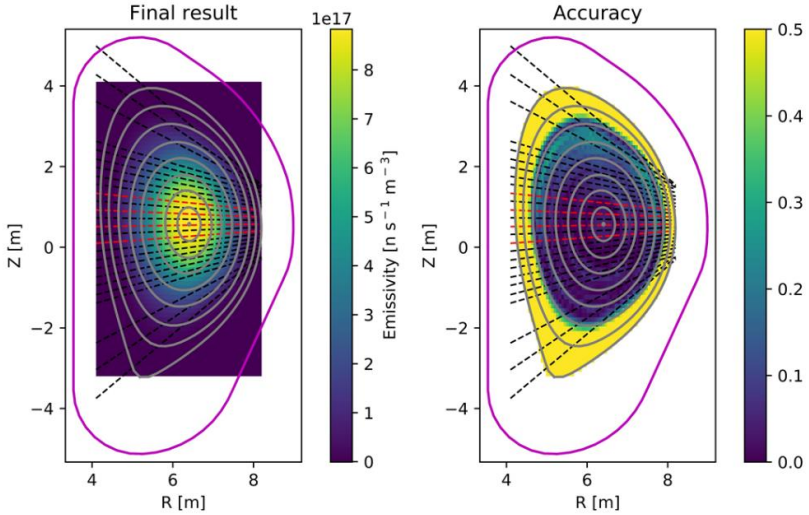

Figure 8.24. Result of the tomography (left) and its accuracy (right) for the baseline layout and scenario (b) with the total neutron yield constraint.

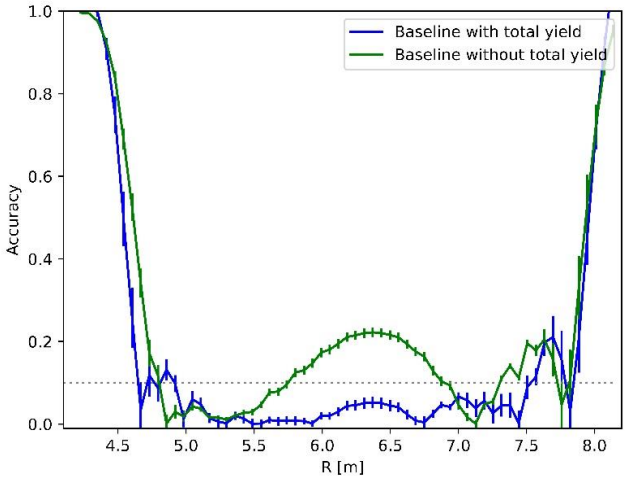

Figure 8.25. The comparison of the tomography accuracy 1D profiles for results obtained with and without the additional constraint for scenario (b).

8.3.4 Tomography robustness against the noise level

The measurement error connected with the count rates for a short observation time has a Poisson character [Kno2010]. Another source of the errors is the background, including scattered neutrons and gamma radiation. The scattered neutrons are taken into account in the simulations of RNC measurement. The influence of the gamma radiation will be reduced by the pulse shape discrimination analysis made for scintillators and sCD or by the tuning signal threshold level in fission chambers. The temperature and magnetic field fluctuations in the measurement environment can disturb the signal from the detectors. Other sources of the errors are electronics, cables, connectors and data acquisition system. The overall noise can be characterised by Gaussian distribution.

The goal of this subchapter is to analyse the influence of increasing measurement noise on tomography reconstruction. Gaussian distribution with different amplitudes simulates the error growth. The results with noise amplitude of: 1%, 5%, 10%, and 15% were compared to the solution for the data with Poisson noise. The error influence on the tomography was analysed for the data with and without the additional constraint. The total neutron yield error is described by Gaussian statistics with 10% amplitude for all cases.

The comparison of RMS calculated for neutron emissivity distributions reconstructed with data for scenario (a) using different error levels is presented in table 8.6. The examples of the results for 10% noise amplitude are shown in figures 8.26 and 8.27, obtained without and with the total neutron yield constraint, respectively. RMS for tomography with the additional constraint is lower by 0.1 to 0.2 than standard reconstruction. The higher values of standard deviation were obtained with the total neutron yield constraint due to the 10% uncertainty characterised by this data. The comparison of the 1D accuracy profiles for all considered noise levels is presented in figure 8.28. The loss of accuracy in tomography calculations with the standard dataset is substantial. The results obtained with 10% noise have 30% accuracy in the core centre. The limit of the measurement data errors that allow for the trustworthy interpretation of the neutron emissivity profiles is 5%. A growing error has a strong influence on the results. The tomography performed with the additional constraint has the accuracy better than 10% in a wide range of flux surfaces. Only the dataset with 15% Gaussian noise does not fulfil the reconstruction requirement. The final result is more robust to the noise if the total neutron yield is used.

Table 8.6. RMS for the tomography reconstruction results obtained with and without the additional constraint for scenario (a) with different noise levels.

Additional constraint	Poisson noise	Gaussian noise			
		1%	5%	10%	15%
Without	0.51 ± 0.13	0.50 ± 0.10	0.57 ± 0.09	0.62 ± 0.04	0.71 ± 0.05
With	0.41 ± 0.05	0.40 ± 0.12	0.45 ± 0.13	0.47 ± 0.09	0.51 ± 0.13

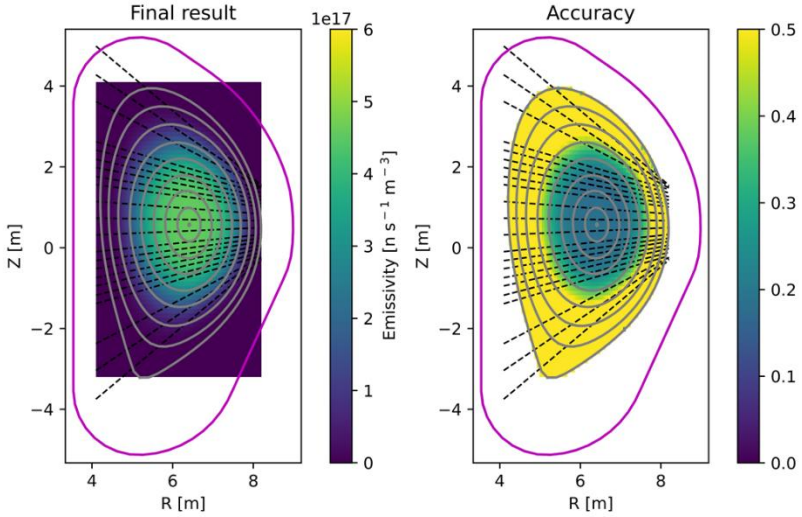

Figure 8.26. Result of the tomography (left) obtained without the total neutron yield constraint and its accuracy (right) for the baseline layout and scenario (a) with 10% Gaussian noise.

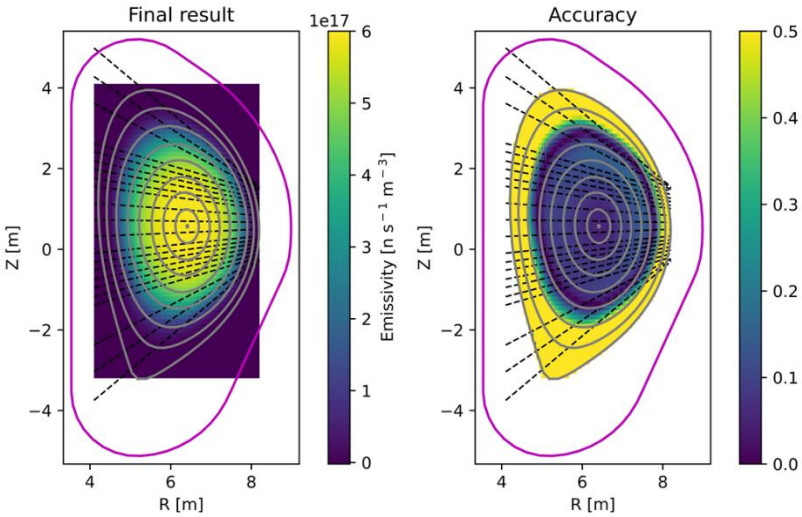

Figure 8.27. Result of the tomography (left) obtained with the total neutron yield constraint and its accuracy (right) for the baseline layout and scenario (a) with 10% Gaussian noise.

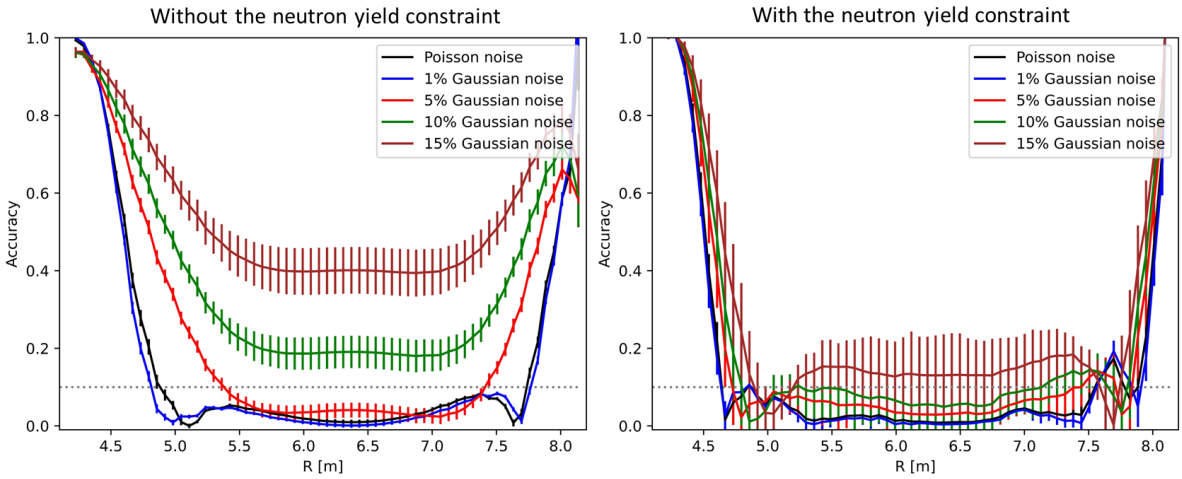

Figure 8.28. The comparison of the tomography accuracy of 1D profiles for results obtained with different noise levels and without (left) or with (right) the additional constraint for scenario (a).

The neutron emissivity distribution obtained without and with the additional constraint applied to the dataset with 5% Gaussian noise for scenario (b) is presented in figures 8.29 and 8.30. The tomography without the additional constraint provides the solution with significant accuracy loss in the core centre. The result obtained with the total neutron yield is similar to the reconstruction with Poisson noise. The comparison of 1D profiles for all considered noise levels is presented in figure 8.31, and RMS is shown in table 8.7. The core reconstruction of the peaked neutron emissivity is the main issue for scenario (b). The result for 1% noise has lower RMS than reconstruction with Poisson noise. The tomography with datasets not considering the additional constraint provides accuracy worse than 30% for other noise levels. The presented results cannot be used for physical phenomena interpretation. The reconstruction with the total neutron yield constraint provides RMS below 0.52. The accuracy loss is observed in the upper LFS, but the reconstruction precision is better than 20% in the core centre for all noise levels.

The analysis of robustness against the growing noise shows that the error strongly influences the tomography calculations even for the approach with 100 datasets. Usage of the total neutron yield value can reduce the loss of reconstruction accuracy related to the decrease in the measurement precision. If noise rises only for a single detector, excluding it from the calculations may improve reconstruction. The analysis of the proposed solution is discussed in the following subchapter.

Table 8.7. RMS for the tomography reconstruction results obtained with and without the additional constraint for scenario (b) with different noise levels.

Additional constraint	Poisson noise	Gaussian noise			
		1%	5%	10%	15%
Without	0.55 ± 0.06	0.53 ± 0.04	0.58 ± 0.04	0.59 ± 0.08	0.64 ± 0.07
With	0.44 ± 0.04	0.43 ± 0.04	0.46 ± 0.05	0.49 ± 0.07	0.51 ± 0.08

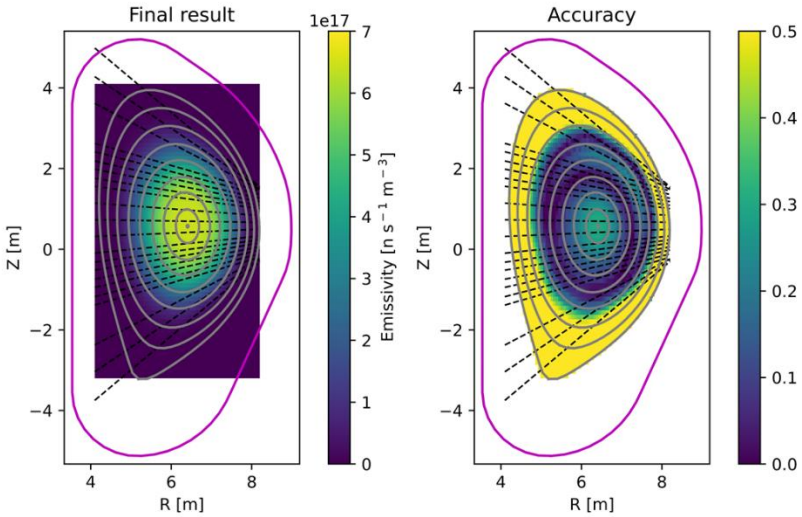

Figure 8.29. Result of the tomography (left) obtained without the total neutron yield constraint and its accuracy (right) for the baseline layout and scenario (b) with 5% Gaussian noise.

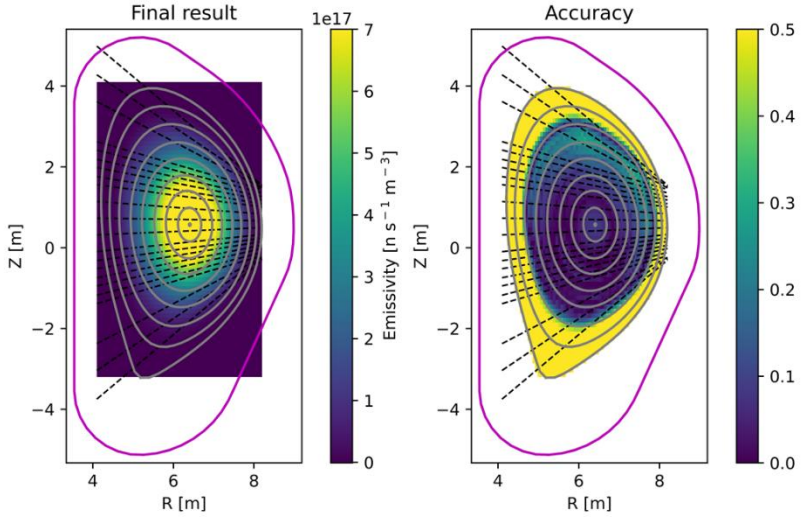

Figure 8.30. Result of the tomography (left) obtained with the total neutron yield constraint and its accuracy (right) for the baseline layout and scenario (b) with 5% Gaussian noise.

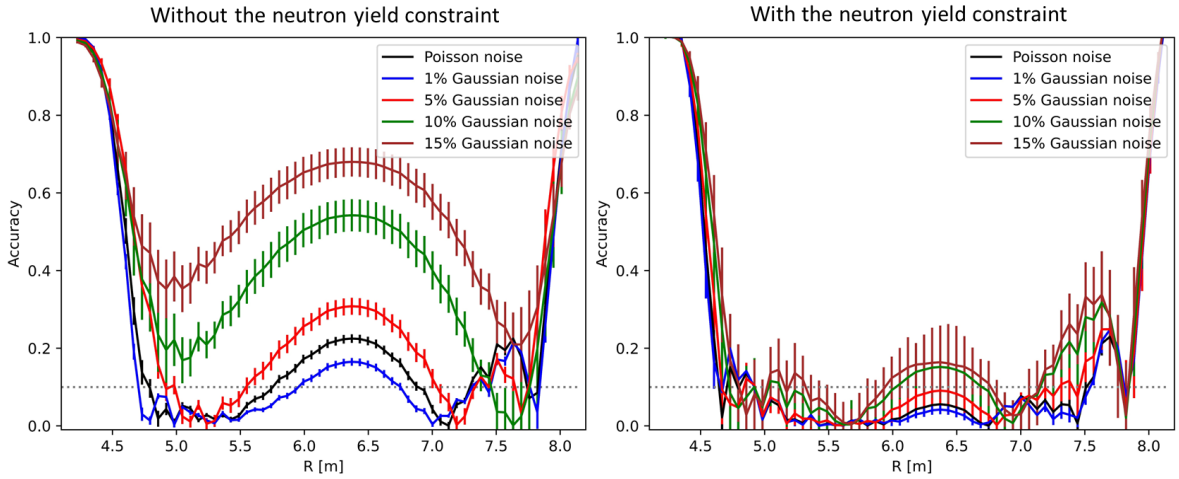

Figure 8.31. The comparison of the tomography accuracy of 1D profiles for results obtained with different noise levels and without (left) or with (right) the additional constraint for scenario (b).

8.3.5 Tomography robustness test against detectors exclusion

In the experiment, there is a possibility of detector failure, a noise rise in the signal or another event that makes the count rate values unreliable. There can be many sources of measurement disruptions originating in the plasma or diagnostics electronic system. The robustness test includes the analysis of excluding a single LOS from the tomography calculations.

After elimination of the single LOS from 1 to 23 from the reconstruction for scenario (a) without additional constraint, RMS equals 0.51 (with a precision of two decimal places), which is a result similar to that obtained without the exclusion. Standard deviation in these cases varied from 0.06 to 0.15. The worst RMS, 0.55, was provided by tomography calculations with excluded LOS #26. The examples of the results without LOSs #8 and #26 are presented in figures 8.32 and 8.33, respectively. The difference between 2D accuracy maps is not clearly visible. After the elimination of LOS #26, the broader part of the plasma edge is reconstructed with higher accuracy than in the case of exclusion of LOS from the ex-port part of the camera. The influence of the exclusion is stronger for neutron emissivity reconstruction, including the additional constraint, than without it. RMS is not changed significantly only in the case of exclusion of LOS from 1 to 7. It is connected with positioning further from collimators excluded from the ISA architecture and asymmetry of the ex-port part of the camera. The exclusion of the detectors monitoring the upper part of the plasma has a stronger influence on the reconstruction due to the higher count rates statistics related to the smaller length of their collimators. RMS obtained without LOS from 8 to 25 equals 0.51 with a standard deviation varying from 0.07 to 0.16. The exclusion of LOS #26 provides the same RMS as tomography without the total neutron yield constraint. Significant accuracy loss is observed on the plasma edges and in the core centre. The two-dimensional neutron emissivity distributions obtained without LOSs #8 and #26 and with additional constraint are presented in figures 8.34 and 8.35, respectively. Again, the slight change in the 2D map is difficult to observe. The comparison of the 1D accuracy profiles for all possible exclusions divided into groups connected with the LOS locations (in-port from two cassettes upper and lower, ex-port, and ex-port placed near LOSs excluded from the ISA layout) is presented in figure 8.36. The accuracy change in the core centre after excluding the detector from the ex-port is not visible. All tomography calculations provide an accuracy better than 10% in the range of 5 - 7.5 m on the R tokamak axis. The strongest variations are observed on the plasma edges, where accuracy improvement was noted, for results obtained with the total neutron yield constraint. The influence of the additional constraint on this area of reconstruction depends on the set of synthetic data. The exclusion of LOS from the ex-port part makes calculating the neutron emissivity on edge more difficult, and the total neutron yield constraint is insufficient to improve it. The significant impact on the neutron emissivity reconstruction has the omission of the LOS from the lower cassette. There is a significant accuracy loss on LFS due to the lack of information about the neutron emission on the plasma edge. Instead of improving the result on LFS, the total neutron yield constraint emphasises the problem of reconstructing the area characterised by dense magnetic field lines. The exclusion of the two LOSs simultaneously is related to the RMS increase at the level of 0.1 and depends strongly on the detectors' positions.

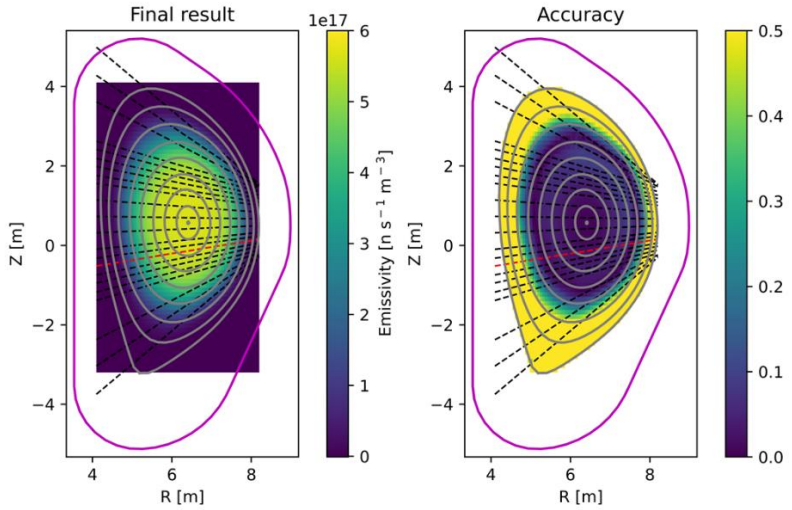

Figure 8.32. Result of the tomography (left) obtained without the total neutron yield constraint and its accuracy (right) for the baseline layout and scenario (a) after LOS #8 exclusion.

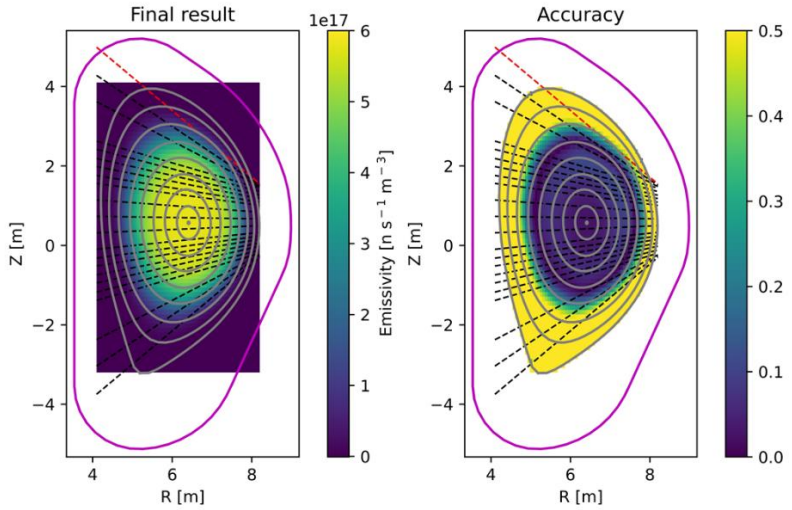

Figure 8.33. Result of the tomography (left) obtained without the total neutron yield constraint and its accuracy (right) for the baseline layout and scenario (a) after LOS #26 exclusion.

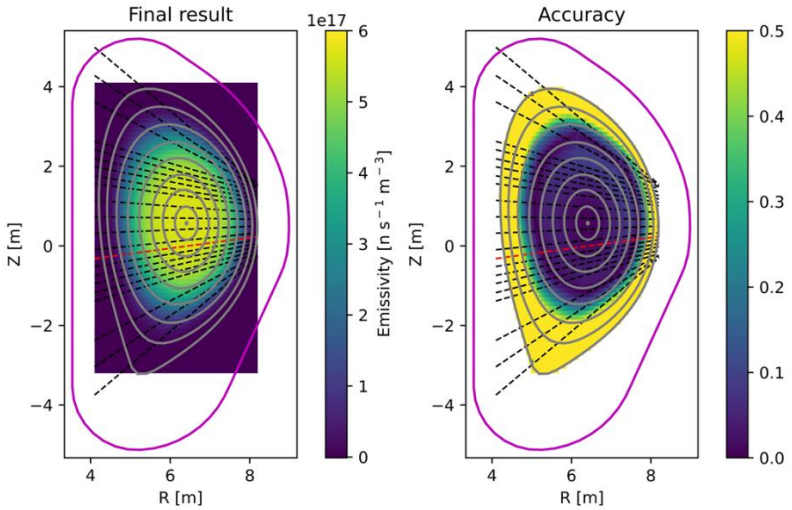

Figure 8.34. Result of the tomography (left) obtained with the total neutron yield constraint and its accuracy (right) for the baseline layout and scenario (a) after LOS #8 exclusion.

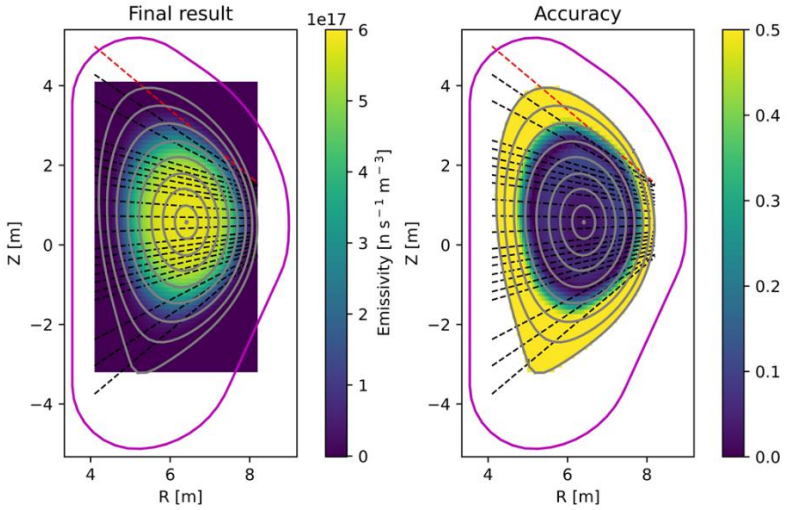

Figure 8.35. Result of the tomography (left) obtained with the total neutron yield constraint and its accuracy (right) for the baseline layout and scenario (a) after LOS #26 exclusion.

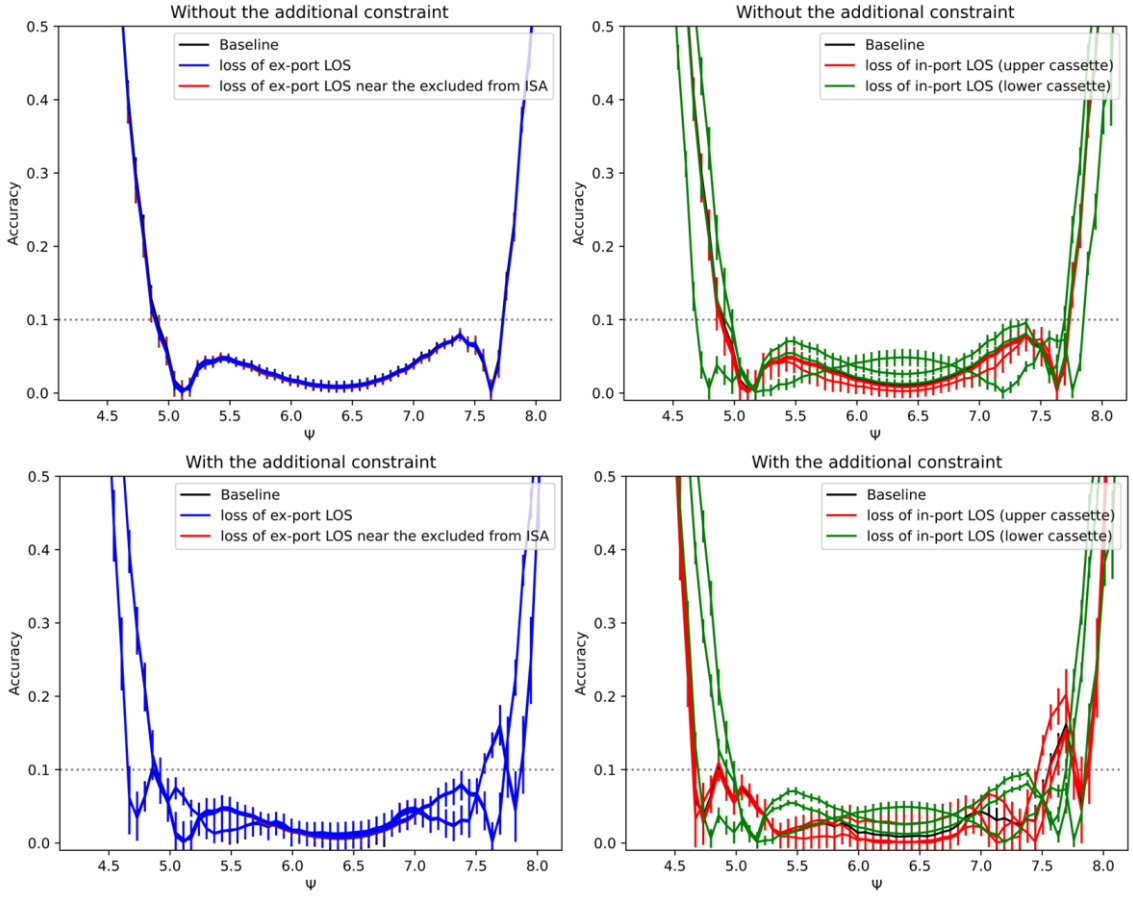

Figure 8.36. The comparison of the tomography accuracy 1D profiles for the results obtained after exclusion of the single LOS from different position and without (top) or with (bottom) the additional constraint for scenario (a).

The significant RMS change is observed only for the exclusion of a single LOS from the in-port part of the system in the case of scenario (b). RMS obtained without the total neutron yield constraint after exclusion of the single LOS from #2 to #26 equals 0.55 with standard deviation varying from 0.03 to 0.15. The exclusion of LOS #1 provides the result with RMS

equalled 0.59. Figures 8.37 and 8.38 present the 2D neutron emissivity distribution calculated without the additional constraint and LOSs #1 and #26, respectively. In both cases, an accuracy worse than 10% is observed in the plasma core centre and upper edge. The highest precision loss is seen for LOS #1. The results of tomography calculations with the additional constraint and single LOS from #2 to #25 elimination have RMS equalled 0.44 (with a precision of two decimal places). There is a negligible difference between the accuracies in these cases. The reconstruction without LOS #1 and #26 provides the results with RMS equal 0.47 ± 0.03 and 0.46 ± 0.04, respectively. The examples of the neutron emissivity distributions are presented in figures 8.39 and 8.40. A visible accuracy loss in the upper part of the plasma is stronger in the case of LOS #1 exclusion. The comparison of the 1D accuracy profiles for all cases is shown in figure 8.41. The accuracy in the plasma core centre for tomography calculation without the additional constraint is worse than 20%. The accuracy loss for collimators close to the excluded from the ISA architecture is observed in the plasma core centre. The reconstruction with the total neutron yield is more robust to removing LOS from the dataset than it was observed in the case of scenario (a). The accuracy change due to the exclusion of the ex-port LOS is negligible. Variations of the results related to the in-port LOSs omission are the strongest on LFS, like for scenario (a). Disruptions connected with smoothing the plasma area with very dense magnetic field lines distribution are strongest for data sets without full information about the plasma edges. The results obtained with the total neutron yield constraint are always better than reconstruction without it. The exclusion of the two detectors simultaneously provides the RMS increase above 10%.

The analysis shows that a better approach is to exclude the data point instead of using count rates with an error higher than 5 – 10%. The exclusion of LOS from the ex-port system provides the results with a similar RMS as for the complete baseline architecture. The strongest influence on the reconstruction has the elimination of the detector observing plasma edges. The exclusion of a higher number of LOSs usually provides insufficient accuracy.

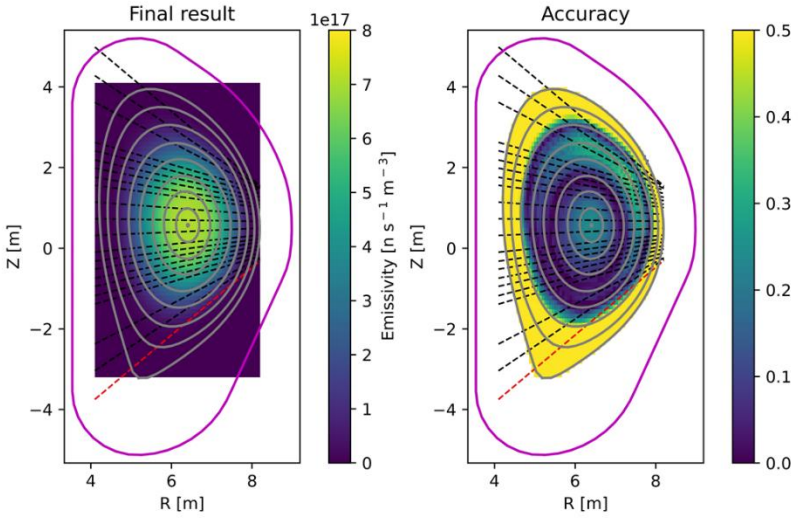

Figure 8.37. Result of the tomography (left) obtained without the total neutron yield constraint and its accuracy (right) for the baseline layout and scenario (b) after LOS #1 exclusion.

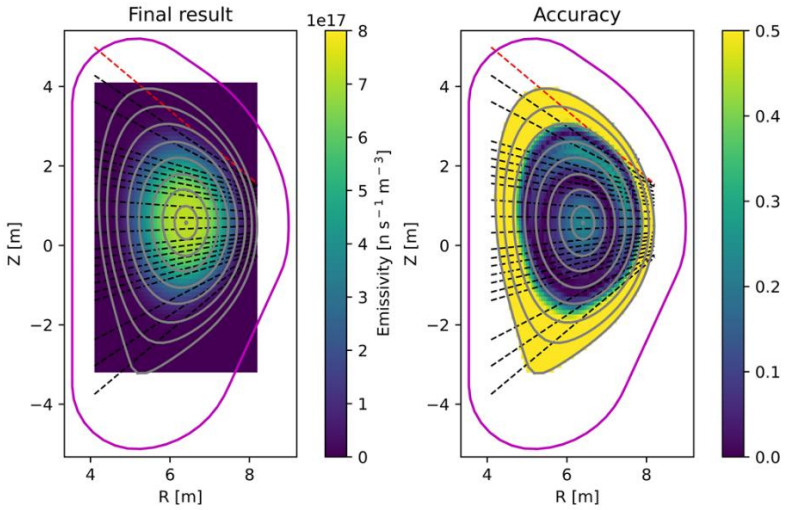

Figure 8.38. Result of the tomography (left) obtained without the total neutron yield constraint and its accuracy (right) for the baseline layout and scenario (b) after LOS #26 exclusion.

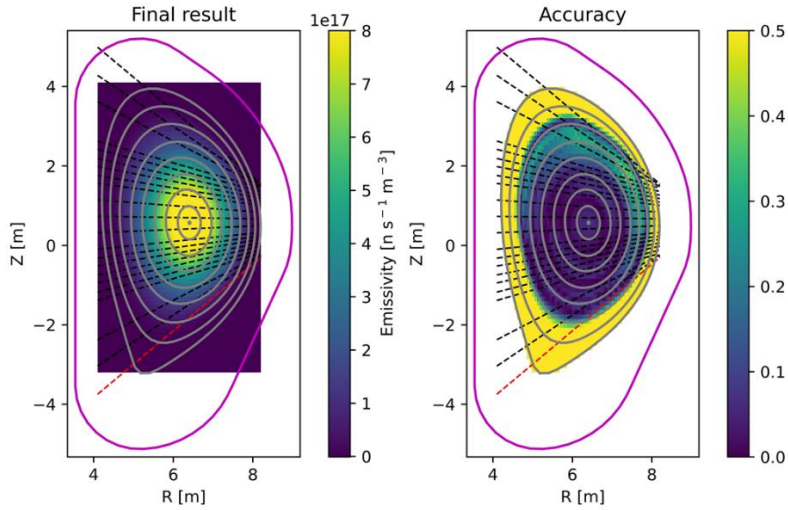

Figure 8.39. Result of the tomography (left) obtained with the total neutron yield constraint and its accuracy (right) for the baseline layout and scenario (b) after LOS #1 exclusion.

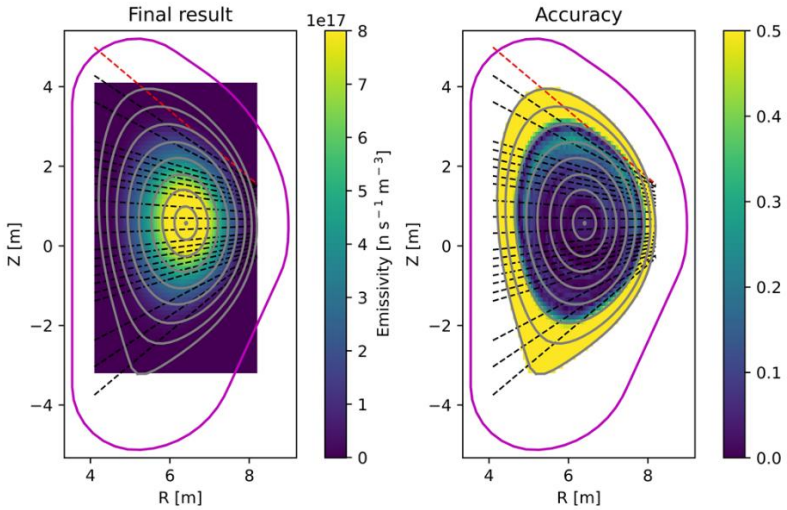

Figure 8.40. Result of the tomography (left) obtained with the total neutron yield constraint and its accuracy (right) for the baseline layout and scenario (b) after LOS #26 exclusion.

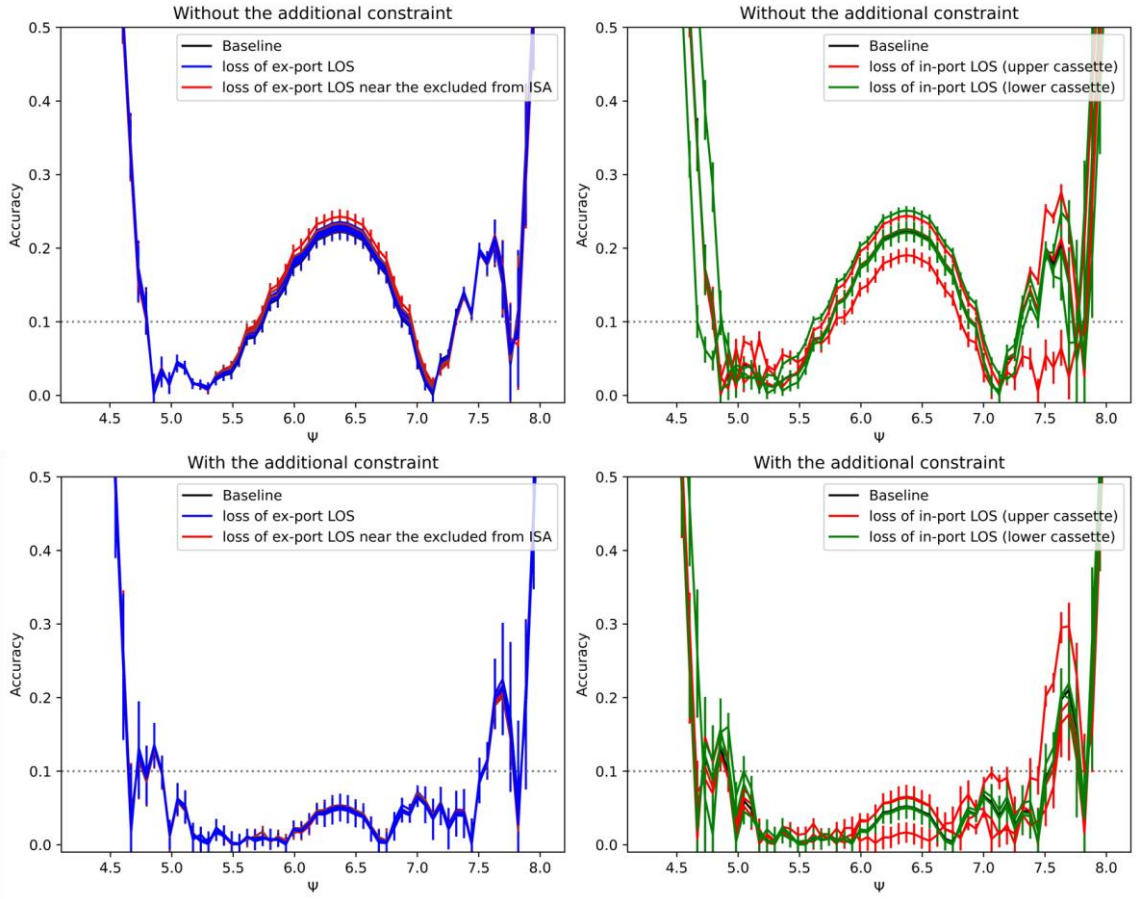

Figure 8.41. The comparison of the tomography accuracy 1D profiles for the results obtained after exclusion of the single LOS from different position and without (top) or with (bottom) the additional constraint for scenario (b).

8.4 Tomography performance test for different types of detectors in the ex-port system

The influence of the detector type used in the ex-port system on the tomography performance has been analysed in this subchapter. The plastic scintillators EJ-276G, sCD detectors, and ^{4}He Arktis scintillators described in subchapter 8.1 (see table 8.3) are considered as a potential choice for neutron measurement by RNC. In this analysis, three scenarios (c), (d), and (e) are investigated. A detailed explanation of the simulation methodology is presented in subchapter 8.2. The comparison of the count rates predicted for each kind of detector is shown in figure 8.42. The parameters directly affecting the tomography calculations are detection efficiency for 14.1 MeV neutrons and background level. The background calculation depends on the scattered neutrons amount for a particular scenario, and the mechanism of processing registered signals determined by the sensitivity for all neutron energies, energy resolution, and the possibility of noise discrimination. In this analysis, the noise described by Poisson statistics has been considered. The mean error added to the data is 6% for plastic scintillators, 10% for sCD, and 7% for ^{4}He scintillators. The noise levels for considered scenarios vary by about 0.5%.

Subchapter 8.4.1 presents the tomography calculation results for different types of detectors. Asymmetrical distribution of the count rates in the camera detectors ensues from differences in the length and diameter of the collimators. Additionally, the robustness test against the changes in the magnetic field has been done and described in subchapter 8.4.2.

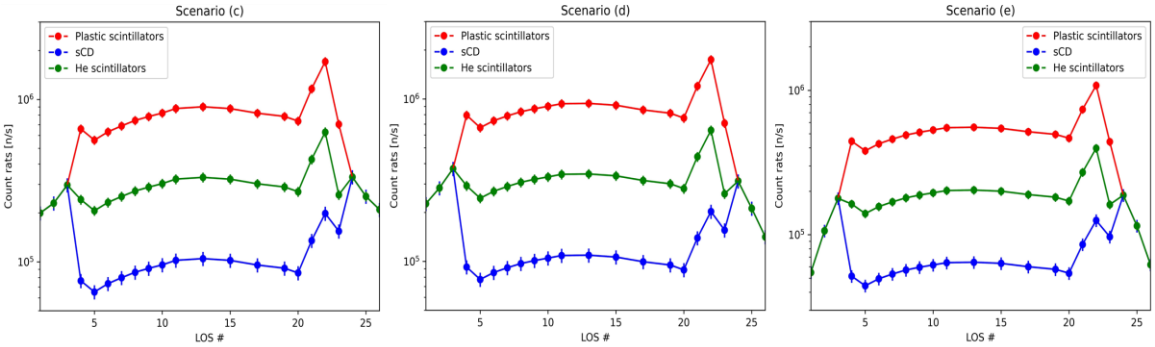

Figure 8.42. The simulated count rates per second for ITER RNC baseline layout with different type of the detectors in the ex-port part and scenarios (c) (left), (d) (centre), and (e) (right).

8.4.1 Comparison of the tomography performance for different types of detectors

This analysis aims to select the type of detectors that provide the tomography reconstruction with the best accuracy. The results for plastic scintillators EJ-276G, sCD detectors, and ^{4}He Arktis scintillators have been compared for three plasma operation scenarios.

The equilibrium files for scenarios (c), (d), and (e) are defined with resolutions 257x129 and 129x65. In these cases, the magnetic field lines are defined with low precision, letting the presence of unphysical artefacts, e.g. intersections of magnetic field lines. The smoothing matrix is generated based on that files. The pixel grid needs to be optimised to reduce the number of elements defined with low precision in the regularisation operator and avoid accuracy loss. Very high precision connected with a great number of pixels is impossible because of the low number of LOSs. Pixels with a large area can contain two different flux surfaces where emissivity can differ. It can make the reconstruction procedure unstable and results unreliable. A wide range of pixel grids (x: 25 – 110, y: 40 - 110) was tested, and one characterised by the best accuracy for a particular scenario has been presented in the thesis.

The emissivity in the H-mode scenario has been reconstructed for the 40x50 pixel grid. The 2D accuracy maps obtained for different detectors are presented in figure 8.43. The difference between the results for plastic and ^{4}He scintillators is not visible. The diamond detectors deteriorate the accuracy in the core and lower edge of the plasma. The comparison of the 1D profiles is shown in figure 8.44. For all detectors, there is a peak with accuracy higher than 10% on LFS (≈ 7.5 m). The source of the issue may be the poor resolution of the magnetic field configuration, especially in the area where the field lines are very dense. Interpolation of the magnetic field lines is the source of the unphysical intersections. They are reduced by decreasing the number of pixels, but the accuracy loss was not completely eliminated. The difference in RMS for plastic and ^{4}He scintillators is negligible (0.01). The accuracy is the worst for sCD detectors.

The best results for scenario (d) have been obtained for the 50x60 pixel grid. The accuracy of the reconstructions is compared in figure 8.45. The most significant difference is observed on the bottom plasma edge. The accuracy better than 20% is in a very wide plasma range. The 1D cuts of the presented profiles are shown in figure 8.46. Again, the accuracy on HFS and in the plasma core is the worst for sCD detectors. The difference between two the types of scintillators is negligible; RMS equals 0.31 ± 0.05 for plastic and 0.32 ± 0.05 for ^{4}He. The highest RMS is for the sCD detectors, equal to 0.36 ± 0.04.

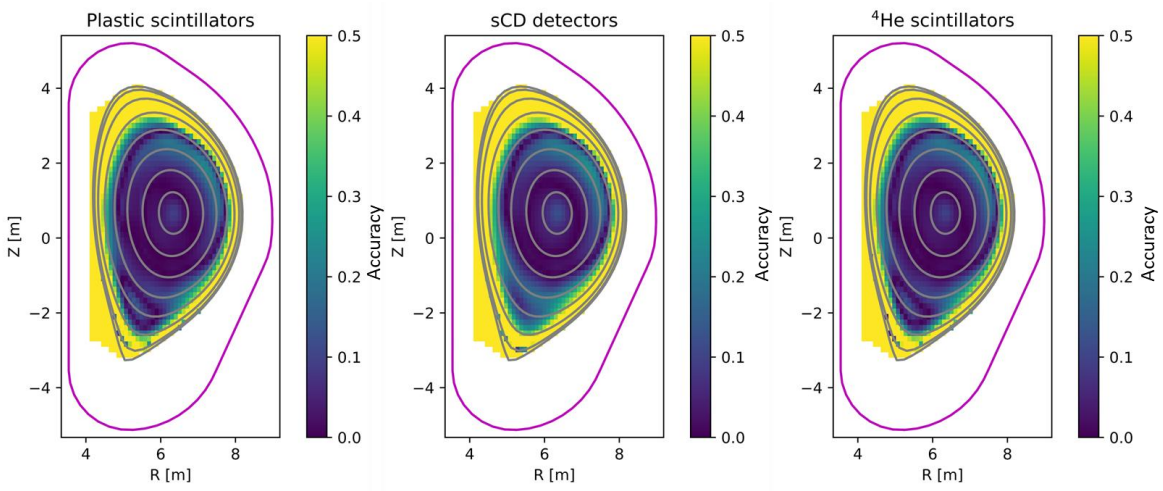

Figure 8.43. The accuracy of the 2D neutron emissivity profiles for scenario (c) reconstructed with plastic scintillators (left), sCD (centre), or ^{4}He scintillators (right).

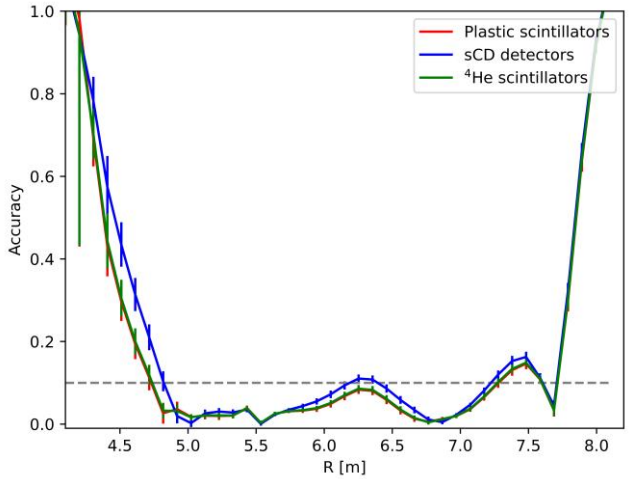

Figure 8.44. The comparison of the 1D accuracy profiles for scenario (c) with different types of the detectors in the ex-port system.

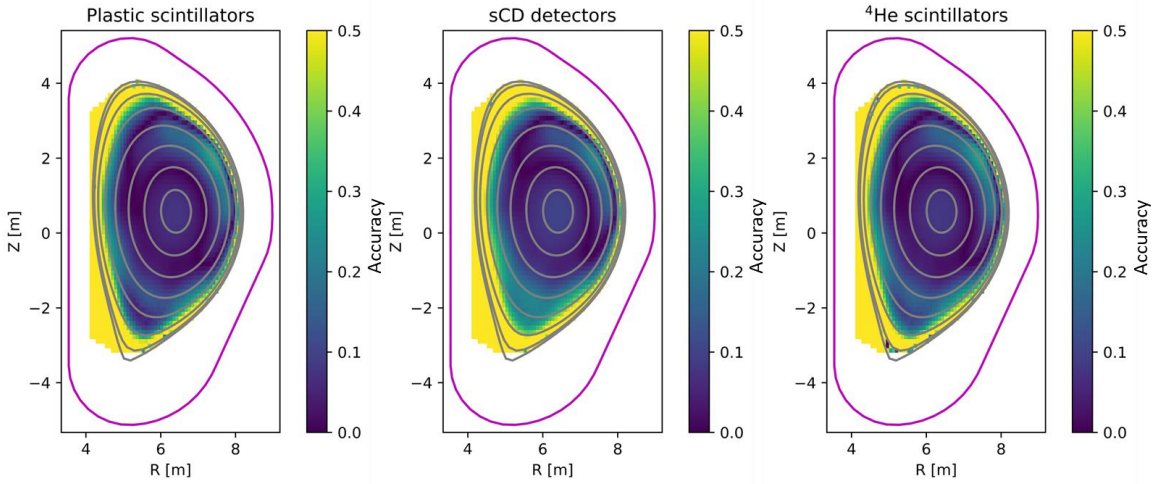

Figure 8.45. The accuracy of the 2D neutron emissivity profiles for scenario (d) reconstructed with plastic scintillators (left), sCD (centre), or ^{4}He scintillators (right).

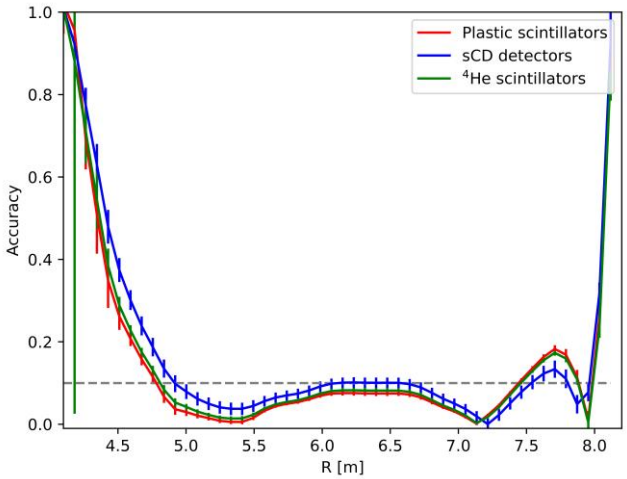

Figure 8.46. The comparison of the 1D accuracy profiles for scenario (d) with different types of the detectors in the ex-port system.

The neutron emissivity distribution for scenario (e) was reconstructed on the 40x50 grid. The accuracies for the three detector types are presented in figure 8.47. For all detectors, accuracy is better in the bottom part of the plasma. However, the lack of precision in the pixels on the upper edge is observed. The source of the discrepancy is the asymmetry of RNC and magnetic field configuration. The last ex-port collimator has a smaller diameter, and the length of the three collimators directed to the upper plasma part is shorter than the others. The differences between the detector types are not visible. The 1D accuracy profiles comparison is presented in figure 8.48. The differences between detectors for scenario (e) are insignificant. RMS equals 0.36 ± 0.02, 0.37 ± 0.12, and 0.38 ± 0.09 for plastic scintillators, sCD detectors and ^{4}He scintillators, respectively. The 1D profile indicates that the best result is obtained with the plastic scintillators.

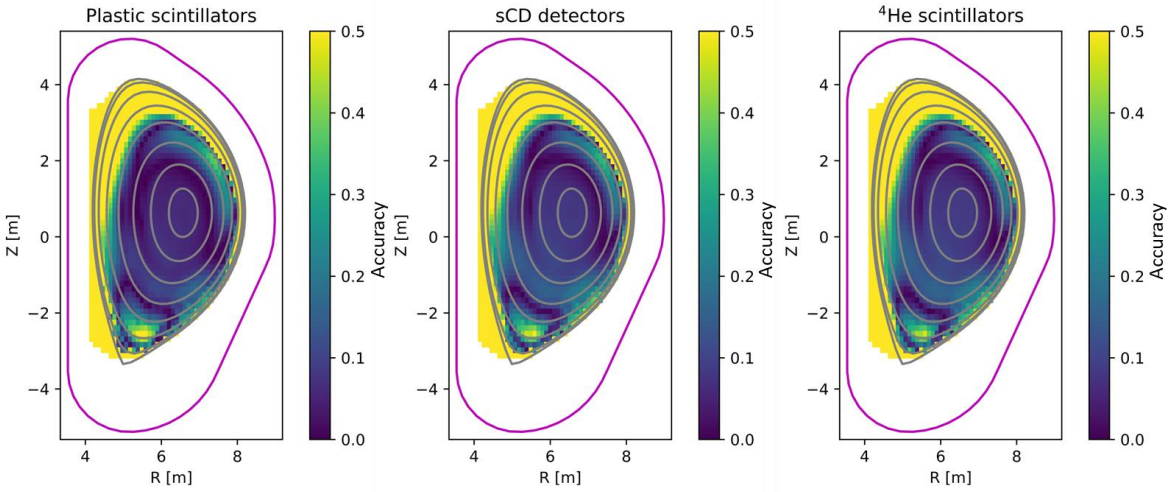

Figure 8.47. The accuracy of the 2D neutron emissivity profiles for scenario (e) reconstructed with plastic scintillators (left), sCD (centre), or ^{4}He scintillators (right).

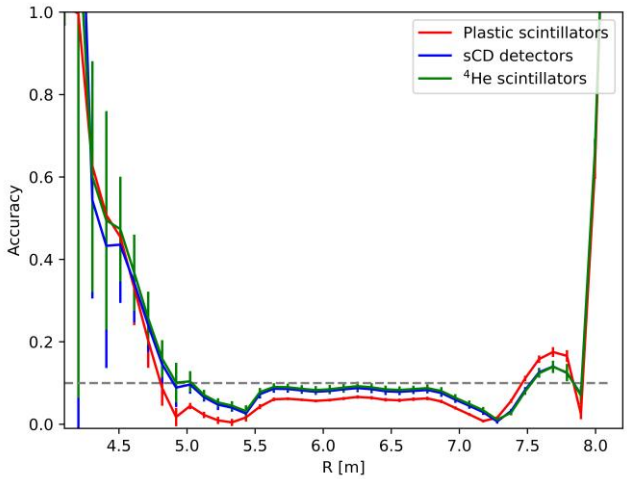

Figure 8.48. The comparison of the 1D accuracy profiles for scenario (e) with different types of the detectors in the ex-port system.

The tomography performance was evaluated by comparing RMS and standard deviation (see table 8.8). The best accuracy for all considered options is for the plastic scintillators. It is in agreement with the predictions connected with the lowest noise. The worst results, especially in the plasma core centre, are obtained for the sCD detectors. The accuracy loss is also observed on HFS, where the standard deviation is the highest due to the limited cover of the area far from the camera. The difference of RMS varies with scenarios and is equal to 5% at maximum, which is smaller than standard deviations. The decision of what kind of detectors will be used in the ex-port system will be made after prototype testing at high temperatures because all options allow fulfilling the design requirement related to the tomography performance.

Table 8.8. Comparison of RMS for tomography reconstruction for the different types of the ex-port detectors and three operation scenarios.

Scenario	Plastic scintillators	sCD detectors	^{4}He scintillators
(c)	0.39 ± 0.12	0.43 ± 0.11	0.40 ± 0.07
(d)	0.31 ± 0.05	0.36 ± 0.04	0.33 ± 0.05
(e)	0.36 ± 0.02	0.37 ± 0.12	0.38 ± 0.09

8.4.2 Tomography robustness against variations in the magnetic field

Scenarios (c), (d), and (e) with simulated count rates for plastic scintillators, sCD detectors and ^{4}He scintillators have been used in the test of tomography robustness against the changes in the magnetic field. The tomography calculations by the MFR method for tokamaks include regularisation dependent on the magnetic field configuration. Especially for the camera in one poloidal position, the smoothing along the magnetic field lines strongly influences the result. The changeable parameter that controls the smoothing anisotropy is Ω. This factor determines how strongly the magnetic field influences the result.

This chapter aims to evaluate the influence of inconsistency in plasma magnetic field configuration used as input on the accuracy of the tomography calculations. The analysis has proceeded by optimising the smoothing parameter Ω (see subchapter 8.4.2.1). The study concerning plasma position shifts is described in subchapter 8.4.2.2. The purpose of this analysis is to determine the maximum uncertainty of the magnetic field position that allows for fulfilling the requirement of the tomography reconstruction accuracy better than 10%. The robustness test also includes the study of the differences between results obtained with a replaced magnetic field,

e.g. count rates simulated for equilibrium (c) reconstructed with the magnetic field for scenario (d) (see subchapter 8.4.2.3). The results of the analysis were reported in [Mik2021R].

8.4.2.1 Smoothing parameter optimisation

The smoothing parameter Ω (defined in equation (7.1)) optimisation has been done separately for all considered scenarios. The low Ω values provide the solutions more robust against the changes in the magnetic field. In the case of thermonuclear plasma with constant neutron emission on the magnetic flux surfaces, the growth of the smoothing parameter Ω improves the result. Therefore, the best smoothing parameter was selected as minimal, which provides a solution without significant accuracy loss. It means RMS changes on the level of 0.01. However, it is acceptable if the difference for one detector type is higher than 0.01 but less than 0.03. A detailed analysis of the results obtained for various Ω has been done to understand better the robustness against the disruptions in the magnetic field. The differences in the results obtained for Ω changes below 2 are negligible.

The best smoothing parameter Ω for preliminary analysis concerning scenarios (a) and (b) equals 50. In the case of the adequately defined magnetic field configuration with high resolution, RMS decreases continuously with increasing Ω values (see figure 8.49). The smaller smoothing parameters are connected with higher standard deviations. The parameter Ω equalled 50 causes very strong smoothing along magnetic field lines, and even minor changes in the magnetic field can affect substantial disruptions in the results. This issue was not discussed in the previous subchapters.

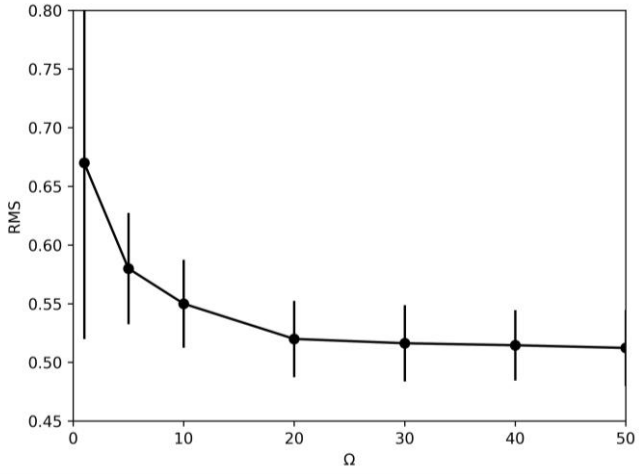

Figure 8.49. RMS for different values of smoothing parameter Ω for scenario (a) and the baseline architecture.

The comparison of RMS obtained for scenario (c) for plastic scintillators, sCD detectors, and ^{4}He scintillators with different smoothing parameters Ω is presented in figure 8.50. The curves obtained for all detectors have the same character. RMS and standard deviation decrease with increasing smoothing parameter. The differences between RMS obtained for Ω equalled 10 and higher vary from 0 to 0.03. The examples of two-dimensional accuracy of the neutron emissivity distribution are shown in figure 8.51. The 1D horizontal cuts through Z=0.6 m and vertical cuts through R=6.3 m for different Ω are presented in figure 8.52. The differences in the profiles obtained with Ω higher than 10 are not visible. The accuracy loss in the plasma centre and upper LFS is observed for the sCD detectors. In these areas, the precision of the magnetic field configuration has a more substantial influence due to the distribution of the lines and possible artefacts presence. The stronger smoothing enhances the reconstruction issues in the pixels in these regions. The optimal Ω value is 10 for scenario (c).

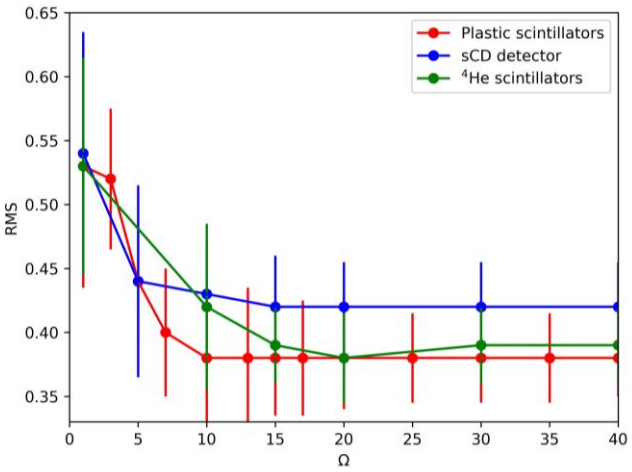

Figure 8.50. RMS for different values of smoothing parameter Ω for scenario (c) and different types of the detectors in the ex-port camera part.

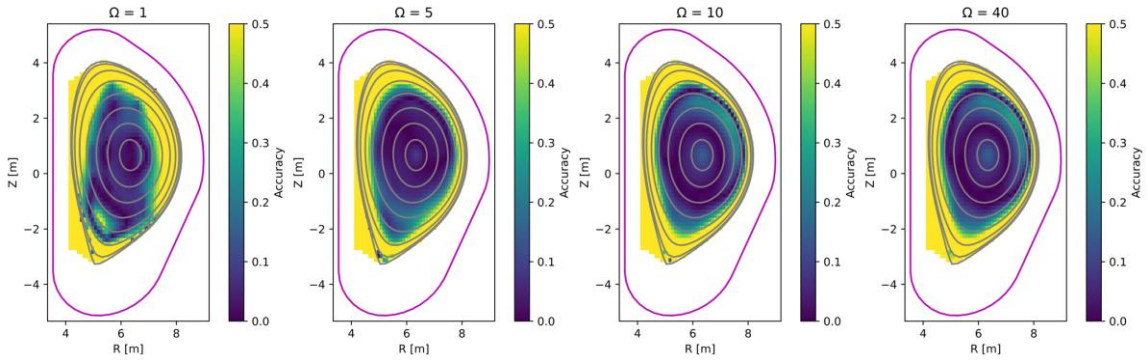

Figure 8.51. The comparison of the 2D accuracy profiles obtained with different values of smoothing parameter for scenario (c) and the sCD detectors in the ex-port system.

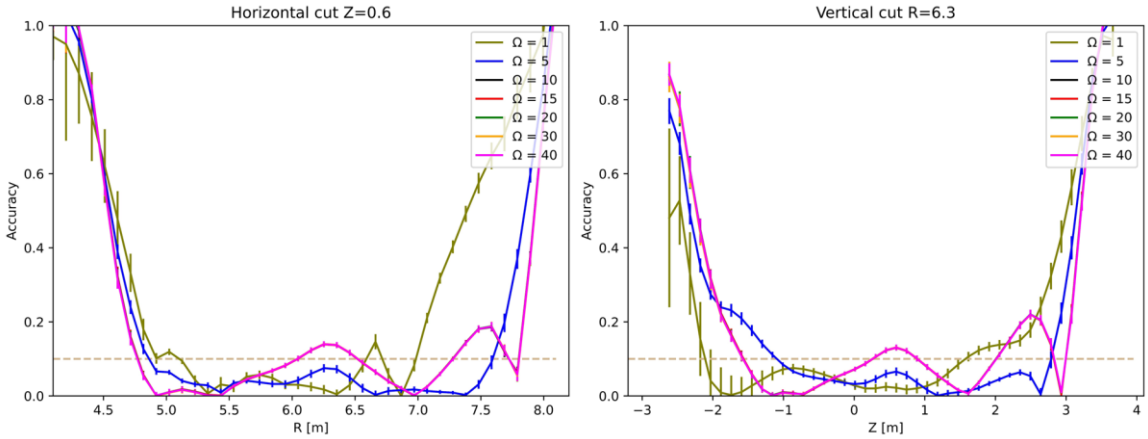

Figure 8.52. The comparison of the 1D accuracy profiles horizontal (left) and vertical (right) obtained with different values of smoothing parameter for scenario (c) and the sCD detectors in the ex-port system.

RMS calculated for tomography results for scenario (d) and three types of neutron detectors is presented in figure 8.53. It rapidly decreases for smoothing parameter Ω in the range 1 – 10. The differences between RMS obtained with higher Ω values do not exceed 0.01. The highest discrepancy, 0.02, between results for smoothing parameter Ω equalled 10 and 20, is observed for the plastic scintillators. The two-dimensional accuracy maps of the neutron

emissivity obtained in the calculations with the ^{4}He scintillator and different smoothing parameters Ω are presented in figure 8.54. The comparisons of the horizontal and vertical cuts are shown in figure 8.55. The accuracy for Ω equalled 1 varies strongly in the whole plasma poloidal cross-section. The 1D profile for smoothing parameter Ω equalled 5 indicates the best result in the plasma core, but a significant accuracy loss is observed on the bottom of the tokamak vessel. The optimal Ω for scenario (d) equals 10.

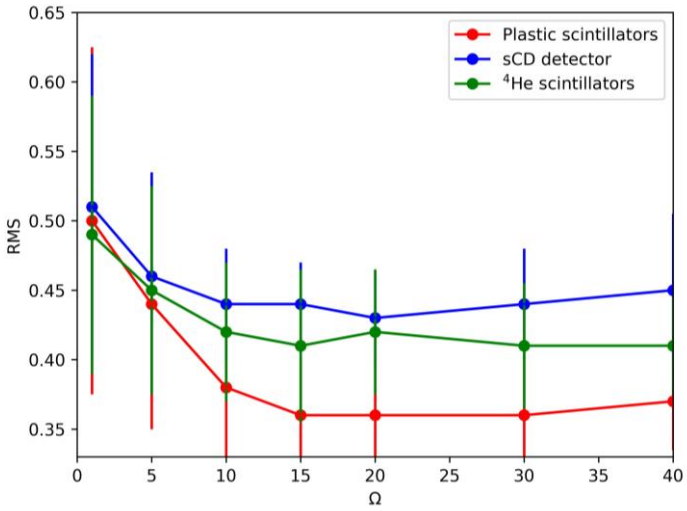

Figure 8.53. RMS for different values of smoothing parameter Ω for scenario (d) and different types of the detectors in the ex-port camera part.

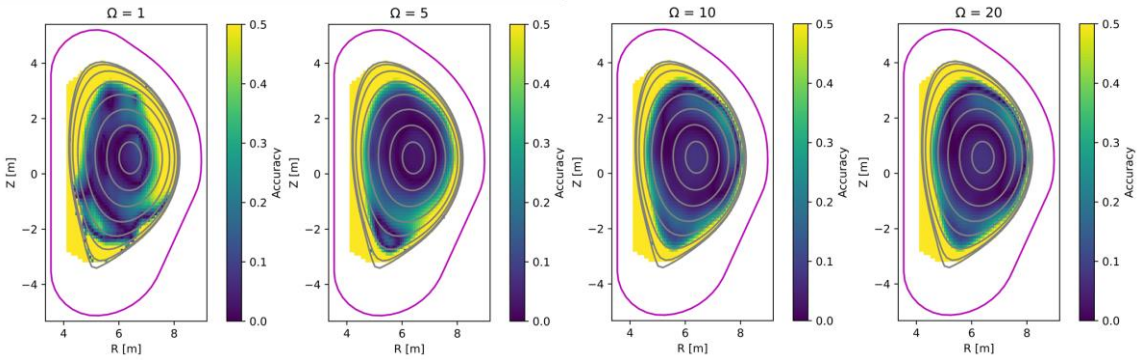

Figure 8.54. The comparison of the 2D accuracy profiles obtained with different values of smoothing parameter for scenario (d) and the ^{4}He scintillators in the ex-port system.

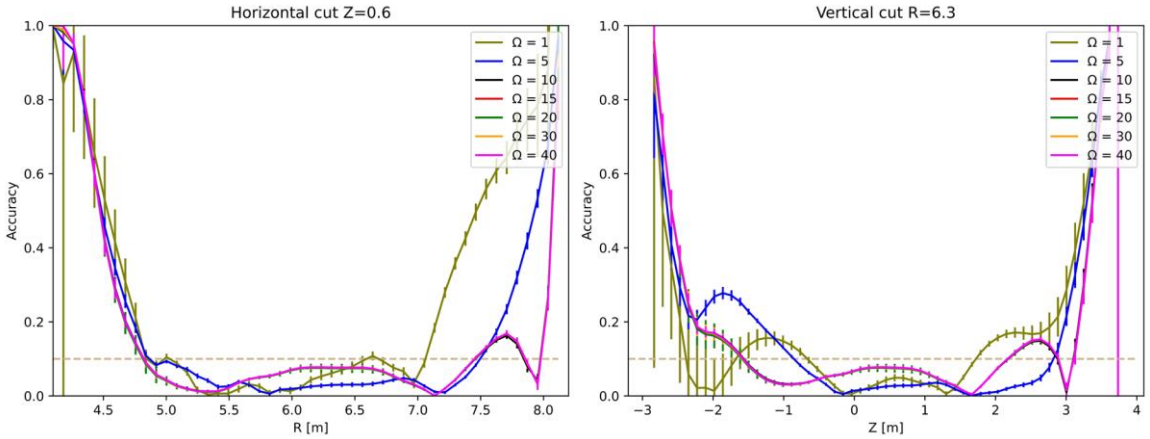

Figure 8.55. The comparison of the 1D accuracy profiles horizontal (left) and vertical (right) obtained with different values of smoothing parameter for scenario (d) and the ^{4}He scintillators in the ex-port system.

The comparison of RMS for various smoothing parameters Ω and scenario (e) is presented in figure 8.56. In this case, the minimum is observed for Ω equalled 5. The shape of the curves is related to the magnetic field configuration containing artefacts that disturb smoothing. A similar character is observed in the case of other disruptions in the magnetic field definition. The two-dimensional accuracy distribution of the results for the plastic scintillators is shown in figure 8.57. The corresponding comparison of the 1D profiles is presented in figure 8.58. The differences between results obtained with $\Omega \geq 10$ are not observed. The optimal smoothing parameter Ω does not reproduce the problem with reconstructing the upper LFS where the agnetic field lines are dense, and their intersections disrupt the tomography calculation.

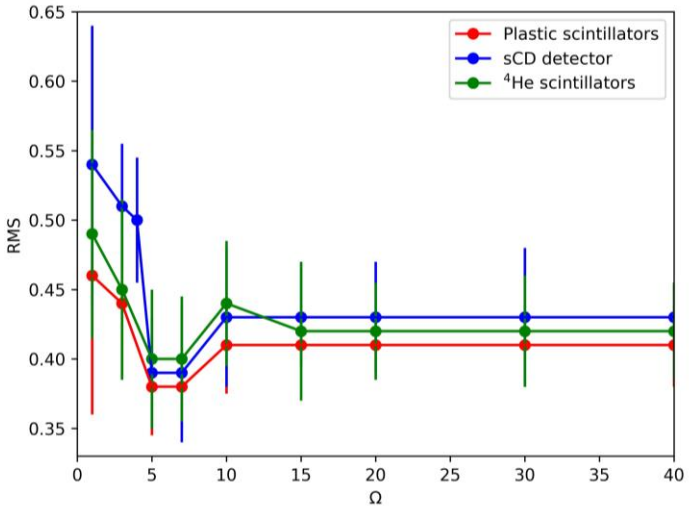

Figure 8.56. RMS for different values of smoothing parameter Ω for scenario (e) and different types of the detectors in the ex-port camera part.

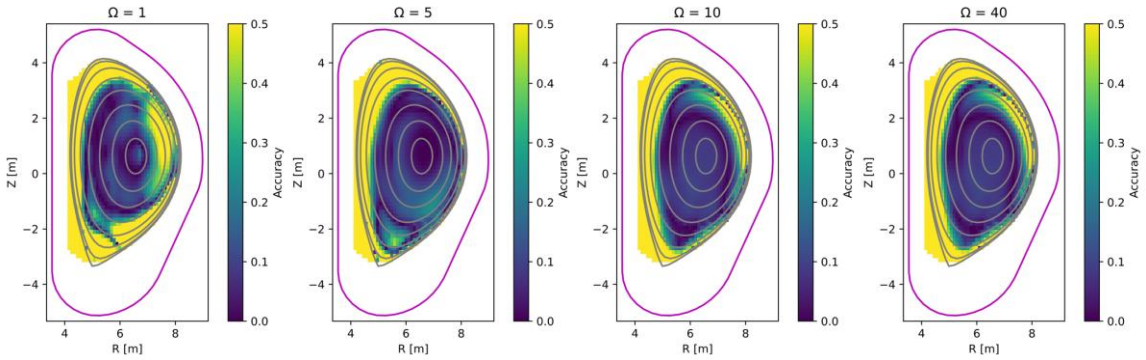

Figure 8.57. The comparison of the 2D accuracy profiles obtained with different values of smoothing parameter for scenario (e) and the plastic scintillators in the ex-port system.

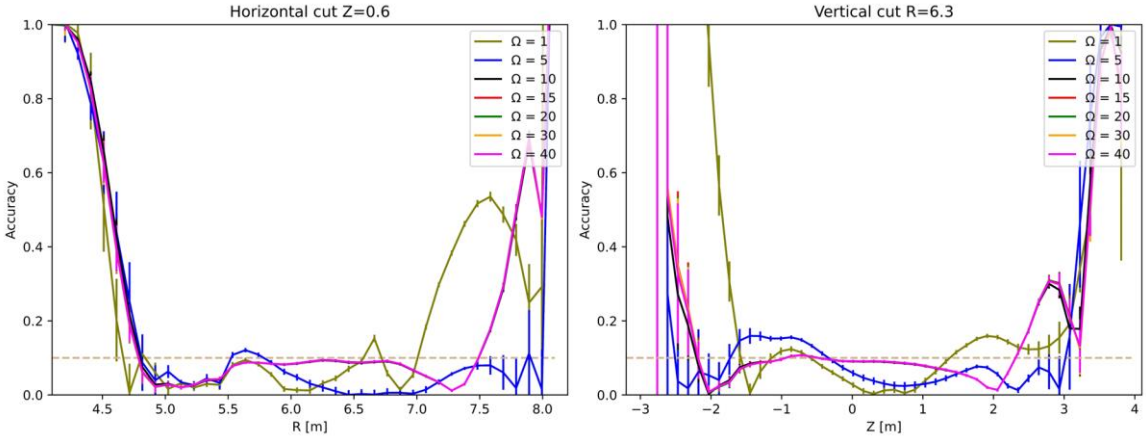

Figure 8.58. The comparison of the 1D accuracy profiles horizontal (left) and vertical (right) obtained with different values of smoothing parameter for scenario (e) and the plastic scintillators in the ex-port system.

RMS decreases continuously with increasing smoothing parameter Ω for scenarios with the magnetic field defined with high resolution. The analysis of the results for scenarios (c) and (d) indicates that the optimal Ω is 10. For all types of detectors, differences between solutions with smoothing parameters in the range 10 – 40 are negligible. Therefore, the minimum value provided the tomography result with the best accuracy was selected for further analysis due to lower sensitivity against variations in the magnetic field. The chosen value does not reduce the issue with the reconstruction in the area where magnetic field lines are dense, and artefacts occur because of the lower resolution of the magnetic field configuration. In the case of scenario (e), the minimum of RMS is observed, and the optimal smoothing parameter equals 5. For this value, the accuracy is below 20% for the broadest plasma part.

The execution of the smoothing parameter Ω optimisation procedure will not be possible during the experiment. The magnetic field configuration can change during the discharge. Low differences between results obtained in calculation with Ω from 10 to 40 for all scenarios indicate that the smoothing parameter can be constant for all considered times. The approximation of Ω equalled 10 for all experimental studies will be the source of RMS increase by 0.05 at the maximum, which is a value lower than standard deviation.

8.4.2.2 Reconstruction with shifted magnetic field

During the experiment, plasma can be shifted in relation to the vacuum vessel centre. Therefore, the actual plasma position can differ from that assumed in the simulation. The following analysis aims at evaluating the tomography calculations' robustness due to the magnetic field displacement. The analysis concerns the plasma movement through the R and Z tokamak axis separately or together to reproduce every possible direction. The smoothing matrix is generated with the shifted magnetic field in the tomography reconstruction. The analysis includes a comparison of the neutron emissivity distribution for scenarios (c), (d), and (e) obtained in the reconstruction with three types of detectors. The optimal smoothing parameters specified in the previous subchapter 8.4.2.1 were used in the calculations.

At first, scenario (c) was analysed. The character of the changes due to the shifts of the magnetic field used for tomography reconstruction was tested for all detector types in the ex-port system. RMS calculated for displacement in the positive R direction is presented in figure 8.59. The magnetic field shift up to 2 cm does not change RMS. The rise of RMS is up to 0.01 for the movements of 5 cm towards RNC. The maximal RMS increase for 10 cm displacement is 0.05. Standard deviation for the results obtained with moving magnetic fields varies between 0.09 to 0.15. The examples of the 2D accuracy maps for these magnetic field shifts are shown in figure 8.60. The accuracy loss on LFS is observed clearly from 5 cm displacement. The comparison of the 1D profiles is presented in figure 8.61. It shows that the accuracy loss in the plasma core is significant for all reconstructions. The accuracy is worse than 10%, and differences between shifts are at the level of 1%. The only area reconstructed with a precision better than 10% is the bottom HFS.

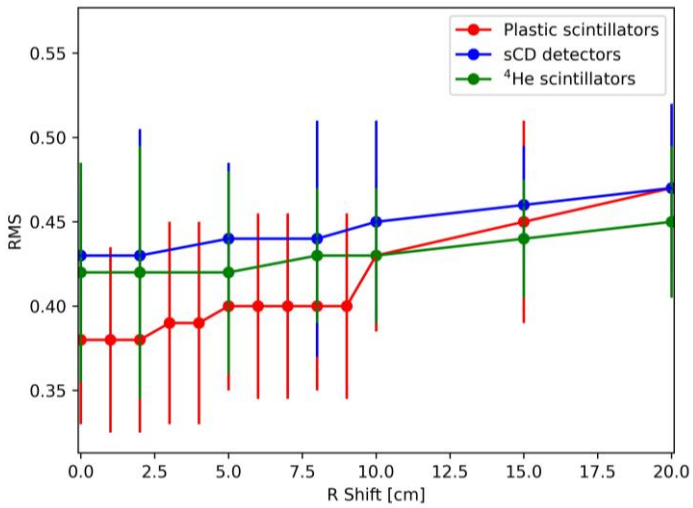

Figure 8.59. RMS for magnetic field displacement in R positive direction for scenario (c) and different types of the detectors in the ex-port camera part.

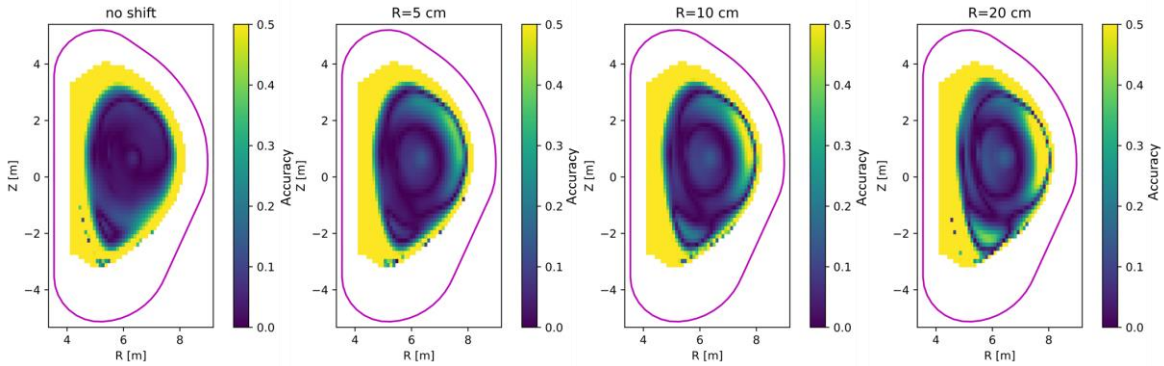

Figure 8.60. The comparison of the 2D accuracy profiles obtained with magnetic field shift along R-axis in the positive direction for scenario (c) and the ^{4}He scintillators in the ex-port system.

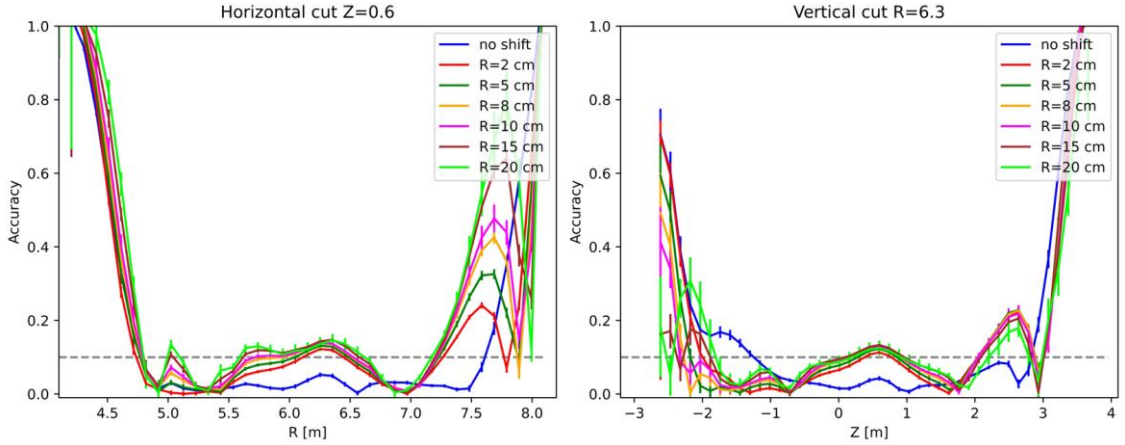

Figure 8.61. The comparison of the 1D accuracy profiles obtained with magnetic field shift along R-axis in the positive direction for scenario (c) and the ^{4}He scintillators in the ex-port system.

The dependency of RMS from the R negative shift is presented in figure 8.62. The changes up to 2 cm do not cause visible changes in RMS for all detector types, as in the case of scenario (c). The displacements equal to 5 cm and 10 cm correspond to the increases of RMS of 0.01 and 0.03, respectively. The examples of 2D accuracy of reconstruction are shown in figure 8.63. The accuracy loss for the magnetic field movement of 3 cm is observed in the core centre and the upper part of the plasma. The visible accuracy loss on HFS is noted for shifts from 10 cm. The comparison of the 1D accuracy is presented in figure 8.64. All results with magnetic field movements below 15 cm have a precision better than 10% in the plasma core. The changes in the accuracy in the whole plasma cross-section for bigger displacements exceed 20%.

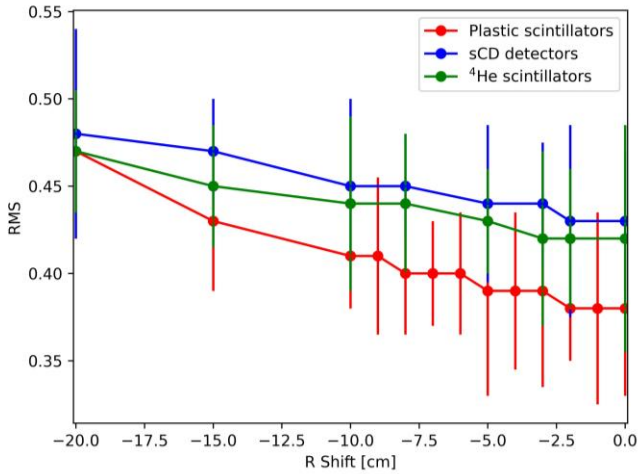

Figure 8.62. RMS for magnetic field displacement in R negative direction for scenario (c) and different types of the detectors in the ex-port camera part.

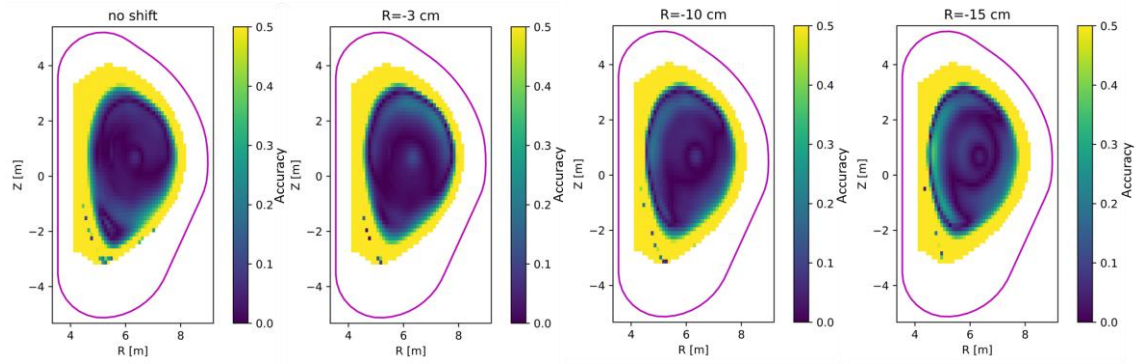

Figure 8.63. The comparison of the 2D accuracy profiles obtained with magnetic field shift along R-axis in the negative direction for scenario (c) and the ^{4}He scintillators in the ex-port system.

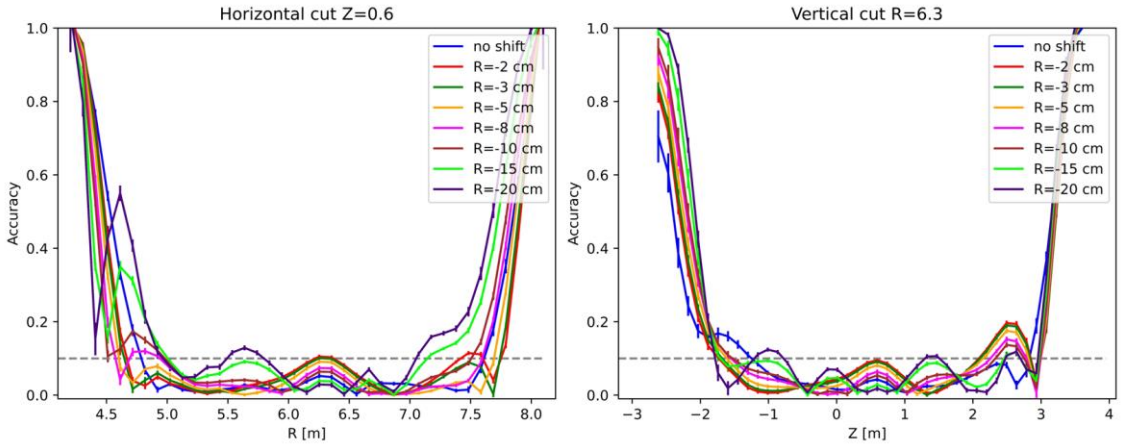

Figure 8.64. The comparison of the 1D accuracy profiles obtained with magnetic field shift along R-axis in the negative direction for scenario (c) and the ^{4}He scintillators in the ex-port system.

RMS for various magnetic field displacements in the Z positive direction is presented in figure 8.65. The character of the changes is similar to the negative shifts through R-axis. The magnetic field movement of 2 cm has negligible influence on RMS for ^{4}He scintillators and sCD detectors. The 5 cm shift provides the result with RMS worse of about 0.02. There is the increase in standard deviation with the displacements. The comparisons of the 2D and 1D accuracy profiles are presented in figures 8.66 and 8.67, respectively. The accuracy in the plasma core is about 10%

for all cases. Surprisingly, the accuracy in the 1D horizontal cut corresponding to the 20 cm shift is lower in the plasma core centre than the result obtained with the actual magnetic field configuration. It is a consequence of the upward movement of the central magnetic flux surface, defined with a low resolution which causes disruptions in the smoothing. Neighbour magnetic field lines are defined with the better precision and allow to obtain lower accuracy. The differences in the neutron emission for these magnetic flux surfaces are negligible. Therefore, the 1D horizontal cut through the result obtained for movements omits the problematic area. Other regions are reconstructed with higher error. The 2D accuracy distribution shows an intense loss on the bottom and top parts of the plasma.

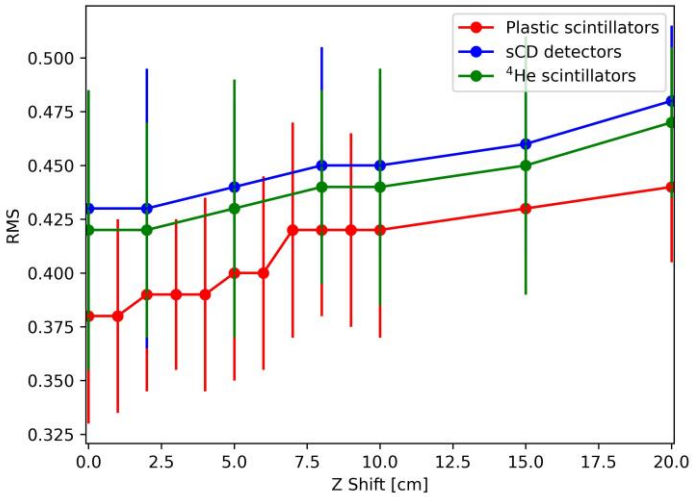

Figure 8.65. RMS for magnetic field displacement in Z positive direction for scenario (c) and different types of the detectors in the ex-port camera part.

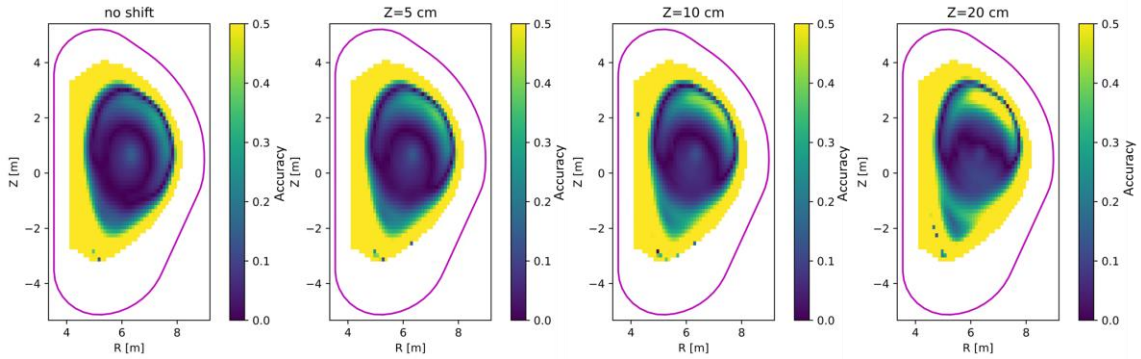

Figure 8.66. The comparison of the 2D accuracy profiles obtained with magnetic field shift along Z-axis in the positive direction for scenario (c) and the sCD detectors in the ex-port system.

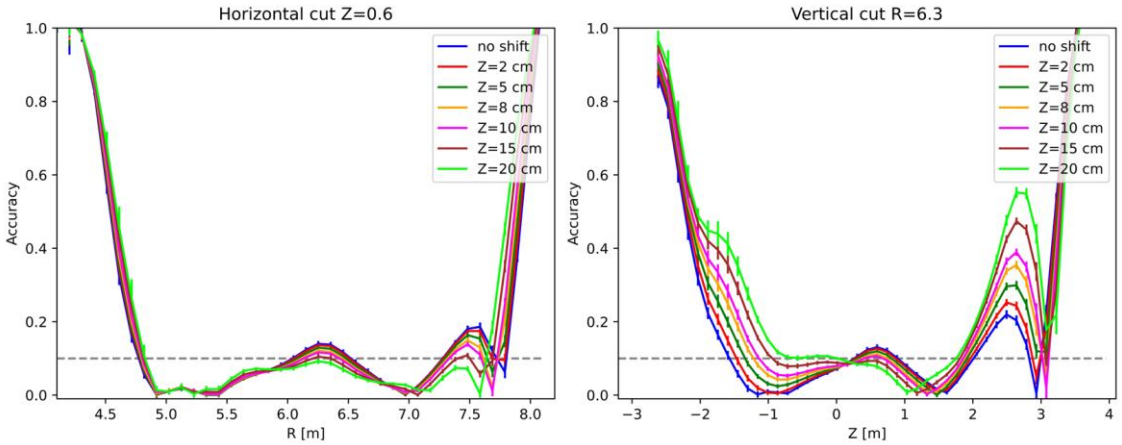

Figure 8.67. The comparison of the 1D accuracy profiles obtained with magnetic field shift along Z-axis in the positive direction for scenario (c) and the sCD detectors in the ex-port system.

The comparison of RMS for Z negative direction displacement is presented in figure 8.68. There are negligible changes in RMS for magnetic field shifts up to 10 cm, but standard deviation varies from 0.09 to 0.14. The movement of 15 cm corresponds to the increase of RMS by about 0.02. The examples of 2D accuracy distribution are presented in figure 8.69. The corresponding 1D profiles comparison is shown in figure 8.70. The horizontal cut confirms the negligible changes between results in the plasma core. The top and bottom plasma parts' accuracy differs by more than 20% for shifts higher than 10 cm.

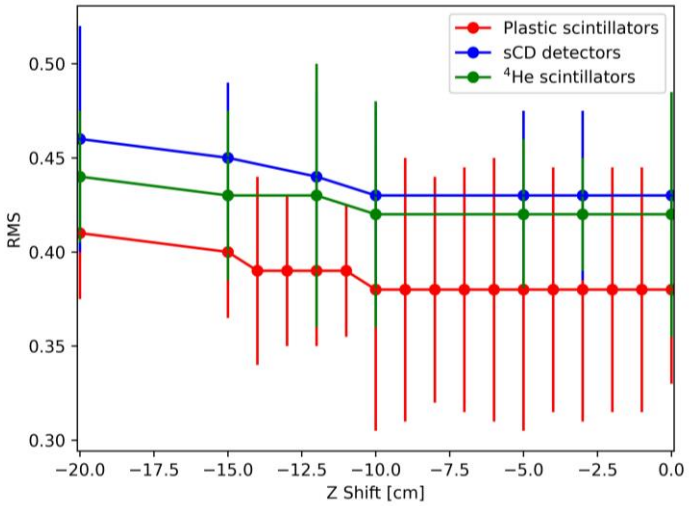

Figure 8.68. RMS for magnetic field displacement in Z negative direction for scenario (c) and different types of the detectors in the ex-port camera part.

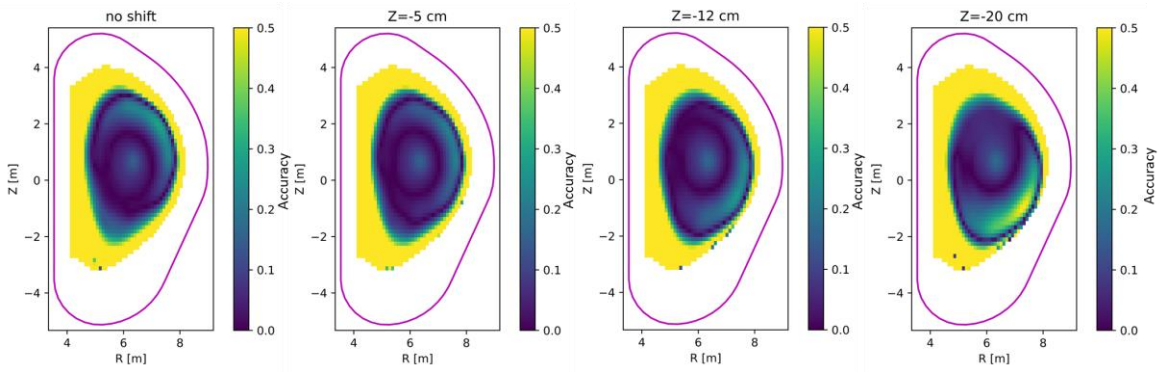

Figure 8.69. The comparison of the 2D accuracy profiles obtained with magnetic field shift along Z-axis in the negative direction for scenario (c) and the sCD detectors in the ex-port system.

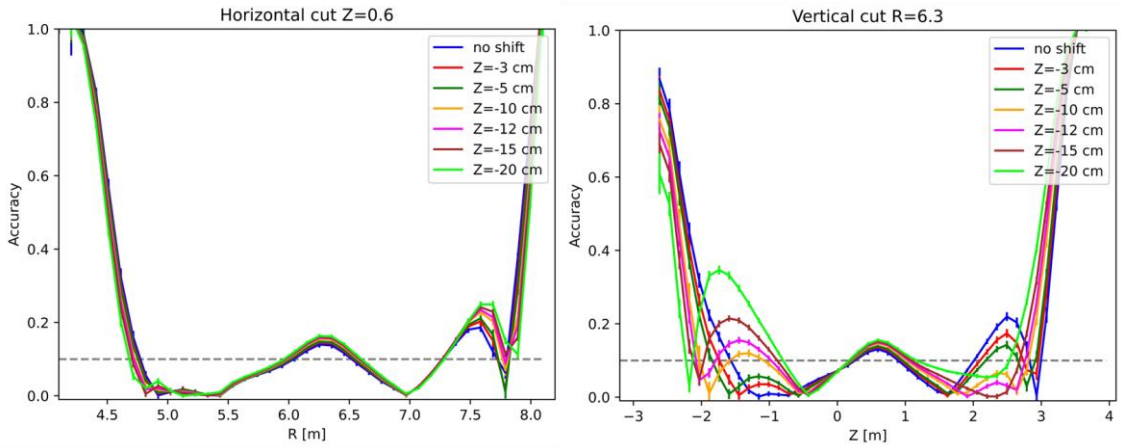

Figure 8.70. The comparison of the 1D accuracy profiles obtained with magnetic field shift along Z-axis in the negative direction for scenario (c) and the sCD detectors in the ex-port system.

The single magnetic field displacements analysis for scenario (c) indicates that the shifts towards R direction up to 2 cm have negligible influence on RMS. However, a slight accuracy loss on the plasma edges is observed. The positive displacements on the Z-axis show the same character. The upward movements have the lowest influence on tomography reconstruction. RMS (with two decimal places precision) obtained for shifts up to 10 cm is constant, but accuracy variations are observed on the top and bottom plasma edges. It is connected with displacing the areas where the smoothing along magnetic field lines is disrupted. The regions with the highest accuracy loss are shifted, and some parts of plasma are seemingly reconstructed with better precision.

The combined displacements in the two directions have also been analysed. RMS changes for the shifts along the R axis in negative and positive directions with the constant Z position of the magnetic field are presented in figure 8.71. The increase of RMS for Z values from – 5 cm to 5 cm fluctuates from 0 to 0.02. The highest RMS is obtained for the displacement in the R and Z positive directions. A similar comparison of RMS for magnetic field Z movements with constant R shifts is presented in figure 8.72. Only the displacements of 1 cm in both directions do not influence the reconstruction results. The magnetic field movements in the positive Z direction for R=2/-2 cm and R=3/-3 cm correspond to a negligible difference in RMS compared to the result with the proper magnetic field configuration. For the negative Z, RMS difference between the reconstructions for these two R values is about 0.01. The examples of the 2D and 1D accuracy distributions are presented in figures 8.73 and 8.74, respectively. The displacements in both directions up to 5 cm allow obtaining the accuracy better than 10% in the plasma core.

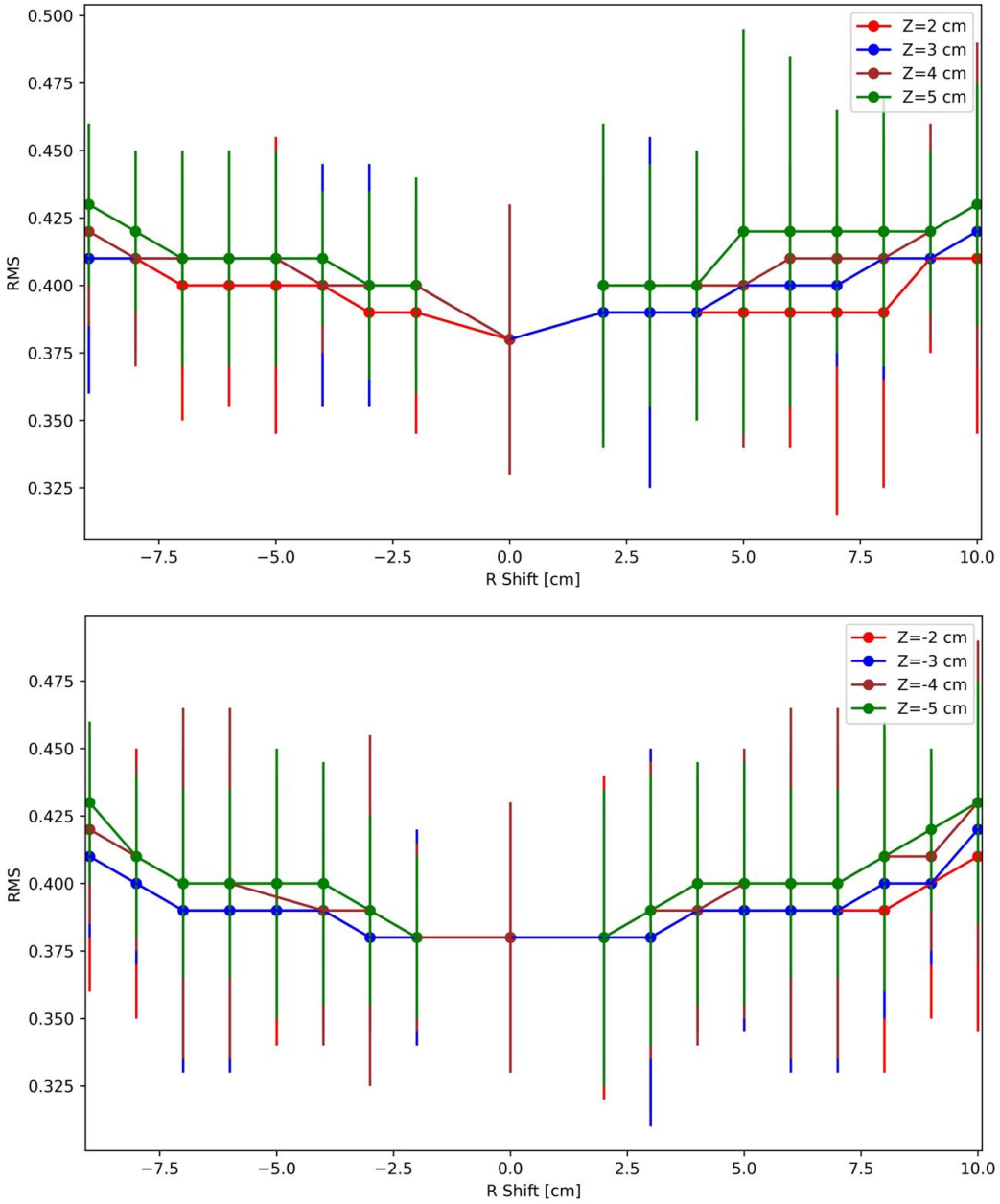

Figure 8.71. RMS comparison for magnetic field displacement in R direction with constant Z shift (positive – top, negative – bottom) for scenario (c) and the plastic scintillators in the ex-port camera part.

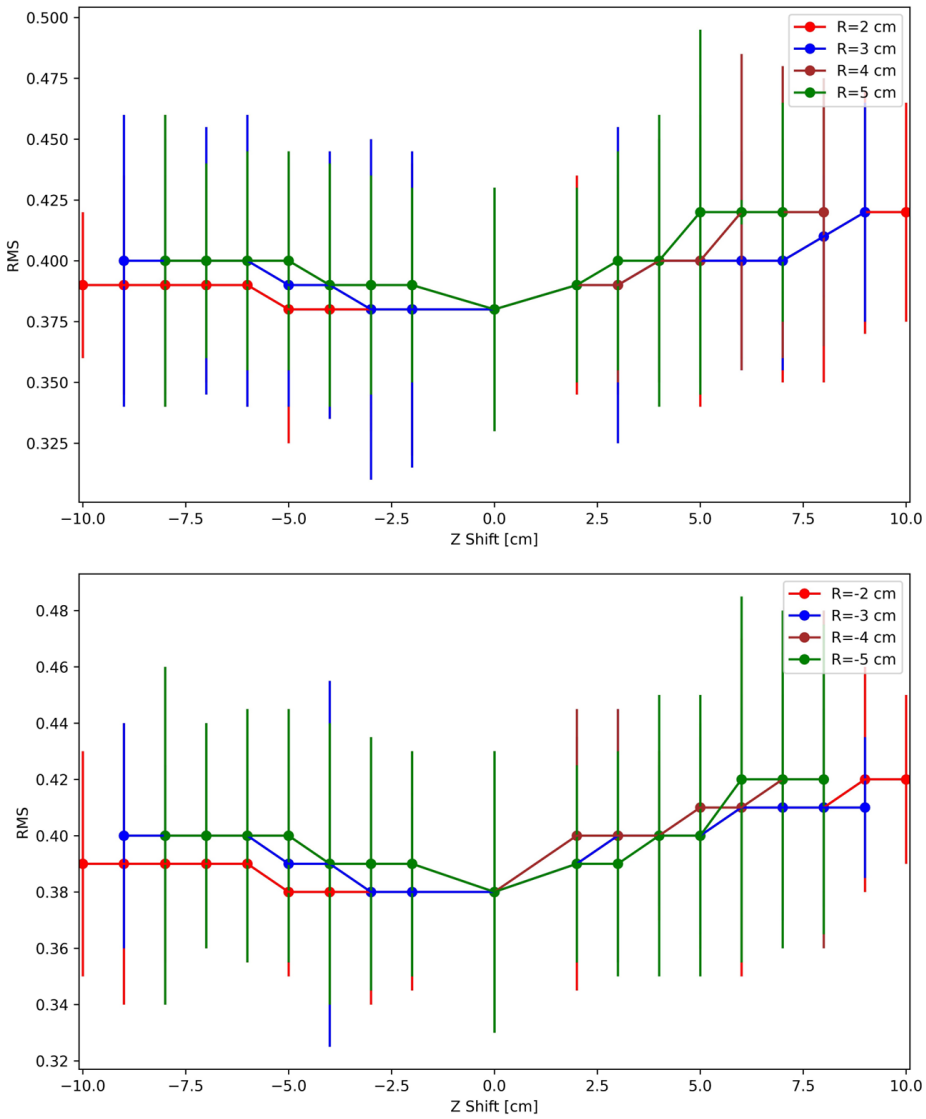

Figure 8.72. RMS comparison for magnetic field displacement in Z direction with constant R shift (positive – top, negative – bottom) for scenario (c) and the plastic scintillators in the ex-port camera part.

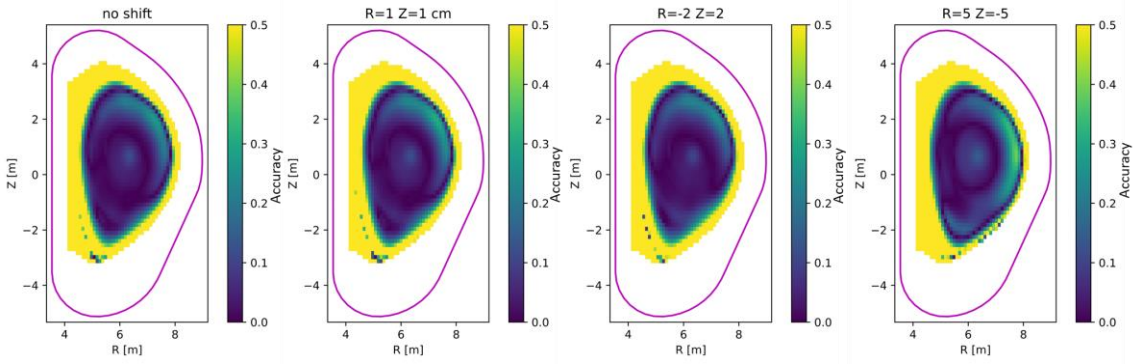

Figure 8.73. The comparison of the 2D accuracy profiles obtained with magnetic field shift along R and Z axis for scenario (c) and the plastic scintillators in the ex-port system.

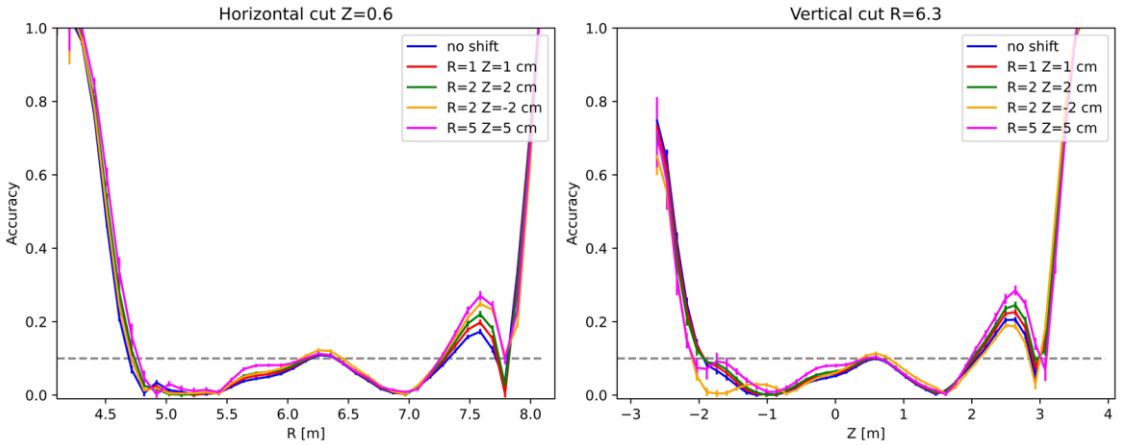

Figure 8.74. The comparison of the 1D accuracy profiles obtained with magnetic field shift along R and Z axis for scenario (c) and the plastic scintillators in the ex-port system.

A similar analysis of the magnetic field displacement influence has been made for scenario (d). RMS calculated for the tomography results obtained with smoothing matrix defined with magnetic field configuration shifted along R-axis in the positive direction is presented in figure 8.75. The change in RMS is not observed for movement up to 3 cm. The 5 cm and 10 cm displacements are connected with the rise of RMS by 0.01 and 0.04, respectively. The 2D accuracy distributions are presented in figure 8.76. The accuracy loss is observed on LFS for all shifts. The comparison of the 1D profiles is shown in figure 8.77. The discrepancy between the reconstruction results and the simulated neutron emissivity increases on the plasma edges with the magnetic field shift length. Only results with magnetic field displacement below 6 cm have an accuracy better than 10% in the plasma core.

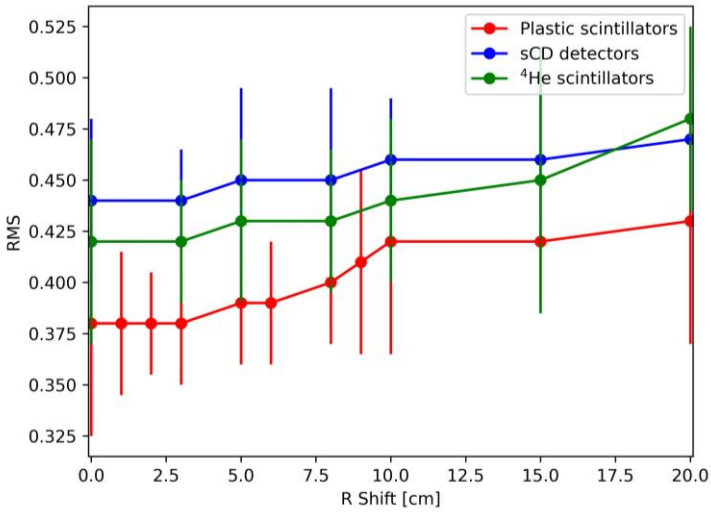

Figure 8.75. RMS for magnetic field displacement in R positive direction for scenario (d) and different types of the detectors in the ex-port camera part.

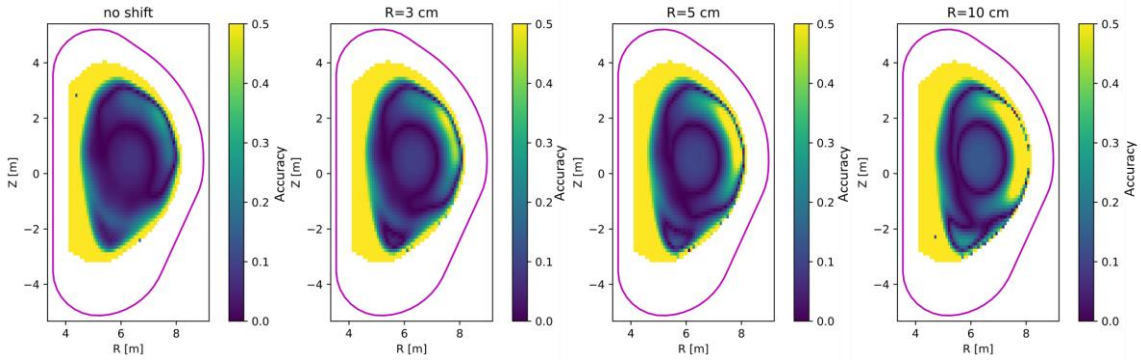

Figure 8.76. The comparison of the 2D accuracy profiles obtained with magnetic field shift along R-axis in the positive direction for scenario (d) and the plastic scintillators in the ex-port system.

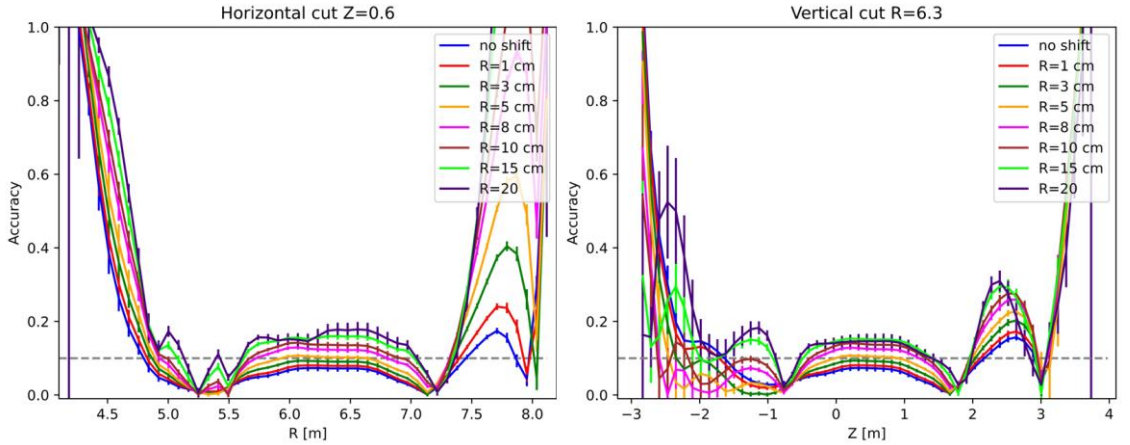

Figure 8.77. The comparison of the 1D accuracy profiles obtained with magnetic field shift along R-axis in the positive direction for scenario (d) and the plastic scintillators in the ex-port system.

The comparison of RMS obtained for displacements along R-axis in the negative direction is presented in figure 8.78. RMS changes for shifts start from 1 cm. The magnetic field movements of 5 cm are connected with the rise of RMS and vary from 0.02 to 0.04. The shift of 10 cm causes the increase of RMS up to 0.08, which is statistically significant. The 2D accuracy of the tomography reconstructions is presented in figure 8.79. The evident changes are visible only for the results obtained with the magnetic field movement higher than 10 cm. The 1D accuracy profiles comparison is shown in figure 8.80. Only results for displacements of 11 cm and higher have accuracy higher than 10% in the plasma core.

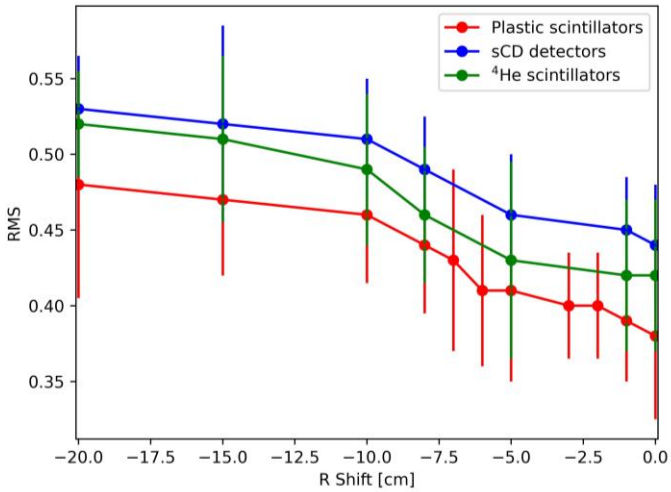

Figure 8.78. RMS for magnetic field displacement in R negative direction for scenario (d) and different types of the detectors in the ex-port camera part.

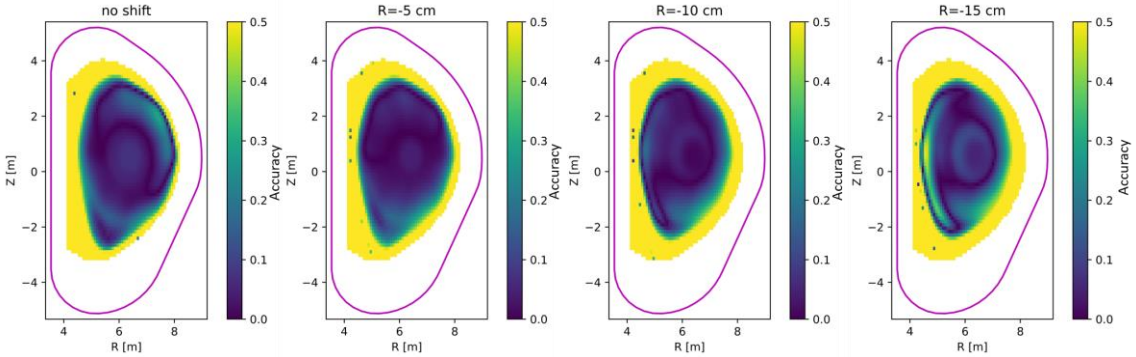

Figure 8.79. The comparison of the 2D accuracy profiles obtained with magnetic field shift along R-axis in the negative direction for scenario (d) and the plastic scintillators in the ex-port system.

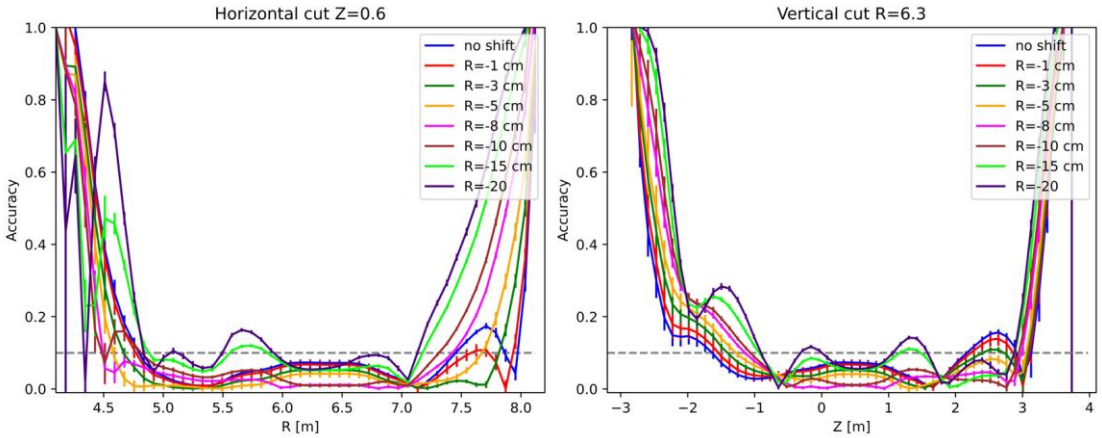

Figure 8.80. The comparison of the 1D accuracy profiles obtained with magnetic field shift along R-axis in the negative direction for scenario (d) and the plastic scintillators in the ex-port system.

RMS calculated for the reconstruction results obtained with the magnetic field movements along Z-axis in the positive direction are presented in figure 8.81. The shift that causes a negligible change in RMS varies for different detectors from 1 cm to 2 cm. The 5 cm or 10 cm displacements correspond to the increase of RMS from 0.03 to 0.08. The 2D accuracy distributions of the neutron emissivity obtained by tomography calculation are shown in figure 8.82.

The corresponding 1D cuts are presented in figure 8.83. The same effect as for scenario (c) with the delusory improvement of the accuracy in the plasma core is observed. All the results have an accuracy better than 10% in the plasma core.

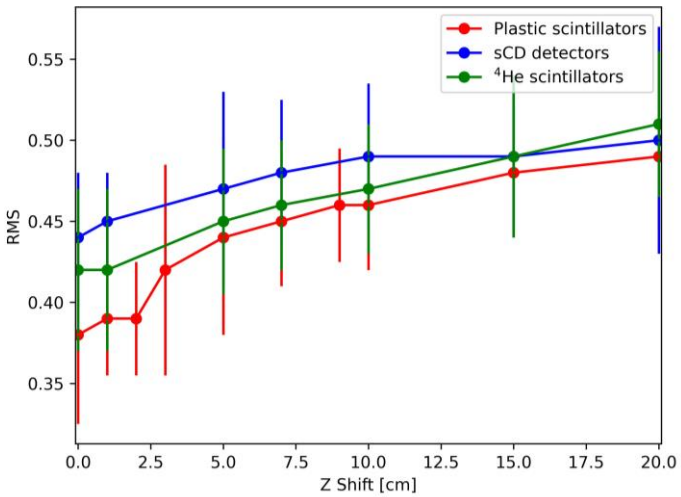

Figure 8.81. RMS for magnetic field displacement in Z positive direction for scenario (d) and different types of the detectors in the ex-port camera part.

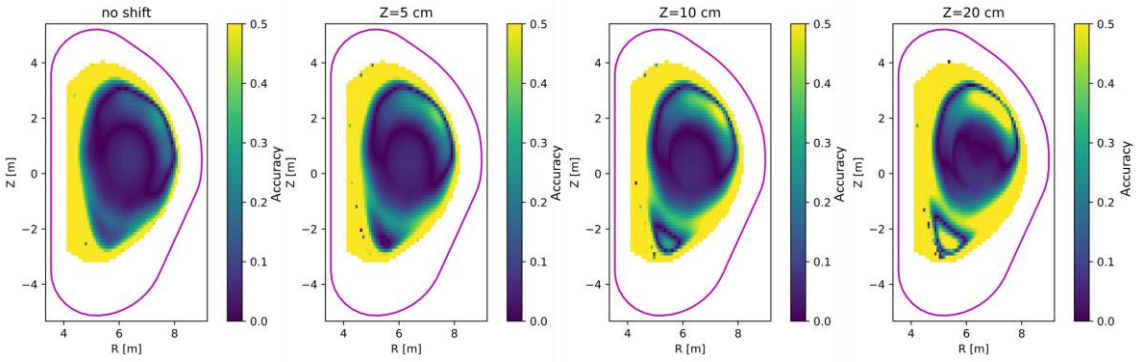

Figure 8.82. The comparison of the 2D accuracy profiles obtained with magnetic field shift along Z-axis in the positive direction for scenario (d) and the ^{4}He scintillators in the ex-port system.

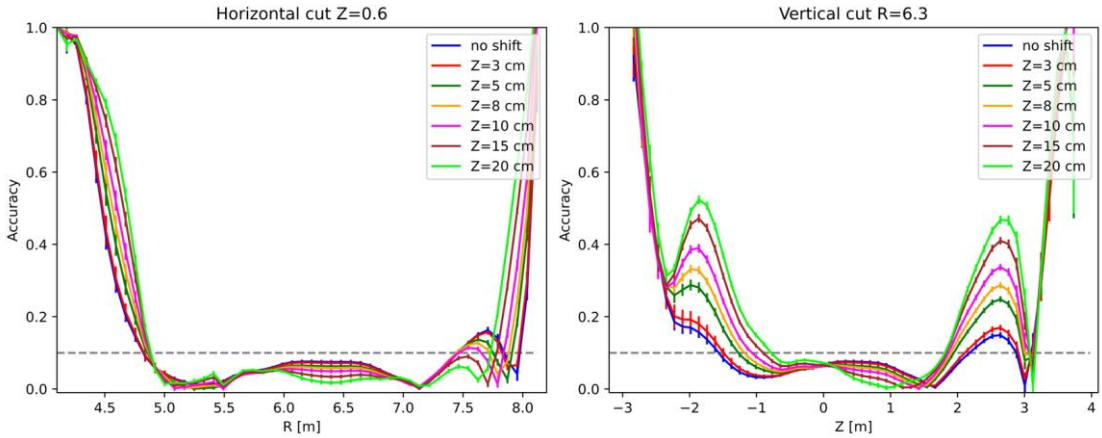

Figure 8.83. The comparison of the 1D accuracy profiles obtained with magnetic field shift along Z-axis in the positive direction for scenario (d) and the ^{4}He scintillators in the ex-port system.

RMS comparison of the results obtained with magnetic field displacement in Z negative direction for all kinds of detectors and scenario (d) is presented in figure 8.84. The shifts up to 5 cm influence on RMS is not observed for the plastic scintillators. The magnetic field movement of 10 cm is related to the increase of RMS by 0.02. The 2D accuracy distributions for ^{4}He scintillators are shown in figure 8.85. The accuracy loss is observed on the bottom of the tokamak. The 1D accuracy profiles comparison is presented in figure 8.86. The differences between various displacements are not visible on the horizontal and vertical cut through the plasma centre. All results have accuracy better than 10% in the plasma core. In the vertical cut, the differences in the results on the edges are observed. Additional accuracy loss is observed in 2D maps on the bottom LFS.

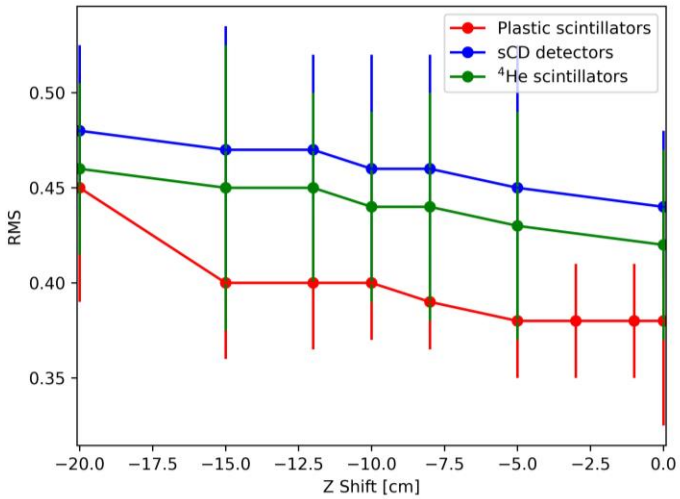

Figure 8.84. RMS for magnetic field displacement in Z negative direction for scenario (d) and different types of the detectors in the ex-port camera part.

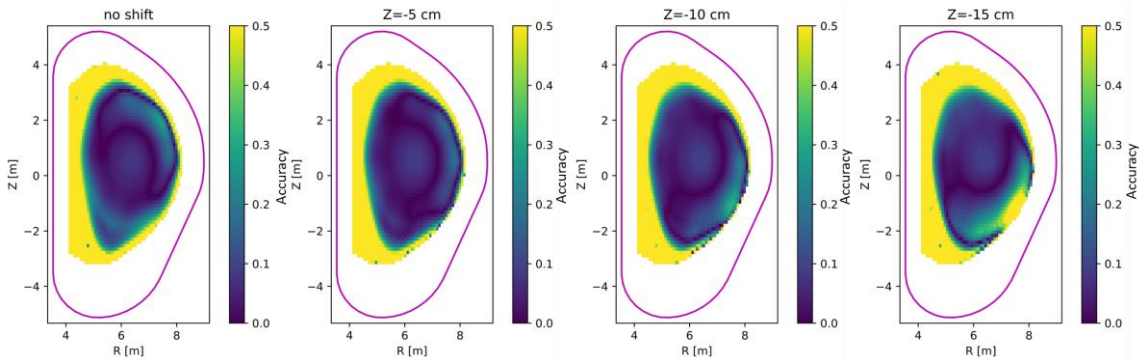

Figure 8.85. The comparison of the 2D accuracy profiles obtained with magnetic field shift along Z-axis in the negative direction for the scenario (d) and the ^{4}He scintillators in the ex-port system.

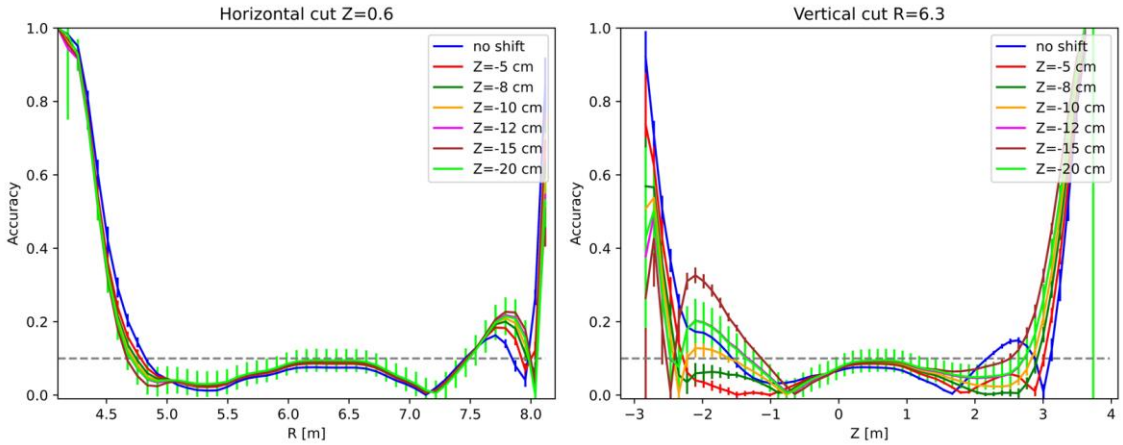

Figure 8.86. The comparison of the 1D accuracy profiles obtained with magnetic field shift along Z-axis in the negative direction for scenario (d) and the ^{4}He scintillators in the ex-port system.

The displacements in two directions have also been analysed and obtained RMS comparison is presented in table 8.9. The examples of the 2D and 1D accuracy profiles are shown in figures 8.87 and 8.88. Only shifts of 1 cm in two directions do not influence RMS. The accuracy loss is observed from 2 cm movements in negative and positive directions. The shifts of the neutron emissivity in the pixels in the plasma centre provide delusory accuracy improvement in this area. It is connected with the same effect as described for scenario (c). When the reconstructed profile is shifted, the cut goes through the area without accuracy loss. However, RMS is worse by 0.03 – 0.09 than the results obtained without disruptions.

Table 8.9. RMS calculated for the results of the tomography calculations obtained with the magnetic field displacements in two directions for the plastic scintillators and scenario (d).

Shift R	Shift Z	RMS	SD
0	0	0.38	0.11
1	1	0.38	0.09
1	-1	0.38	0.10
-1	1	0.38	0.11
-1	-1	0.38	0.12
2	2	0.42	0.09
2	-2	0.41	0.05
-2	2	0.42	0.06
-2	-2	0.41	0.10
3	3	0.42	0.07
3	-3	0.43	0.09
-3	3	0.43	0.08
-3	-3	0.42	0.12
5	5	0.44	0.08
-5	5	0.43	0.12
5	-5	0.45	0.06
-5	-5	0.44	0.08
7	7	0.47	0.12
7	-7	0.46	0.12
-7	7	0.47	0.06
-7	-7	0.45	0.10

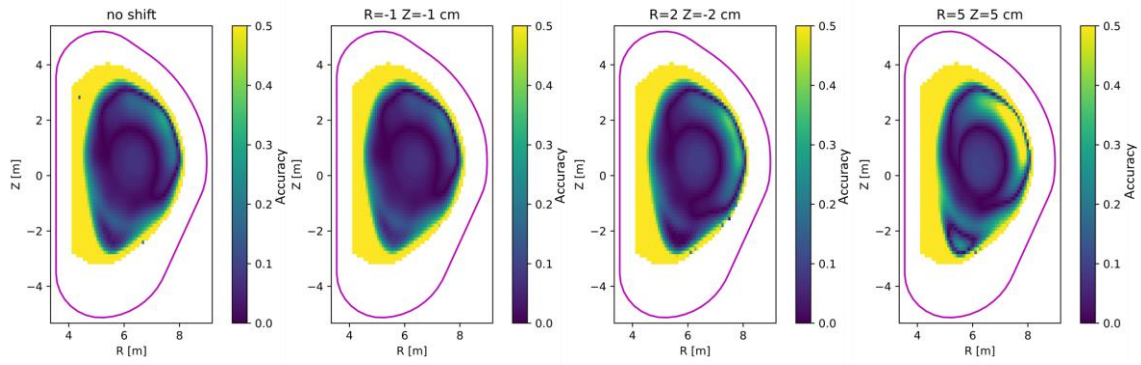

Figure 8.87. The comparison of the 2D accuracy profiles obtained with magnetic field shift along R and Z axis for scenario (d) and the plastic scintillators in the ex-port system.

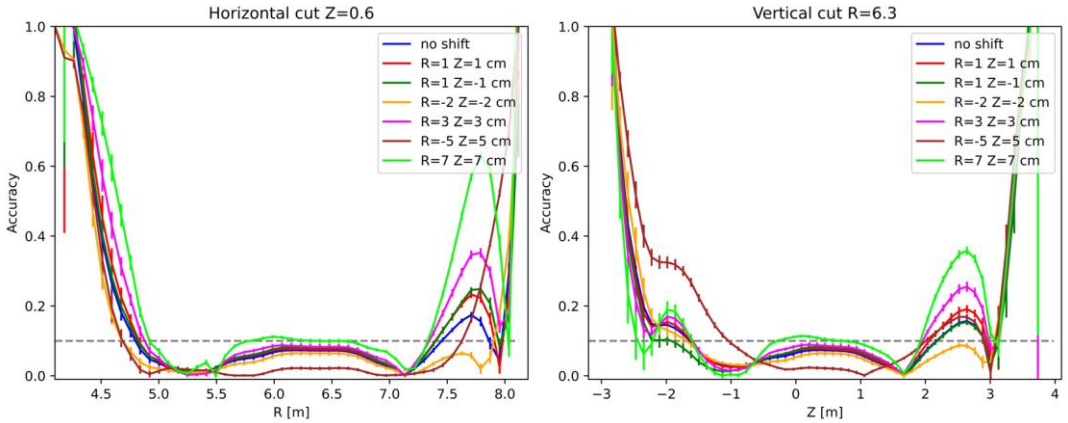

Figure 8.88. The comparison of the 1D accuracy profiles obtained with magnetic field shift along R and Z axis for scenario (d) and the plastic scintillators in the ex-port system.

The analysis was also made for scenario (e). RMS comparison for shifts in R positive direction is presented in figure 8.89. The movements up to 3 cm do not influence RMS. The 5 cm and 10 cm displacements correspond to the increases of RMS by 0.01 to 0.04. The examples of the 2D and 1D accuracy distributions are shown in figures 8.90 and 8.91. The limit of the magnetic field shift that provides an accuracy equal to 10% or better in the plasma core is 5 cm. The accuracy losses are mainly observed on LFS.

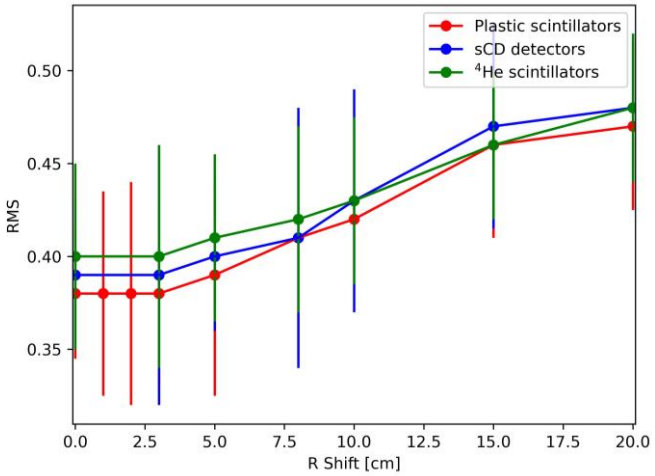

Figure 8.89. RMS for magnetic field displacement in R positive direction for scenario (e) and different types of the detectors in the ex-port camera part.

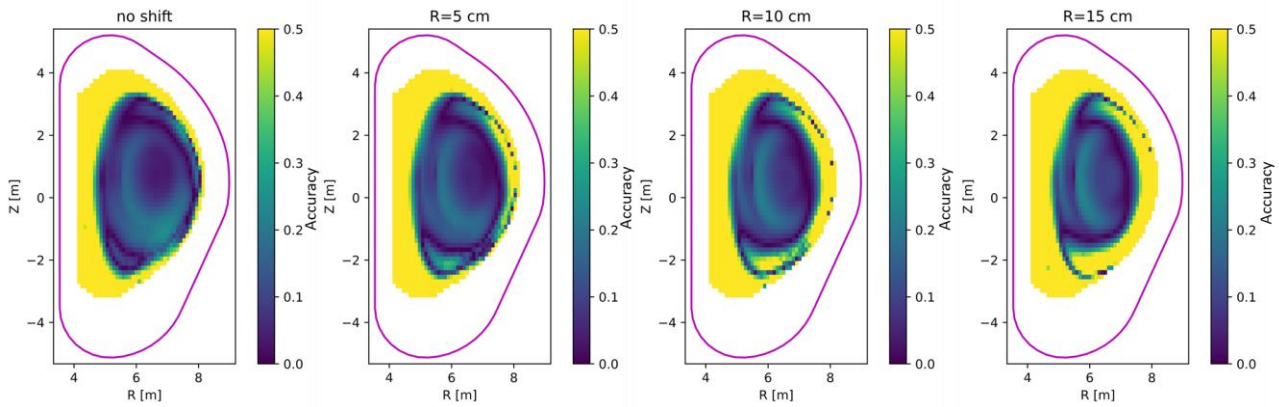

Figure 8.90. The comparison of the 2D accuracy profiles obtained with magnetic field shift along R-axis in the positive direction for scenario (e) and the ^{4}He scintillators in the ex-port system.

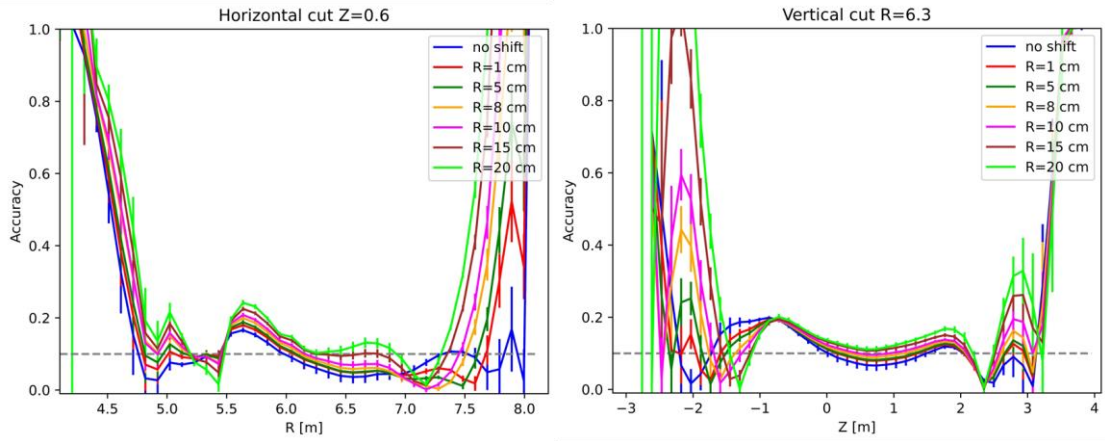

Figure 8.91. The comparison of the 1D accuracy profiles obtained with magnetic field shift along R-axis in the positive direction for scenario (e) and the ^{4}He scintillators in the ex-port system.

RMS for the negative R displacements is presented in figure 8.92. RMS rise is more rapid with the increasing length of the magnetic field movement than for the positive direction. The 1 cm shifts cause the change of RMS from 0 to 0.05. The 5 cm displacement corresponds with the increase of RMS by 0.08 to 0.10. The 2D accuracy distributions obtained for ^{4}He scintillators are presented in figure 8.93. A substantial accuracy loss is observed on LFS. The comparison of the 1D profiles is shown in figure 8.94. Only shifts larger than 15 cm do not provide the results with accuracy better than 10% in the plasma core. A very strong accuracy loss is observed on the plasma edges for displacements higher than 5 cm. The different character of the changes in the reconstruction results compared to other scenarios is connected with the magnetic field configuration with a plasma core centre closer to the outer tokamak wall.

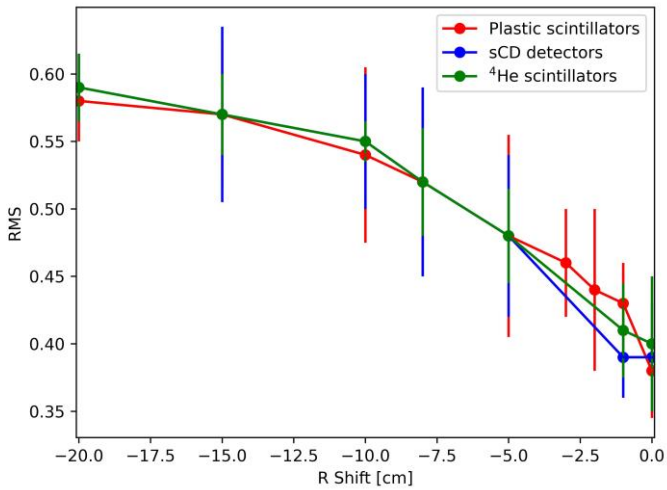

Figure 8.92. RMS for magnetic field displacement in R negative direction for scenario (e) and different types of the detectors in the ex-port camera part.

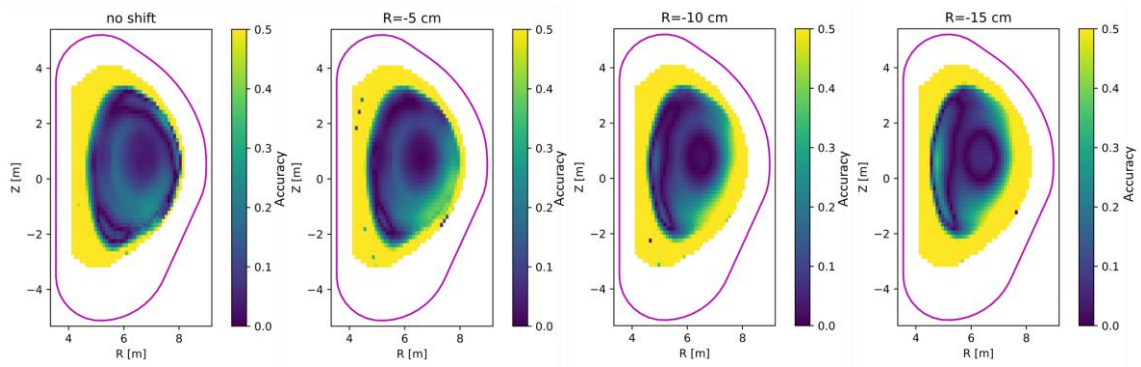

Figure 8.93. The comparison of the 2D accuracy profiles obtained with magnetic field shift along R-axis in the negative direction for scenario (e) and the ^{4}He scintillators in the ex-port system.

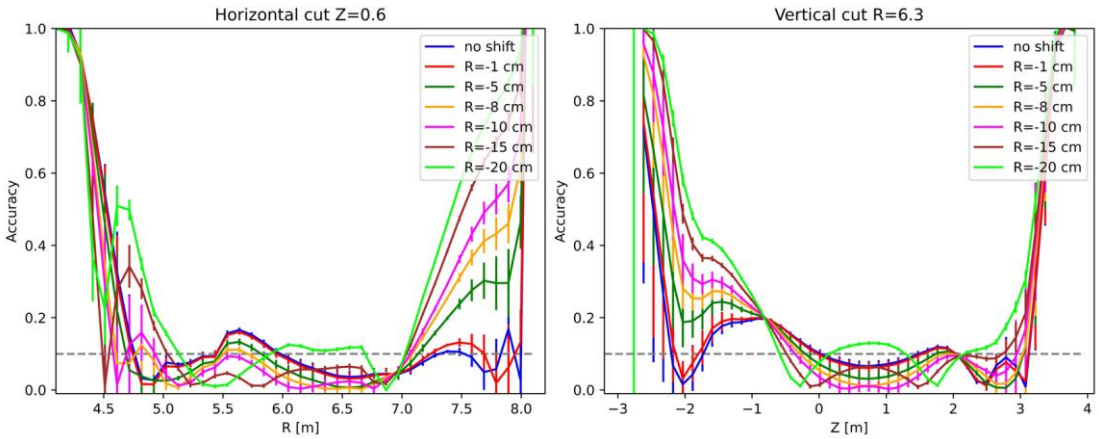

Figure 8.94. The comparison of the 1D accuracy profiles obtained with magnetic field shift along R-axis in the negative direction for scenario (e) and the ^{4}He scintillators in the ex-port system.

The comparison of RMS for the displacement along the Z-axis in the positive direction for scenario (e) is presented in figure 8.95. The changes in RMS connected with the 1 cm magnetic field shift vary from 0 to 0.01 for different detectors. RMS increase due to 5 cm and 10 cm movement is equal to 0.02 and 0.04, respectively. The 2D distributions of the reconstruction accuracy are presented in figure 8.96. The corresponding 1D accuracy profiles are shown in figure 8.97. On the horizontal cut, the accuracy loss is observed only on LFS. The same effect with

the improvement of the accuracy in the core centre with increasing shifts is noted as for scenarios (c) and (d). The accuracy losses on the plasma edges are substantial for displacements higher than 5 cm.

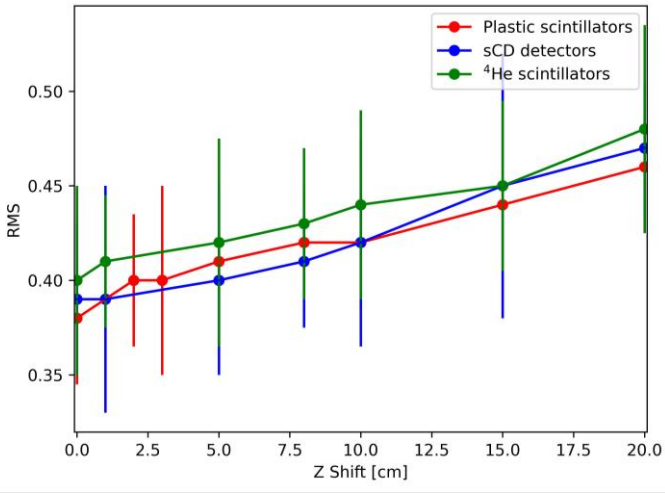

Figure 8.95. RMS for magnetic field displacement in Z positive direction for scenario (e) and different types of the detectors in the ex-port camera part.

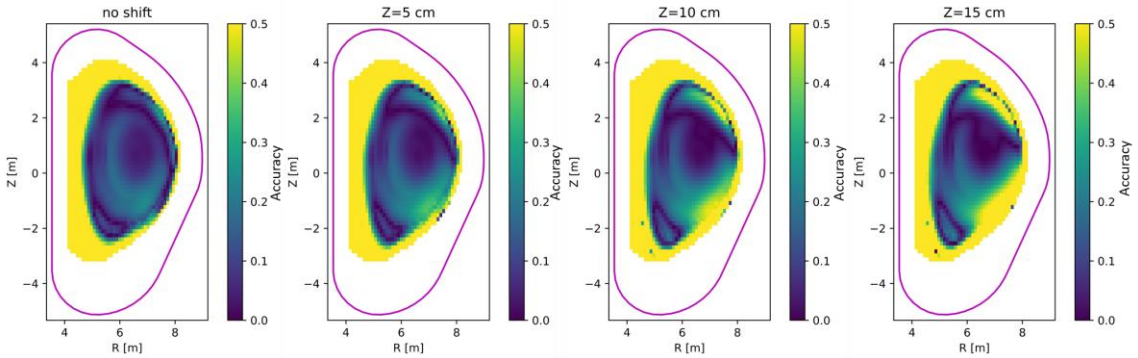

Figure 8.96. The comparison of the 2D accuracy profiles obtained with magnetic field shift along Z-axis in the positive direction for scenario (e) and the sCD detectors in the ex-port system.

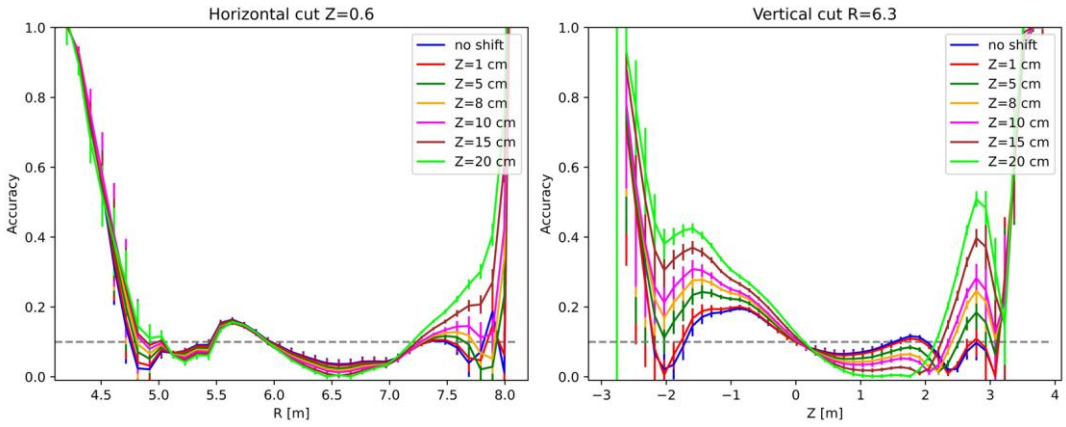

Figure 8.97. The comparison of the 1D accuracy profiles obtained with magnetic field shift along Z-axis in the positive direction for scenario (e) and the sCD detectors in the ex-port system.

RMS comparison for magnetic field displacements in Z negative direction is presented in figure 8.98. The 5 cm magnetic field movement causes RMS increase by about 0.02. The change in RMS for 10 cm displacement varies from 0.03 to 0.05. The examples of the 2D accuracy

distribution in the poloidal tokamak cross-section are presented in figure 8.99. The influence of the magnetic field shifts from 5 cm on LFS is visible. The comparison of the 1D accuracy profiles is shown in figure 8.100. On the horizontal cuts, the differences between results are negligible, but substantial variations of the results are observed on the vertical profiles. The most significant accuracy loss with the increasing magnetic field movement length occurs on the plasma's bottom.

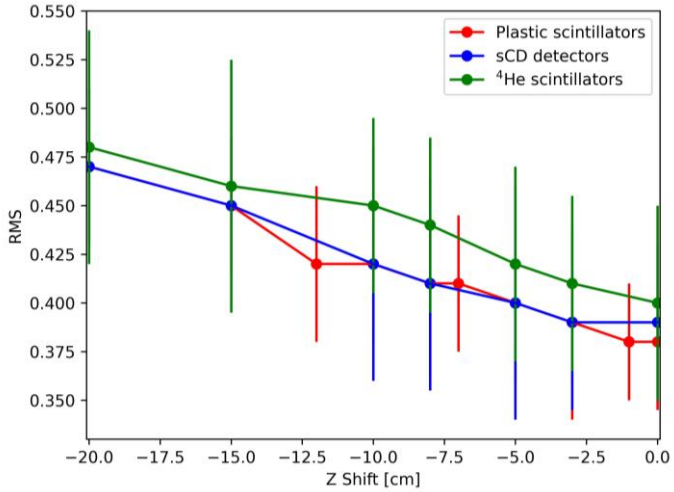

Figure 8.98. RMS for magnetic field displacement in Z negative direction for scenario (e) and different types of the detectors in the ex-port camera part.

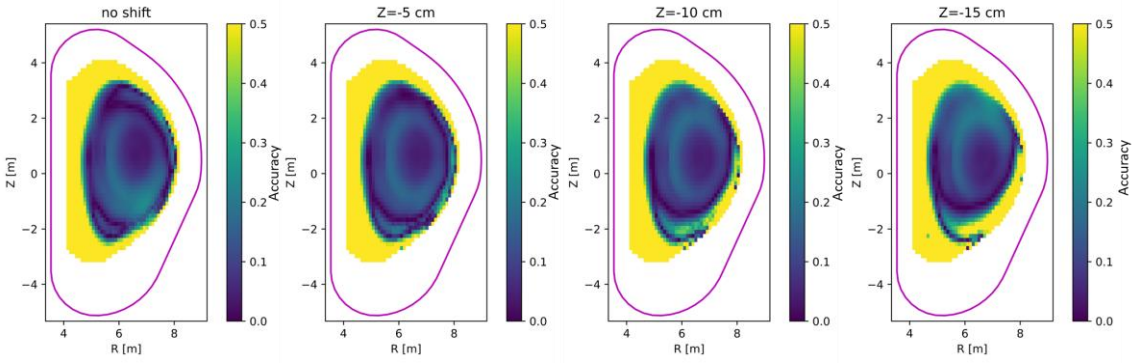

Figure 8.99. The comparison of the 2D accuracy profiles obtained with magnetic field shift along Z-axis in the negative direction for scenario (e) and the sCD detectors in the ex-port system.

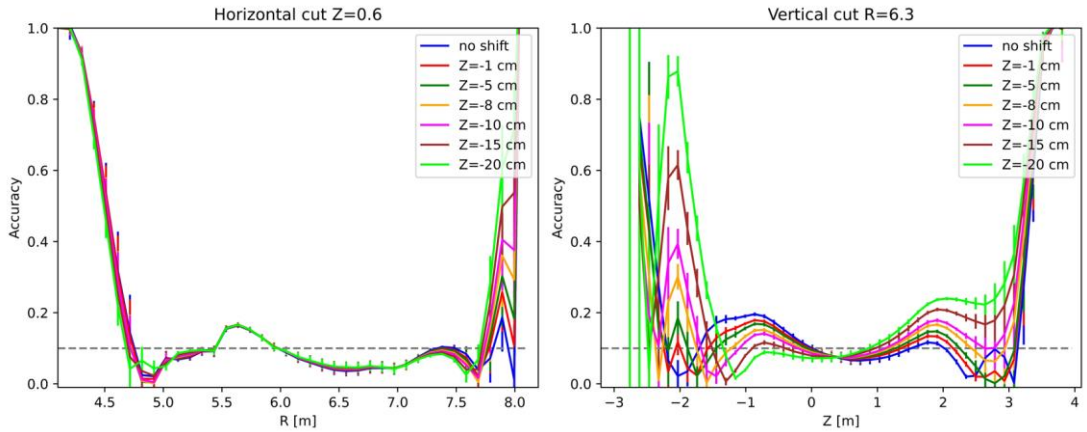

Figure 8.100. The comparison of the 1D accuracy profiles obtained with magnetic field shift along Z-axis in the negative direction for scenario (e) and the sCD detectors in the ex-port system.

The last analysed displacements concern two directions simultaneously. RMS calculated for shifts along R-axis and Z-axis is presented in table 8.10. The 1 cm movements in two directions cause an increase of RMS from 0.01 to 0.06. A stronger influence has displacement in the negative R direction with no dependence on the Z direction. The examples of the 2D accuracy distribution are presented in figure 8.101. The differences between results in the plasma core are negligible (see figure 8.102). The accuracy in the tokamak core centre is better than 10% for all cases. The acceptable accuracy loss on the edges (< 20%) is only for shifts up to 3 cm.

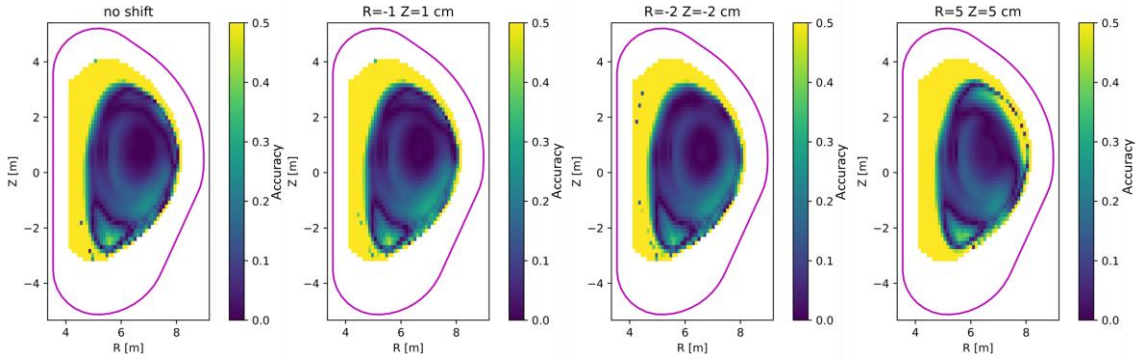

Figure 8.101. The comparison of the 2D accuracy profiles obtained with magnetic field shift along R and Z axis for scenario (e) and the plastic scintillators in the ex-port system.

Table 8.10. RMS calculated for the results of the tomography calculations obtained with the magnetic field displacements in two directions for the plastic scintillators and scenario (e).

Shift R	Shift Z	RMS	SD
0	0	0.38	0.07
1	1	0.39	0.15
1	-1	0.44	0.15
-1	1	0.39	0.10
-1	-1	0.44	0.12
2	2	0.39	0.12
2	-2	0.45	0.07
-2	2	0.39	0.11
-2	-2	0.45	0.07
3	3	0.40	0.15
5	5	0.42	0.12
-5	5	0.48	0.08
5	-5	0.42	0.10
-5	-5	0.48	0.13
8	8	0.44	0.09
-8	8	0.51	0.09
8	-8	0.44	0.07
-8	-8	0.54	0.13

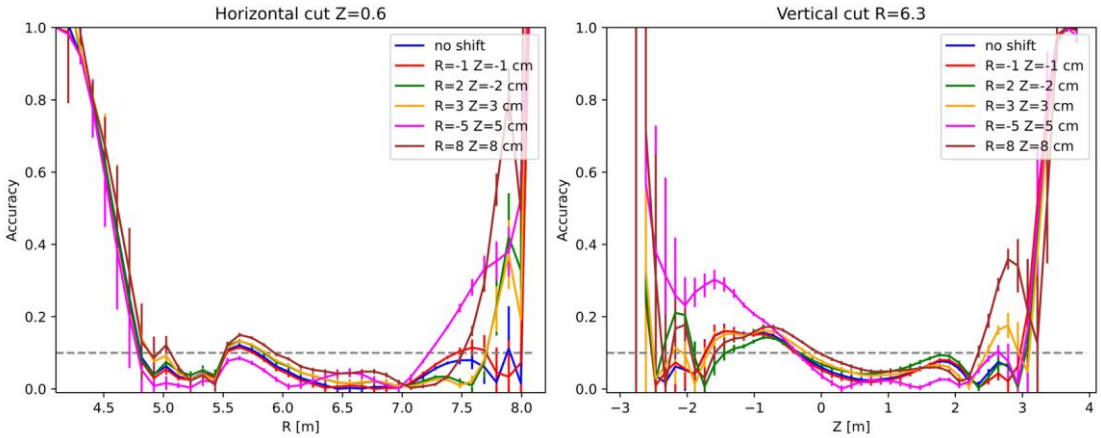

Figure 8.102. The comparison of the 1D accuracy profiles obtained with magnetic field shift along R and Z axis for scenario (e) and the plastic scintillators in the ex-port system.

The tendency of changes is reproducible despite the statistical irrelevance of the differences in RMS below 0.1. The discrepancies in RMS on the level of 0.01 – 0.02 can be observed in the 2D and 1D accuracy profiles. Therefore, the maximal displacements assumed as limits correspond to the results without RMS change with the precision of two decimal places. Only differences in RMS below 0.01 were estimated as negligible.

The level of accuracy loss due to the magnetic field displacement for the tomography reconstruction depends on the considered scenario. The trend of the changes for all detectors is the same and it is reproducible for datasets with different noises. The performed analysis showed that there are limits to the plasma shifts with respect to the camera that provide the results with an accuracy better than 10%. The required precision of the magnetic field definition and RNC positioning was settled. In general, the input used in the calculations should be established with at least 2 cm precision. All possible directions of the magnetic field displacements have different limits for substantial accuracy loss. For all scenarios, the 5 cm is the maximal shift that provides reconstruction accuracy better than 10% in the plasma core without not acceptable losses (accuracy worse than 30%) on the plasma edges. The movements along the R-axis in the negative direction in the reconstruction of scenario (c) have a lower impact on the results due to the plasma position further from the area where LOSs intersect. The changes' character for scenario (d) due to the shift length increase is similar to the effects observed for scenario (c). The plasma core centre for scenario (e) is closer to the outer tokamak wall, and movements to R positive direction cause lower changes in the calculated RMS. The displacements on the level of 10 cm can provide accuracy better than 10% in the plasma core but do not guarantee stable reconstruction in the whole plasma poloidal cross-section.

8.4.2.3 Reconstruction with magnetic field from different scenario

The following analysis aims to evaluate the tomography reconstruction capability with the input magnetic field different from the one related to the measurement. The possibility of the precise reconstruction of neutron emissivity if the magnetic field configuration is miscalculated during the experiment was investigated. The calculations were done for count rates connected with scenarios (c), (d), and (e) and sequentially with all magnetic field configurations. The character of the changes for three detectors has been analysed by swapping the input files, e.g. in tomography with synthetic data obtained for scenario (c), the magnetic file configuration for scenario (d) was used. The optimal smoothing parameters Ω selected for each scenario in subchapter 8.4.2.1 was considered in the calculations. Furthermore, the influence of the magnetic field configuration resolution was studied by adding scenario (a), which was defined with significantly higher precision than others.

An example of the comparison of the results obtained for simulated data for the plastic scintillators and scenario (c) with all magnetic field configurations used in the tomography is presented in figure 8.103. The horizontal and vertical cuts of the accuracy are shown in figure 8.104. In the upper part of the plasma, the accuracy loss is not observed for the reconstruction with scenarios (a) and (d). In this area, the magnetic field lines are very dense, and artefacts presented in the input files with low resolution disrupt the reconstruction. The absence of the nonphysical lines related to the interpolation issues improves the accuracy in this region. The discrepancy between magnetic field configuration for scenarios (c) and (e) is the highest. Therefore, the accuracy loss is observed in the whole plasma poloidal cross-section for the result obtained with the magnetic field input from scenario (e). Table 8.11 presents RMS for three detectors. The differences in RMS are statistically irrelevant in comparison to the standard deviations, but accuracy losses are observed in the 2D and 1D plots.

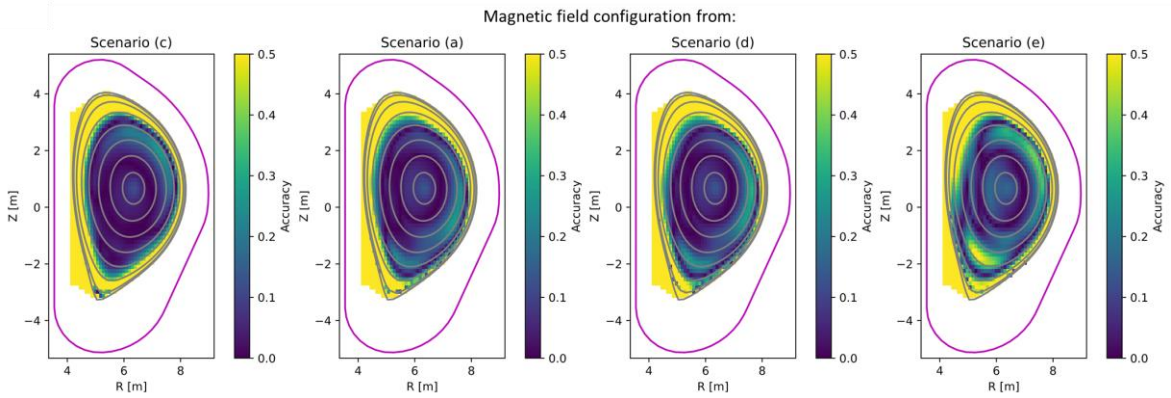

Figure 8.103. The accuracy of the neutron emissivity reconstruction obtained for simulated data related to scenario (c) and the plastic scintillators with different magnetic field configurations and the smoothing parameter equal to 10.

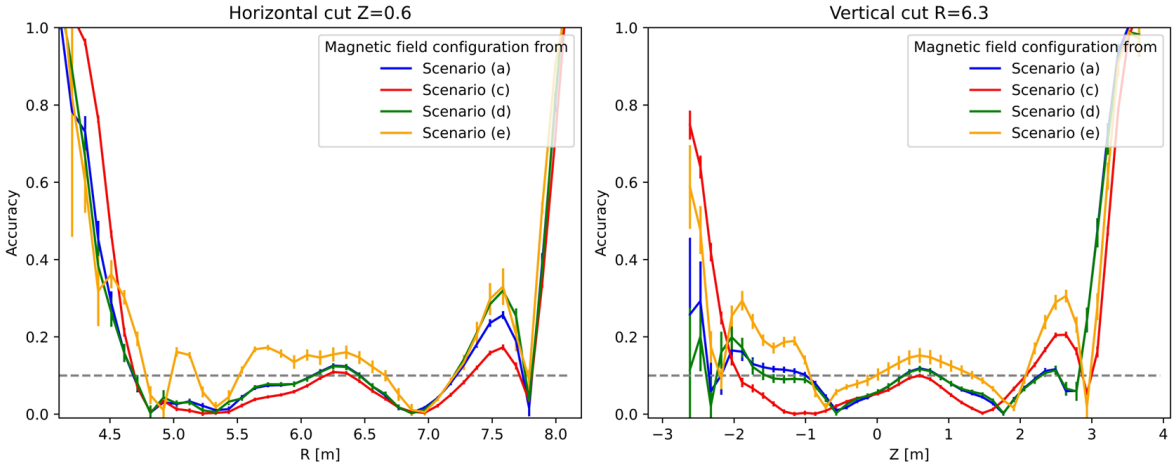

Figure 8.104. The comparison of the 1D accuracy profiles horizontal (left) and vertical (right) obtained for simulated data related to scenario (c) and the plastic scintillators with different magnetic field configurations and the smoothing parameter equal to 10.

Table 8.11. RMS for the tomography reconstruction results obtained for simulated data related to scenario (c) and three types of the detectors with different magnetic field configuration.

Plastic scintillators			sCD detectors			^{4}He scintillators		
Magnetic field	RMS	SD	Magnetic field	RMS	SD	Magnetic field	RMS	SD
(c)	0.38	0.10	(c)	0.40	0.08	(c)	0.40	0.10
(a)	0.39	0.11	(a)	0.42	0.13	(a)	0.43	0.09
(d)	0.39	0.11	(d)	0.41	0.07	(d)	0.42	0.08
(e)	0.40	0.12	(e)	0.42	0.08	(e)	0.43	0.09

The two-dimensional maps of the accuracy obtained for scenario (d) and the sCD detectors with different magnetic field configurations are presented in figure 8.105. The corresponding 1D profiles are shown in figure 8.106. The accuracy loss is the most significant for the tomography calculations using the magnetic field from scenario (e). In the case of the input from scenario (c), the bottom and top plasma part is reconstructed with a precision worse of 10% - 30%, but the accuracy is the lowest in the plasma core centre. It can be connected with the definition of the first magnetic flux surface. Scenarios (d) and (a) have similar magnetic lines distribution in plasma, but the second one is defined with much higher precision. Therefore, a small reduction of the accuracy loss on LFS due to the absence of artefacts in the magnetic field configuration is observed. The comparison of RMS calculated for all types of detectors in this case is presented in table 8.12. For plastic and ^{4}He scintillators, the lowest RMS is for scenario (a). It is connected with a high-resolution magnetic field without artefacts. The tomography reconstruction with this magnetic field for the sCD detectors has RMS higher by 0.02. RMS for other results is higher than obtained with the same magnetic field as used in the count rates simulation, but the differences are smaller than standard deviations.

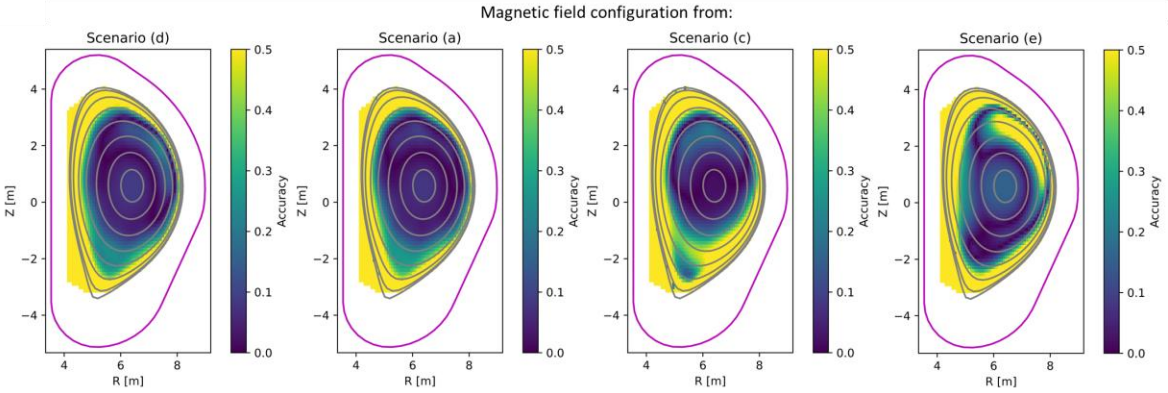

Figure 8.105. The accuracy of the neutron emissivity reconstruction obtained for simulated data related to scenario (d) and the sCD detectors with different magnetic field configuration and the smoothing parameter equal to 10.

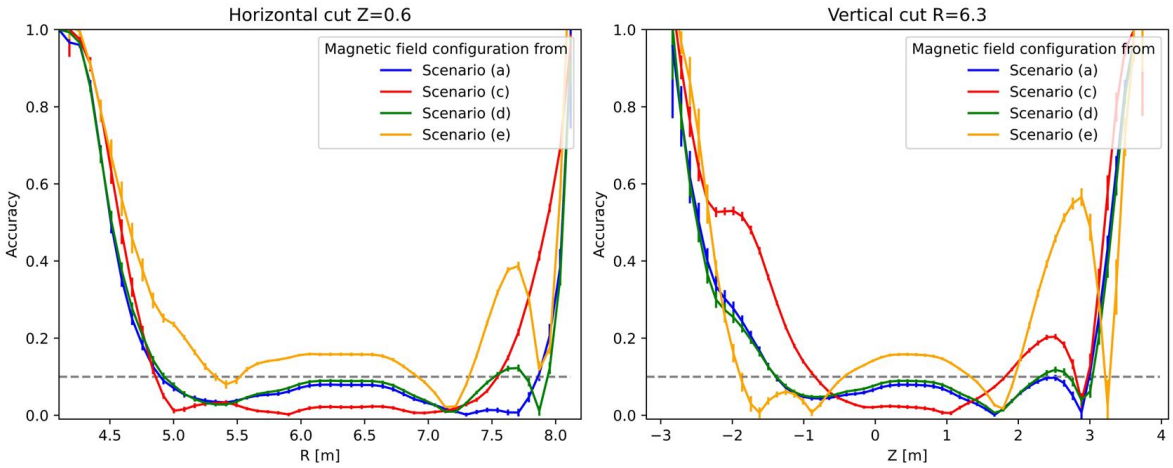

Figure 8.106. The comparison of the 1D accuracy profiles horizontal (left) and vertical (right) obtained for simulated data related to scenario (d) and the sCD detectors with different magnetic field configurations and the smoothing parameter equal to 10.

Table 8.12. RMS for the tomography reconstruction results obtained for simulated data related to scenario (d) and three types of the detectors with different magnetic field configurations.

Plastic scintillators			sCD detectors			^{4}He scintillators		
Magnetic field	RMS	SD	Magnetic field	RMS	SD	Magnetic field	RMS	SD
(d)	0.38	0.08	(d)	0.44	0.08	(d)	0.43	0.11
(a)	0.28	0.14	(a)	0.46	0.15	(a)	0.42	0.12
(c)	0.45	0.11	(c)	0.51	0.11	(c)	0.48	0.12
(e)	0.40	0.13	(e)	0.47	0.05	(e)	0.44	0.09

The comparison of the tomography reconstruction accuracy obtained with simulated data for scenario (e) and the ^{4}He scintillators with different magnetic field configurations is presented in figure 8.107. The corresponding horizontal and vertical 1D profiles are shown in figure 8.108. All considered magnetic fields provide the tomography reconstruction with an accuracy better than 10% in the centre of the plasma core. The improvement of the neutron emissivity reconstruction in the central magnetic flux surface is connected with the higher resolution of magnetic configuration definition. The comparison of RMS obtained for scenario (e) and three different detector types is presented in table 8.13. The results obtained with scenario (e) have RMS lower than others, at least by 0.1, which is statistically relevant. The differences between RMS calculated for reconstructed neutron emissivity profiles with other magnetic fields varies from 0.01 to 0.03. The worst result was obtained with magnetic field configuration from scenario (a).

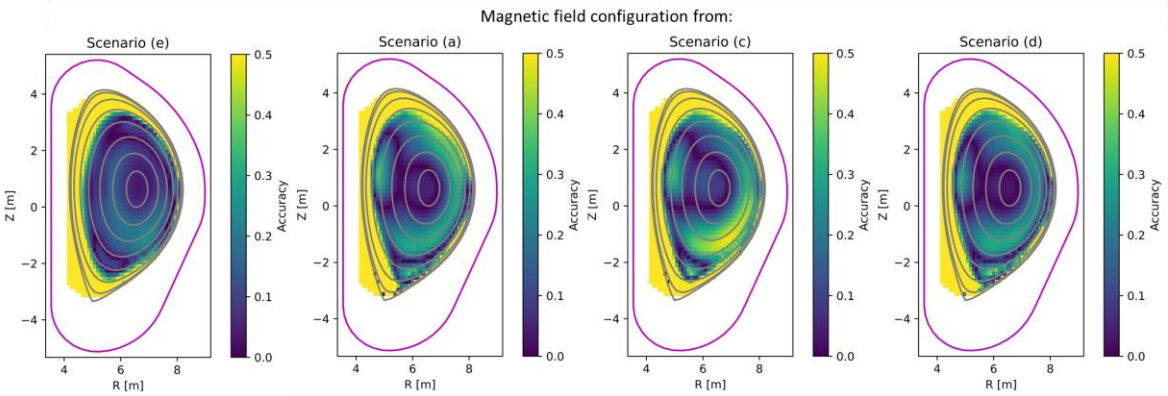

Figure 8.107. The accuracy of the neutron emissivity reconstruction obtained for simulated data related to scenario (e) and the ^{4}He scintillators with different magnetic field configurations and the smoothing parameter equal to 5.

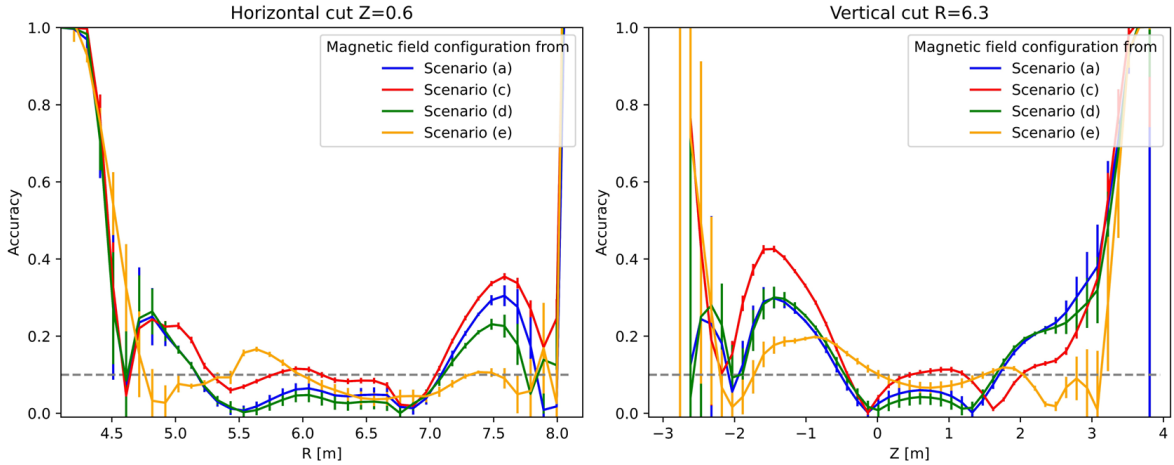

Figure 8.108. The comparison of the 1D accuracy profiles horizontal (left) and vertical (right) obtained for simulated data related to scenario (e) and the ^{4}He scintillators with different magnetic field configurations and the smoothing parameter equal to 5.

Table 8.13. RMS for the tomography reconstruction results obtained for simulated data related to scenario (e) and three types of the detectors with different magnetic field configurations.

Plastic scintillators			sCD detectors			^{4}He scintillators		
Magnetic field	RMS	SD	Magnetic field	RMS	SD	Magnetic field	RMS	SD
(e)	0.40	0.08	(e)	0.39	0.06	(e)	0.38	0.07
(a)	0.53	0.07	(a)	0.52	0.08	(a)	0.52	0.08
(c)	0.52	0.08	(c)	0.51	0.12	(c)	0.51	0.09
(d)	0.50	0.09	(d)	0.49	0.07	(d)	0.49	0.07

The level of the accuracy loss in the reconstruction caused by the not correctly defined magnetic field used in the calculation depends on the scenario and the difference between magnetic flux surfaces distribution in the plasma. The comparison of the results for the scenarios with similar magnetic field configurations shows that the resolution of the used data significantly influences the tomography. When the differences in the magnetic field configurations are significant, the precision does not affect the character of the changes in the accuracy. The differences in RMS obtained for different magnetic field configurations are mostly statistically irrelevant, but the accuracy losses are observed in the 2D and 1D plots. The accuracy of data

processing required by ITER Organisation from RNC was obtained in tomography calculations even if an input magnetic field differs from the one used in the measurement simulation. The MFR method is very sensitive to the magnetic field configuration, but it was proven that the precise neutron emissivity in the plasma core could be obtained even if the magnetic field is not correctly defined what can happen in the experiment. The analysed disruption in the magnetic field configuration covered the most important operation scenarios for ITER. The possibility of achieving the required 10% accuracy is independent of these types of errors connected with the data processing not related to RNC itself.

Chapter 9: Analysis of the neutron emissivity profiles on JET during the DT Campaign

In 2021, the DT Campaign DTE2 (C41) on JET tokamak took place. The first deuterium-tritium experiment, DTE1, was carried out in 1997. Fusion power production up to 16 MW was achieved. One of the main DTE1 goals was to study the retention and removal of hydrogen isotopes. The tritium accumulation in the tokamak components is a critical safety issue for ITER. During the DTE1 campaign, JET was equipped with carbon PFCs, and co-deposition was found as the dominant retention mechanism [Loa2013]. The study of the isotopes effect showed a reduction of the H-mode threshold power inversely proportional to effective mass. The results from DTE1 have been used for confinement scaling calculations [Wei2014]. During the campaign, the ICRH heating scenarios were rehearsed. The heating schemes gave tritons enough energy for super thermal reactions domination in fusion reactivity [Sta1999]. In the first DT campaign, the studies of the alpha particles were not possible due to a lack of neutron and gamma rays diagnostics. The experiments during DTE1 left many open questions, and the next deuterium-tritium campaign was required, especially for fusion reactors [Wei2014]. The second DT campaign on JET allowed studying fusion physics and test technologies before ITER operation. JET operates currently with the ITER-like wall made of beryllium and the tungsten divertor. The scientific goals of the campaign were:

- Demonstration of production up to 15 MW fusion power sustained for 5 s,
- Demonstration of the plasma scenarios in conditions relevant for ITER,
- Study of the alpha particle physics,
- Analysis of the isotope effects on particle and energy transport, e.g., density peaking, fuel composition control, confinement, power exhaust, and detachment,
- Investigation of the plasma-wall interactions (e.g. impurity source, tritium retention),
- Demonstration of the heating schemes relevant for ITER.

The relevant conditions correspond to very high temperatures and densities that lead to the study of new plasma physics issues. Now, JET is equipped with advanced diagnostics, providing the data for theoretical models. The demonstration of the ITER scenarios includes the baseline and the hybrid H-mode.

The neutron measurements are crucial for investigating the fusion reaction and ions transport. The neutron rate on JET is monitored by three pairs of fission chambers (FCs). The detectors are located in Octants 2, 6 and 8. The fission chambers containing ^{235}U and ^{238}U are positioned in the midplane in moderator packages. The FCs operate in counting and current modes [Sym2014]. The total neutron yield per second is calculated based on the calibration [Bat2018] and archived in the database. The value concerns neutrons from both DT and DD reactions. The uncertainty of the provided yield is equal to 10%. JET is equipped with the neutron activation system [Pro2011], the time-of-flight spectrometer TOFOR [Joh2008] and the neutron emission spectroscopy diagnostics [Gia2005]. This thesis focuses on the data analysis from the neutron camera described in the following subchapter.

The results of tomography analysis can be improved by applying the additional constraints connected with the approximations appropriate for thermal plasma to the calculations. The magnetic field configuration was calculated based on the poloidal flux distribution provided by EFIT code [Bri2008]. The supplementary information allows obtaining a realistic solution with the discrepancy between physics in auxiliary heating plasma and simplification used in calculations. The fission chambers provide the total neutron yield on JET. The ion temperature, which can be used to calculate the relative reactivity distribution in the tokamak, is measured by Charge Exchange Recombination Spectroscopy (CXRS). The diagnostic is based on injecting of the neutral atoms into the plasma. The atoms exchange charge with plasma species and end up in an excited state. The photons emitted due to relaxation are observed [Mer2019]. The ion temperature is determined based on Doppler broadening of the emission lines. Additionally, plasma rotation is established from the Doppler shift and impurity densities from line intensities.

The diagnostics consist of two periscopes with 44 viewing lines each and three views from the vessel top. Figure 9.1. presents the system schematic view. The periscopes are equipped with aluminium-coated nickel mirrors and fused silica telecentric lenses that image the plasma onto optical fibres. The visible radiation is transmitted to the spectrometers, CCD cameras and Czerny-Turner spectrometers. The time resolution is from 10 to 50 ms. The neutral beams are 2 - 3 m from the mirrors. The intersection of the beams with viewing paths defines measurement volumes that are inclined cylinders. The typical width of the paths is 5 cm. The position of the viewing line has been calibrated with lasers. The intensity calibration was made with a standard lamp placed in front of the periscope [Neg2006]. The result of the CXRS measurement of this thesis interest is the ion temperature profile given in eV with an uncertainty of 5-10%. Before the reconstruction, values are projected on the pixel grid according to magnetic field configuration. The profiles are symmetric due to the measurement results representation in function of radial tokamak coordinate (*r*). Based on the ion temperature in the pixel, the normalised reaction rate is calculated and added as a supplementary constraint to the tomography analysis.

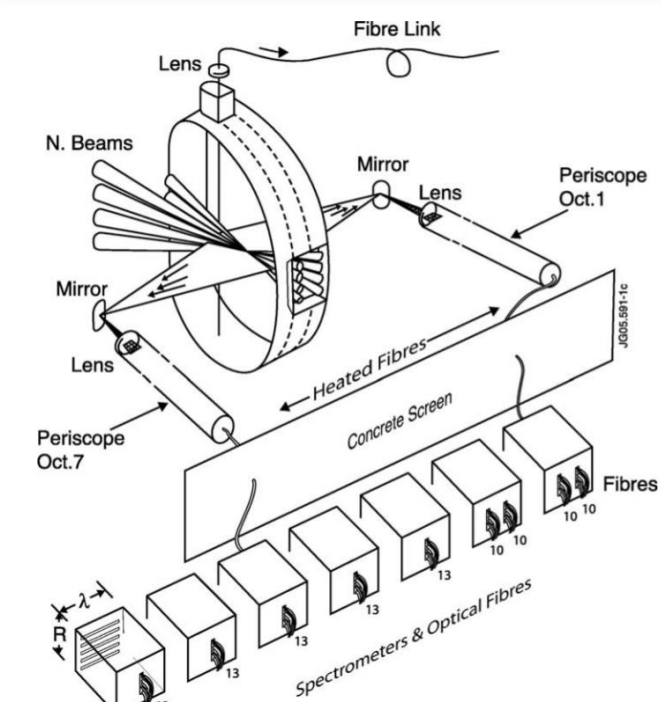

Figure 9.1. The CXRS diagnostic on JET tokamak [Neg2006].

As an introduction in subchapter 9.2, the influence of the application of the additional constraints is described. The final tomography analysis has been performed for two scientific research topics. In subchapter 9.3, results for the hybrid scenario are presented. The reconstructions for the baseline scenario discharges are reported in subchapter 9.4.

9.1 Diagnostic description

The neutron camera on JET consists of two multi-collimator arrays (see figure 9.2.). The horizontal part comprises ten collimators of length from 1.15 m to 1.20 m and diameter equal to 1.1 cm. The nine collimators in the vertical part have a length from 1.36 m to 1.39 m and a diameter from 5 mm to 1.1 cm. The size of the collimators increases towards the right side [Private communication with D. Marocco]. The camera geometry provides similar viewing efficiency for each LOS and complete coverage of the plasma cross-section. The spatial resolution in the core is about 12 cm. The removable detector boxes are placed in high-density concrete

shielding [Ada1993]. All collimators are equipped with two neutron detectors. The liquid scintillators NE213 are prepared to detect 2.5 MeV neutrons and low emission of 14.1 MeV neutrons. The energy window for DD neutrons measurement is 1.8 – 3.7 MeV. The DT neutrons are detected with a threshold equal to 8 MeV. The plastic scintillators Bicron BC418 are designed to monitor DT reaction products in intense fluxes of DD neutrons. Their energy threshold is equal to 10 MeV. The time resolution of the camera is 10 ms. The upgrade of the data acquisition system allows analysis of the neutron energy based on the recorded signals. The detectors have been coupled with Field Programmable Gate Arrays (FPGA)-based digital acquisition system that allows for 200 MS/s sampling rate and pulse high spectra analysis [Riv2017]. The background in the measurement consists of gamma radiation and neutrons scattered in the tokamak vessel and camera surroundings [Bin2018]. The impact of gamma radiation is reduced with pulse shape discrimination analysis for NE213 scintillators [Riv2014]. In the BC418 detectors, gamma rejection is due to threshold selection. The influence of scattered neutrons is lowered by a set of high energy thresholds for neutron detection. The backscattering effects are simulated as 8% - 24% of total emission for DD plasma [Bin2017]. The high threshold for Bicron detectors reduces the impact from backscattered neutrons to a negligible level.

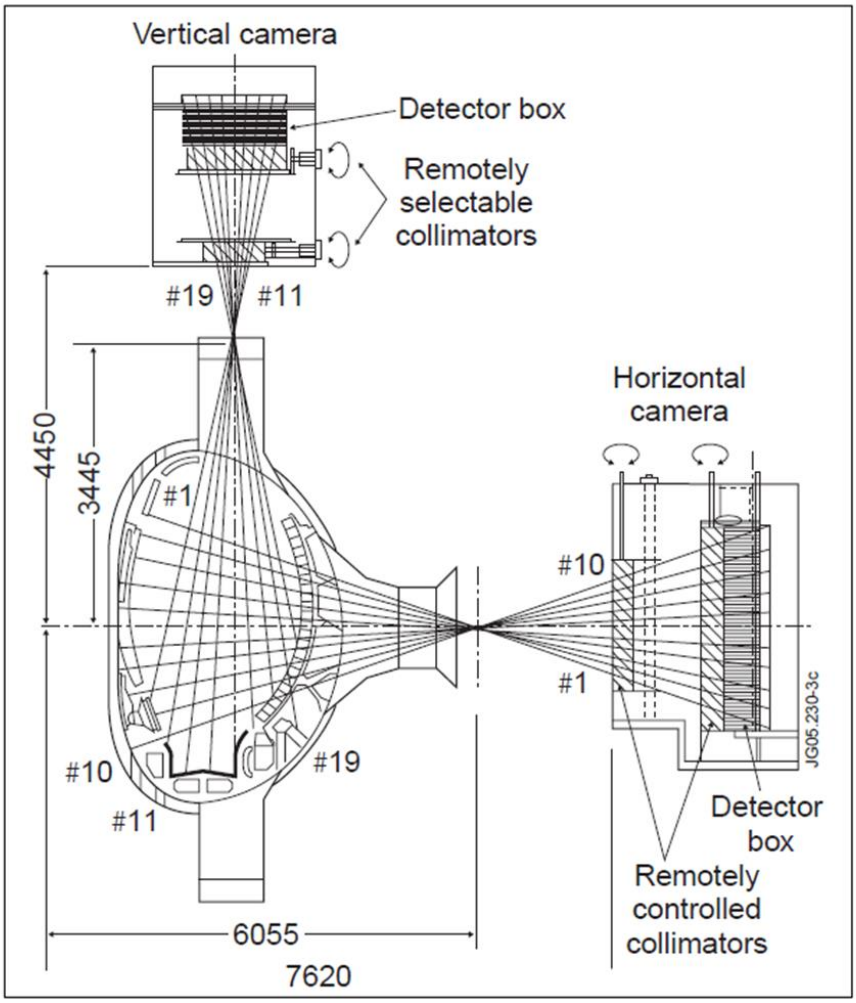

Figure 9.2. JET neutron camera layout [Mur2005].

9.2 Investigation of the influence of the additional constraint on the reconstruction results

At first, the total neutron yield influence on the tomography result was investigated. This additional constraint, in general, does not affect the shape of the neutron profiles. The examples of comparisons of the tomography results are presented in figures 9.3 (discharge #99510 is described in detail in subchapter 9.3) and 9.4 (discharge #99945 is described in detail in subchapter 9.4). The difference in the neutron emissivity distribution is not observed. The additional constraint in the analysis of the data simulated for ITER improves the absolute value of neutron emissivity. The same effect is expected for the JET neutron emissivity reconstructions.

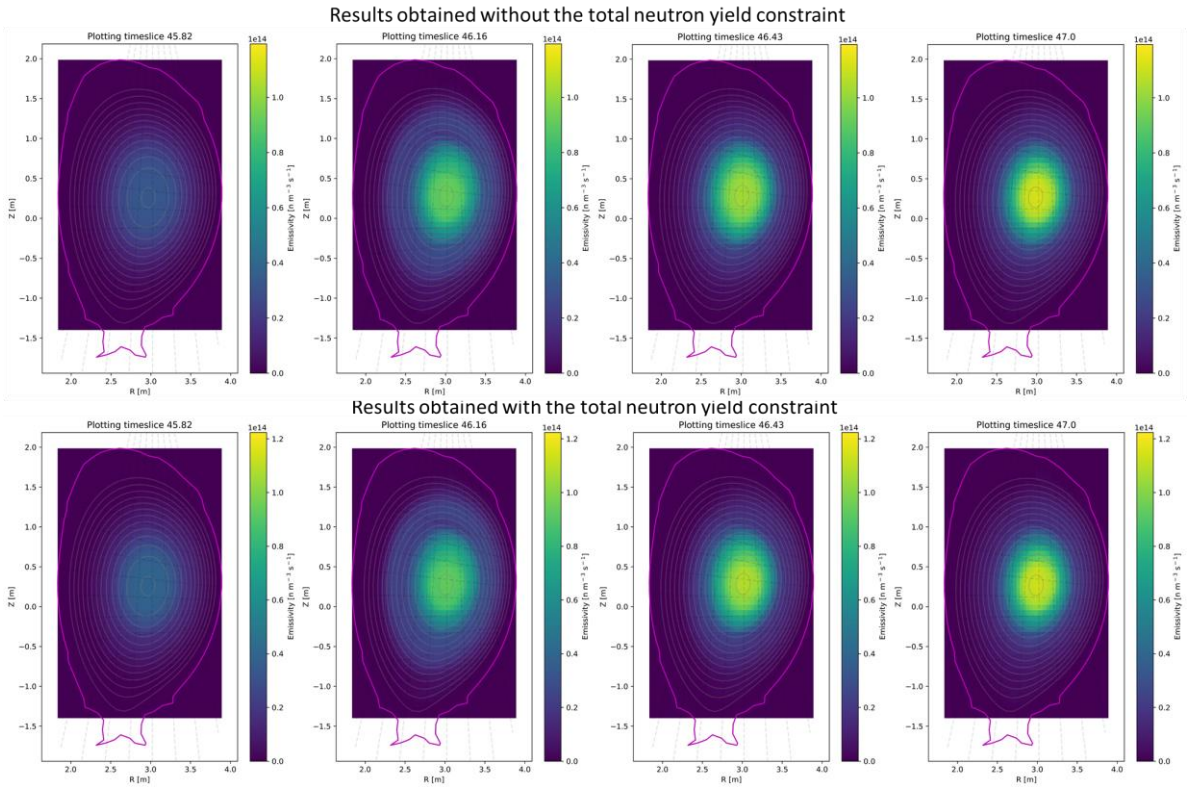

Figure 9.3. Comparison of the neutron emissivity distribution obtained for discharge #99510 with and without the total neutron yield constraint added to the calculations.

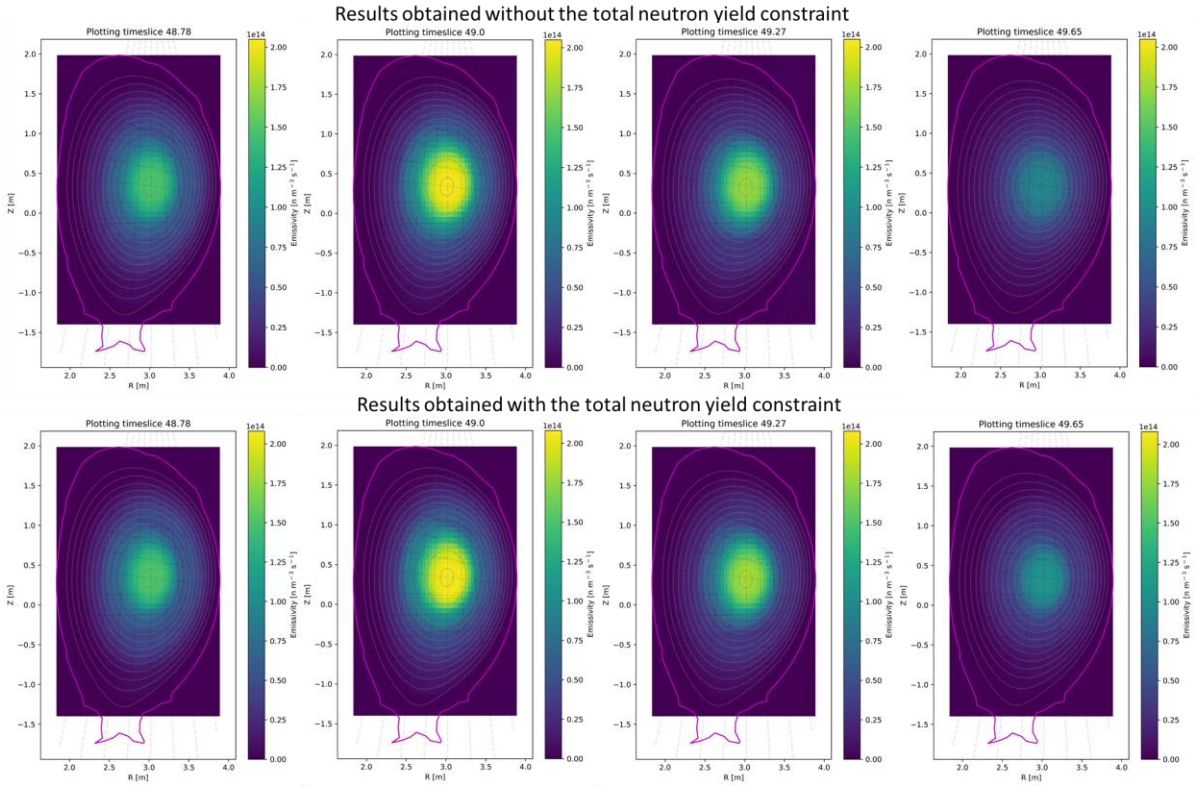

Figure 9.4. Comparison of the neutron emissivity distribution obtained for discharge #99945 with and without the total neutron yield constraint added to the calculations.

The total neutron yield measured by FCs is the DT and DD neutrons sum. The data used in the tomography reconstruction concerns only 14.1 MeV neutrons. Therefore, the value obtained from the integration over the reconstructed plasma emissivity is smaller than the total neutron yield originating from the independent monitors. The variations of this parameter in time should be similar because the DT neutrons dominate the number of the total neutrons. Due to the huge differences in the absolute values, comparing the functions of the neutron yield in time is difficult. The normalised neutron rates have been calculated and presented in figures. RMS of the disagreement between the normalised values has been found as an appropriate coefficient for evaluating the reconstructed shape. Two kinds of RMS have been introduced as figures of merit in the comparison of the results:

$$RMS_a = \sqrt{\frac{1}{o}\sum_t \left(\frac{Y_{nt} - RY_{nt}}{Y_{nt}}\right)^2}, \tag{9.2.1}$$

$$RMS_n = \sqrt{\frac{1}{o}\sum_t \left(\frac{NY_{nt} - NRY_{nt}}{NY_{nt}}\right)^2}, \tag{9.2.2}$$

where t is index that numerate the time slice, Y_n is the total neutron yield measured by the fission chambers, RY_n is the reconstructed total neutron yield from the tomography calculations, NY_n is the normalised total neutron yield to the highest value for the particular discharge measured by FC, and accordingly RNY_n is the reconstructed normalised total neutron yield to the maximal value obtained in the tomography.

The accuracy of the reconstructed 2D neutron emissivity distribution have been evaluated by comparison of the experimental data and retrofit which is defined as:

$$\overrightarrow{Retrofit} = \boldsymbol{G} \cdot \vec{m}'. \tag{9.2.3}$$

The reconstructed total neutron yields obtained with and without the additional constraint for reference baseline deuterium discharges (their parameters are described in subchapter 9.4) have been compared in figures 9.5 and 9.6. The neutron rate is overestimated in the tomography calculations for both cases. The calibration should compensate for the differences between the threshold energies, geometry, and background in the neutron camera detectors and the fission chambers. Therefore, the absolute values of the total neutron yield are expected to be at least the same order of magnitude, which is not valid. The reason can be not correctly calibrated measurement data for both diagnostics. The tomography without the additional constraint gave RMS_a lower than the reconstruction after its application (see table 1). The shape of the total neutron yield as the function in time obtained with the additional constraint has RMS lower by 0.001, which is a statistically irrelevant result. The positive impact of the additional constraint on neutron tomography for JET is not observed like for ITER. It can be connected with the more complicated nature of the emission in the nonthermal plasma that was not taken into account during geometry matrix preparation. It would require an analysis by sophisticated transport codes that is not the subject of this thesis. The relative changes in the neutron emissivity intensity in time have been reconstructed correctly. Therefore, the problem of the tomography calculation refers only to the absolute values estimation.

The examples of comparing the reconstructed total neutron yields with and without the additional constraint applied to the tomography calculations for the DT plasma with the experimental data are presented in figures 9.7 (discharge #99520 is described in detail in subchapter 9.4) and 9.8 (discharge #99949 is described in detail in subchapter 9.3). Two kinds of RMS calculated for all analysed discharges are presented in table 9.1. RMS for absolute values of the neutron rate varies from 0.92 to 0.97. The RMS_a obtained with additional constraint are lower for all discharges, but the difference is negligible (0.001 – 0.004). The shape of the function in time is reproduced for all discharges. The RMS_n varies from 0.07 to 0.53. Half of the results obtained with the total neutron yield constraint have lower RMS than reconstruction made without it. It is impossible to distinguish which tomography calculations better reproduce the neutron rate fluctuations in time.

The total neutron yield constraint does not influence the spatial distribution of the reconstructed neutron emissivity in JET deuterium-tritium plasma. The reconstructed total neutron yield is slightly better for results with additional constraint but is underestimated in all discharges. The discrepancy can be connected with the differences in the neutron energies measured by the neutron camera detectors and fission chambers as well as the geometry matrix definition based on the estimation of isotropic emission in a single pixel. The results presented in the following subchapter have been obtained without the additional constraint because it does not significantly influence the tomography reconstruction.

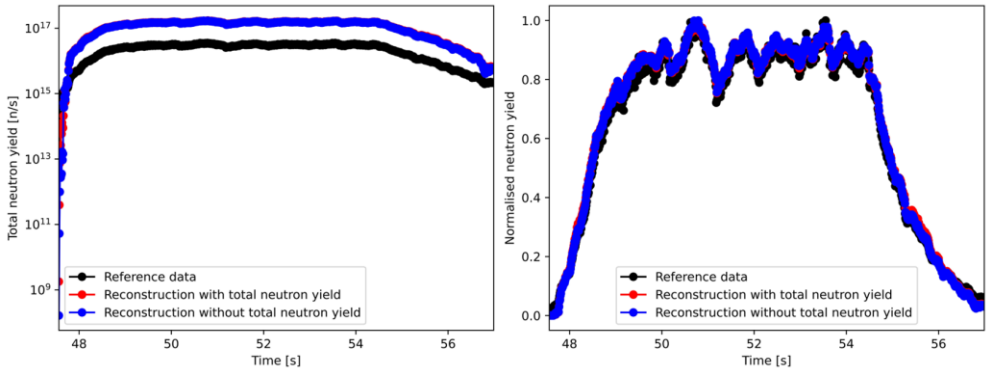

Figure 9.5. Comparison of the reconstructed total neutron yield obtained in calculations with and without the additional constraint for discharge #96994 with values measured by the fission chambers (left side – comparison of the absolute values, right side – comparison of the changes dynamics).

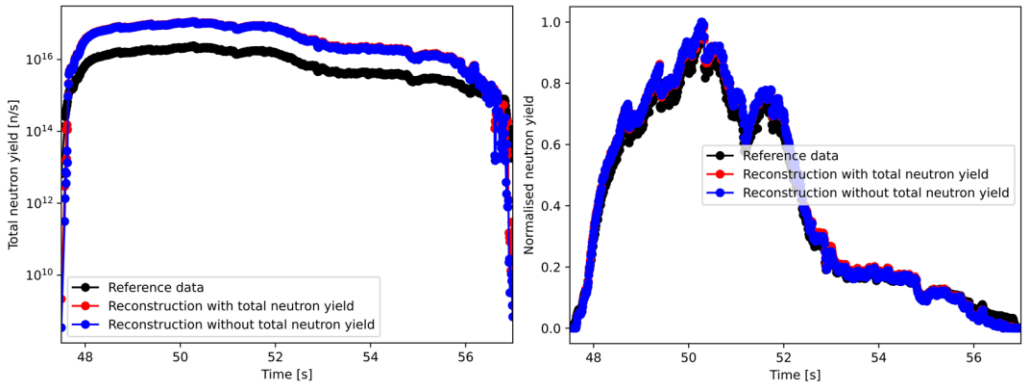

Figure 9.6. Comparison of the reconstructed total neutron yield obtained in calculations with and without the additional constraint for discharge #97995 with values measured by the fission chambers (left side – comparison of the absolute values, right side – comparison of the changes dynamics).

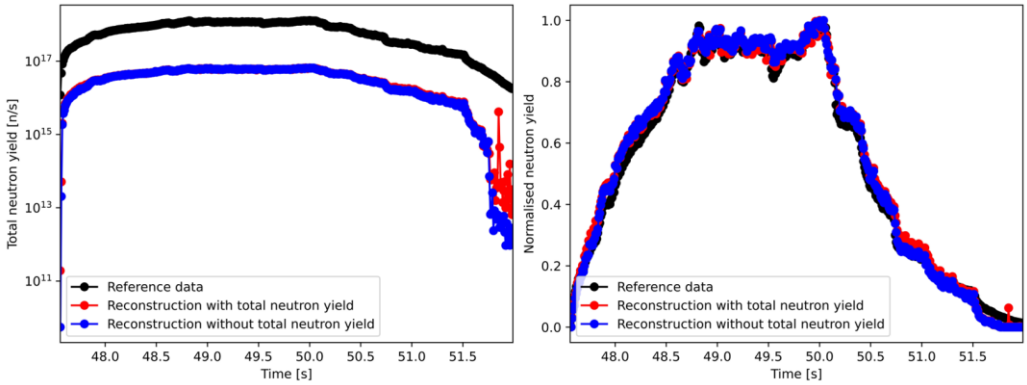

Figure 9.7. Comparison of the reconstructed total neutron yield obtained in calculations with and without the additional constraint for discharge #99520 with values measured by the fission chambers (left side – comparison of the absolute values, right side – comparison of the changes dynamics).

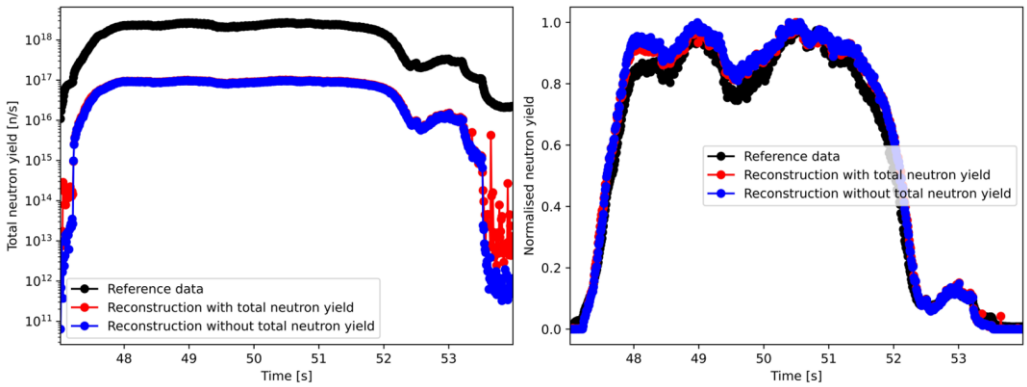

Figure 9.8. Comparison of the reconstructed total neutron yield obtained in calculations with and without the additional constraint for discharge #99949 with values measured by the fission chambers (left side – comparison of the absolute values, right side – comparison of the changes dynamics).

Table 9.1. Comparison of RMS_a and RMS_n for the reconstructed total neutron yield with and without additional constraint.

	RMS_a		RMS_n	
Discharge	without total neutron yield	with total neutron yield	without total neutron yield	with total neutron yield
96994	3.681	3.800	0.258	0.257
97995	3.562	3.739	0.273	0.267
99423	0.945	0.944	0.199	0.202
99448	0.951	0.948	0.274	0.270
99510	0.956	0.952	0.332	0.313
99866	0.972	0.970	0.520	0.518
99868	0.969	0.967	0.412	0.414
99914	0.968	0.967	0.348	0.348
99949	0.967	0.965	0.353	0.363
99512	0.923	0.921	0.383	0.393
99513	0.952	0.951	0.173	0.189
99460	0.954	0.951	0.371	0.359
99520	0.954	0.951	0.293	0.292
99522	0.944	0.943	0.073	0.083
99523	0.953	0.951	0.251	0.249
99797	0.956	0.955	0.192	0.198
99799	0.957	0.956	0.190	0.213
99861	0.955	0.953	0.216	0.232
99863	0.960	0.958	0.282	0.291
99878	0.952	0.951	0.528	0.282
99916	0.959	0.957	0.212	0.222
99944	0.959	0.957	0.279	0.272
99945	0.960	0.958	0.314	0.308

A second analysis has been done for the additional constraint in the form of the normalised reactivity calculated based on the ion temperature distribution. The ion temperature constraint applied to the tomography analysis has been investigated due to inconsistency in the presence of hollowness in the 2D profiles obtained from the CXRS measurement and neutron emissivity. The reactivity calculated based on the ion temperature has been compared with the reconstructed profiles and neutron camera measurements. In various discharges, the slight hollowness observed for the temperature (clearly visible in the normalised reactivity) does not correspond to the distribution of the count rates in the neutron detectors. The examples are presented in figures 9.9 (discharge #99423 is described in detail in subchapter 9.3), 9.10 (discharge #99522 is described in detail in subchapter 9.4), and 9.11 (discharge #99516 is described in detail in subchapter 9.4).

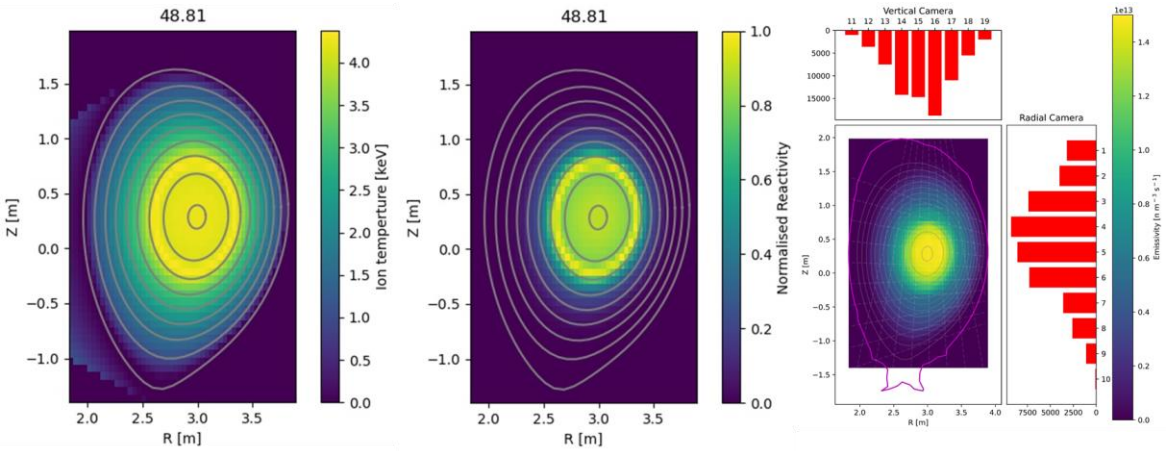

Figure 9.9. The comparison of the ion temperature measured by CXRS, normalised reactivity, and reconstructed neutron emission profile with count rates registered by the camera for time 48.81 s in discharge #99423.

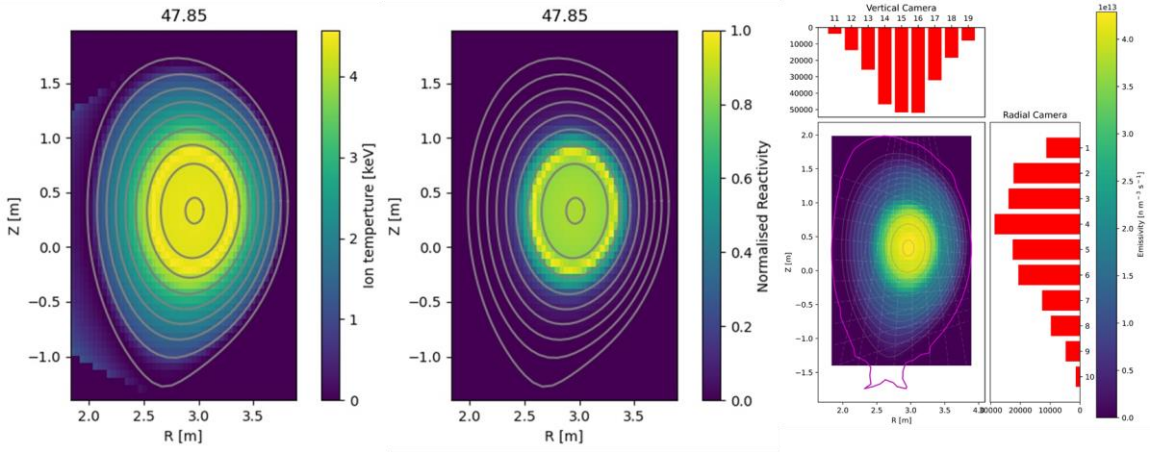

Figure 9.10. The comparison of the ion temperature measured by CXRS, normalised reactivity, and reconstructed neutron emission profile with count rates registered by the camera for time 47.85 s in discharge #99522.

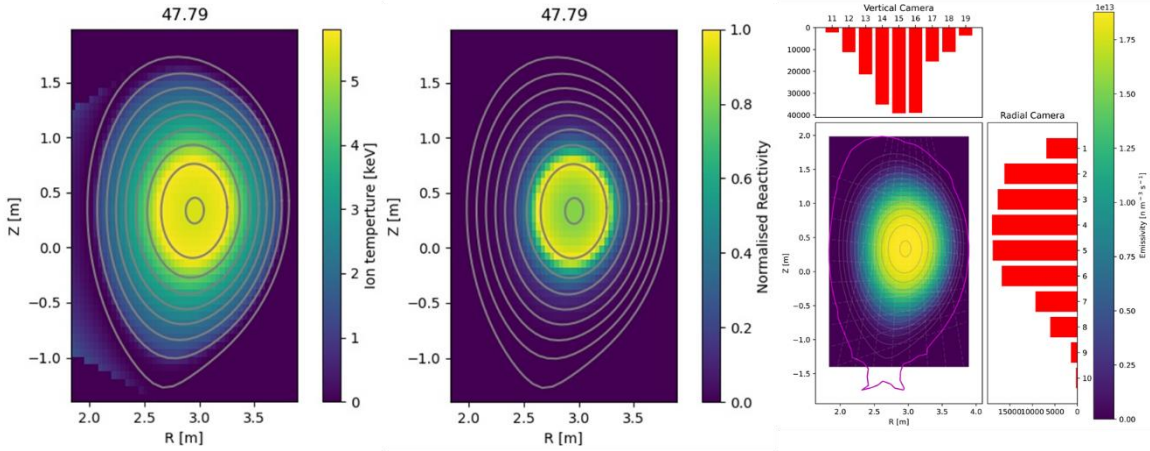

Figure 9.11. The comparison of the ion temperature measured by CXRS, normalised reactivity, and reconstructed neutron emission profile with count rates registered by the camera for time 47.79 s in discharge #99916.

The few cases where strong ion temperature hollowness was connected with the asymmetry in neutron camera data lower than measurement uncertainty were observed. The examples are presented in figures 9.12 and 9.13. In discharge #99520 (discharge parameters are described in subchapter 9.4), the influence of the lower temperature in the core is visible only for one camera. The differences between count rates are covered by measurement uncertainty. The radial part of the detectors registered maximal emission in the plasma centre. In discharge #99866 (discharge parameters are described in subchapter 9.3), the asymmetries were not observed in the measurement. These measurement results indicate that not all variations in the ion temperature significantly impact the neutron emissivity. It can be connected to the limited measurement performance by neutron camera, the errors in the CXRS measurement or differences between time resolution for considered diagnostics. The other reason for the neutron emission hollowness absence can be the delay in the ion temperature influence on the DT reactions or domination of the processes connected to the beam injected into the plasma. Neutron emission in the non-thermal plasma is very complicated, and the correlation of the tomography calculations with ion temperature constraint can disrupt the results. Therefore, the reconstructed neutron emission profiles for JET tokamak presented in the following subchapters were obtained without additional constraints.

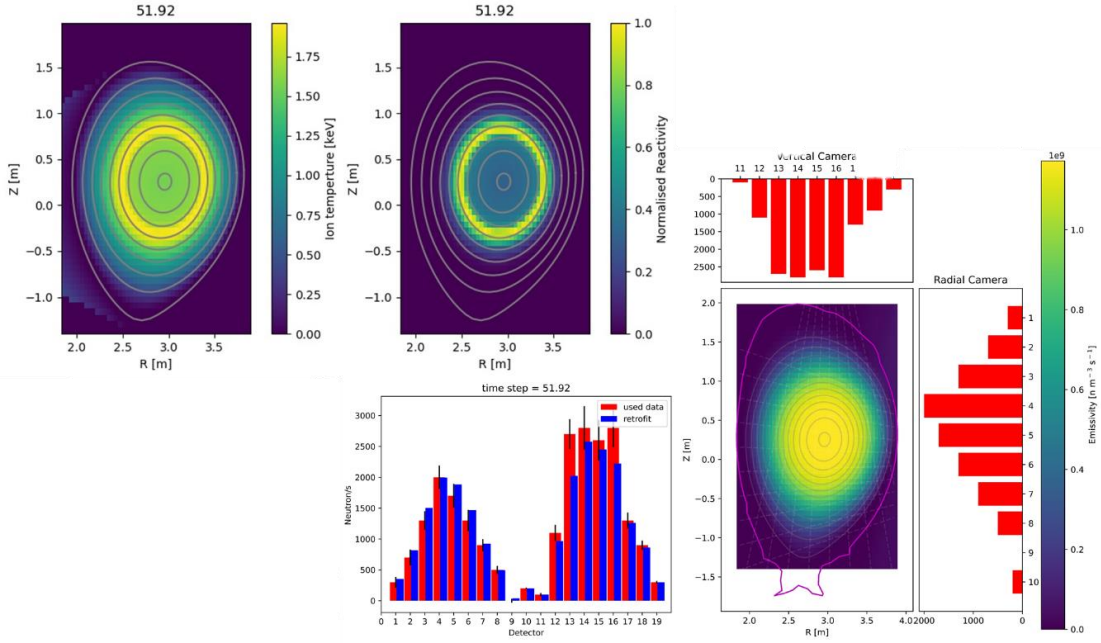

Figure 9.12. The comparison of the ion temperature measured by CXRS, normalised reactivity, and reconstructed neutron emission profile with count rates registered by the camera for time 51.92 s in discharge #99520.

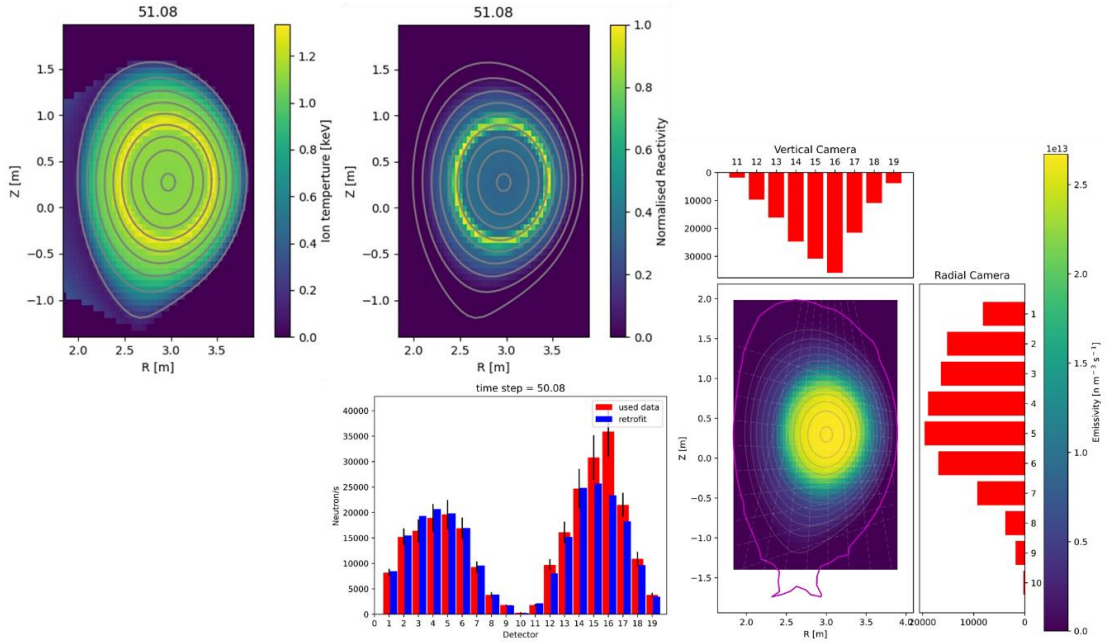

Figure 9.13. The comparison of the ion temperature measured by CXRS, normalised reactivity, and reconstructed neutron emission profile with count rates registered by the camera for time 50.08 s in discharge #99866.

9.3 Neutron emissivity reconstruction for the hybrid scenario

The hybrid scenario is an alternative to conventional ELMy H-mode for ITER operation, which was validated on various tokamaks [Vil2007]. It is a low triangularity advanced inductive scenario with a high normalised β [Beu2012]. The desired current density profile improves the stability and confinement but limits the duration of the high power phase [Ang2014]. The plasma is characterised by safety factor q of about 1, and low magnetic shear in the central plasma. The expected sawtooth activity is not present or low, which helps to prevent the triggering of Neoclassical Tearing Modes [Vil2007]. Balancing the NBI beams reduces the toroidal plasma rotation, which improves the confinement. The hybrid operation is characterised by low density. On JET, the scenario has been performed for both high and low triangularity [Beu2012]. The thermonuclear reactions impact on the total neutron yield is estimated at 35% [Gar2019].

The scientific objectives of the experimental topic “Hybrid scenario for high fusion performance in DT” for the C41 JET campaign are:

- Demonstration of the production of high fusion power for 5 s.
- Establishment of the reference performance for comparison with DD and TT plasmas with high β and low collisionality for studying the hydrogen isotopes and alpha particles effects.
- Investigation of ion transport and plasma stability [EFwiki].

The analysis of the neutron data obtained during the DTE2 campaign aimed to study the tritium content influence on the neutron emission profiles and investigate the abnormal ion transport during hybrid operation. The desired tritium to deuterium content is 50:50, but the isotope ratio varies in time and from discharge to discharge. The comparison of the operation parameters of analysed discharges is shown in table 9.2. Only two cases differ by the used toroidal magnetic field and three by the plasma current. The tritium amount variation in time is presented in figure 9.14. Two discharges, #99423 and #99510, characterised by low tritium content, have the lowest electron temperature. This parameter for other discharges varies from 8 keV up to 9.9 keV, which should not significantly impact the plasma stability. The electron density has approximately the same order of magnitude for all discharges.

Table 9.2. The operation parameters of the hybrid discharges.

Discharge	Toroidal magnetic field [T]	Plasma current [MA]	Electron temperature [keV]	Electron density [10^{19}/m^3]
99423	2.3	2.6	4.5	14
99448	2.3	3.45	8	9.2
99510	3.4	2.8	6.2	10.9
99866	3.4	2.3	9.7	13.3
99868	3.4	2.3	9.9	13.8
99914	3.4	2.3	9.9	17
99949	3.4	2.3	9.1	14.2

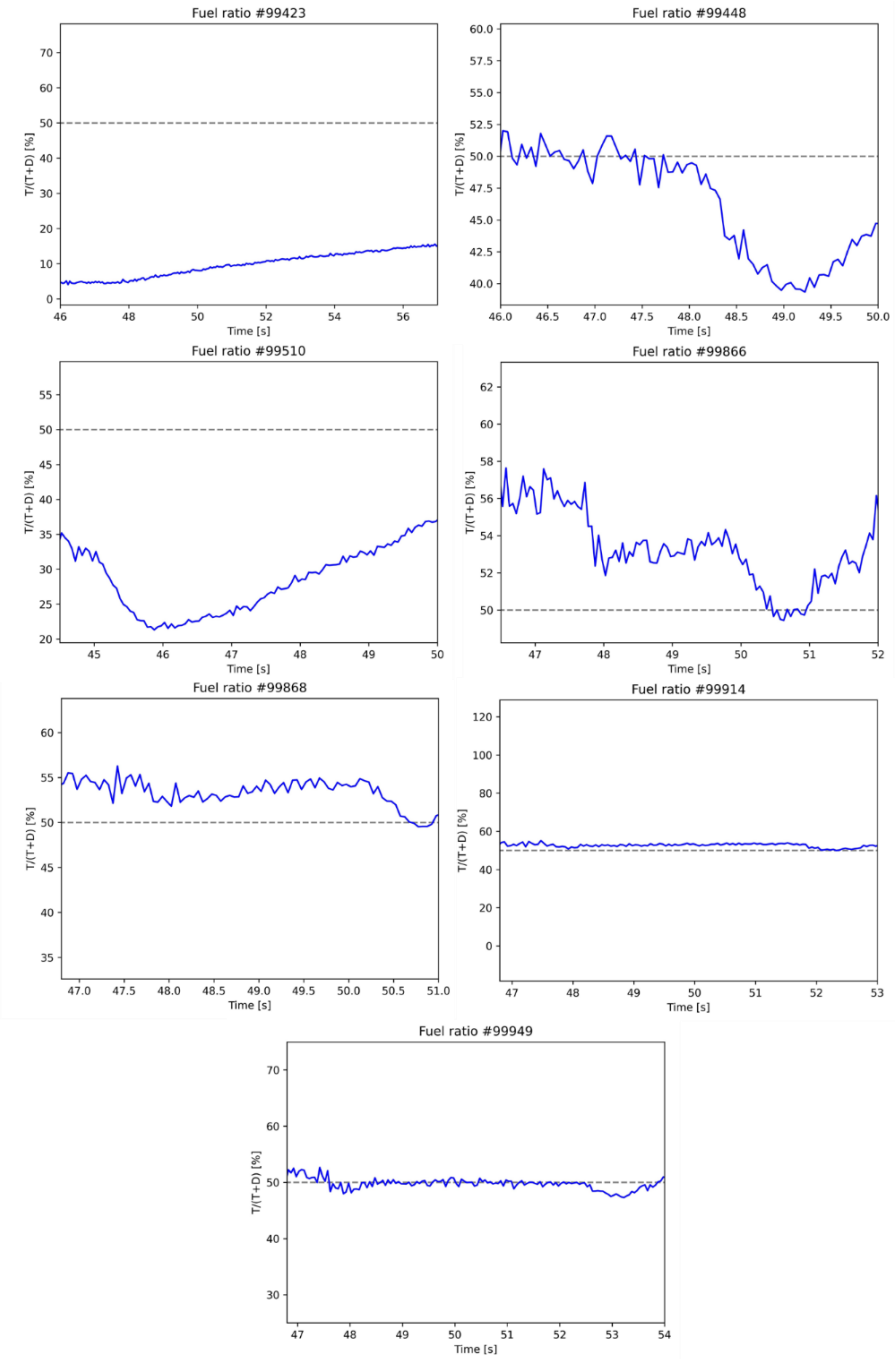

Figure 9.14. Comparison of the tritium amount in the plasma during the different discharges of the experiment with the hybrid scenario.

The comparison of the normalised NBI power and total neutron yield for #99423 is presented in figure 9.15. The ICRH heating system was not used during this discharge. The maximal neutron rate is about $5 \cdot 10^{17}$ n/s. Discharge #99423 is characterised by the lowest tritium content. The neutron emissivity has been calculated with a time resolution of 0.01 s. The standard profile that is expected to observe is symmetric with maximum intensity in the plasma core centre. The neutron emissivity distribution in #99423 is disrupted in many time slices; asymmetries and hollowness are observed. The neutron emission in a given area fluctuates strongly in time. An example of the changes in the neutron emission shape in the discharge phase with the highest total neutron yield is presented in figure 9.16. The hollowness occurs during the whole discharge. The asymmetries are characterised by the strongest emission intensity on LFS. The discrepancy between retrofit and used data varies from 1% to 20%. Higher values are connected with the collimators in vertical camera 14 – 17.

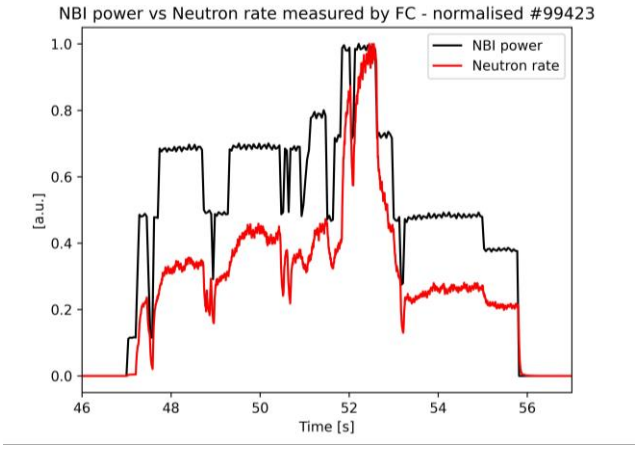

Figure 9.15. Comparison of the normalised NBI power and the total neutron yield from FC functions in time for discharge #99423.

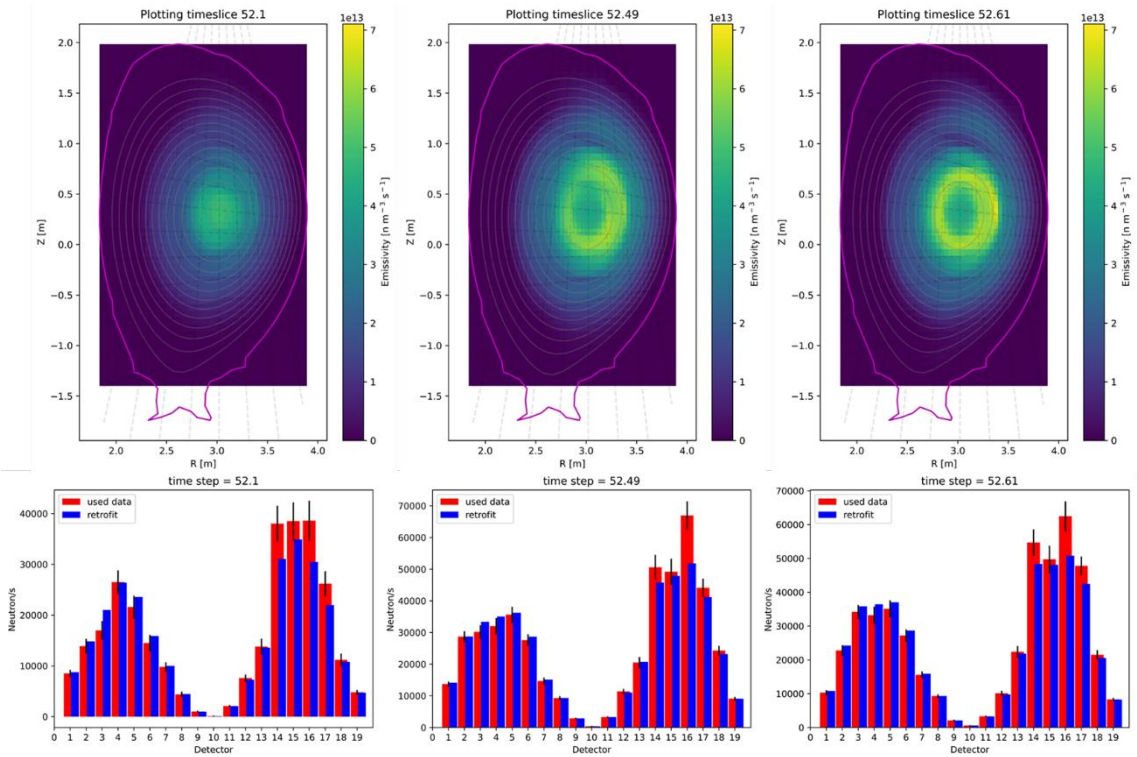

Figure 9.16. The neutron emission profiles reconstructed for time 52.10 s, 52.49 s, and 52.61 s in discharge #99423.

The second analysed discharge with low content of tritium is #99510. Figure 9.17 presents the fluctuation in time of neutron rate and heating power. The NBI power was about 7 MW higher than for #99423. Therefore, plasma temperature was higher, and the neutron yield was up to $8 \cdot 10^{17}$ n/s. The duration of the neutron production was only 4 s, and hollowness frequently occurred in the emissivity profiles. The neutron emissivity evolution from the beginning and the time when the rate reaches the maximum is presented in figure 9.18. The neutron emission profiles before the plasma termination are shown in figure 9.19. The retrofit agreement with the experimental data varies from 1% to 25%. The detectors #14 and #16 are characterised by a much higher error (20% - 25%) than others in the neutron camera (< 10%). The hollowness is also observed in the ion temperature profiles.

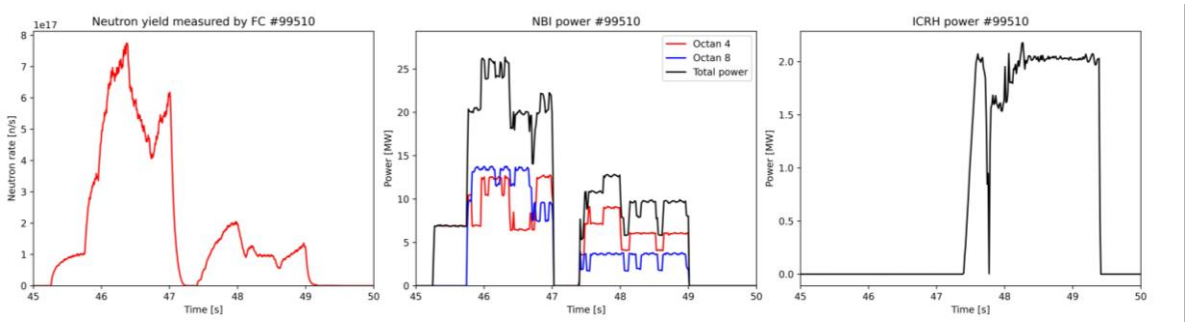

Figure 9.17. The total neutron yield measured by FC (left), NBI power (centre), and ICRH power (right) functions in time for discharge #99510.

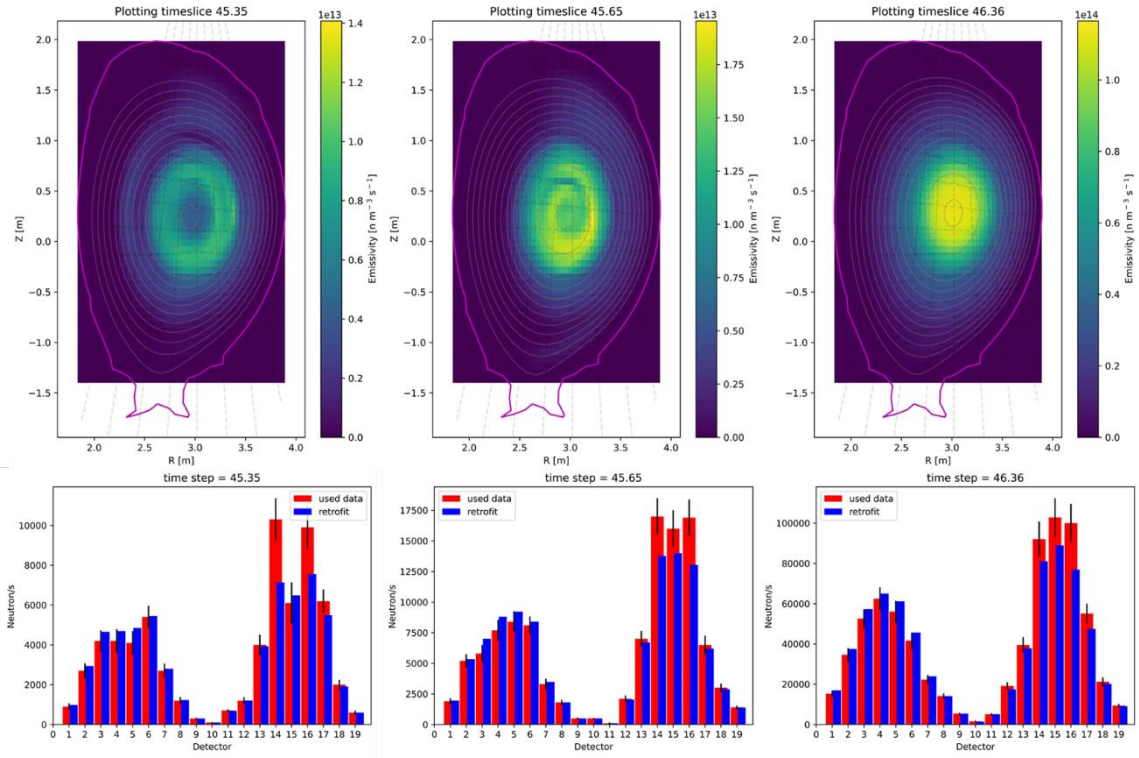

Figure 9.18. The neutron emission profiles reconstructed for time 45.35 s, 45.65 s, and 46.36 s in discharge #99510.

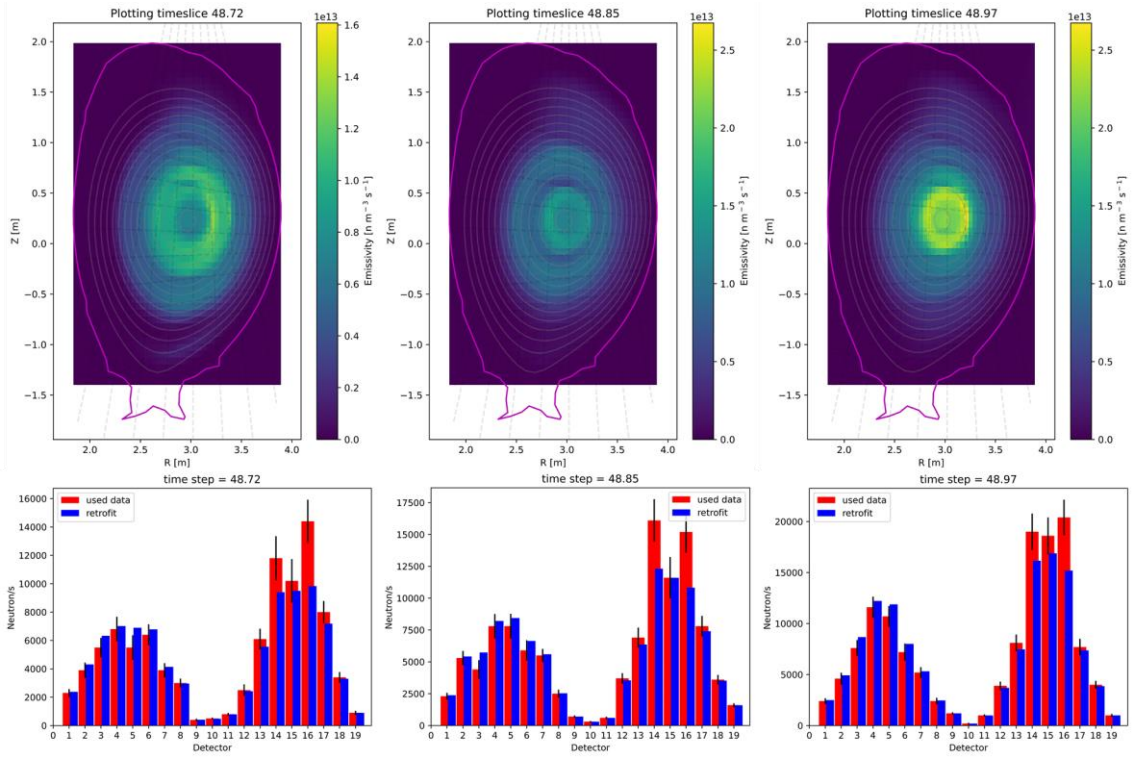

Figure 9.19. The neutron emission profiles reconstructed for time 48.72 s, 48.85 s, and 48.97 s in discharge #99510.

The tritium content in discharge #99448 up to 48 s was about 50% but later occurs abundance drop. The neutron yield and heating power are presented in figure 9.20. The neutron rate dropped with a slight delay start after switching off the NBI system in Octan #8. This discharge was very short due to the problems with the heating system. The neutron production continues by only 2.5 s. The neutron emissivity was strongly focused in the core centre. After the neutron rate drop, the emission area is slightly wider, and fluctuations occur. The evaluation of the neutron emissivity in the plasma during discharge #99448 is presented in figures 9.21 and 9.22. The mean discrepancy between retrofit and experimental data is 7%.

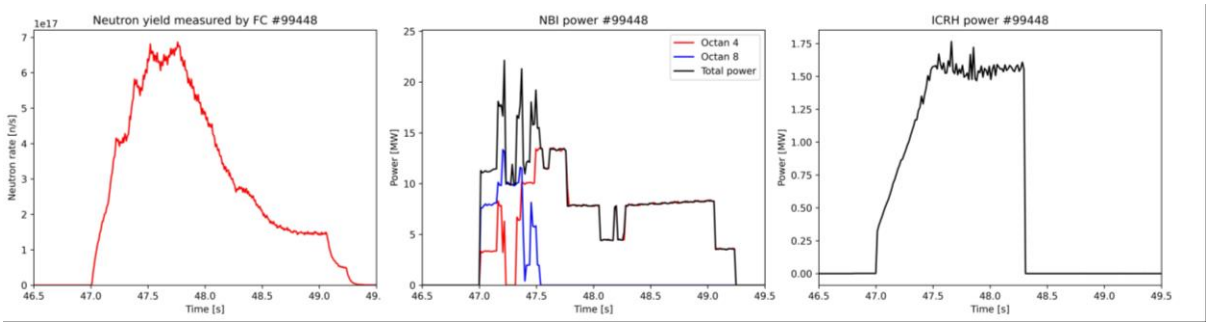

Figure 9.20. The total neutron yield measured by FC (left), NBI power (centre), and ICRH power (right) functions in time for discharge #99448.

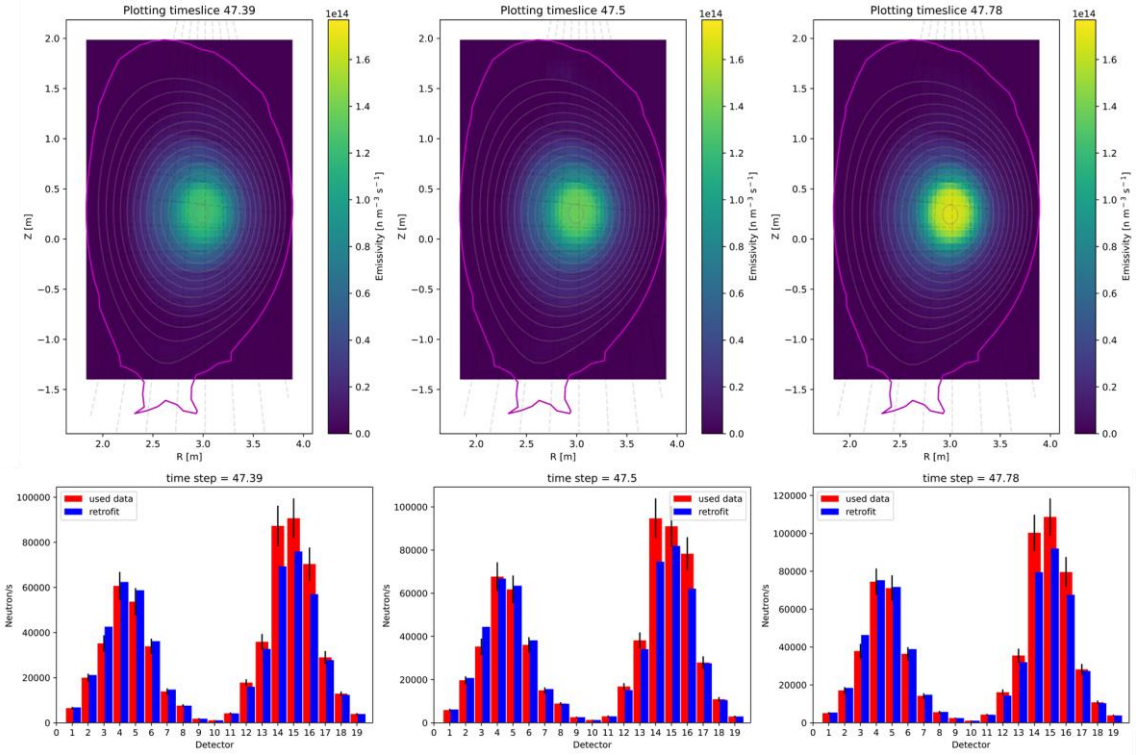

Figure 9.21. The neutron emission profiles reconstructed for time 47.39 s, 47.50 s, and 47.78 s in discharge #99448.

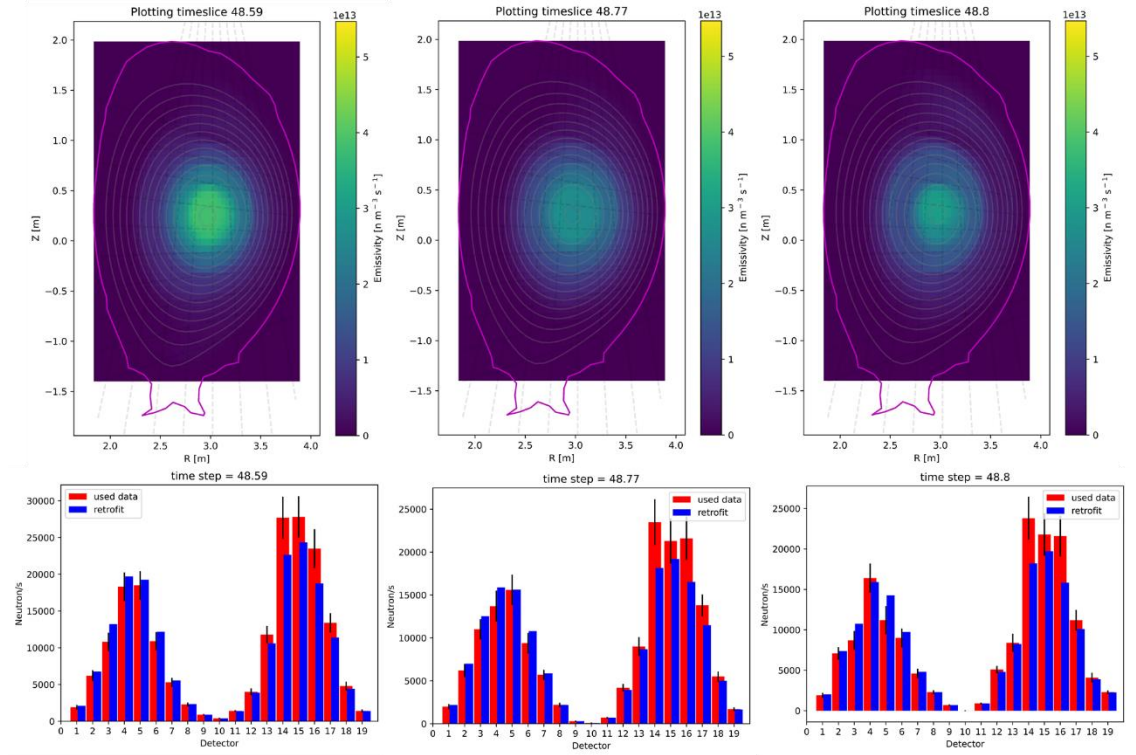

Figure 9.22. The neutron emission profiles reconstructed for time 48.59 s, 48.77 s, and 48.80 s in discharge #99448.

Discharge #99914 has desired tritium content during the whole plasma confinement time. The heating power and neutron rate are presented in figure 9.23. The discharge duration is 5 s with high neutron emission up to $3 \cdot 10^{18}$ n/s. The evolution of the neutron emissivity distribution

in the tokamak is presented in figure 9.24. The retrofit and experimental data discrepancy vary from 1% to 20%, but the mean value is lower than the measurement uncertainty and equal to 10%. The neutrons are produced mainly in the plasma core. The neutron emission in this discharge was not disrupted by asymmetries and hollowness.

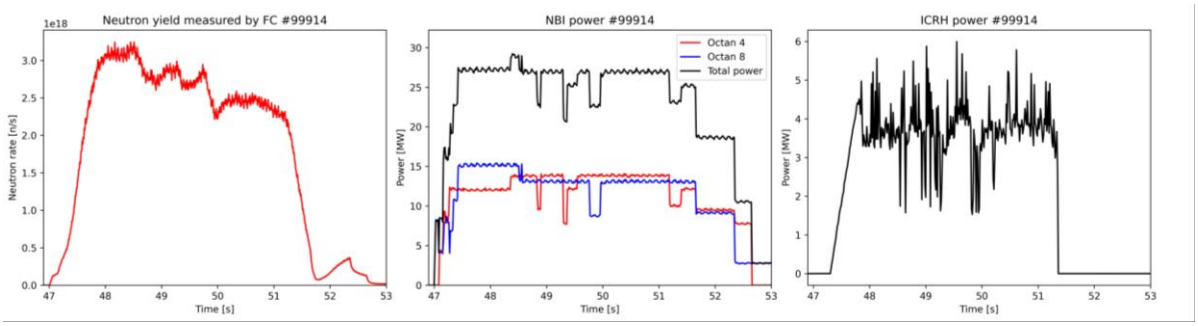

Figure 9.23. The total neutron yield measured by FC (left), NBI power (centre), and ICRH power (right) functions in time for discharge #99914.

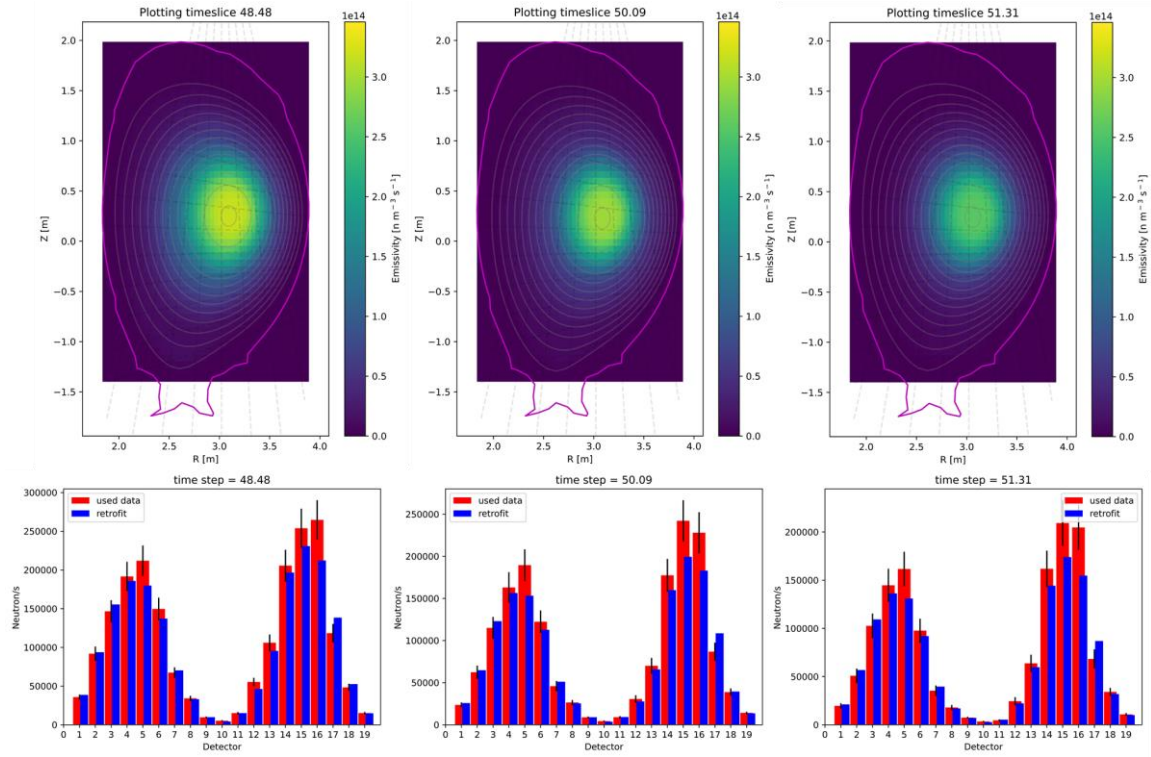

Figure 9.24. The neutron emission profiles reconstructed for time 48.48 s, 50.09 s, and 51.31 s in discharge #99914.

The second analysed discharge with desired hydrogen isotope ratio of 50:50 is #99949. The total neutron yield and heating power functions in time are presented in figure 9.25. The high neutron production was maintained by about 5 s. The examples of the reconstructed neutron emissivity profiles are presented in figure 9.26. The mean discrepancy between retrofit and experimental data equals 8%. The neutron emission is focused on the plasma core without asymmetries and hollowness.

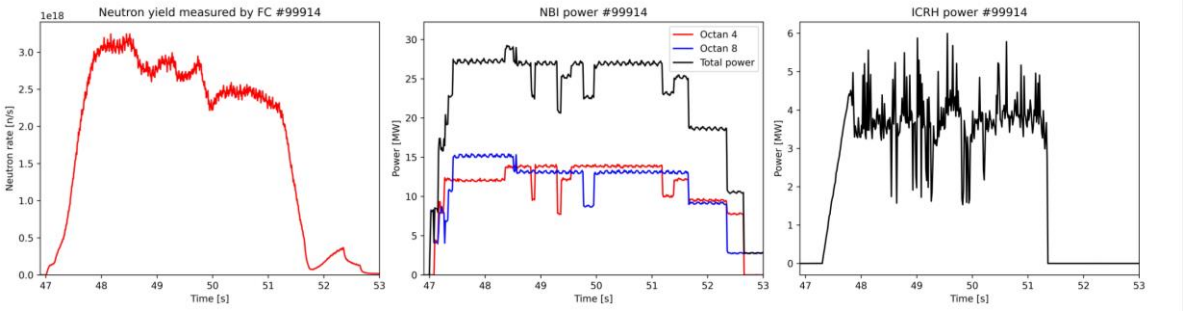

Figure 9.25. The total neutron yield measured by FC (left), NBI power (centre), and ICRH power (right) functions in time for discharge #99949.

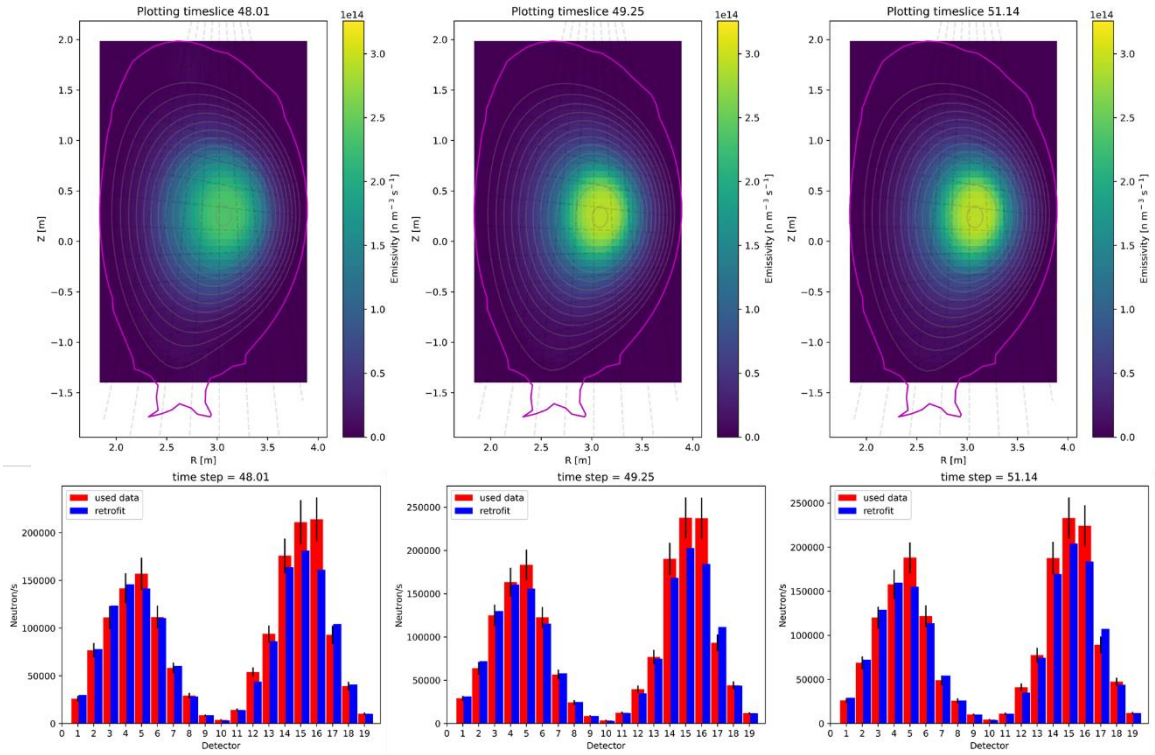

Figure 9.26. The neutron emission profiles reconstructed for time 48.01 s, 49.25 s, and 51.14 s in discharge #99949.

Discharge #99868 is characterized by a tritium amount of about 55%. The total neutron yield and heating power are presented in figure 9.27. The neutron rate reached the maximum at the beginning of discharge and then slowly decreased in time. The plasma confinement time was only about 3 s. The evolution of the neutron emissivity is presented in figure 9.28. The discrepancy between the retrofit and experimental data varies from 1% to 24%. The slight contraction of the emission area is observed with the intensity decrease. The neutron emissivity is stable during the whole shot.

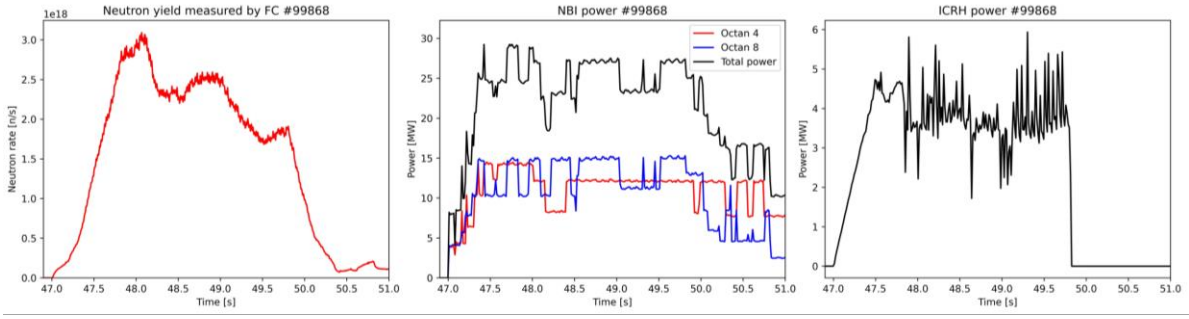

Figure 9.27. The total neutron yield measured by FC (left), NBI power (centre), and ICRH power (right) functions in time for discharge #99868.

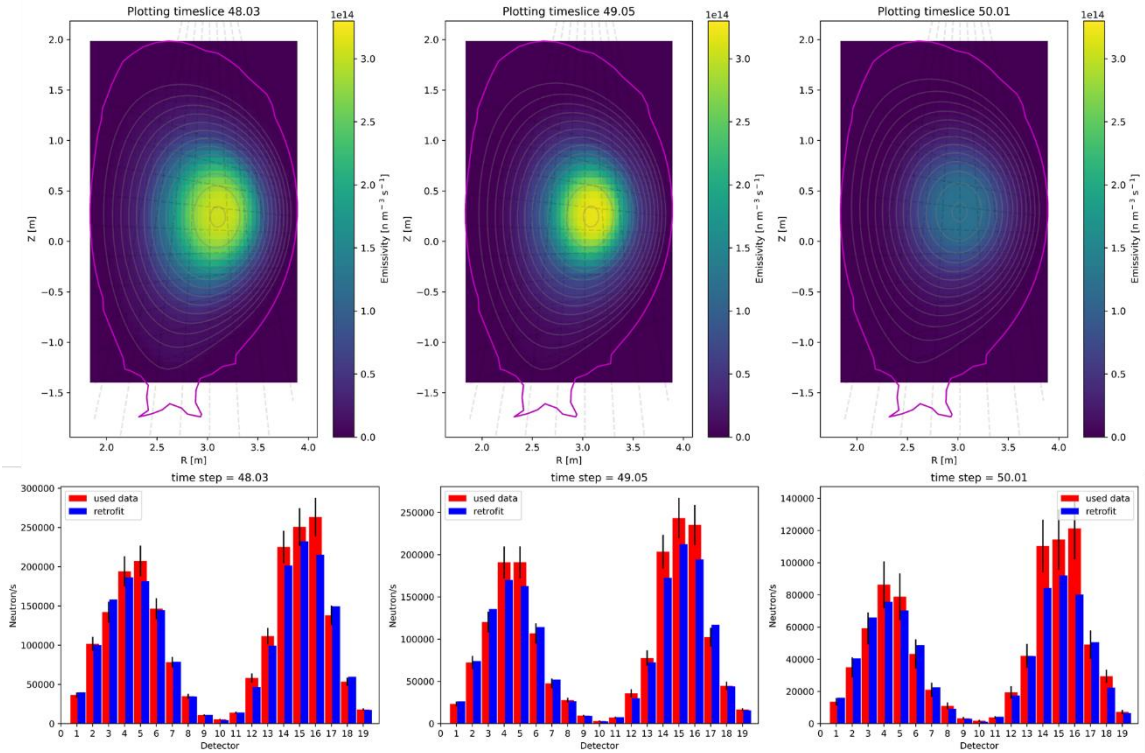

Figure 9.28. The neutron emission profiles reconstructed for time 48.03 s, 49.05 s, and 50.01 s in discharge #99868.

The last analysed hybrid discharge has tritium content higher than 50%. The amount of the hydrogen isotopes varied in time. The neutron rate and heating power are presented in figure 9.29. The discharge was short (≈ 3 s). The results of the tomography reconstruction are shown in figure 9.30. The mean agreement between retrofit and measurement data is 8%. The emission is symmetric with the intensity maximum in the plasma centre in all reconstructed time slices.

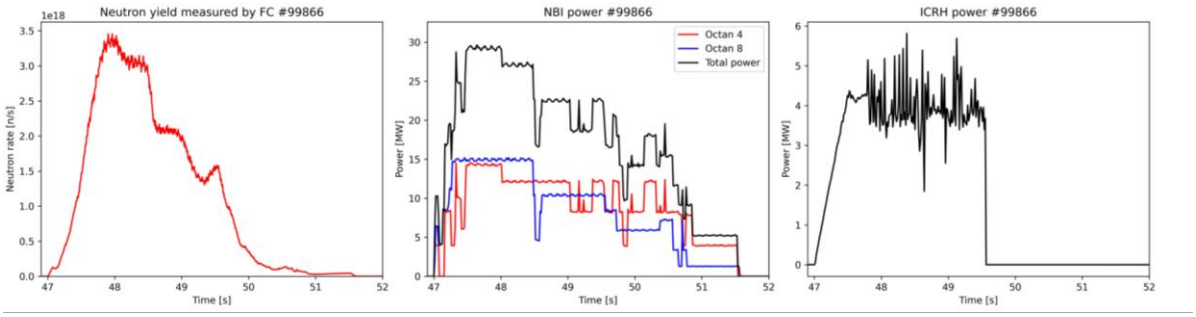

Figure 9.29. The total neutron yield measured by FC (left), NBI power (centre), and ICRH power (right) functions in time for discharge #99866.

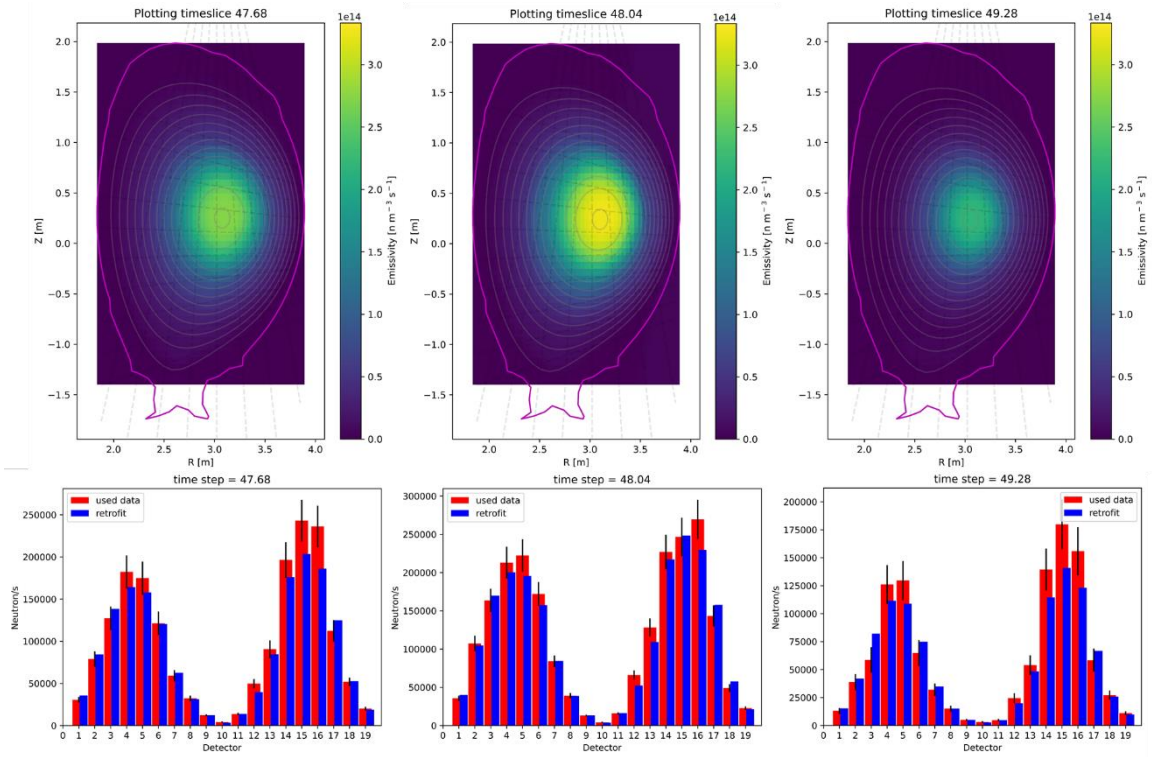

Figure 9.30. The neutron emission profiles reconstructed for time 47.68 s, 48.04 s, and 49.28 s in discharge #99866.

All analysed discharges were reconstructed with a satisfying discrepancy between retrofit and experimental data from the neutron camera (mean error < 10%). Therefore, the interpretation of the obtained neutron emissivity profiles was found reliable. In the discharges with low tritium content, hollowness and asymmetry were observed. The disruptions in the neutron emissivity distributions are connected with anomalous ion transport. The symmetric neutron emissivity distribution characterises the tritium-rich discharges with maximum intensity in the plasma core. When the amount of tritium in the plasma increases, fewer disruptions in the discharges occur, and no abnormal ion transport is observed. The most prolonged discharge has a 50% amount of tritium. The results of the analysis indicate that the isotope ratio influences discharge stability. The demonstration of the high fusion power production during hybrid operation, which is the scientific goal of the experiment, was possible only with a tritium content of about 50%. In general, plasma stability is influenced by more parameters, e.g. electron density and temperature, magnetic field, and safety factor. Therefore, the overall discharge permanence evaluation required a more comprehensive analysis of all changeable plasma parameters, radiation power, impurities content and distribution.

9.4 Neutron profile reconstruction for the baseline scenario

The baseline scenario for ITER is ELMy H-mode regime with 15 MA plasma current and 5.3 T magnetic field. The operation assumed domination of the alpha particle heating and production of significant fusion gain $Q \approx 10$ [Sip2016]. The discharges are characterised by the high plasma current, moderate β, and low edge safety factor. The thermal contribution to the neutron emission is 45% of the total intensity due to the high density. A low number of neutral particles at high power provides low collisionality and strong core confinement [Gar2019]. The accumulation of tungsten and other high-Z impurities results in the hollowing of electron temperature profiles and radiation-induced disruptions connected with the tearing modes. These effects can be avoided by gas fuelling (D pellets) and low-Z impurity seeding application. The injection of D pellets also impacts ELMs. A high level of gas puffing increases the frequency of ELMs to 20 – 50 Hz. The additional effects are the reduction of the pedestal temperature and pressure. The rise of the fuelling rate increases the density on the separatrix and results in turbulent heat transport. The ICRH is used for L/H mode transition and to avoid impurity accumulation during plasma termination. Runaway radiation events occur in the discharges [Fie2021].

The scientific goals of the research topic “Baseline scenario for high fusion performance in DT” are:

- Demonstration of steady-state performance with fusion power higher than 10 MW for 5 s. Due to problems with MHD activity, which leads to discharge termination, obtaining non-disruptive operation with limited performance and a high-performance regime with stronger disruptions.
- Investigation of gas and pairs of gas+pellets influence on plasma stability and parameters.
- Study the confinement dependence on isotope mass, RF heating schemes, and alpha particle heating [EFwiki].

During the experiment, the problem with a sawtooth crash was observed. It causes a sudden drop in the neutron rate. There is a theory that this disruption is connected with ion transport, which causes asymmetry in neutron emission. The crash is proceeded by toroidal precession and longitudinal motion of ions. This effect can be observed in the production of the magnetic field islands with the domination of the neutron production on LFS [Kol1996]. The tomography analysis has been focused on the investigation of the disruptive neutron emission distribution connected with this MHD activity. The results of the research might confirm the theory if the asymmetry in neutron emission is detected.

Table 9.3 presents the operation parameters of the analysed baseline discharges. It includes the reference deuterium discharges #96994 and #97995. They can be divided into three groups with the same toroidal magnetic field and plasma current. The electron temperature varies from 6 to 10 keV, and electron density from $17 \cdot 10^{19}$ to $24 \cdot 10^{19}$ m^{-3}. The temperature and density profiles deduced from CXRS and Thomson scattering measurements and archived after automatic calculations in JET database were used in the analysis [CHAIN2]. The time resolution of this data is 200 ms. The MHD activity presence was investigated by the experts from the experimental group and presented in internal meetings based on plasma radiation, current, ion density and temperature measurements by different diagnostics [EFwiki].

Table 9.3. The operation parameters of the baseline discharges.

Discharge	Toroidal magnetic field [T]	Plasma current [MA]	Electron temperature [keV]	Electron density [$10^{19}/m^3$]
96994	2.85	3	8.2	17.2
99512	2.85	3	8.8	23.7
99513	2.85	3	7.8	19.6
97995	3.35	3.5	6	22
99460	3.35	3.5	6.3	19.5
99520	3.35	3.5	8	20
99522	3.35	3.5	6.5	20
99523	3.35	3.5	8.1	21.5
99797	3.3	3.5	8	23.9
99799	3.3	3.5	8.4	21.4
99861	3.3	3.5	7.7	22
99863	3.3	3.5	10	22
99878	3.3	3.5	8.2	18.4
99916	3.3	3.5	7.8	21.9
99944	3.3	3.5	7.4	17
99945	3.3	3.5	7	19

At first, the baseline discharges with the toroidal magnetic field equal to 2.85 T, and 3 MA plasma current has been analysed. The deuterium reference discharge #96994 and DT #99513 are neon seeded. The comparison of the neutron rate measured by FC and heating power changes in time for #96994, #99512, and #99513 is presented in figure 9.31. In both deuterium-tritium discharges, the fuel isotope ratio is 50:50. The total neutron rate for the DT discharges is 102 times higher than for only deuterium plasma. The #96994 is a long discharge (≈ 10 s) with relatively stable neutron production intensity. The #99512 and #99513 reach the maximal neutron yield at 49 s. The neon seeded discharge terminated about 2 s earlier. The evolution of the neutron emissivity profiles for the reference discharge is presented in figure 9.32. During the DD campaign, the detector #5 was not working. Therefore, its measurement result has been excluded from the tomography analysis. The retrofit and experimental data discrepancy varies from 1% to 20%. The neutron emissivity is focused on the core centre with slightly more emission on LFS. Additional, weak intensity also occurs near the edge of LFS. The evolution of the neutron emissivity in discharge #99512 is presented in figure 9.33. The mean agreement between retrofit and experimental data equals 10%. The neutron emissivity is symmetric during the whole discharge. The area of maximal emission becomes wider after the neutron rate drop for approximately 0.05 s and contracts again. No disruptive effects that can be connected with the MHD activity are observed. The results of the neutron emissivity reconstruction for discharge #99513 are presented in figure 9.34. The mean discrepancy between retrofit and experimental data is 9%. The neutron emissivity is symmetric and focused in the plasma centre in the first part of the discharge when the neutron rate is maximal. Then, when the neutron rate increases, the hollowness starts to occur frequently. It cannot be correlated with the sawtooth crash. The neutron emissivity distribution is more disrupted in the case of the neon seeding DT discharge. The asymmetry observed for deuterium plasma is not reproduced when tritium is added.

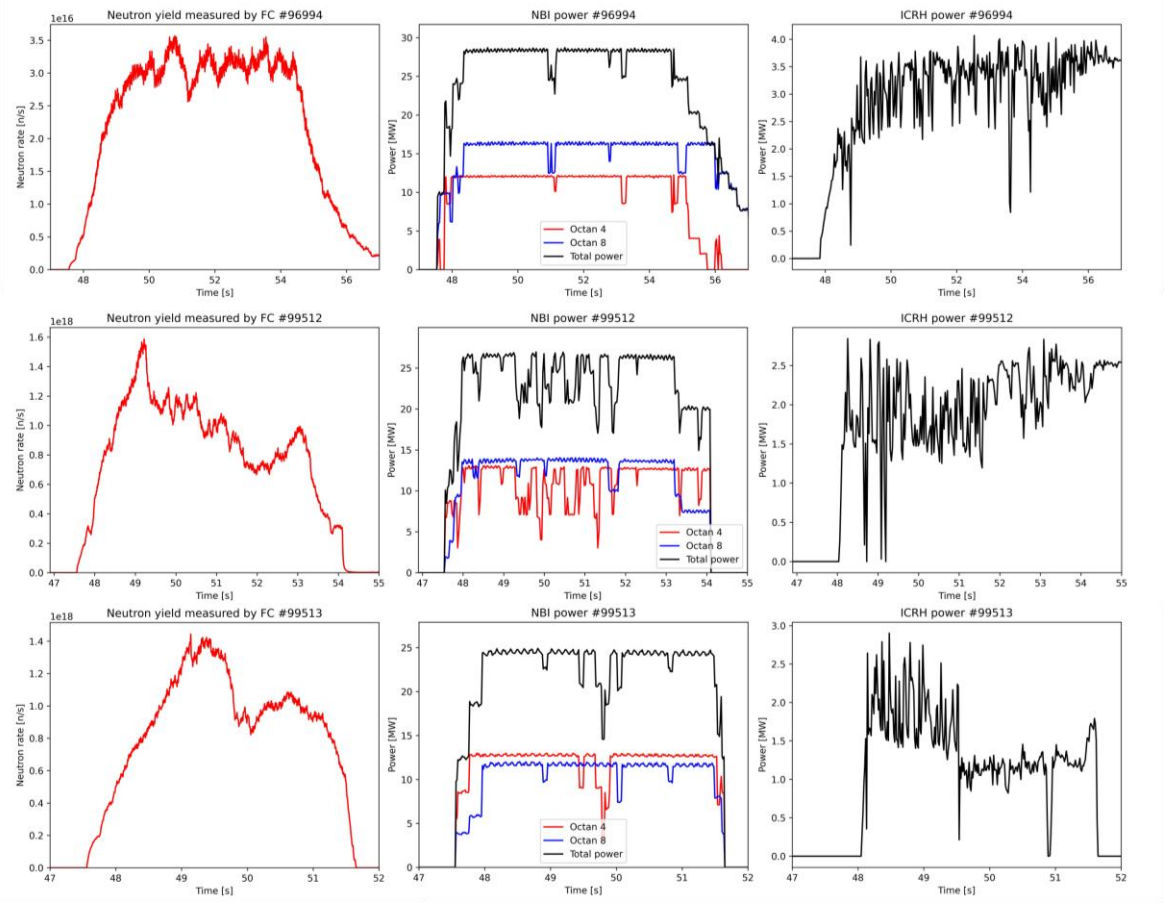

Figure 9.31. The total neutron yield measured by FC (left), NBI power (centre), and ICRH power (right) functions in time for discharges #96994 (top), #99512 (centre), and #99513 (bottom).

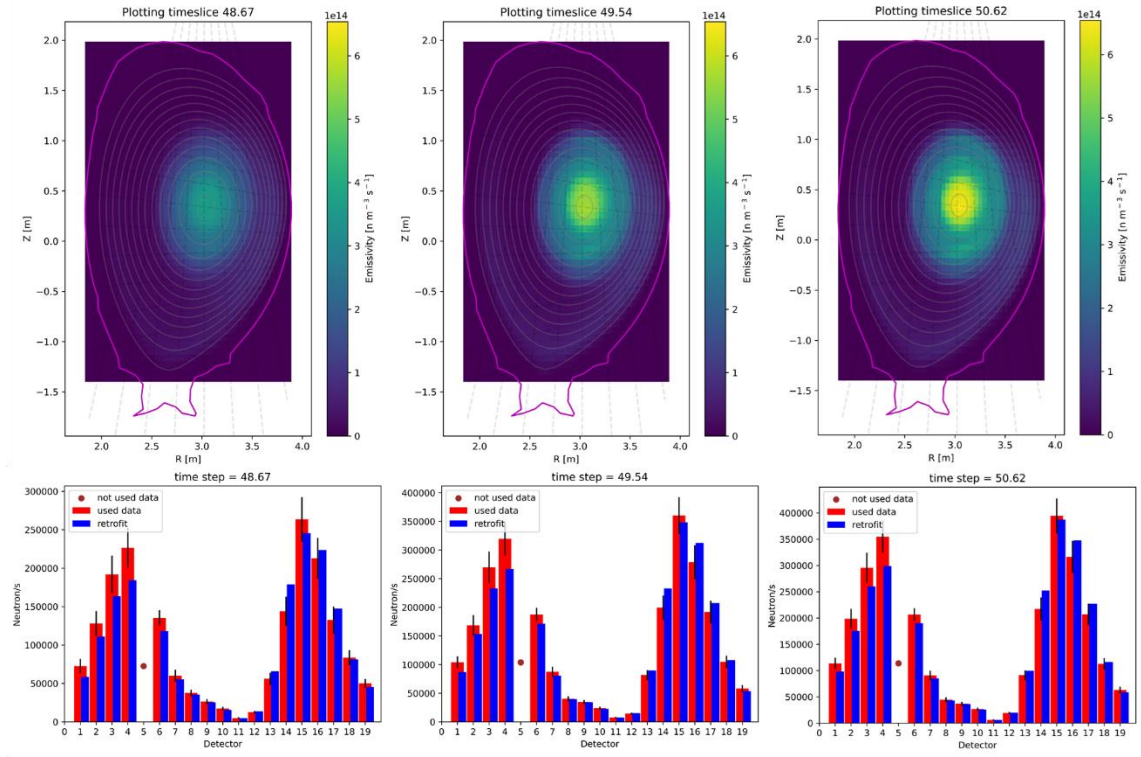

Figure 9.32. The neutron emission profiles reconstructed for time 48.67 s, 49.54 s, and 50.62 s in discharge #96994.

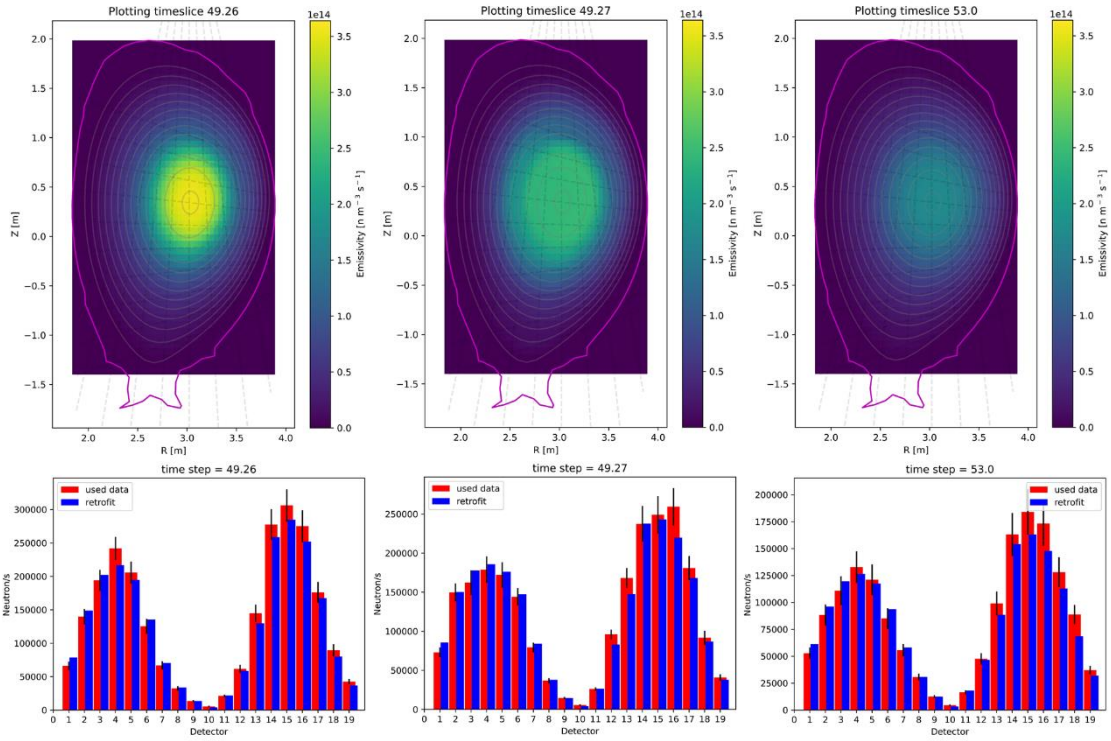

Figure 9.33. The neutron emission profiles reconstructed for time 49.26 s, 49.27 s, and 53.00 s in discharge #99512.

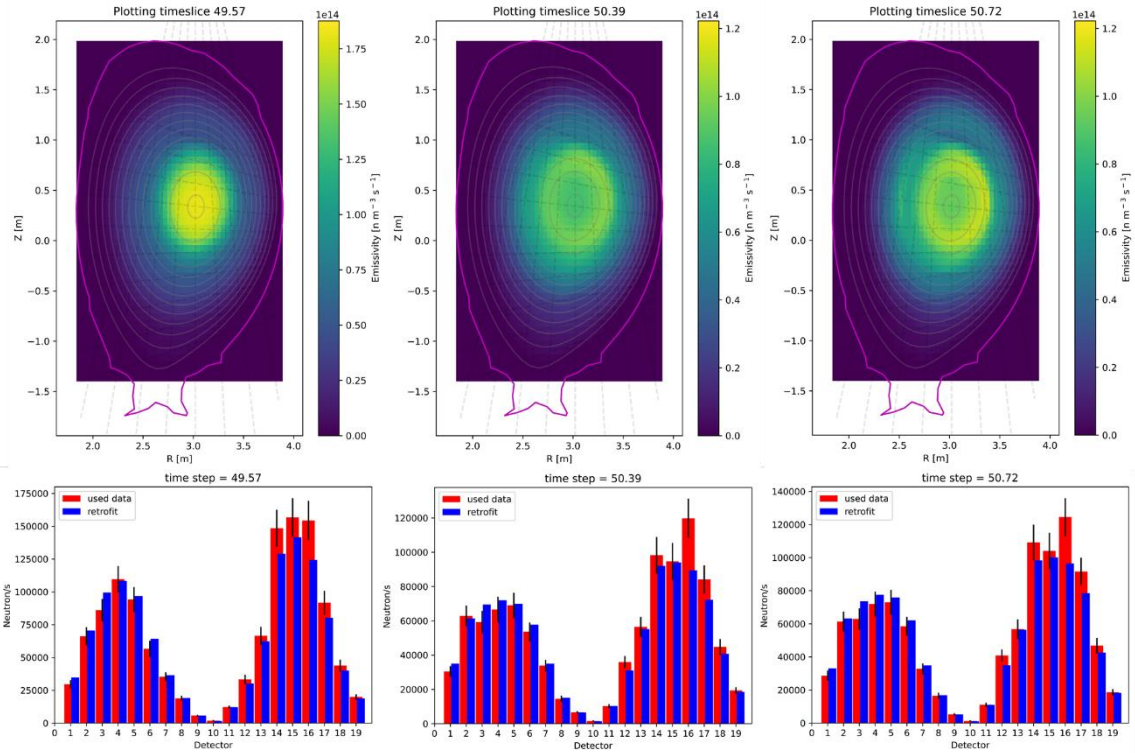

Figure 9.34. The neutron emission profiles reconstructed for time 49.57 s, 50.39 s, and 50.72 s in discharge #99513.

Other discharges have a plasma current of 3.5 MA and a toroidal magnetic field of 3.35 T or 3.3 T. The total neutron yield and heating power for the deuterium reference discharge #97995 are presented in figure 9.35. The neutron rate drop observed after 50.2 s is not connected with

the change in the heating power but with the sawtooth crash. The reconstructed emissivity profile around this time is presented in figure 9.36. The detector #5 was also excluded from these tomography calculations due to the failure during the measurement. The mean agreement between retrofit and experimental data equals 8%. No fluctuation in the emission area is observed during and after the sawtooth crash. Similar to #96994, the asymmetry with weak emission on the LFS edge is present in the reconstruction results. This observation agrees with the theory of ion transport during the sawtooth crash. However, it is not resolved that it is related with the physical phenomena or background in the measurement connected with the scattered neutrons.

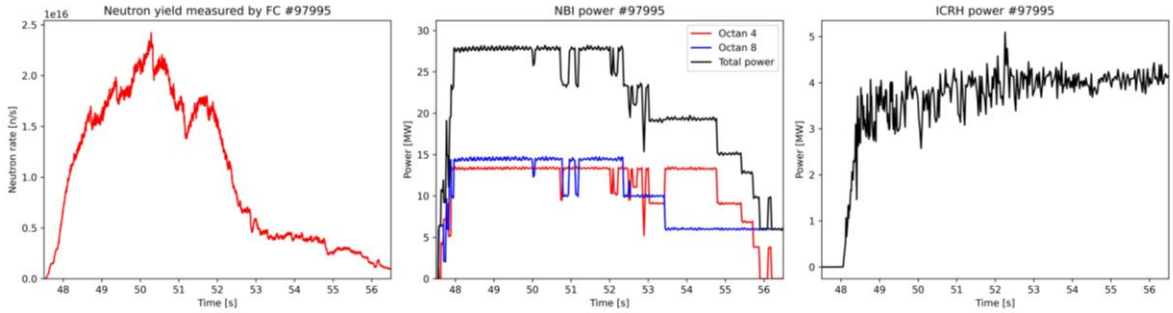

Figure 9.35. The total neutron yield measured by FC (left), NBI power (centre), and ICRH power (right) functions in time for discharges #97995.

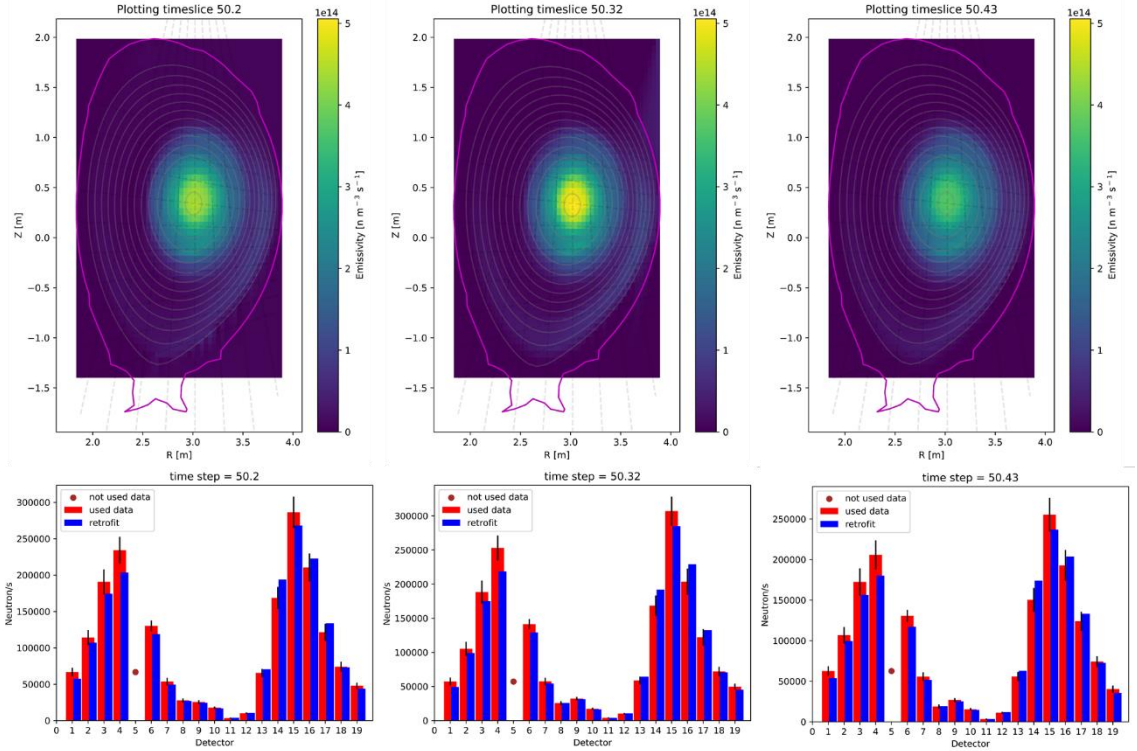

Figure 9.36. The neutron emission profiles reconstructed for time 50.20 s, 50.32 s, and 50.43 s in discharge #97995.

The comparison of the neutron rate with heating power for discharge #99460 is presented in figure 9.37. The evaluation of the neutron emissivity from plasma is shown in figure 9.38. In the first stage of the discharge during the growth of neutron production, the hollowness occurs in the reconstructed distribution. The maximal total neutron yield is $7 \cdot 10^{17}$ n/s. The neutron rate drop is connected with the problem with NBI system. In the second part of the discharge, neutron

emissivity is symmetric, with the maximum in the plasma core centre. No correlation with the MHD activity was found in this case. The ion density and temperature profiles are presented in figure 9.39. The ion density profile is measured by CXRS diagnostics. The ion density distribution is calculated based on the results from Thomson scattering and visible spectroscopy diagnostics. The uncertainties of the results are not available [CHAIN2]. The hollowness is observed in density measurement.

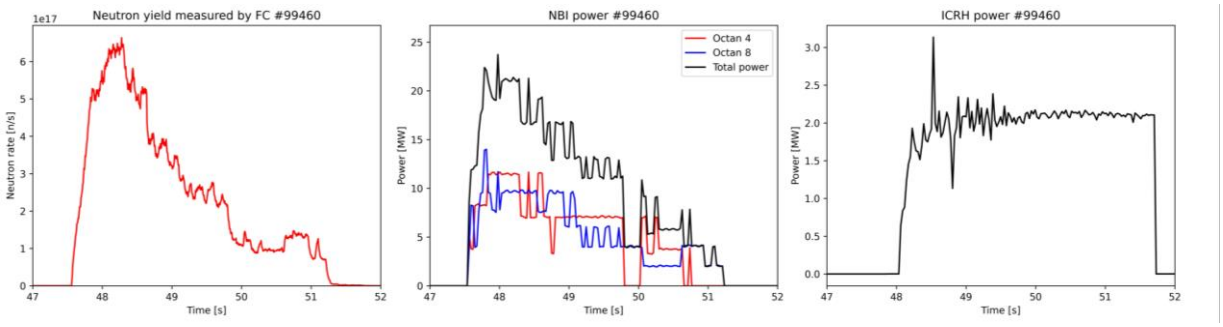

Figure 9.37. The total neutron yield measured by FC (left), NBI power (centre), and ICRH power (right) functions in time for discharges #99460.

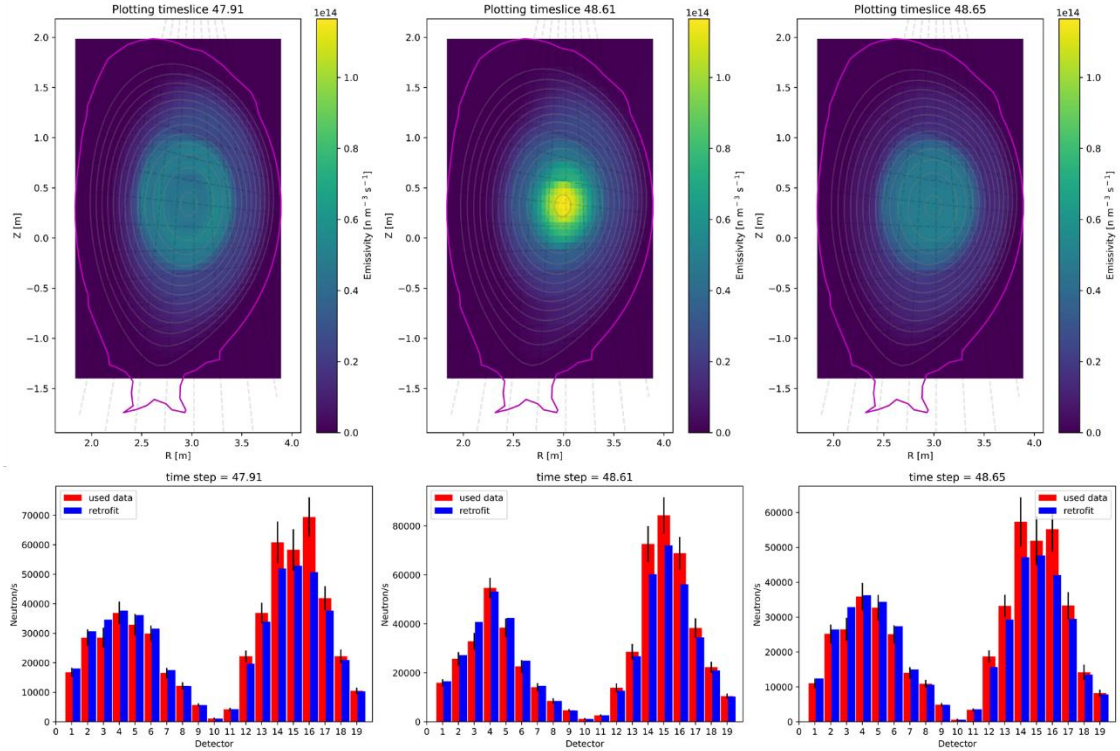

Figure 9.38. The neutron emission profiles reconstructed for time 47.91 s, 48.61 s, and 48.65 s in discharge #99460.

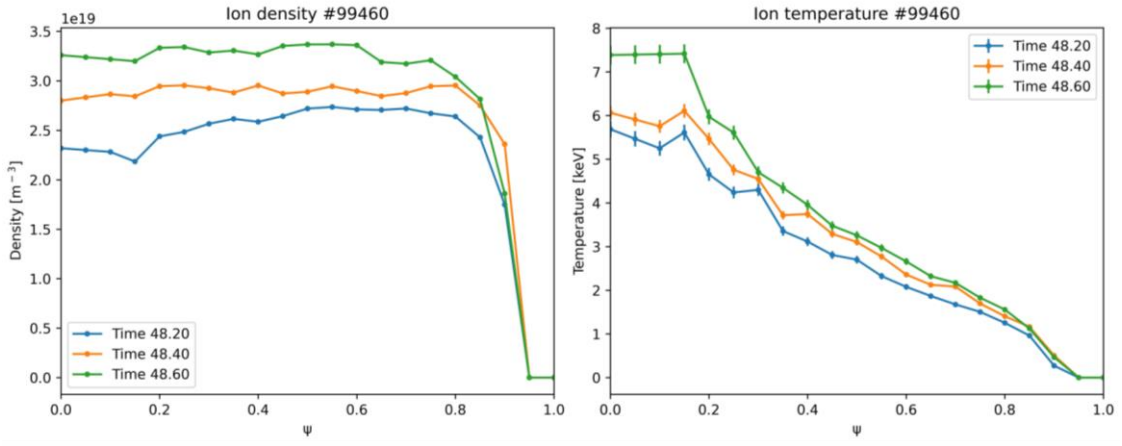

Figure 9.39. Ion density (left) and temperature (right) profiles measured during discharge #99460.

The neutron rate and heating power changes in time for discharge #99520 are presented in figure 9.40. The discharge termination was connected with the lowered NBI beam power. The sawtooth activity was observed at about 48.84 s. The evaluation of the neutron emissivity in this discharge part is shown in figure 9.41. The mean discrepancy between retrofit and experimental data equals 9%. The neutron emissivity profiles during whole discharge have a maximum at the plasma core centre. No asymmetries are observed. A slight loss of intensity in the centre was found after the sawtooth crash and around 50 s. The hollowness is not clearly visible in the plot. The changes in the ion density and temperature profiles are presented in figure 9.42. The significant disruptions in the ions parameters measurement are not observed during MHD activity.

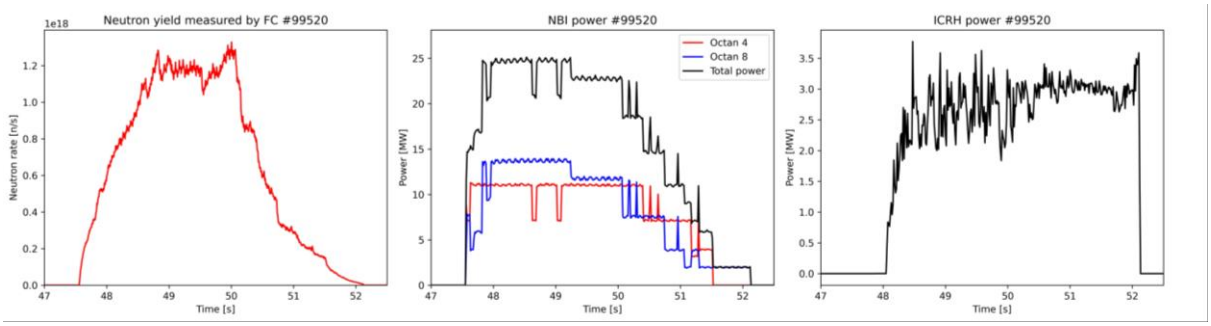

Figure 9.40. The total neutron yield measured by FC (left), NBI power (centre), and ICRH power (right) functions in time for discharges #99520.

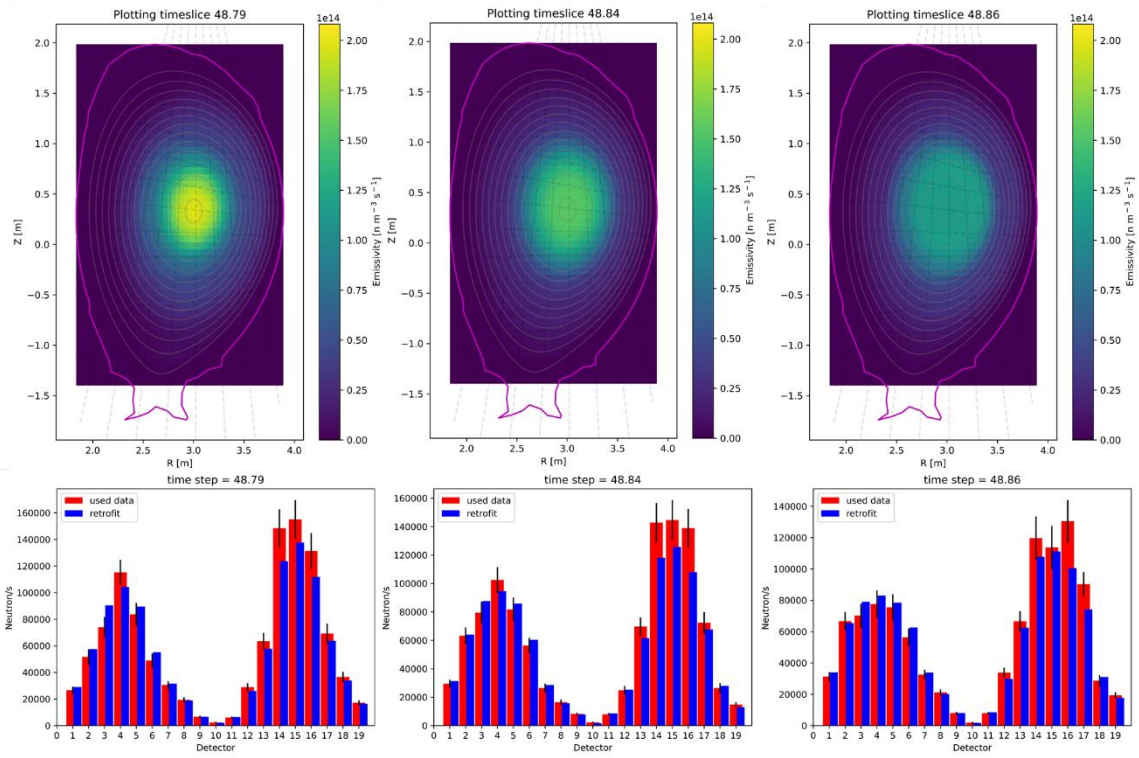

Figure 9.41. The neutron emission profiles reconstructed for time 48.79 s, 48.84 s, and 48.86 s in discharge #99520.

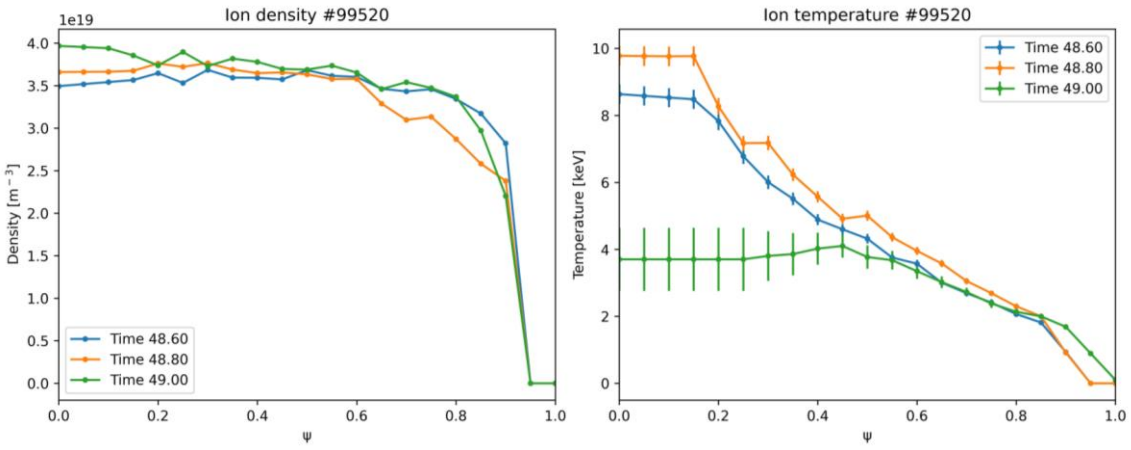

Figure 9.42. Ion density (left) and temperature (right) profiles measured during discharge #99520.

The parameters of discharge #99522 are presented in figure 9.43. The sawtooth crash occurs in 48.76 s. After that, the neutron rate decreases to the end of the discharge. During the total neutron yield rise, the hollowness and asymmetry with the domination of the emission on LFS are observed in the emission profiles. The evolution of the neutron emissivity distribution in part of the discharge with the sawtooth crash is presented in figure 9.44. Before triggering the MHD activity, the emission is strongly focused on the plasma core. After the sawtooth crash, neutron profiles are disrupted. The loss of intensity in the centre is observed. The retrofit and experimental data agreement are lower than the measurement uncertainty, equalled 10%. The maximal ion temperature is always in the plasma centre, and the hollowness observed in the ion density profile is negligible (see figure 9.45).

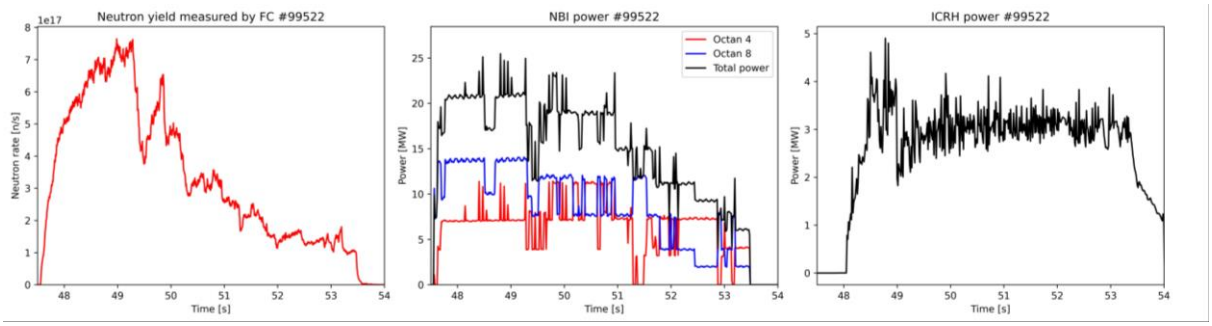

Figure 9.43. The total neutron yield measured by FC (left), NBI power (centre), and ICRH power (right) functions in time for discharges #99522.

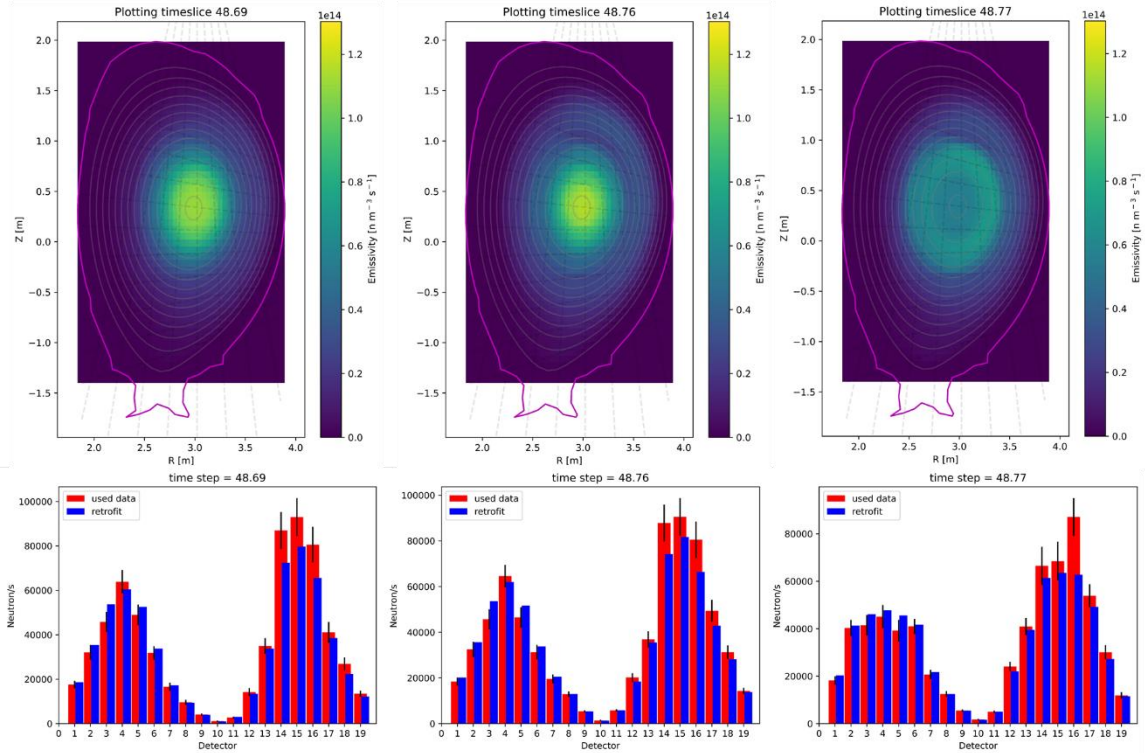

Figure 9.44. The neutron emission profiles reconstructed for time 48.69 s, 48.76 s, and 48.77 s in discharge #99522.

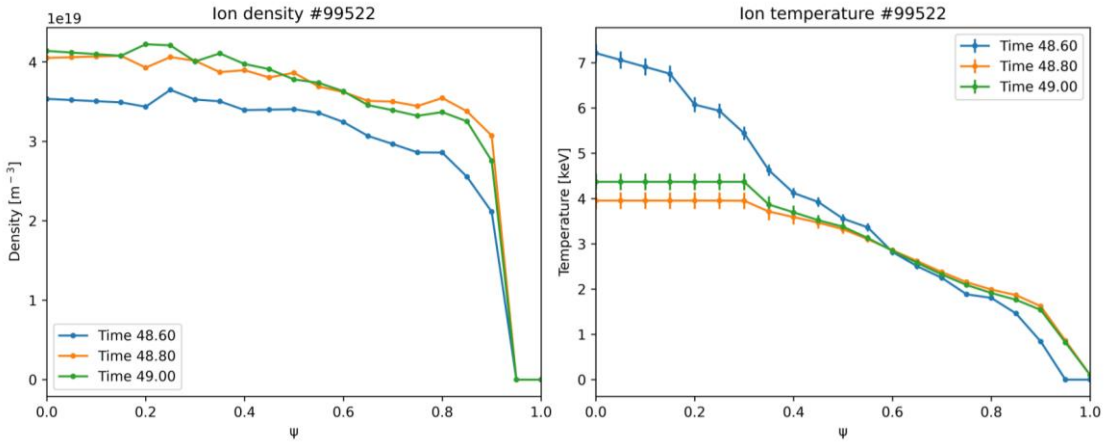

Figure 9.45. Ion density (left) and temperature (right) profiles measured during discharge #99522.

The changes in the neutron rate and heating power for discharge #99523 are presented in figure 9.46. The maximal total neutron yield is $1.6 \cdot 10^{18}$ n/s. The evolution of the neutron emissivity during the sawtooth crash in 49.73 s is shown in figure 9.47. Before triggering the MHD activity, the neutron emission was highly concentrated in the plasma centre. The hollowness occurs just after the sawtooth crash and is present up to 49.82 s. A slight asymmetry with higher intensity on HFS is also present. The neutron emission is stable with the maximal values in the plasma core centre in other discharge parts. The mean difference between retrofit and experimental data is about 9%. The ion density and temperature profiles are presented in figure 9.48. In the case of both parameters, a slight decrease in values in the plasma centre is observed.

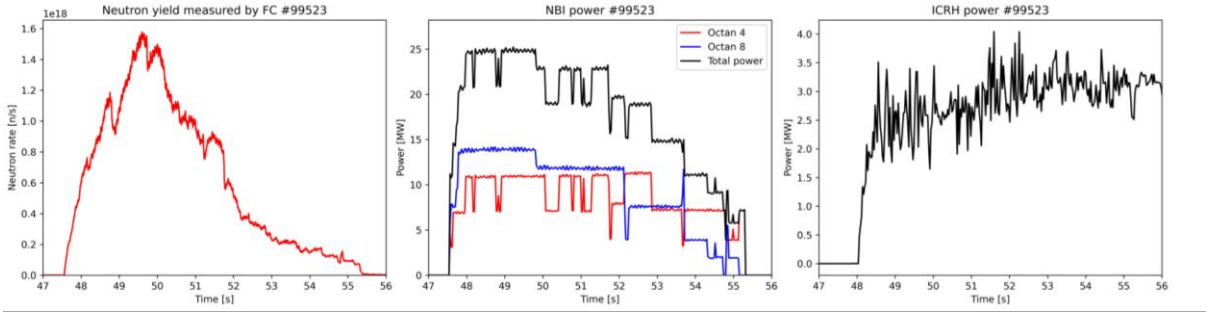

Figure 9.46. The total neutron yield measured by FC (left), NBI power (centre), and ICRH power (right) functions in time for discharges #99523.

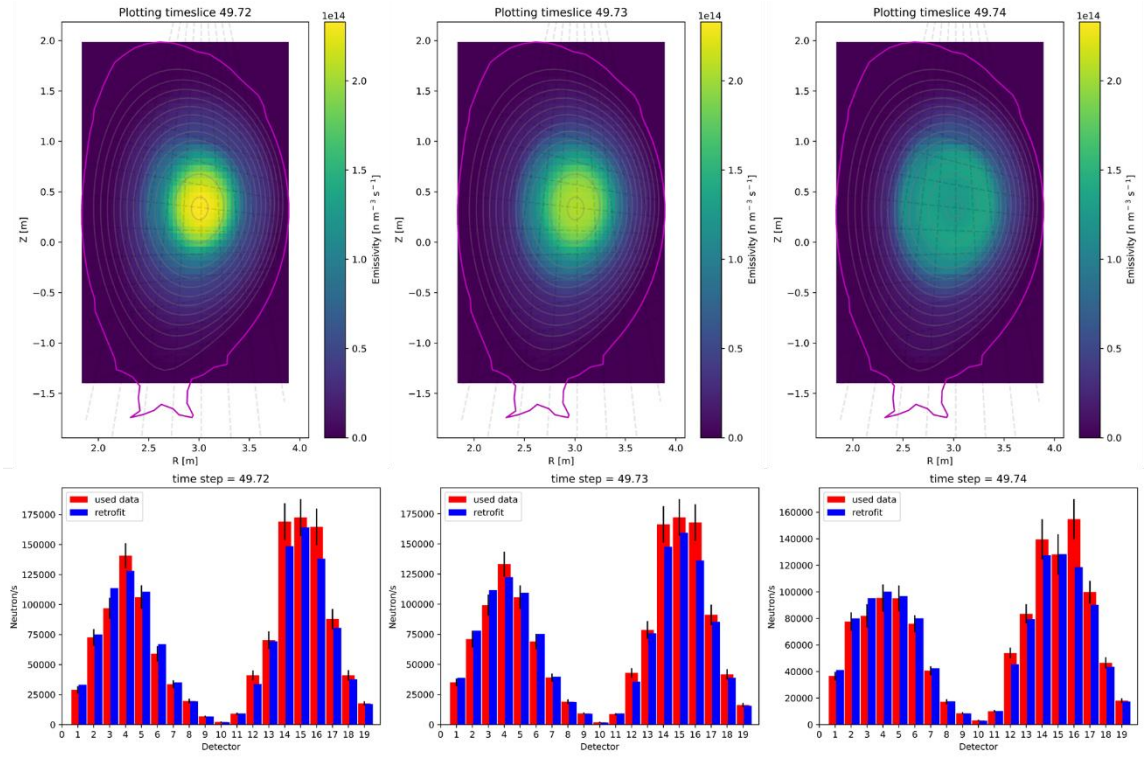

Figure 9.47. The neutron emission profiles reconstructed for time 49.72 s, 49.73 s, and 49.74 s in discharge #99523.

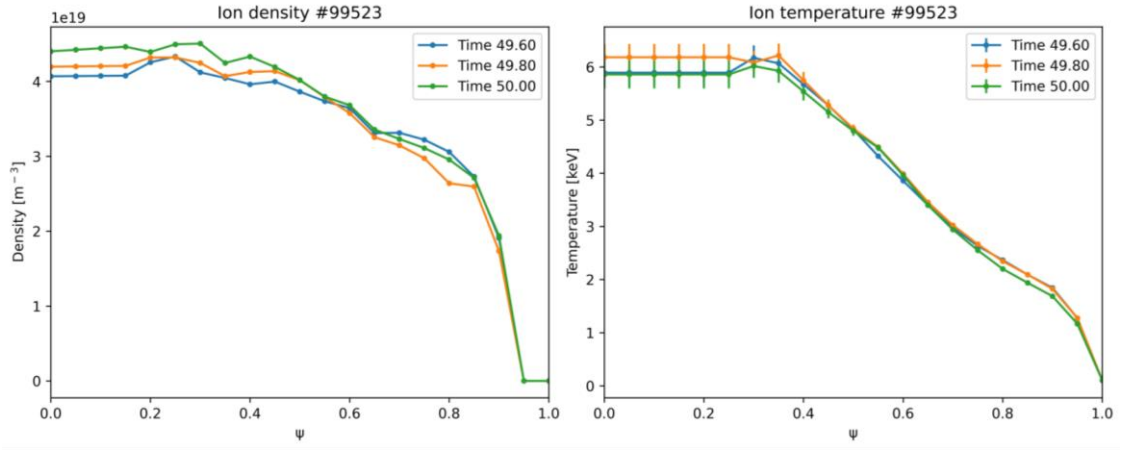

Figure 9.48. Ion density (left) and temperature (right) profiles measured during discharge #99523.

The total neutron yield and heating power for discharge #99797 are presented in figure 9.49. The discharge part with a rising neutron rate is long, 2 s. The neutron emission intensity drop is stepped. The evolution of the neutron emissivity distribution is shown in figure 9.50. The mean discrepancy between retrofit and measurement data is 9%. The neutron emission is stable with no asymmetries and maximal intensity in the plasma centre before the sudden neutron rate drop. After the significant total neutron yield change, the hollowness occurs. The disruption duration is less than 0.1 s. The effect is repeated for all neutron intensity falls. The ion density and temperature profiles are presented in figure 9.51. The hollowness in the temperature distribution occurs before the neutron rate drop.

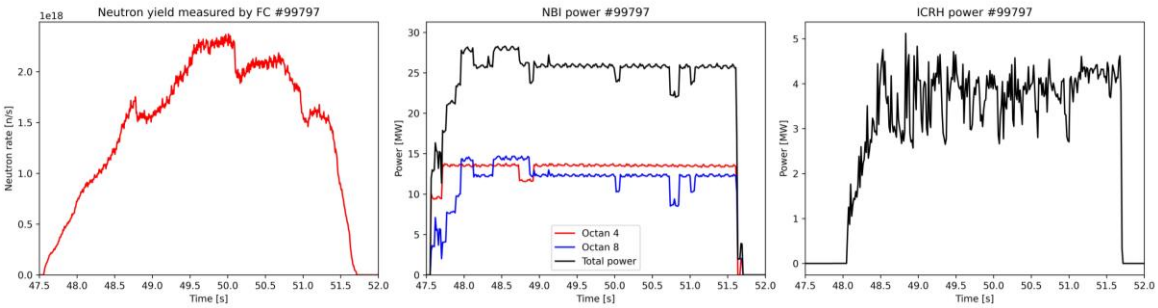

Figure 9.49. The total neutron yield measured by FC (left), NBI power (centre), and ICRH power (right) functions in time for discharges #99797.

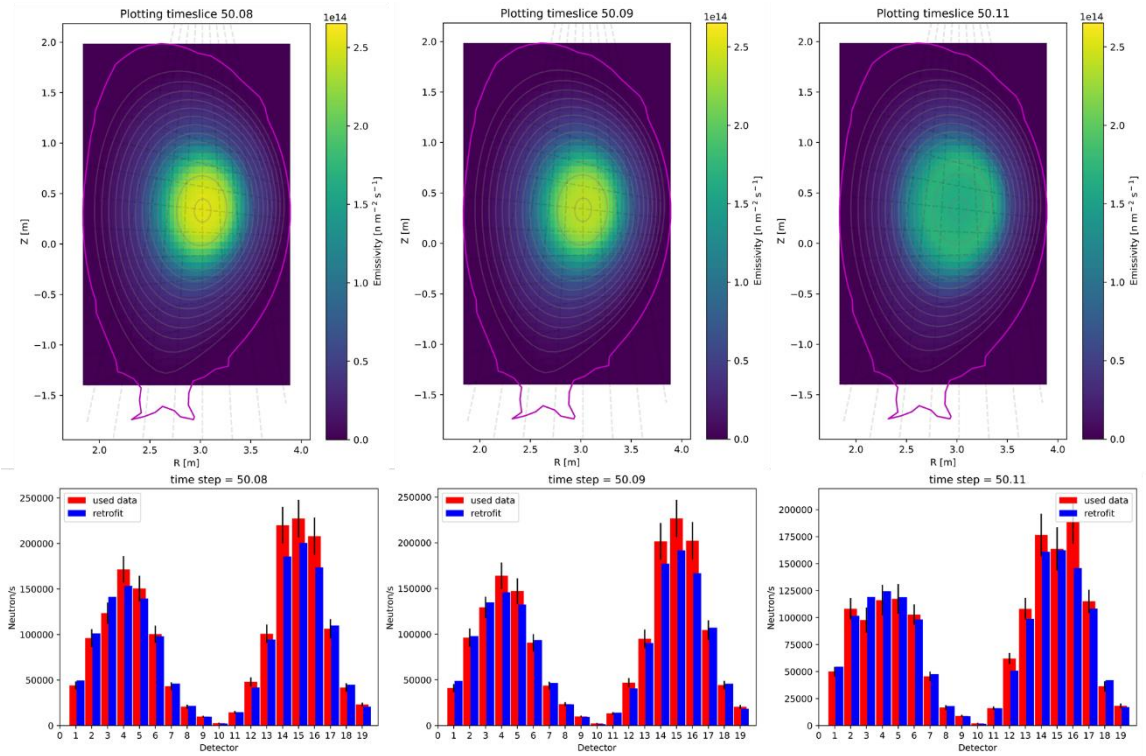

Figure 9.50. The neutron emission profiles reconstructed for time 50.08 s, 50.09 s, and 50.11 s in discharge #99797.

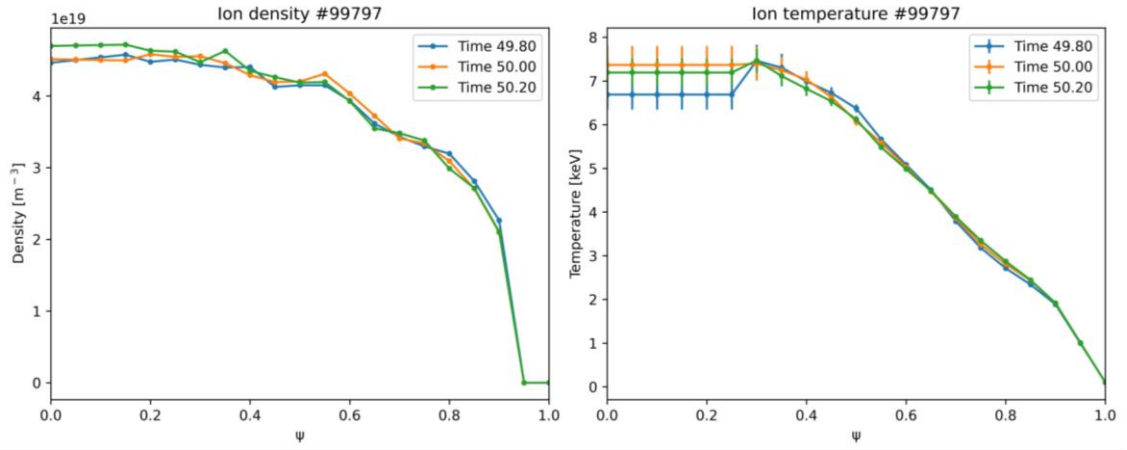

Figure 9.51. Ion density (left) and temperature (right) profiles measured during discharge #99797.

The neutron rate and heating power for discharge #99799 are presented in figure 9.52. In this case, the total neutron rate drop is connected with the loss of the NBI power. The evolution of the neutron emissivity distribution is shown in figure 9.53. The discrepancy between retrofit and experimental data varies from 1% to 20%. The neutron production is stable, with a broad emission area at the beginning of the discharge. Later the contraction of the emissivity region to the plasma core is observed. There is no hollowness or asymmetry in neutron emissivity after the neutron rate drop. The significant temperature decrease in the plasma centre is observed before the neutron rate drop (see figure 9.54). It is not reflected in the same effect in the neutron emissivity profiles.

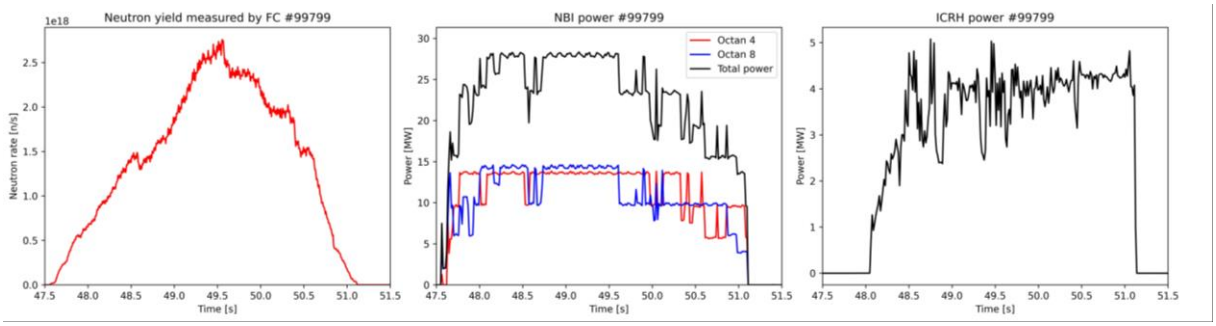

Figure 9.52. The total neutron yield measured by FC (left), NBI power (centre), and ICRH power (right) functions in time for discharges #99799.

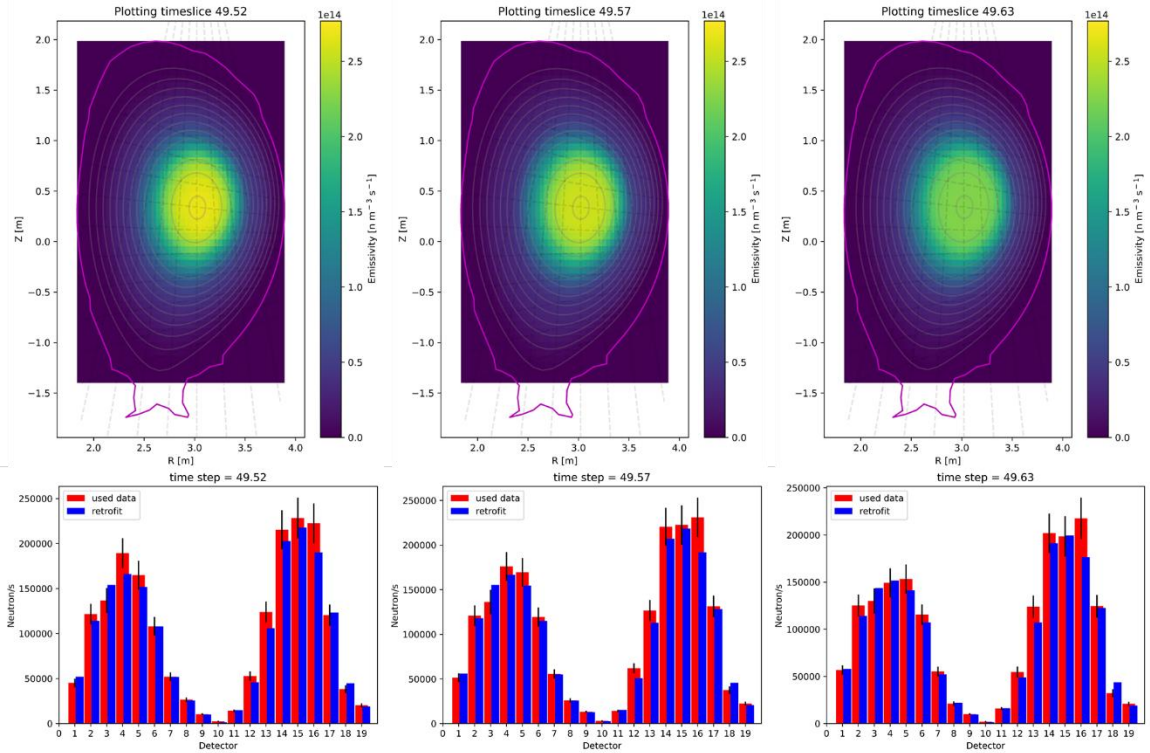

Figure 9.53. The neutron emission profiles reconstructed for time 49.52 s, 49.57 s, and 49.63 s in discharge #99799.

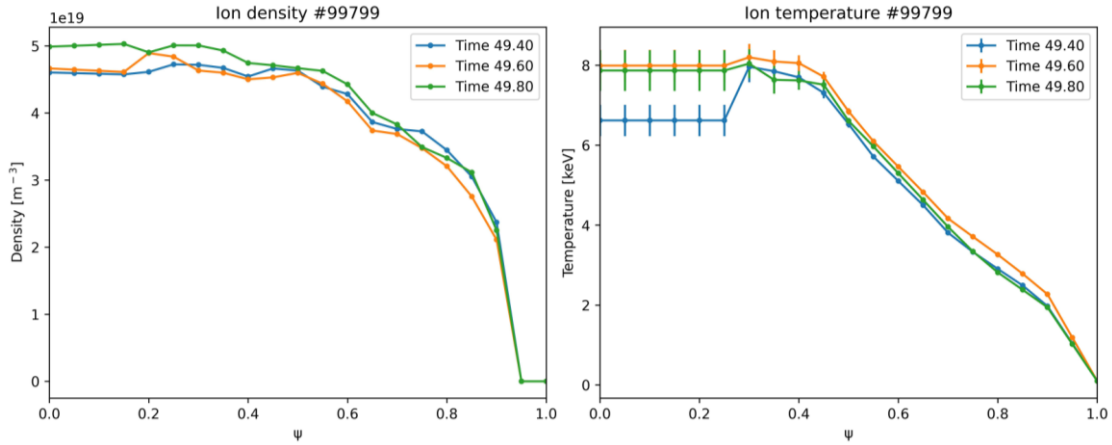

Figure 9.54. Ion density (left) and temperature (right) profiles measured during discharge #99799.

The total neutron yield and heating power for discharge #99861 are presented in figure 9.55. The neutron rate decrease is connected with plasma disruption in this case. The evolution of the neutron emissivity during the sawtooth crash in 49.9 s is shown in figure 9.56. The mean discrepancy between retrofit and measurement data is about 8%. The emissivity profiles are generally symmetric with maximal values inside the core centre. A couple of slightly hollow profiles are connected with the neutron rate fluctuations. The ion density and temperature profiles are presented in figure 9.57. No hollowness in the distributions was found.

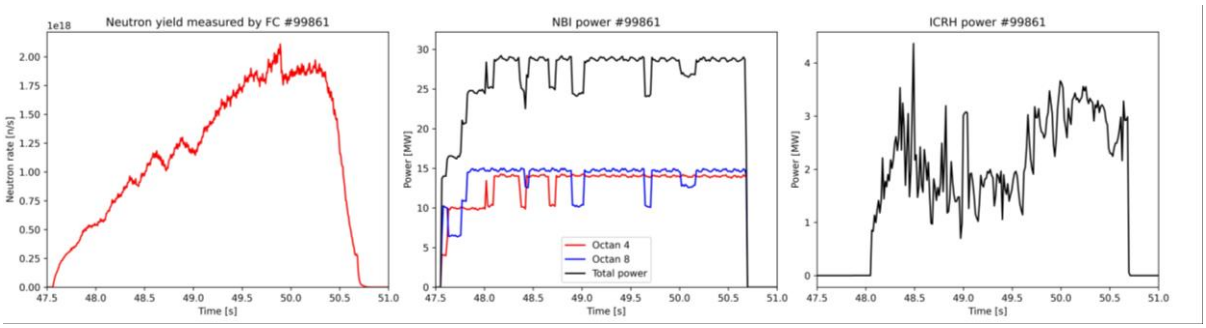

Figure 9.55. The total neutron yield measured by FC (left), NBI power (centre), and ICRH power (right) functions in time for discharges #99861.

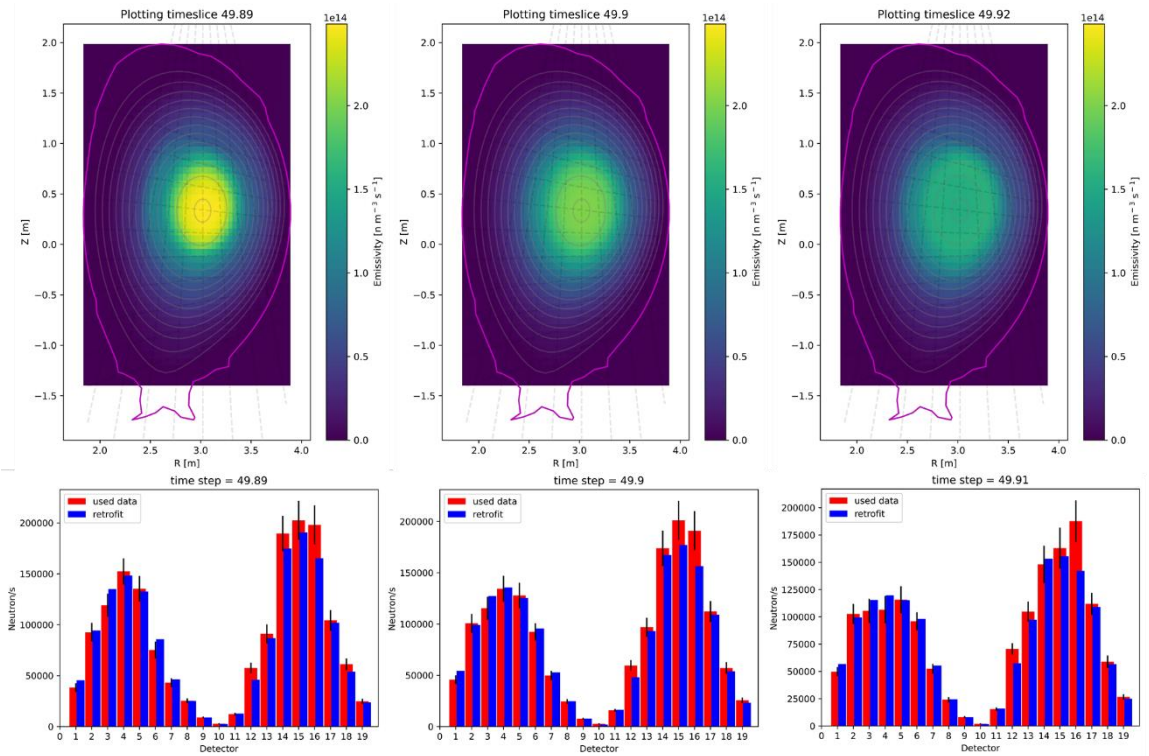

Figure 9.56. The neutron emission profiles reconstructed for time 49.89 s, 49.90 s, and 49.91 s in discharge #99861.

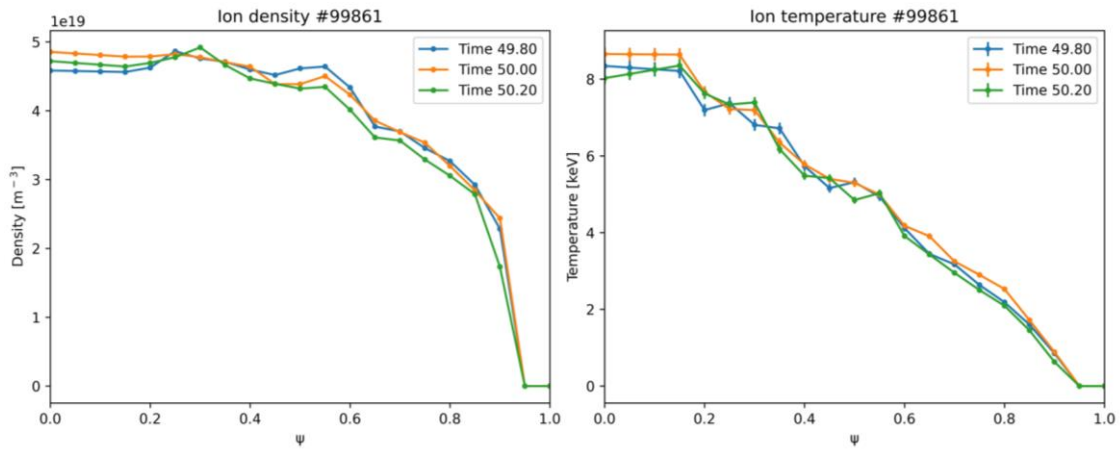

Figure 9.57. Ion density (left) and temperature (right) profiles measured during discharge #99861.

Figure 9.58 presents the neutron rate and heating power in discharge #99863. The neutron emission profiles are smooth and symmetric, with the maximum in the plasma core centre during the whole discharge. The absence of the disruptions in the neutron emissivity distribution is presented in figure 9.59. The mean agreement between the retrofit and experimental data equals 10%. There is no abnormal behaviour of neutron emissivity distribution connected with the sawtooth crash in 50.07 s of this discharge. The ion density and temperature profiles are also not significantly disrupted (see figure 9.60).

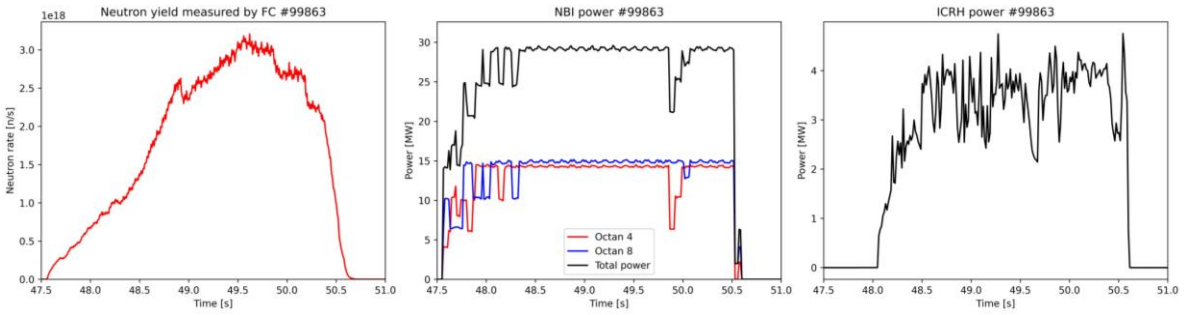

Figure 9.58. The total neutron yield measured by FC (left), NBI power (centre), and ICRH power (right) functions in time for discharges #99863.

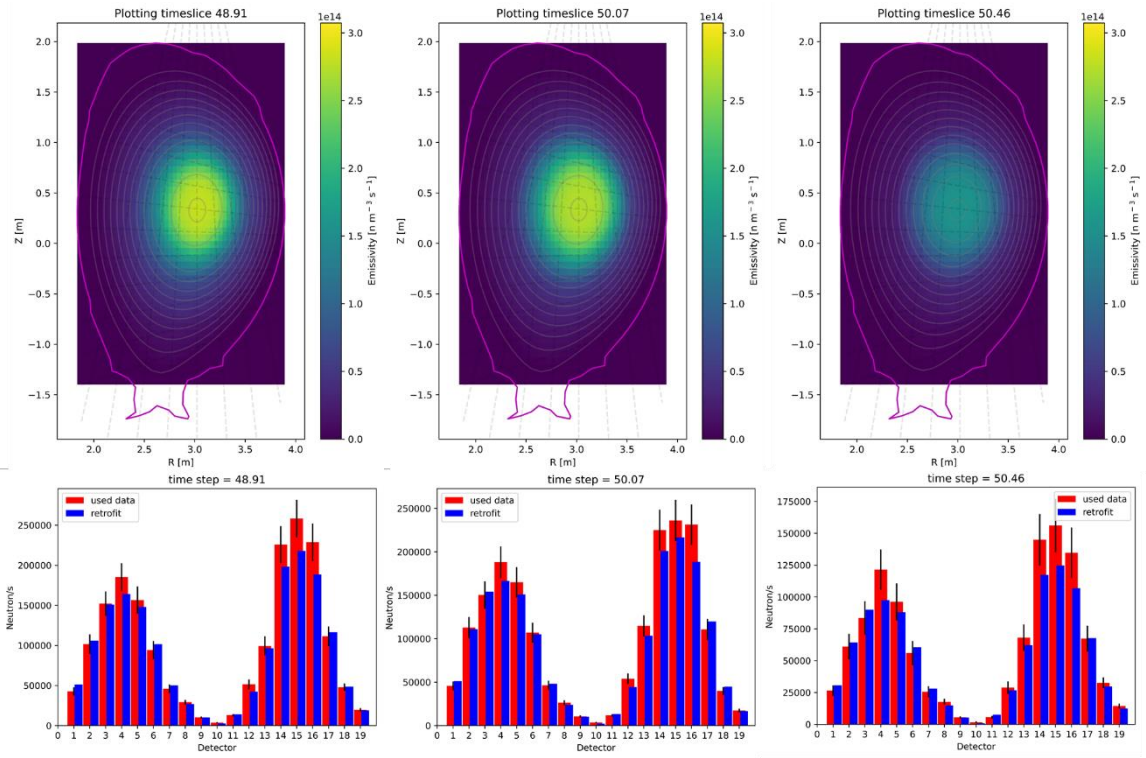

Figure 9.59. The neutron emission profiles reconstructed for time 48.91 s, 50.07 s, and 50.46 s in discharge #99863.

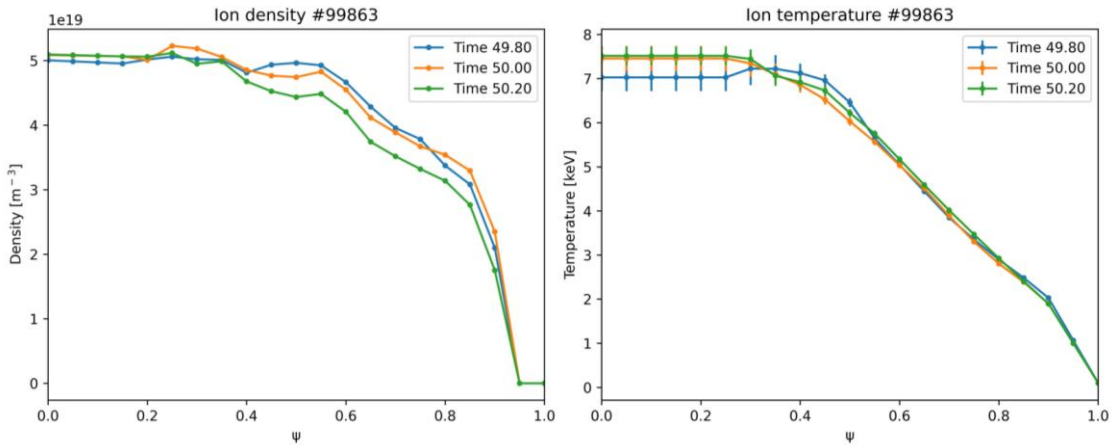

Figure 9.60. Ion density (left) and temperature (right) profiles measured during discharge #99863.

Discharge #99878 is similar to those previously analysed. The total neutron yield and heating power are presented in figure 9.61. The neutron rate increased up to disruption in 48.52 s. Then neutron intensity sharply drops to zero. The NBI heating system was shut down just after the sawtooth crash in 48.52 s. The evolution of the neutron emissivity distribution is shown in figure 9.62. The discrepancy for retrofit and experimental data is about 15%, which is higher than for other discharges. The reconstructed emission profiles are highly focused in the plasma core centre during the whole discharge. No disruption in the emissivity is observed. Significant hollowness was identified in the ion density profiles (see figure 9.63).

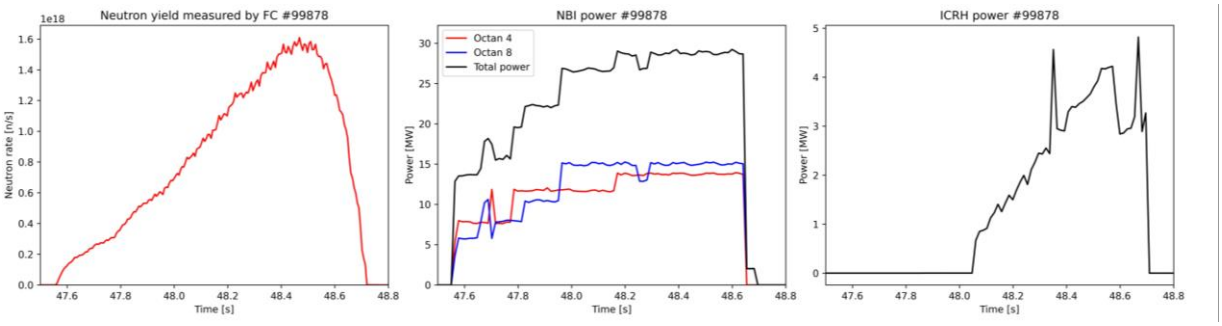

Figure 9.61. The total neutron yield measured by FC (left), NBI power (centre), and ICRH power (right) functions in time for discharges #99878.

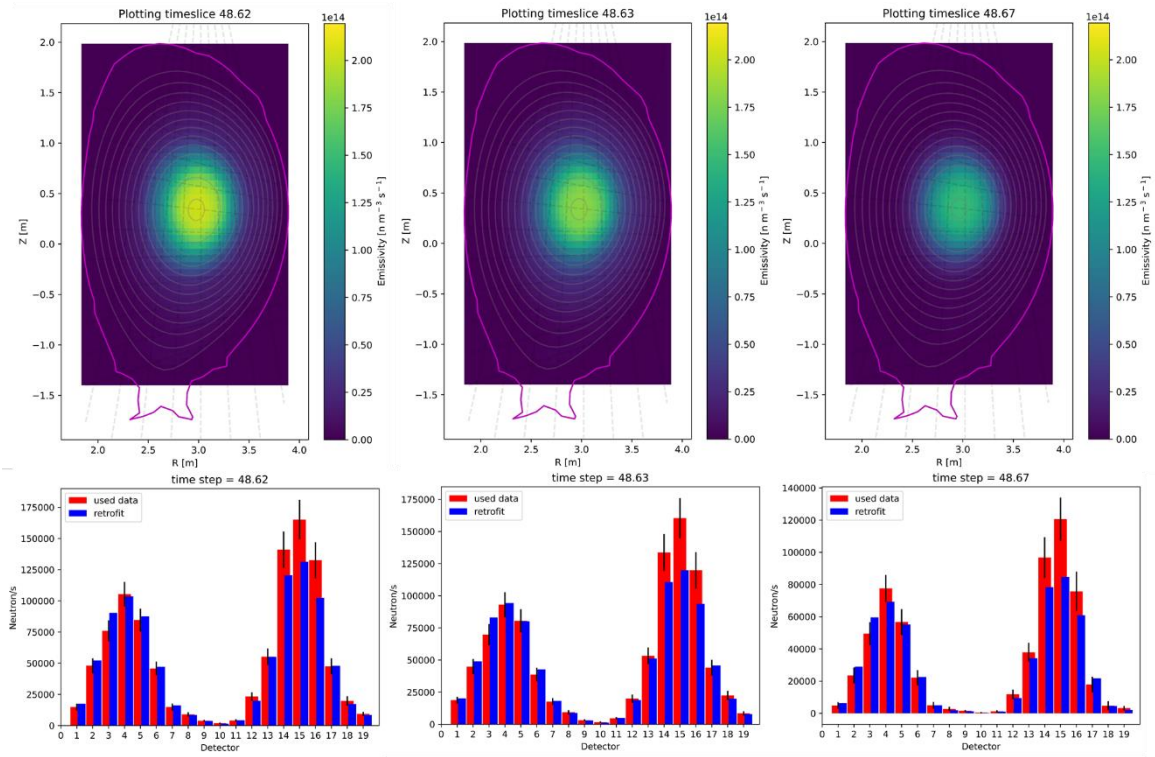

Figure 9.62. The neutron emission profiles reconstructed for time 48.62 s, 48.63 s, and 48.67 s in discharge #99878.

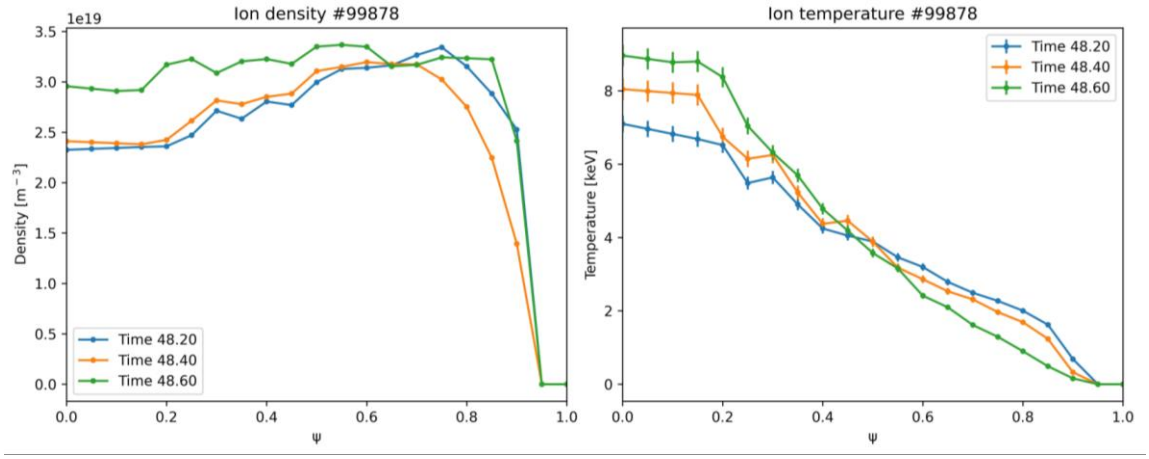

Figure 9.63. Ion density (left) and temperature (right) profiles measured during discharge #99878.

The total neutron yield and heating power for discharge #99916 are presented in figure 9.64. The MHD activity occurs in 50.07 s and 51.7 s. The evaluation of the neutron emissivity profiles during the sawtooth crash is shown in figure 9.65. In the whole discharge, slightly more neutron emission is observed on HFS. The effect is stronger after the sawtooth crash. No hollowness occurs in this discharge. The mean agreement between retrofit and measurement data is about 8%. Generally, the maximal ion density and temperature values are observed in the plasma centre before and after the sawtooth crash (see figure 9.66).

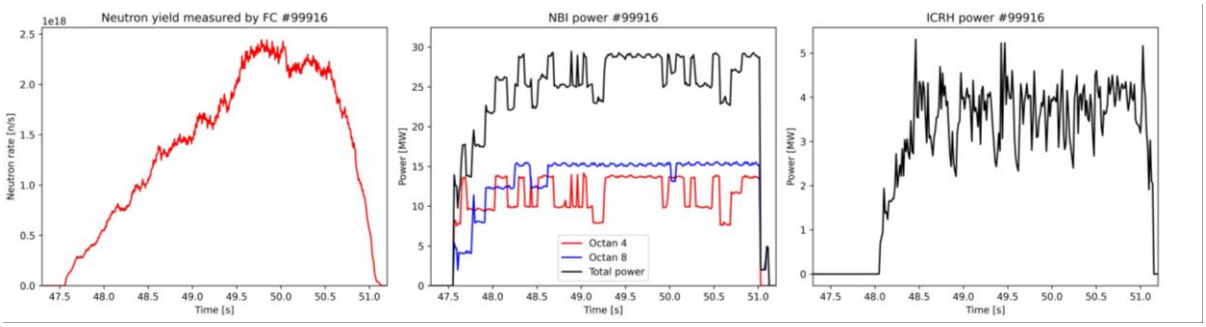

Figure 9.64. The total neutron yield measured by FC (left), NBI power (centre), and ICRH power (right) functions in time for discharges #99916.

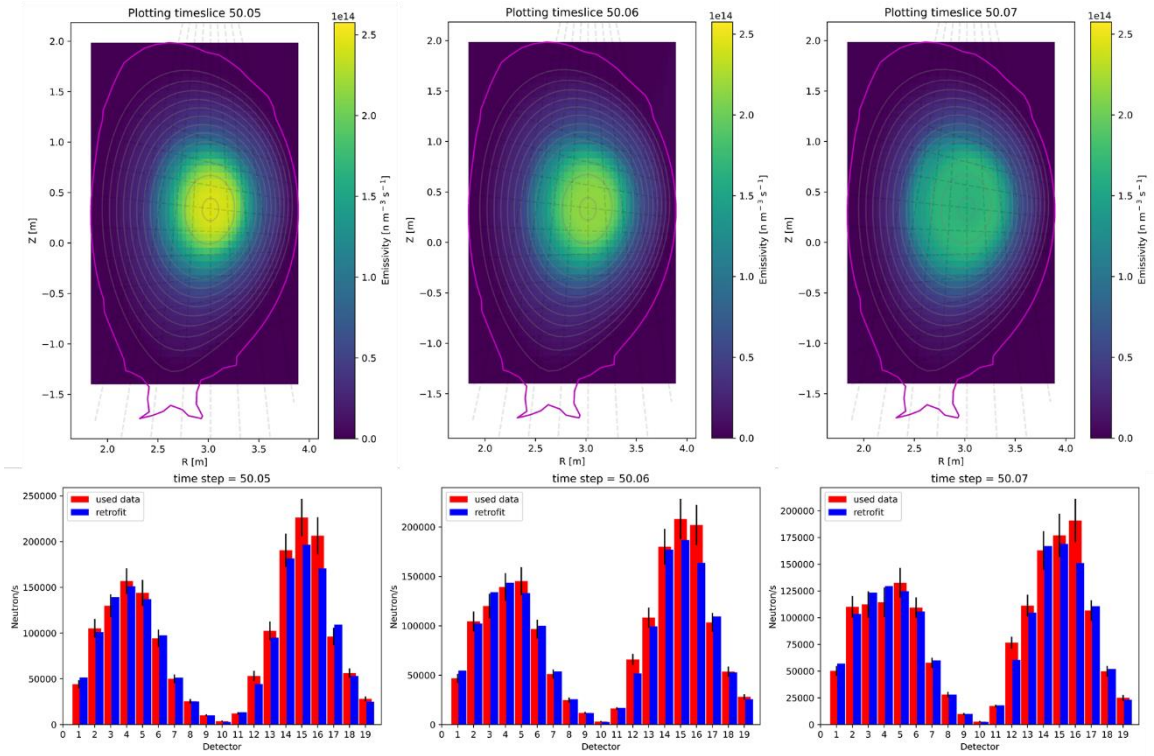

Figure 9.65. The neutron emission profiles reconstructed for time 50.05 s, 50.06 s, and 50.07 s in discharge #99916.

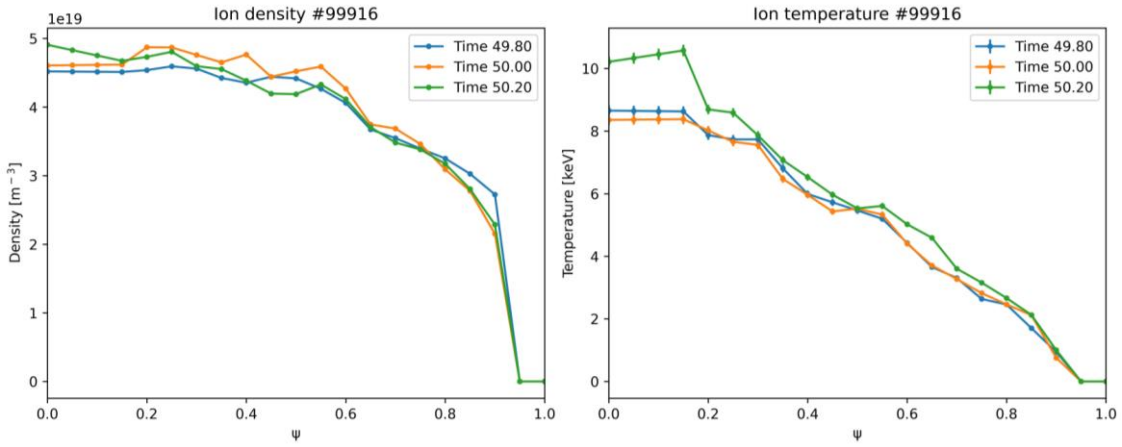

Figure 9.66. Ion density (left) and temperature (right) profiles measured during discharge #99916.

The neutron rate and heating power for discharge #99944 are presented in figure 9.67. The total neutron yield decrease is connected with the loss of the NBI beam power. The evolution of the neutron emissivity distribution is shown in figure 9.68. The mean discrepancy between retrofit and experimental data is about 7%. A few hollow neutron emissivity profiles occur in the first part of the discharge and after the neutron rate drop. The emission is symmetric with the maximum at the plasma centre in the other time slices. The ion density and temperature profiles are presented in figure 9.69. The hollowness in the temperature distribution occurs during the decrease of the neutron emission.

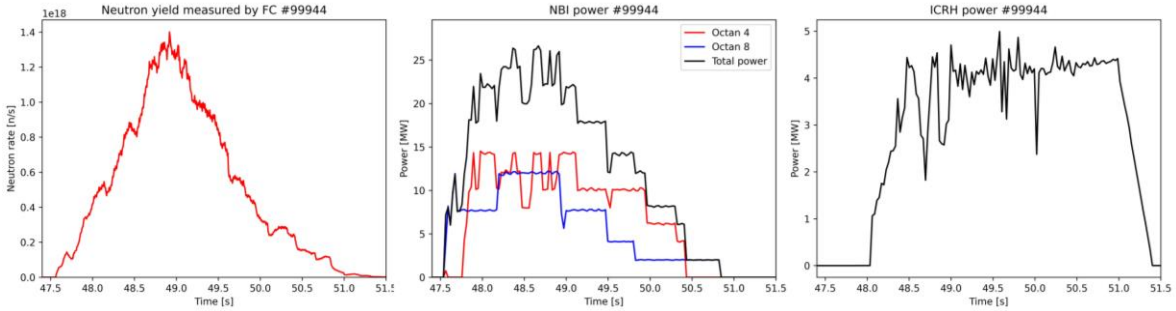

Figure 9.67. The total neutron yield measured by FC (left), NBI power (centre), and ICRH power (right) functions in time for discharges #99944.

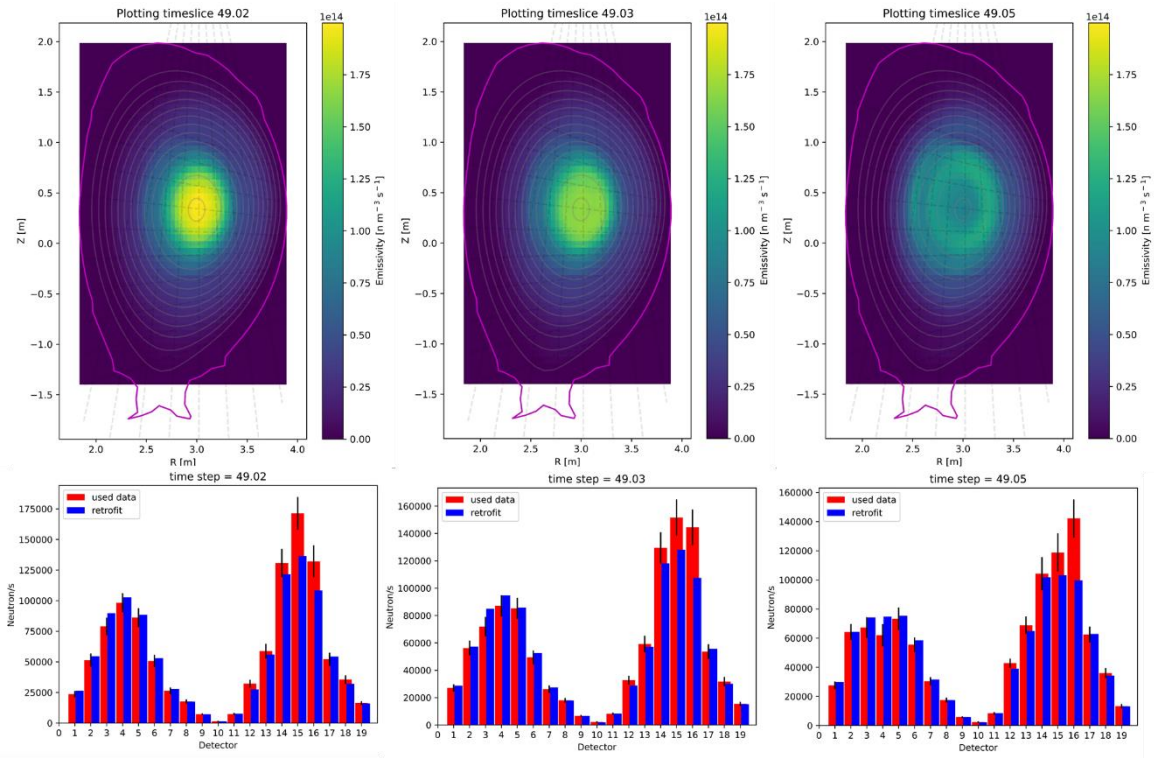

Figure 9.68. The neutron emission profiles reconstructed for time 49.02 s, 49.03 s, and 49.05 s in discharge #99944.

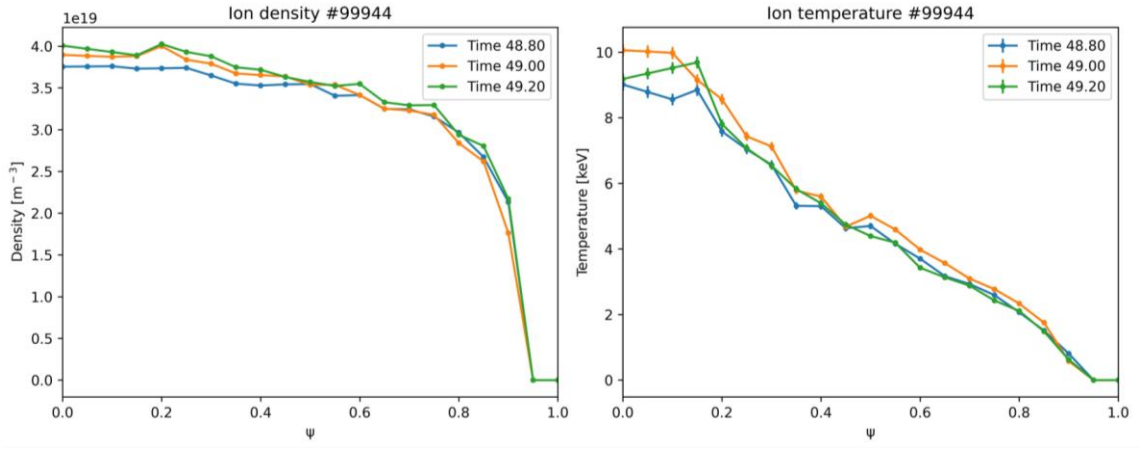

Figure 9.69. Ion density (left) and temperature (right) profiles measured during discharge #99944.

The last analysed discharge is #99945. The total neutron yield and heating power functions in time are presented in figure 9.70. The neutron rate drop is connected with the NBI beam power loss in 48.90 s. The evolution of the neutron emissivity profiles is shown in figure 9.71. In discharge #99945, slight asymmetry and hollowness frequently occur. For the total neutron yield in the range of 10^{18} n/s, there is a contraction of the emission area to the plasma core centre. The neutron rate sudden decrease is reconstructed in 49.03 s. The hollowness and more emissions on HFS are connected with the rapid change in the neutron intensity. The mean discrepancy between retrofit and experimental data is about 7%. The ion density and temperature profiles are smooth, with the maximum in the plasma centre (see figure 9.72).

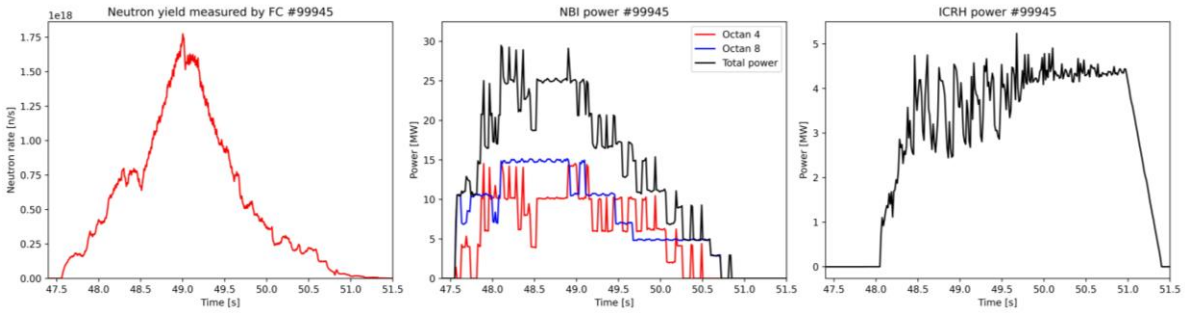

Figure 9.70. The total neutron yield measured by FC (left), NBI power (centre), and ICRH power (right) functions in time for discharges #99945.

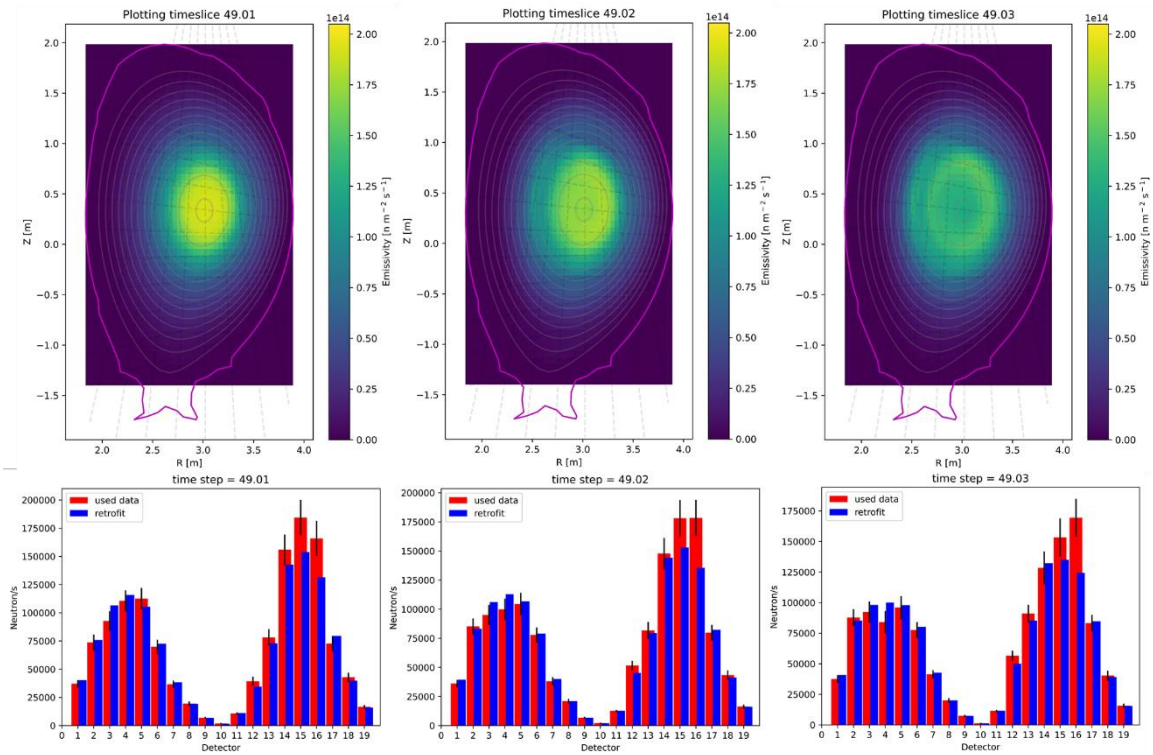

Figure 9.71. The neutron emission profiles reconstructed for time 49.01 s, 49.02 s, and 49.03 s in discharge #99945.

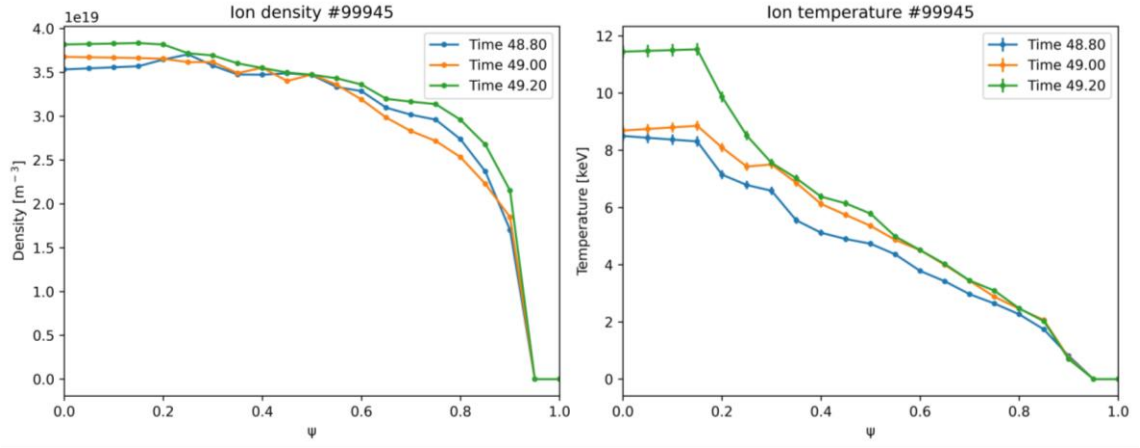

Figure 9.72. Ion density (left) and temperature (right) profiles measured during discharge #99945.

Various baseline scenario discharges have been analysed to investigate the sawtooth crash influence on the neutron emissivity distribution in JET. The reference deuterium discharges were compared with the DT results. In the deuterium plasma occurs the asymmetry with neutron production on LFS edge that is in agreement with the theory about ion transport during this MHD activity. This effect is not observed in the DT plasma. Therefore, the observed asymmetry is not proven to be connected with the physical phenomena or with the measurement background. It is possible that only deuterons are subjected to the precession and modified motion, which can be observed in the asymmetrical neutron emission profiles. However, it is also probable that the investigated effect was caused by scattered neutrons detected by the neutron camera. The sawtooth crash is connected with the sudden drop in the neutron rate. Therefore, the changes in the neutron emissivity profiles were investigated during the total neutron yield variations. In some analysed DT discharges, the neutron rate decrease has not been related to the MHD activity but the problems with heating power from the NBI system. In all discharges, the neutron emissivity was highly focused in the plasma core centre when the neutron production was the highest. During the sawtooth crash, no disruptions were found in the neutron emissivity distribution. The dynamics of the changes in the ion density and temperature profiles were too fast to be detected from the measurements with the time resolution of 200 ms. The hollowness in neutron emissivity occurs after the MHD activity and the neutron rate drop. The loss of neutron intensity in the plasma core centre was not observed in all discharges. The hollowness of the neutron profiles is not reflected in the ion temperature distribution, which has lower time resolution. The disruption in the ion density profiles is observed only in one discharge The same effect is seen for the total neutron yield decrease connected with the NBI power loss but is highly correlated with the temperature decrease in the plasma core. The problem needs to be further investigated. The sawtooth crash has no influence on the neutron emissivity in JET, or the time resolution of the neutron camera is not high enough to measure it. The theory about ion transport presented in [Kol1996] disagrees with the DT campaign's experimental observation.

Chapter 10: Reconstruction of the neutron spectra from activation measurement

Another example of the ill-posed inverse problem in interpreting the neutron diagnostics measurement results on fusion devices is a reconstruction of the neutron spectrum. The methods used in neutron tomography can be applied to analyse the data from activation measurement.

The neutron spectrum determination cannot be done by a direct measurement. The energy of the particles might be reconstructed from measurement by the time of flight or proton recoil methods. The alternative approach is the use of the neutron activation technique. It does not require a huge system like in diagnostics based on the time of flight measurement and is not sensitive to gamma radiation, magnetic field, and temperature like scintillators. The reconstruction of the neutron spectrum is based on the known cross-sections for induced reactions and dedicated inversion methods. The problem is one-dimensional, but the amount of experimental data is very limited.

The neutron spectrum determination in tokamaks can be used for:
- fast ions transport studies,
- ion temperature estimation,
- triton burn-up studies,
- detection of the neutrons associated with runaway electrons,
- monitoring the neutron production from different reactions, also involving fuel and impurities [Jar1994].

The characterisation of the portable neutron generators allows for monitoring the changes in neutron emission in time due to isotope content in the beams and targets. The neutron spectrum determination provides information about reactions that take place in NG. The molecular ion presence or accumulation of the isotopes on the target influences the measured energies. The neutron spectrum can also change due to the radioactive decay and a decrease in tritium amount. The characterisation of NGs is required to calibrate neutron diagnostics and interpret the experimental results.

This chapter aims to reconstruct the neutron spectra emitted by two kinds of neutron generators to investigate the physical phenomena connected with a long-term operation that influences neutron production characteristics. The author of the thesis took part in the experiment concerning the neutron generator Gradel-Fusion NSD 35 2-DT-C-W and analysed the data collected for the Sodern Genie 16C.

The algorithms described in chapter 5 are used to reconstruct the neutron spectrum from the result of activation measurement. The activation method is based on irradiating different materials in the neutron flux (see subchapter 3.1). The induced radioactivity is measured by gamma spectrometry. The activity at the end of irradiation can be calculated from equation (3.1.3). The threshold reactions in different materials supply information on the number of neutrons above specific energy. The activation data in connection with the reaction cross-section allows for a reconstruction of the neutron spectrum with a large number of energy bins. The contribution matrix elements are calculated as activity per single neutron with specified energy (see chapter 6) from equation (6.1). The cross-sections for each reaction were taken from the TENDL-2017 nuclear data library [Kon2012] and have been interpolated to the used bin structures. The procedure of the neutron spectrum reconstruction has high uncertainty. The error sources are: measurement uncertainties, interpolation of the cross-section distribution, and reconstruction methods. In the presented analysis, the reconstruction error was estimated by the evaluation of the synthetic data. The basis of the calculations are two types of accuracy:

$$accuracy_s = \frac{S_R - S_S}{S_S} \tag{10.1}$$

$$accuracy_a = \frac{A_R - A_S}{A_S} \tag{10.2}$$

where S_R is the reconstructed spectrum, S_S is the spectrum used to simulate the synthetic data, A_S is the synthetic activity, in the analysis of the experimental data, has been replaced with measurement activity, and A_R is the activity simulated for the reconstructed spectrum.
The ratio of two accuracies is defined as:

$$C_R = \frac{mean(accuracy_s)}{mean(accuracy_a)} \tag{10.3}$$

The procedure and nomenclature used in this chapter are presented in figure 10.1. The synthetic A_S and reconstructed A_R activity have been obtained by the FISPACT-II inventory code [Sub2017] with cross-section data from the TENDL-2017 nuclear data library [Kon2012]. If the used spectrum was not compatible with FISPACT-II, the conversion was made by the FISPACT-II flux_convert script. The code has provided the uncertainty of the simulated activity. Details about calculations can be found in the code's manual [Sub2015].

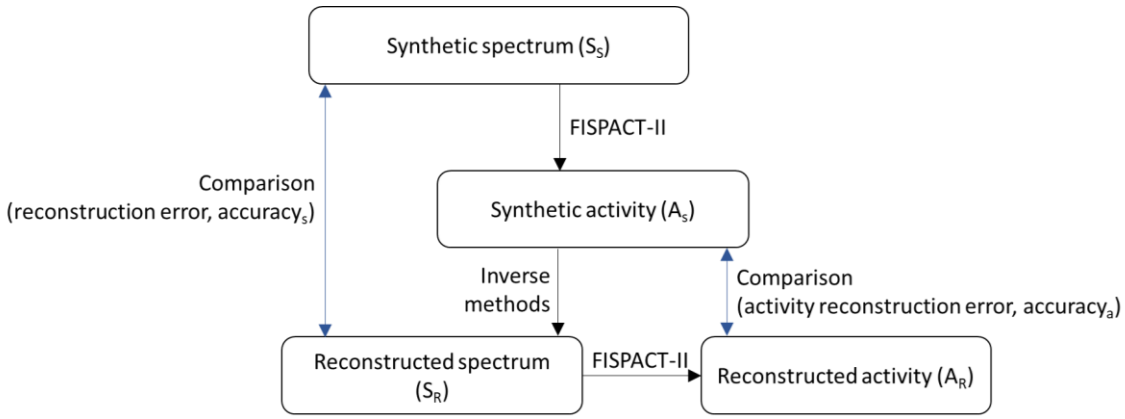

Figure 10.1. Synthetic data analysis methodology for the estimation of the reconstruction uncertainty.

In the analysis of the experimental data, instead of the synthetic activity from FISPACT-II code, the measurement results are used as A_S and compared with reconstructed activation to estimate the uncertainty of calculations. The identical default spectra have been used in both experimental and synthetic analysis. The lower limit of the neutron energy was set as the minimum reaction threshold because the measured activity cannot originate from reactions with neutrons of lower energy. The upper limit was set to 17 MeV because neutron generators cannot produce neutrons with higher energy. The energy bins outside this range are set to zero.

In subchapter 10.1, the analysis of neutron spectra emitted by Gradel-Fusion NSD 35 2-DT-C-W is presented. The neutrons from the generator based on the plasma source were measured by the activation method with radioactivity monitoring by a $LaBr_3$(Ce) (BrilLanCe) scintillation spectrometer. The results of the experiment were described in [Mik2018b], [Kwi2019] and [Mik2021b]. In subchapter 10.2, the results for another type of NG (Sodern Genie 16C) are described. For the activity measurement, an HPGe spectrometer was used, which improved the precision of the data. The experiment is described in [Las2020] and the neutron spectrum reconstruction analysis in [Mik2022b].

10.1 Neutron generator Gradel-Fusion NSD 35 2-DT-C-W

The experiment with the neutron generator Gradel-Fusion NSD 35 2-DT-C-W (described in subchapter 2.3.2) was carried out at National Centre for Nuclear Research in Świerk (NCBJ, Poland). The author of the thesis took part in the measurements. The experiment aimed to

determine neutron source characteristics by the activation method and track detectors [Dur1987]. The activation measurement was used to test the ability of neutron spectrum reconstruction using codes based on TR, MFI, MaxEnt, and ML methods and evaluate the generator exploitation.

10.1.1 Neutron activation measurement

The activation method requires a careful selection of the foils materials. The threshold energy for reactions on the activation foils needs to cover the required range and have a relatively high and well-known cross-section without resonances. The reactions product should have a sufficiently long half-life time and emit gamma radiation of the measurable energy with a satisfying resolution to provide measurement with required uncertainty. In this experiment, Al, Zn, Fe, Ni, Zr, and Au cylindrical samples (foils of 2 mm thickness) have been used. The properties of reactions on the selected foils and their products are presented in table 10.1. The reactions energy thresholds focus on the 14-MeV neutrons, but some of them allow for the measurement also 2.5-MeV neutrons. Figure 10.2 shows the reaction cross-section as a function of energy.

Table 10.1. Properties of the nuclear reactions on the selected activation foils and their products for the experiment with Gradel-Fusion NSD 35 2-DT-C-W and Sodern Genie 16C.

Sample	Reaction	Threshold energy [MeV]	Half-life	Gamma ray energy [MeV]
Al	$^{27}Al(n,p)^{27}Mg$	1.8	9.5 min	0.843 / 1.014
	$^{27}Al(n,\alpha)^{24}Na$	3.2	15 h	1.368 / 2.754
Zn	$^{64}Zn(n,2n)^{63}Zn$	12.0	38.5 min	0.511
Fe	$^{56}Fe(n,p)^{56}Mn$	2.9	2.6 h	0.846 / 1.810
Ni	$^{58}Ni(n,2n)^{57}Ni$	12.4	35.6 h	0.511 / 1.337
Zr	$^{90}Zr(n,2n)^{89}Zr$	12.1	78.4 h	0.511 / 0.909
	$^{90}Zr(n,p)^{90m}Y$	2.6	3.19 h	0.202 / 0.479
Au	$^{197}Au(n,2n)^{196}Au$	8.1	6 days	0.355
Mg	$^{24}Mg(n,p)^{24}Na$	4.9	15 h	1.368 / 2.754
Nb	$^{93}Nb(n,2n)^{92m}Nb$	9.1	10.25 days	0.934

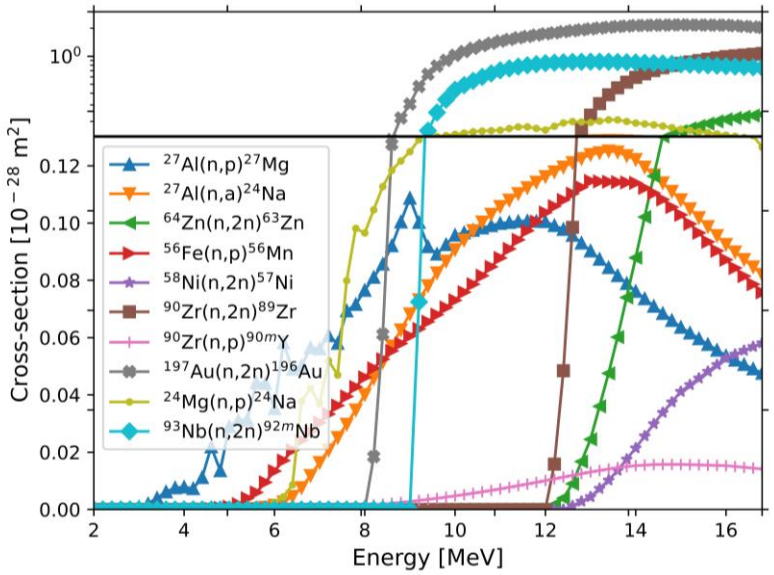

Figure 10.2. Reaction cross-sections for foils selected for experiment with neutron generators [Kon2012].

The samples were placed individually directly on the NG at the same radial distance from the centre of the emission zone to maximise the flux and reduce the influence of scattered neutrons. The measurement by the track detectors indicated that the neutron flux in various positions changes at a maximum of 10%, which is a statistically insignificant difference [Kwi2019]. Therefore, the emission of the neutrons was assumed as isotropic around the NG's reaction chamber. The solid angle connected with the foil and chamber sizes was considered in the calculations. The neutron generator during the experiment was placed in the centre of the large hall to minimise the backscatter neutrons influence on the measurement result.

The irradiation lasted 4 hours with a continuous flux of $2.5 \cdot 10^8$ n/s in 4π (neutron flux was given by the producer). The activity of the samples was measured by the BrilLanCe 380 (2"x2") scintillation detector, equipped with a $LaBr_3(Ce)$ crystal of energy resolution of 3.5% at 662 keV and 2.9% at 1332 keV and 43% efficiency [Bri2009], and Tukan8k multichannel analyser [Tukan]. ^{138}La present in the crystal produces background radiation, limiting the energy that can be measured with low uncertainty. The foils were measured separately after different cooling times (see table 10.2). The products with a short half-life were measured at first. The example of the measured spectrum for Zn is presented in figure 10.3. The peak originated from the scintillator component ^{138}La with energy 1435 keV can be observed in the spectrum. This peak was additionally used in the channel-energy calibration of the spectrometer. The background was subtracted from the measured spectra before activity calculations.

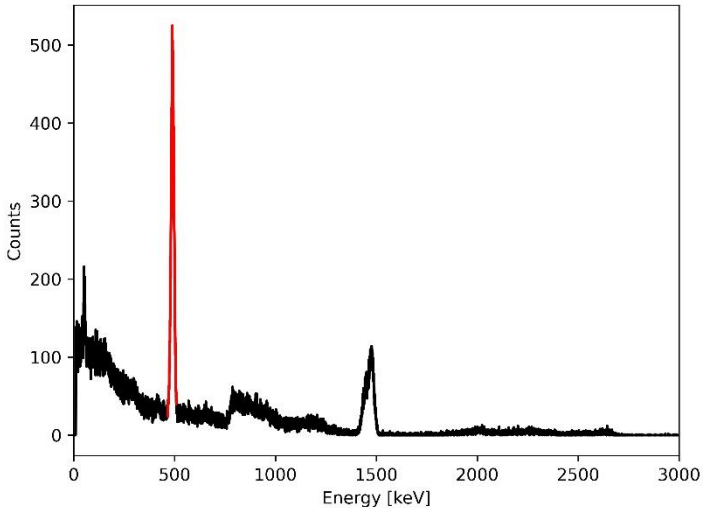

Figure 10.3. The gamma-ray spectrum of Zn sample after 4 h irradiation in the neutron flux emitted by Gradel-Fusion NSD 35 2-DT-C-W measured by the BrilLanCe scintillation detector (red peak corresponds to the activity of ^{63}Zn).

The scintillator efficiency has been calculated by Monte Carlo simulation with PHITS code [Sat2013], including the sell-absorption and geometry, and combined with measurement of the certified point sources containing ^{54}Mn, ^{65}Zn, and ^{60}Co isotopes. The maximum difference between these two methods was 10%. Table 10.2 contains the specific activity calculated at the end of the irradiation and its uncertainty. A high uncertainty of the ^{24}Na activity is connected with the presence of very short-lived radioisotopes that emit gamma radiation of similar energy in the Al sample at the beginning of the measurement. All experimental results are used in the deconvolution codes analysis. The algorithms should consider the influence of the uncertainty, which varies strongly for experimental results obtained by the BrilLanCe scintillation detector.

Table 10.2. The results of the neutron activation measurement of Gradel-Fusion NSD 35 2-DT-C-W measured by the BrilLanCe scintillation detector.

Sample	Reaction	Cooling time	Measurement time	Specific Activity [kBq/g]	Uncertainty [%]
Al	$^{27}Al(n,p)^{27}Mg$	7 min 18 s	15 min	2.99	10
	$^{27}Al(n,\alpha)^{24}Na$			0.81	36
Zn	$^{64}Zn(n,2n)^{63}Zn$	23 min 5 s	20 min	0.91	10
Fe	$^{56}Fe(n,p)^{56}Mn$	1 h 14 min 58 s	34 min	2.14	10
Ni	$^{58}Ni(n,2n)^{57}Ni$	19 h 15 min	5 h 45 min	0.10	11
Zr	$^{90}Zr(n,2n)^{89}Zr$	2 min 20 s	30 min	0.21	19
	$^{90}Zr(n,p)^{90m}Y$			0.17	13
Au	$^{197}Au(n,2n)^{196}Au$	1 h 51 min 17 s	15 h	0.61	17

10.1.2 Neutron spectrum reconstruction

The analysis of the synthetic data is presented in the following subchapter. It was used to investigate the reconstruction uncertainty connected to the methods used and indicate the lowest error of the algorithm. The relation between accuracies C_R has been defined for evaluation of the reliability of the calculations. The influence of the errors in the reconstructed spectrum on the activation simulation was analysed. The ratio C_R has been used to estimate the uncertainty of the methods and their relation with $accuracy_a$, the parameter that can be determined for experimental data. The reconstruction of the neutron spectrum from the experimental data is described in detail in subchapter 10.1.2.2.

10.1.2.1 Synthetic data analysis

The neutron spectrum energy considered in the analysis is from 1.8 MeV to 17 MeV. The emission outside this energy range is approximately zero. The ability of the neutron spectrum reconstruction has been analysed with four bin structures. Three energy distribution configurations compatible with the FISPACT-II code were selected for the tests (see figure 10.4):

- 9 bins spectrum (originated from the 66 elements spectrum from [Sub2015]),
- 16 bins spectrum (originated from the 172 elements spectrum from [Sub2015]),
- 51 bins spectrum (originated from the 175 elements spectrum from [Sub2015]).

The neutron emission intensity is nonzero in all bins inside the considered energy range. During the reconstruction, elements equal to zero usually do not change. Therefore, they are not implemented in the default spectrum. Additionally, the spectrum of 71 bins in the energy range of 2 – 16 MeV with evenly 200 keV spacing was also analysed. The influence of the bin structure conversion to be compatible with FISPACT-II was considered. The overall difference between spectra before and after modification was below 5% for a few tested cases. The errors in the conversion were connected to the discrepancy between energy distribution, e.g. one new bin contained parts of two previous bins.

Three default spectra with a dominant energy peak around 14-MeV have been prepared (see figure 10.5). Spectrum I was provided by the producer from measurement by stilbene scintillator [private communication]. Spectrum II is a result of Monte Carlo simulation of the sealed tube NG [Cuf2017]. The last spectrum (III) is the mean value of these two with an additional random noise.

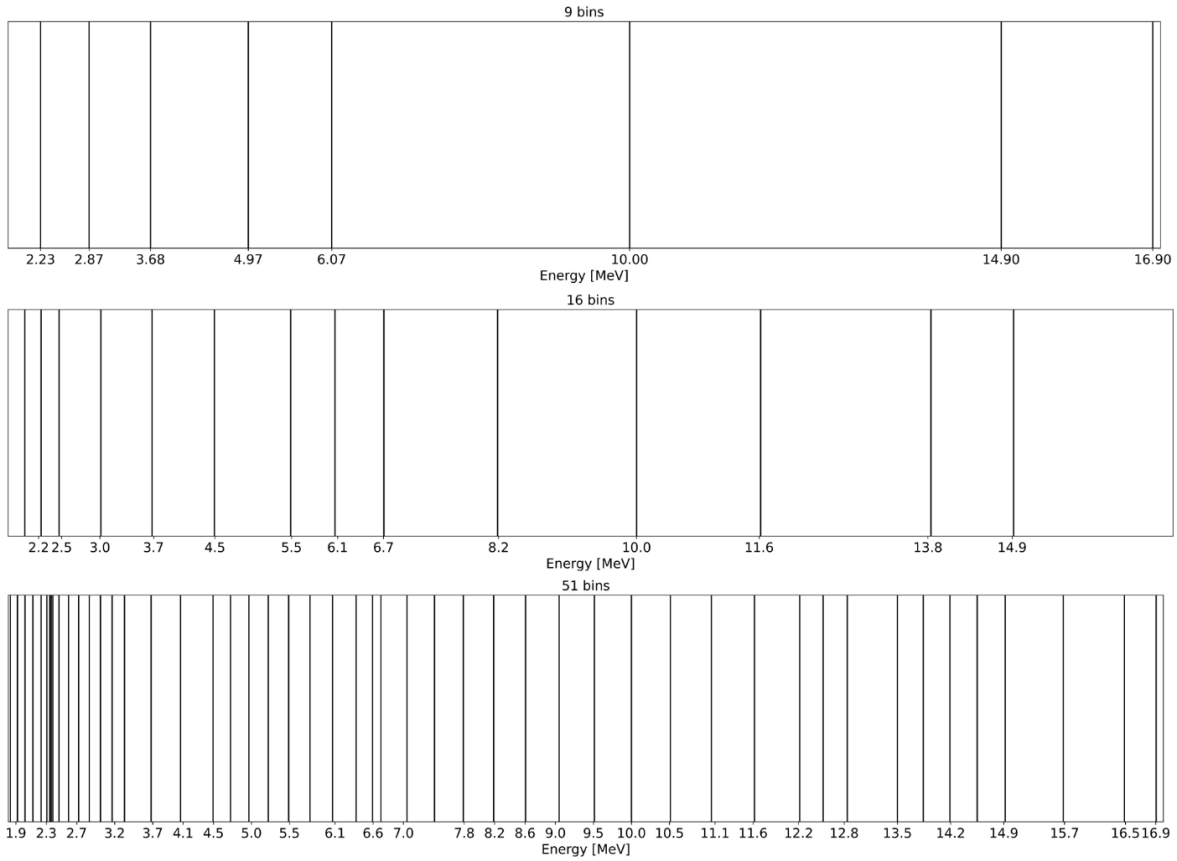

Figure 10.4. The bin structures of considered spectra with 9 (top), 16 (centre), and 51 (bottom) elements compatible with FISPACT-II.

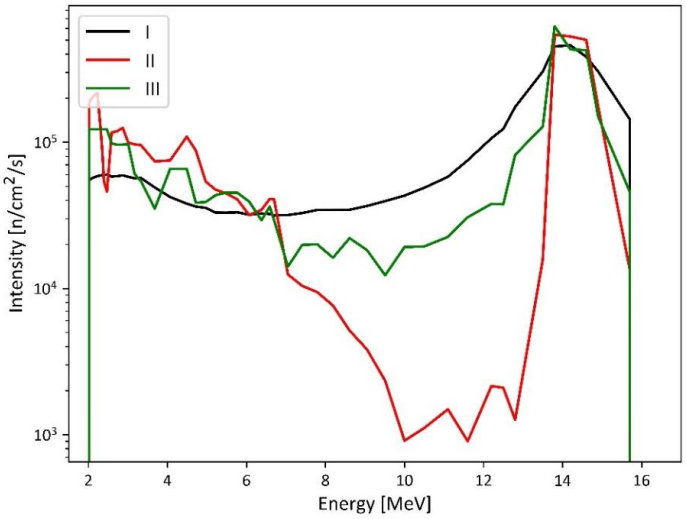

Figure 10.5. The default spectra (51 bin structure) for deconvolution of the neutron spectrum emitted by Gradel-Fusion NSD 35 2-DT-C-W.

Spectrum I was used to obtain the synthetic activation data by the FISPACT-II inventory code. The results and their comparison to the experimental data are presented in table 10.3. These data have been used as input in the deconvolution codes tests.

Table 10.3. The synthetic specific activity calculated by the FISPACT-II inventory code with spectrum I for Gradel-Fusion NSD 35 2-DT-C-W analysis.

Reaction	Specific activity [kBq/g]	Uncertainty [%]	Disagreement with experimental results [%]
$^{27}Al(n,p)^{27}Mg$	5.52	8.7	85
$^{27}Al(n,\alpha)^{24}Na$	1.22	7.7	50
$^{64}Zn(n,2n)^{63}Zn$	0.83	11.2	-9
$^{56}Fe(n,p)^{56}Mn$	1.98	8.8	-8
$^{58}Ni(n,2n)^{57}Ni$	0.02	12.9	-75
$^{90}Zr(n,2n)^{89}Zr$	0.14	7.2	-31
$^{90}Zr(n,p)^{90m}Y$	0.07	17.8	-57
$^{197}Au(n,2n)^{196}Au$	0.29	13.3	-52

At first, the spectrum with the smallest number of bins was analysed. The results of the neutron spectrum reconstruction by the TR, MFI, ML and MaxEnt methods obtained using the synthetic activity related to spectrum I are presented in figure 10.6. The difference between neutron intensity calculated for default spectra I and II are negligible for each method due to the similar neutron emission intensity distribution after modifying the bin number 51 to 9. All algorithms reconstruct the 14 MeV peak precisely. The $accuracy_s$ of each from 9 bins obtained by the TR, MFI, ML and MaxEnt methods is presented in figure 10.7. The energy bins above 6 MeV were reconstructed with the lowest error because of the non-zero cross-sections for all reactions in this energy range. The lower energy bins are poorly characterised, and their reconstruction error can be even more than 100% for the spectrum with low-resolution energy distribution. The MFI method has low sensitivity to the default spectrum. The differences between results obtained by the TR and MFI are negligible. The error for energies above 6 MeV is 3% at maximum, and the mean error for all bins is around 23%. The ML results for the first iteration with spectrum I and II are identical with the synthetic spectrum (with precision to one decimal place). Due to strong variations in the neutron emission intensity for energies below 7 MeV in spectrum III, the ML solution has mean error equal to 14%. The same effect is observed for the MaxEnt method. The difference between results for spectrum I and II is negligible. The reconstruction errors for bins with energy above 5 MeV are below 10%. Lower energies are characterised by $accuracy_s$ higher than 100%. The highest mean $accuracy_s$ has been obtained by the MaxEnt method.

The reconstructed spectra were used for activation simulation by FISPACT-II, and the summary of the obtained $accuracy_a$ is presented in figure 10.8. The results identical to the synthetic values (obtained by the ML method with spectra I and II) were omitted from the plot. The spectra obtained by the TR, MFI and ML methods reconstruct the activities with relatively low standard deviation (< 15%). The accuracy for Au has a significantly lower error. It is related to an error below 5% for the reconstructed part of the spectrum above the $^{197}Au(n,2n)^{196}Au$ reaction threshold energy. The worst $accuracy_a$ characterises reactions $^{58}Ni(n,2n)^{57}Ni$, $^{64}Zn(n,2n)^{63}Zn$, and $^{90}Zr(n,2n)^{89}Zr$. These reactions have a maximum cross-section in the energy between 12 - 17 MeV, where spectrum bins are very wide. Therefore, the cross-sections are interpolated with high uncertainties, which is the source of the activity error. The neutron emission intensity values variations in the energy bins below 6 MeV cause the default spectrum III used in MaxEnt to give results with $accuracy_s$ higher than 1000%, which is an unreliable solution correlated with $accuracy_a$ above 100%. Despite the spectrum reconstruction error higher than 500% for energy range 2 MeV – 4 MeV, spectra I and II provide $accuracy_a$ below 100% for all reactions.

The ratio of the spectrum and activity accuracies for each method is presented in table 10.4. C_R for TR and MFI methods are close to 1. The $accuracy_s$ for ML and spectrum III is smaller than the $accuracy_a$. The mean $accuracy_a$ from MaxEnt with spectra I and II as default is 61%, about 4 times lower than $accuracy_s$.

All methods have the accuracy of reconstructed energy bins around 14 MeV better than 10%. The spectrum accuracy for energies below 6 MeV is up to 100% for the TR, MFI and ML methods, which is not acceptable. The MaxEnt results are connected with spectrum reconstruction error with a maximum of 2000%. The huge error is a consequence of the connection of the entropy as the regularization operator (see equation 5.3.6) to the strong smoothing of the calculated neutron spectrum. In the case of 9 energy bin spectrum, the minimal regularisation parameter is selected during the reconstruction by the automatic method described in subchapter 5.3. In the considered case, the optimal λ value is impossible to determine. It makes the MaxEnt method unreliable. The problem is similar to the one described in subchapter 8.3.1. The results' accuracy is insufficient to interpret the NG's neutron emission.

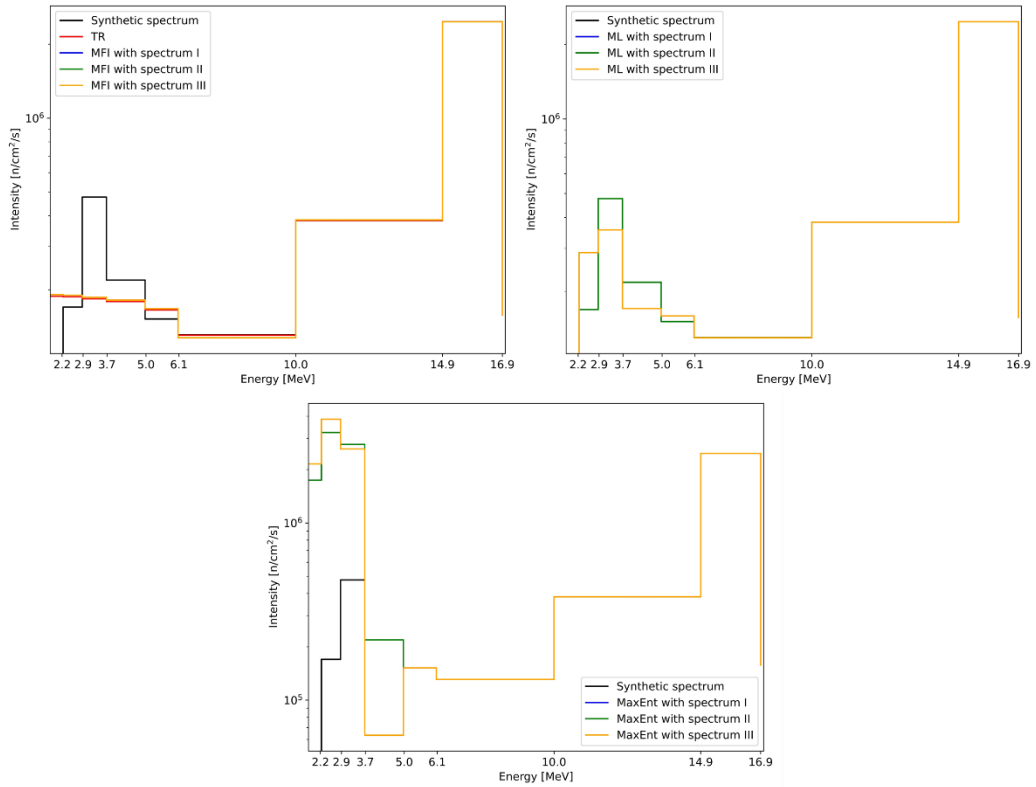

Figure 10.6. The reconstructed spectra (9 bins) obtained with the synthetic data simulated for Gradel-Fusion NSD 35 2-DT-C-W by different methods (TR and MFI – top left, ML – top right, MaxEnt – bottom).

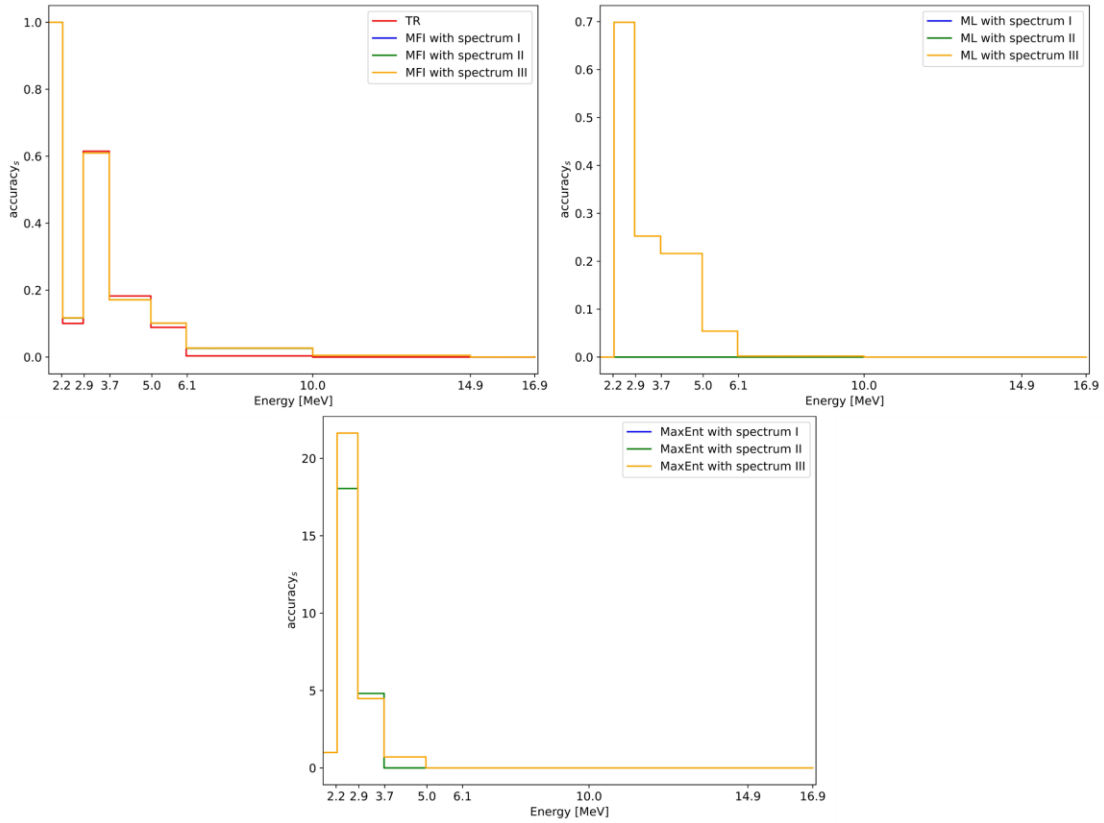

c

Figure 10.7. The accuracy$_s$ (9 bins) for the reconstruction results obtained by different methods with the synthetic activity originated from spectrum I (9 bins) simulated for Gradel-Fusion NSD 35 2-DT-C-W (TR and MFI – top left, ML – top right, MaxEnt – bottom).

Table 10.4. Comparison of C_R for 9 bin spectra obtained with the synthetic data simulated for Gradel-Fusion NSD 35 2-DT-C-W by different methods.

Method	C_R
TR	1.16
MFI with spectrum I	1.05
MFI with spectrum II	1.05
MFI with spectrum III	1.05
ML with spectrum III	0.70
MaxEnt with spectrum I	4.34
MaxEnt with spectrum II	4.34
MaxEnt with spectrum III	0.80

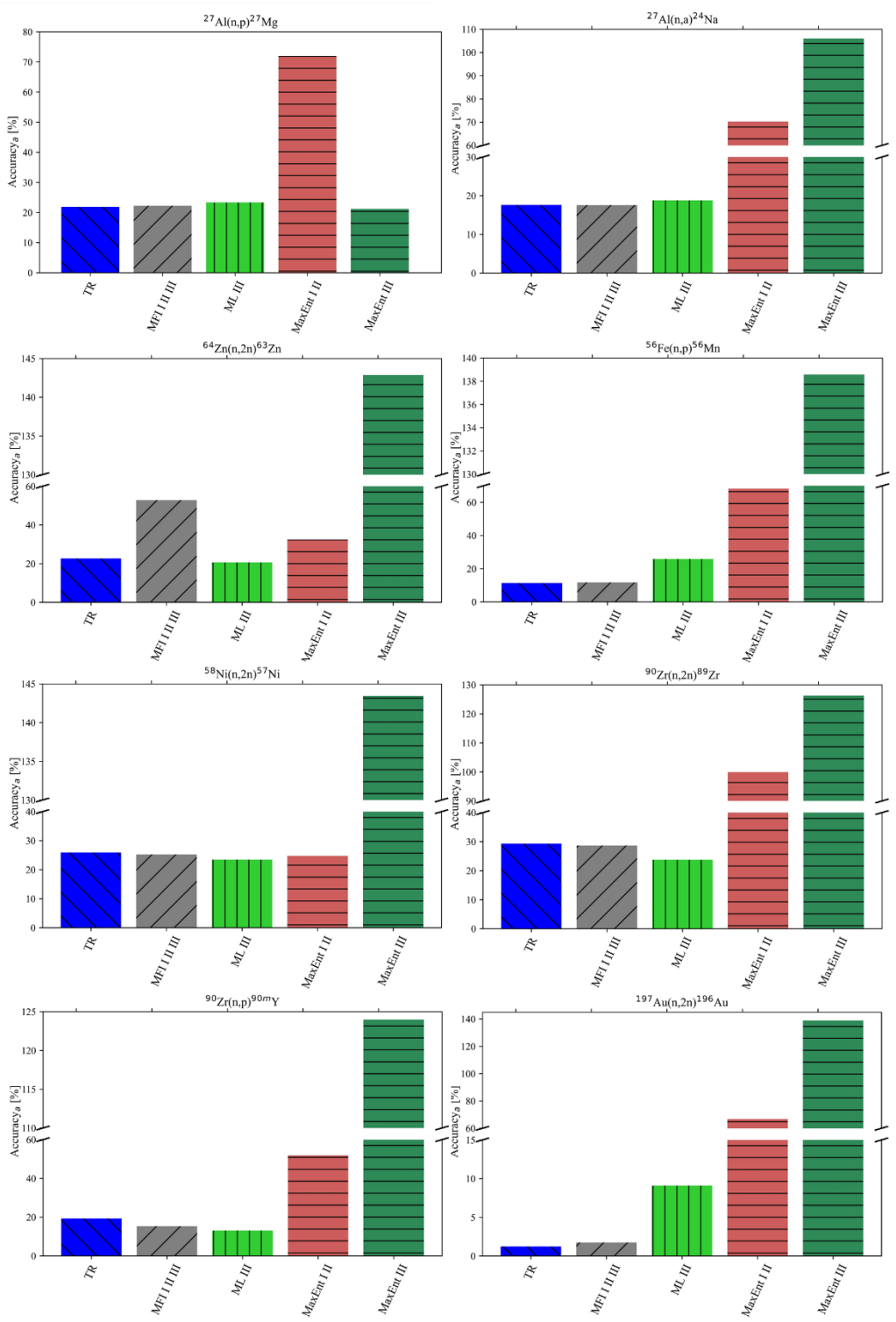

Figure 10.8. Accuracy$_a$ for the reconstruction results obtained by different methods with the synthetic activity originated from spectrum I (9 bins) simulated for Gradel-Fusion NSD 35 2-DT-C-W.

A second analysis of the neutron spectrum reconstruction from activation measurement with low energy resolution has been made for 16 bins. The synthetic activity obtained for spectrum I was used as an input. The reconstruction results by the TR, MFI, ML, and MaxEnt methods are presented in figure 10.9. All algorithms reconstruct the 14 MeV peak with dominant intensity. The relative error of the neutron spectrum reconstruction is shown in figure 10.10.

The mean error of the spectrum reconstructed by the TR method is equal to 36% for the full energy range and 10% in shortened range from 6 MeV to 17 MeV. Again, the differences between results obtained by the MFI algorithm with spectra I, II, and III are negligible. The mean $accuracy_s$ varies from 61% to 62%. The standard deviation is less than 1%. The two iterations of the ML method with spectrum I as default did not change the spectrum values and gave a $accuracy_s$ close to 0%. The number of iterations for default spectra II and III reached a million before the differences between the previous and the last solution was negligibly small. The result for spectrum II as default is characterised by the mean $accurcay_s$ of 22% in the whole energy range and 15% from 6 MeV to 17 MeV. The mean $accuracy_s$ for spectrum II is 17% for the whole spectrum and 7% for the 14-MeV peak. The strong regularisation connected to the matrix $\boldsymbol{L}$ in the MaxEnt method is the reason for the negligible differences between the results for three default spectra. The mean $accurcay_s$ is 44% in the entire energy range and 11% for 6 – 17 MeV.

Figure 10.11 presents the $accuracy_a$ for reconstructed spectra obtained by all methods. Only for reaction $^{90}Zr(n,2n)^{89}Zr$, the error is higher than 10%. The reaction (n,2n) on Zr has a maximum cross-section from 12 – 17 MeV, where energy bins are wide. The small error connected with the last bins strongly influences the activity simulation result due to the interpolation of the cross-section. The activity of ^{89}Zr is overestimated in the result obtained by the MFI method and ML with spectrum II as default. It is connected with the $accuracy_s$ of the penultimate bin on the level of 10%. This problem does not occur in other cases because the bin with energies 11.6 – 13.8 MeV is reconstructed with an accuracy lower than 4%. The $accurcay_a$ calculated for the results of the TR and MFI is 10% for (n,p) reaction on Al because of the lowest threshold energy and influence of the poorly reconstructed part of the spectrum. Other activity reconstruction errors are below 5%. The mean $accuracy_a$ for the MFI method is 3%. The $accuracy_s$ is about 21 times higher than $accuracy_a$ (see table 10.5). The mean $accuracy_a$ for the ML method with spectra II and III are 12% and 3%, respectively. The mean $accuracy_a$ obtained for the MaxEnt method is 3%. The neutron spectrum reconstruction error is 15 times higher than $accuracy_a$.

The $accuracy_s$ for more energy bins are higher for the TR, MFI and ML methods, but $accuracy_a$ is much lower. The improvement in the activity reconstruction is related to the resolution of the spectrum structure. The MaxEnt method is more efficient for 16 bins than for 9 bins. The results are still not satisfying, and an approach that improves the results was investigated for a greater number of bins.

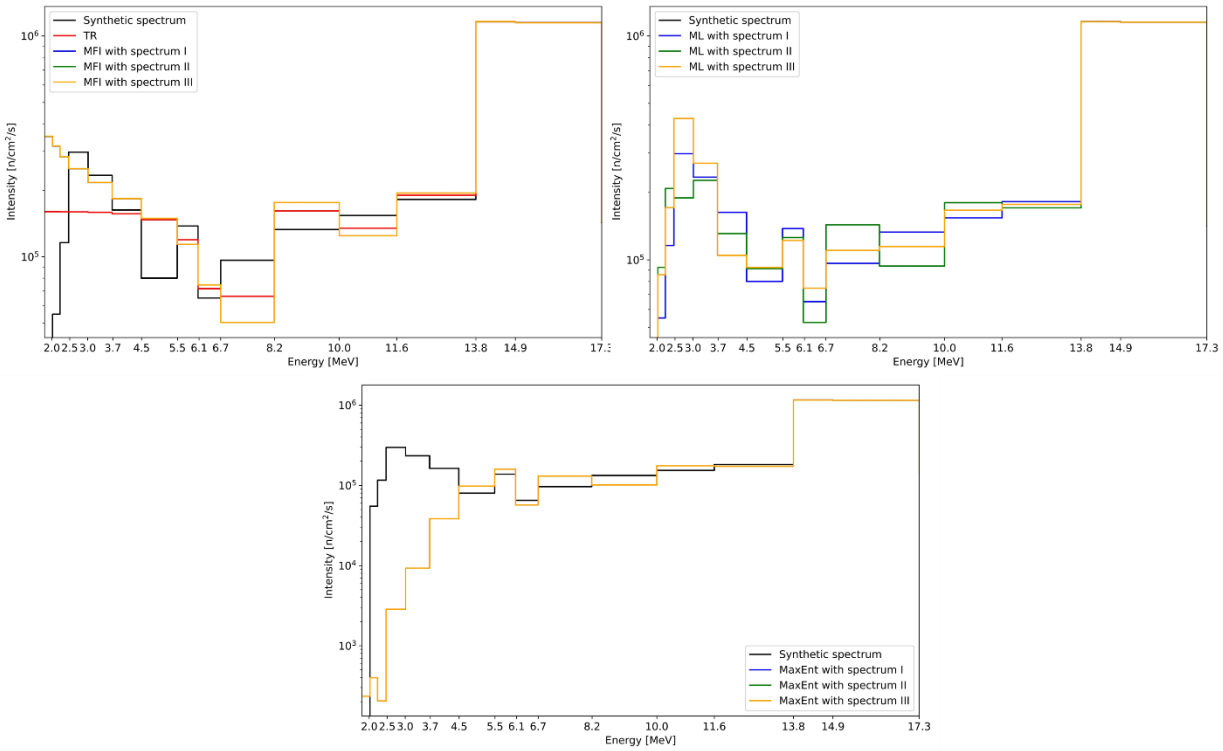

Figure 10.9. The reconstructed spectra (16 bins) obtained with the synthetic data simulated for Gradel-Fusion NSD 35 2-DT-C-W by different methods (TR and MFI – top left, ML – top right, MaxEnt – bottom).

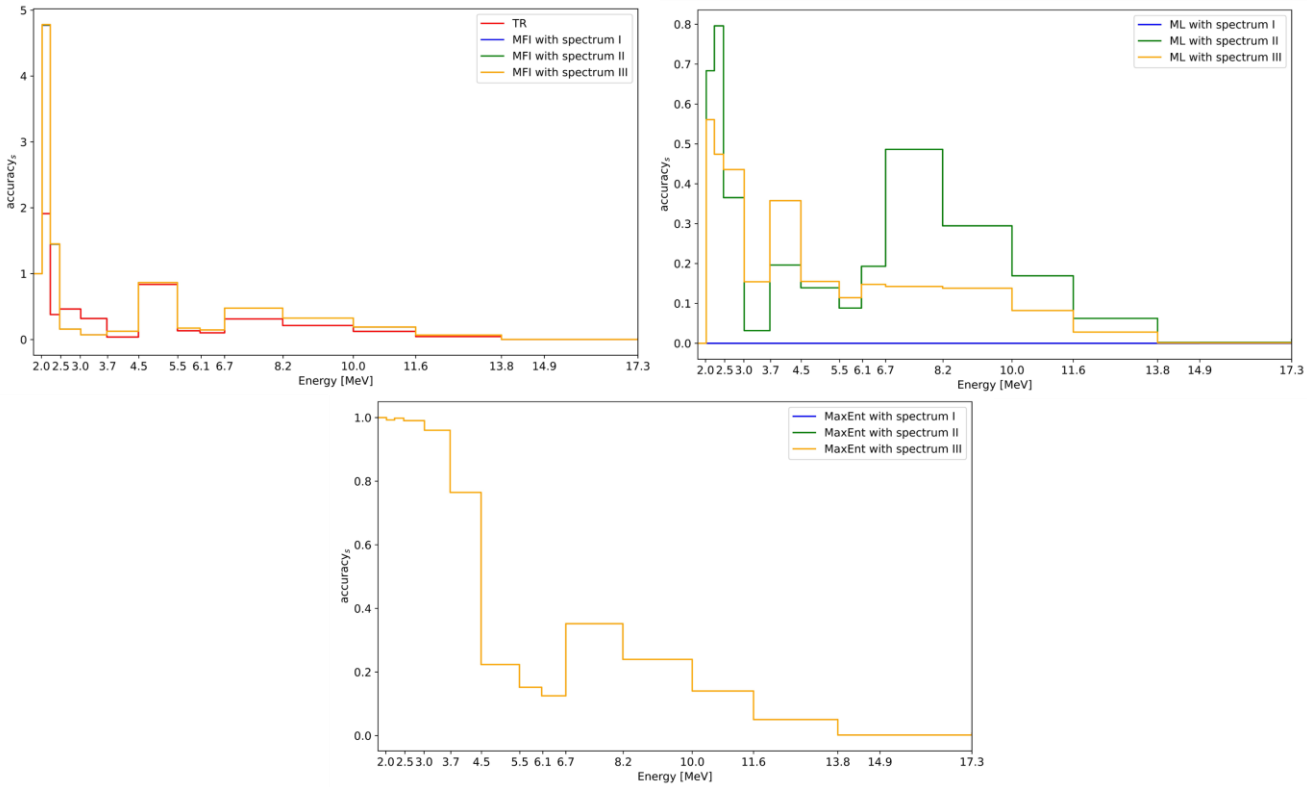

Figure 10.10. Accuracy$_s$ (16 bins) for the reconstruction results obtained by different methods with the synthetic activity originated from spectrum I (16 bins) simulated for Gradel-Fusion NSD 35 2-DT-C-W (TR and MFI – top left, ML – top right, MaxEnt – bottom).

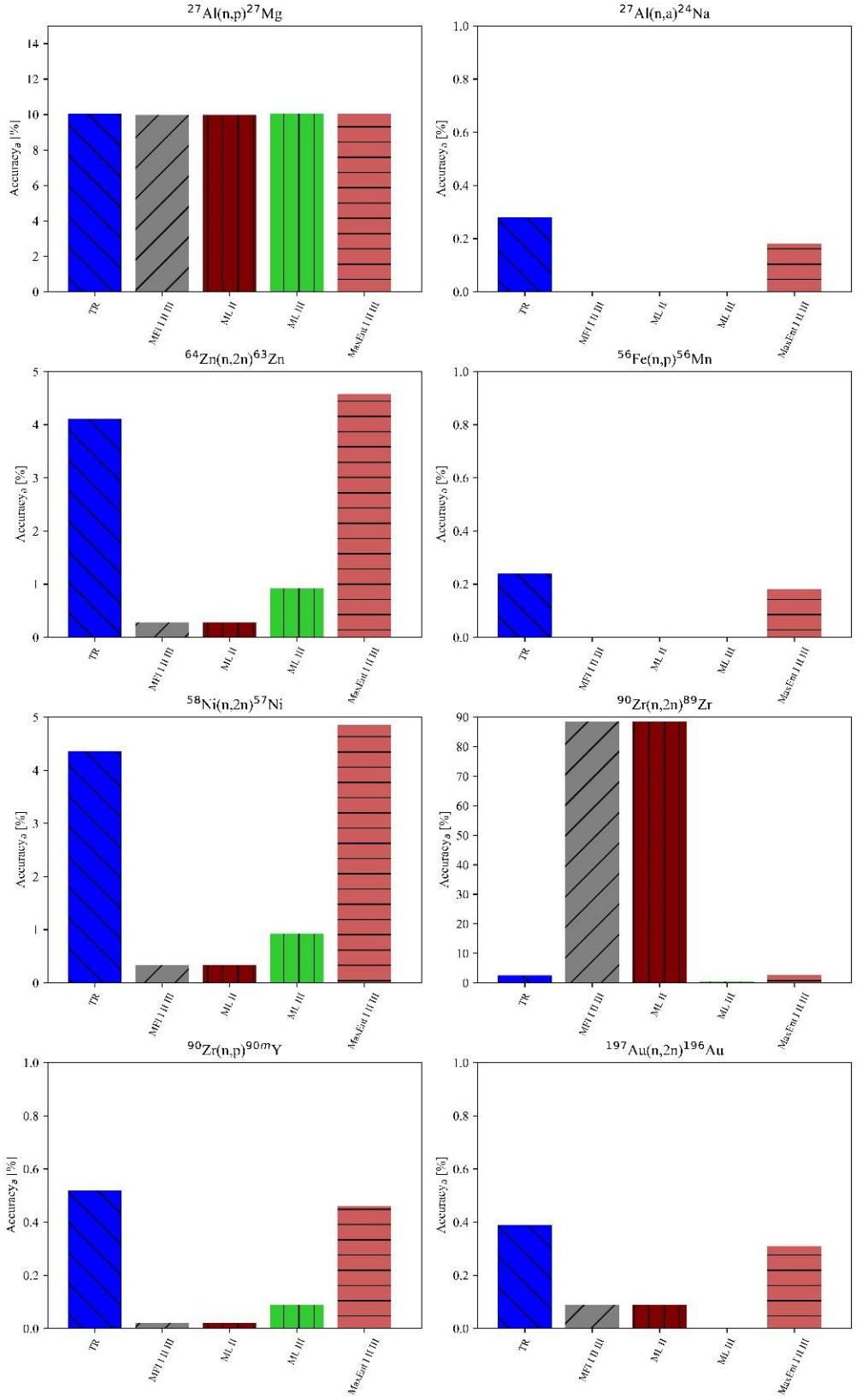

Figure 10.11. Accuracy$_a$ for the reconstruction results obtained by different methods with the synthetic activity originated from spectrum I (16 bins) simulated for Gradel-Fusion NSD 35 2-DT-C-W.

Table 10.5. Comparison of C_R for 16 bin spectra obtained with the synthetic data simulated for Gradel-Fusion NSD 35 2-DT-C-W by different methods.

Method	C_R
TR	18.5
MFI with spectrum I	20.3
MFI with spectrum II	20.7
MFI with spectrum III	20.7
ML with spectrum II	1.8
ML with spectrum III	8.5
MaxEnt with spectrum I	14.7
MaxEnt with spectrum II	14.7
MaxEnt with spectrum III	14.7

The mean spectrum from all results has been calculated to improve the uncertainty of the reconstruction. The different solutions can over or underestimate the spectrum emitted by the NG. A hypothesis is that averaging the emission intensity in each energy bin improves the overall solution. The methodology in the analysis is as follows:

1. Reconstruction of the neutron spectrum using all methods with various default spectra.
2. Calculation of the reconstructed activity.
3. Indication of the results with $accuracy_a$ over the limit described below.
4. Calculation of the mean spectrum from results acknowledged as reliable.
5. Comparison of the synthetic activity with simulation for mean spectrum.

The spectrum that gave $accuracy_a$ higher than 100% for any reaction or its mean activity reconstruction error is higher by about 20% from others is not included in calculating the mean spectrum. The conditions were defined arbitrary based on the experience in the data analysis.

The following analysis concerns the 51 energy bins (analysis was published in [Mik2021b]). The synthetic activation data obtained with spectrum I have been used in the neutron spectrum reconstruction by all presented methods. The results from the TR and MFI methods are presented in figure 10.12. The differences between results for TR and MFI with spectra I and III are not visible. The mean $accuracy_s$ is presented in table 10.6 and equals 32% for the TR algorithm. The result obtained by the MFI method with the default spectrum II has much higher $accuracy_s$ (73%) due to the mistake in the regularisation parameter selection. In many cases, the L-curve has a couple of corners. The automatic method based on calculating the maximum of the L-curve curvature does not always select the proper value. The chosen parameter λ was too low. Therefore, the default spectrum was only slightly changed in the calculations. The mean $accuracy_s$ for other default spectra used in the MFI method equals 29%. The results for the ML algorithm are presented in figure 10.13. The mean $accuracies_s$ obtained by the ML method are 0%, 43%, and 25% for default spectra I, II, and III, respectively. The calculations do not change the default spectrum equal to the synthetic spectrum. The values of spectra obtained by the ML algorithm oscillate strongly over default spectrum I. The reconstructed neutron spectra obtained by the MaxEnt method are presented in figure 10.14. The differences for various default spectra are negligible. The mean spectrum reconstruction error equals 54% in the full energy range and 32% from 10 to 17 MeV. Similar results are a consequence of the very strong regularisation connected to the matrix defined by equation (5.3.6) based on entropy. All methods reconstruct the maximal emission intensity of about 14.1 MeV.

The $accuracies_a$ obtained for the TR, MFI, ML and MaxEnt results are presented in figure 10.15. The mean $accuracy_a$ and C_R are presented in table 10.6. The mean $accuracy_a$ for the TR method is 6%. The $accuracy_s$ is about five times higher. The worst result is for reaction on Au due to overestimation of the bins with energy above 16 MeV. The mean $accuracy_a$ for the MFI method for default spectra I and II is also 6%. The highest activity reconstruction errors are for

the reactions on Zn and Ni, which have a maximal cross-section in the energy range of about 16 MeV, where $accuracy_s$ equals 100%. The MFI result obtained with default spectrum II has a mean $accuracy_a$ of about 20% higher than other solutions. The mean $accuracy_a$ for the ML method equals about 1%. The $accuracy_s$ is much higher (43% for spectrum II and 25% for spectrum III). Despite the differences in the results, the two default spectra used in the ML method gave similar $accuracy_a$ for all reactions. The MaxEnt method gave 2% of mean $accuracy_a$ with the highest error for Ni. It is also connected with the $accuracies_s$ for energies about 16 MeV. The $accurcay_s$ is 27 times higher than the activity error.

The mean value was calculated to improve the solution. The result obtained by the MFI method with default spectra II was excluded from the calculation because $accuracies_a$ are higher by 20% than for other algorithms. The resulting spectrum is presented in figure 10.16. The mean $accuracy_a$ is 26%, with a standard deviation of 3%. Small differences between accuracies for different reactions indicate that the reconstructed spectrum properly represents the relative amounts of neutrons in the energy bins. The mean spectrum improves the reconstruction error, equal to 24%. C_R is close to one that is a desirable result.

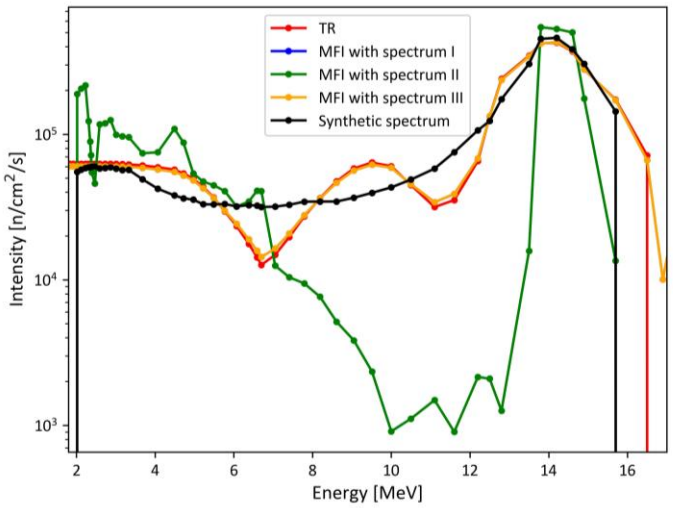

Figure 10.12. The spectra (51 bins) reconstructed by the TR and MFI methods using the synthetic data simulated for Gradel-Fusion NSD 35 2-DT-C-W.

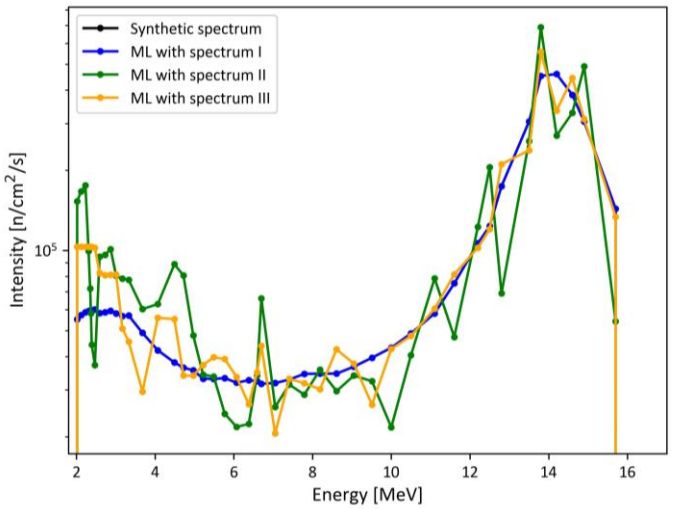

Figure 10.13. The spectra (51 bins) reconstructed by the ML method using the synthetic data simulated for Gradel-Fusion NSD 35 2-DT-C-W.

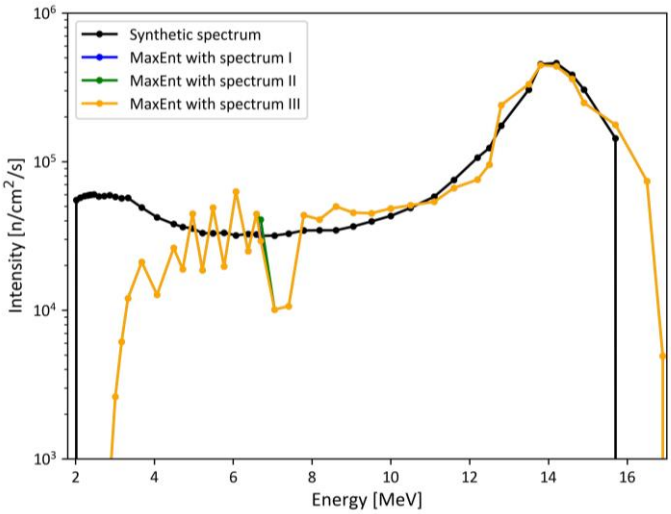

Figure 10.14. The spectra (51 bins) reconstructed by the MaxEnt method using the synthetic data simulated for Gradel-Fusion NSD 35 2-DT-C-W.

Table 10.6. The accuracies$_s$, accuracies$_a$, and C_R obtained for the synthetic data simulated for Gradel-Fusion NSD 35 2-DT-C-W and 51 bin structure by different methods.

Method	Mean accuracy$_s$ [%]	Mean accuracy$_a$ [%]	C_R
TR	32	6	5.3
MFI with spectrum I	29	6	4.8
MFI with spectrum II	73	25	2.9
MFI with spectrum III	29	6	4.8
ML with spectrum I	0	0	1.0
ML with spectrum II	43	1	43.0
ML with spectrum III	25	1	25.0
MaxEnt with spectrum I	54	2	27.0
MaxEnt with spectrum II	54	2	27.0
MaxEnt with spectrum III	54	2	27.0
Mean	24	26	0.9

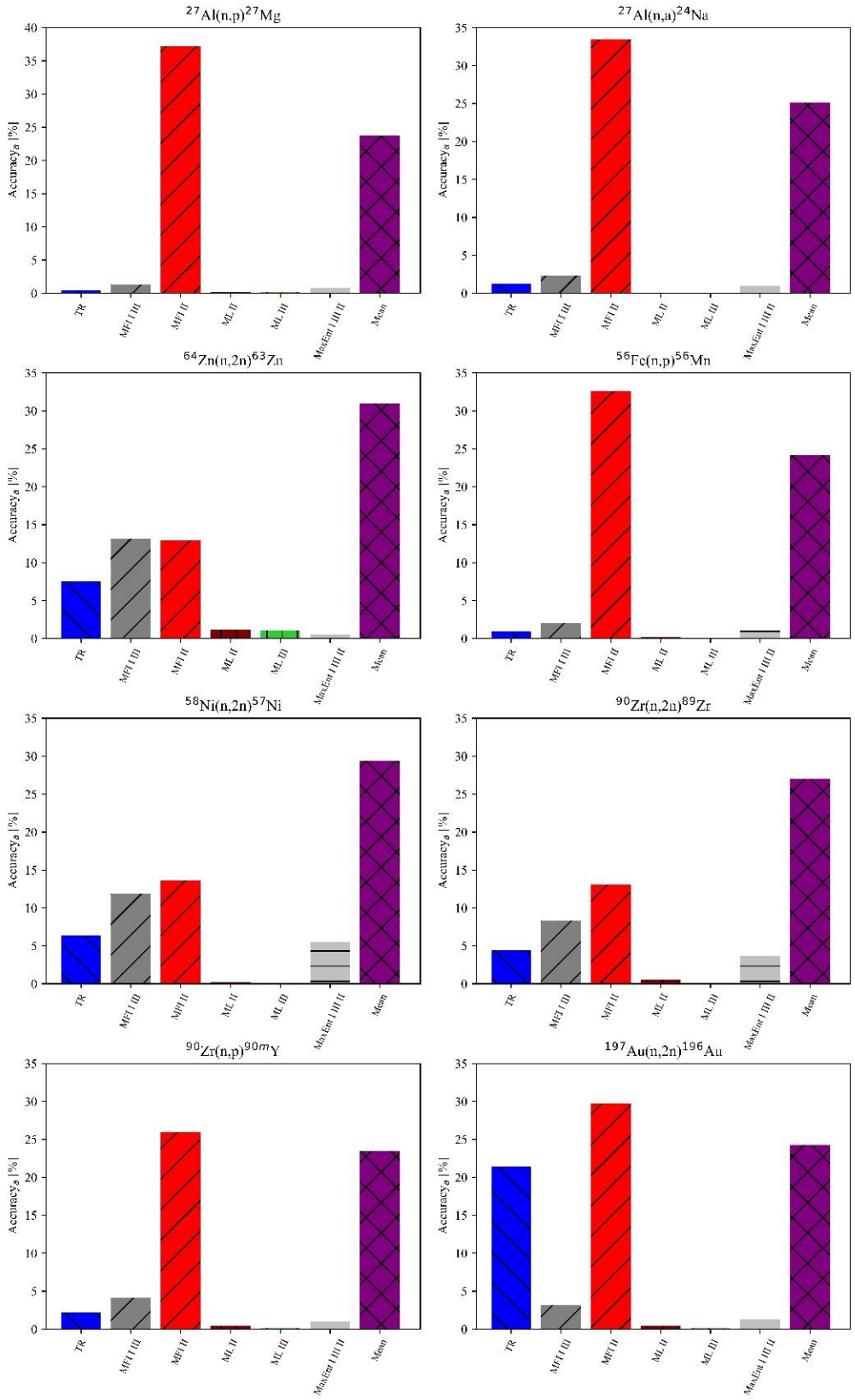

Figure 10.15. Accuracy$_a$ for the reconstruction results obtained by different methods with the synthetic activity originated from spectrum I (51 bins) simulated for Gradel-Fusion NSD 35 2-DT-C-W.

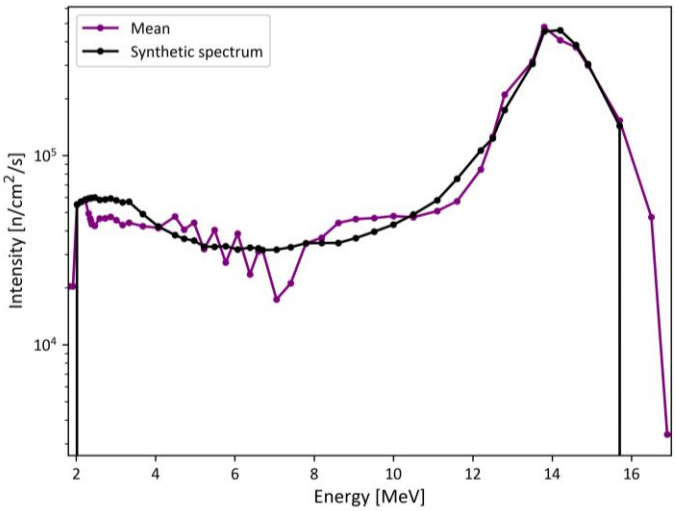

Figure 10.16. The average spectrum (51 bins) from the TR, MFI, ML, and MaxEnt results obtained using the synthetic data simulated for Gradel-Fusion NSD 35 2-DT-C-W.

The last analysis for the synthetic results has been made for 71 bin structure with equal energy intervals (results were presented in [Mik2018b]). The chosen spectrum structure is not compatible with the FISPACT-II inventory code. Before the irradiation simulation, the spectra need to be recalculated. According to the reshaping impact estimation, an additional 5% uncertainty was added to the obtained activity connected with this modification. The results of the neutron spectrum reconstruction by the TR and MFI methods are presented in figure 10.17. There are strong variations of the intensity values below 12 MeV. The mean $accuracy_s$ for the TR algorithm is 51%. The MFI method with different default spectra gave the mean $accuracy_s$ from 35% to 61%. The shape of the spectra is the effect of the applied derivative as a regularisation matrix. The lowest error is for the 14 MeV energy peak. The results from the ML method are presented in figure 10.18. Spectrum I, as default, did not change during the calculations. The mean $accuracies_s$ equal 40% and 57% for spectra II and III as default, respectively. The general shape of the spectrum is reproduced, but steep changes in the neutron intensity values were observed. The neutron spectra obtained by the MaxEnt method are presented in figure 10.19. The mean $accuracy_s$ for spectrum I as default is 34%. The shape of the 14-MeV peak is similar for various default spectra. The mean $accuracy_s$ for default spectra II is 86%. The unexpected rise of the emission intensities occurs between 2 – 6 MeV and around 10 MeV, which are artefacts related to the used method. The results obtained with spectrum III underestimate the 14 MeV peak and reconstruct a sharp peak around 3 MeV that is also found as an artefact. In this case, the mean $accuracy_s$ is 57%. The comparison of the accuracies obtained by different methods is presented in table 10.7.

The activity reconstruction errors for all methods are shown in figure 10.20. The $accuracy_a$ obtained by the TR method is higher than 100% for (n,p) reaction on Al, which disqualified it from further analysis. The $accuracies_a$ for the MFI algorithm are surprisingly small (1% - 16%). The activity simulation was done for the ML method with spectrum I as default to show the influence of the spectrum structure modification. The mean $accuracy_a$ obtained by the MaxEnt method equals 13%, 7%, and 9% for default spectra I, II, and III, respectively. The $accuracies_s$ are much higher than $accuracy_a$. The standard deviation of each reaction errors is lower than 2%.

The mean spectrum was calculated to improve the $accuracy_s$. The result only from the TR algorithm was not included in the calculations. The average spectrum is presented in figure 10.21. The mean $accuracy_s$ is 24%, which is the best result. The highest discrepancy is for energy around 2 MeV. The $accuracy_a$ is about 18%. Fe, Zn, and Ni activity have the highest errors. The Zn and Ni have high thresholds and maximum cross-sections of about 16 MeV. There is a problem with the reconstruction of neutron emission intensity about this energy due to the high uncertainties

for boundary bins. The accuracy$_s$ has the strongest influence on Fe in the energy range from 6 MeV to 12 MeV.

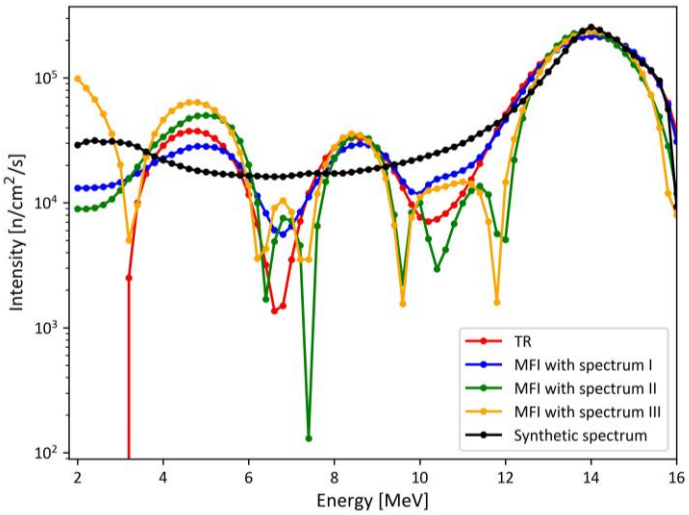

Figure 10.17. The spectra (71 bins) reconstructed by the TR and MFI methods using the synthetic data simulated for Gradel-Fusion NSD 35 2-DT-C-W.

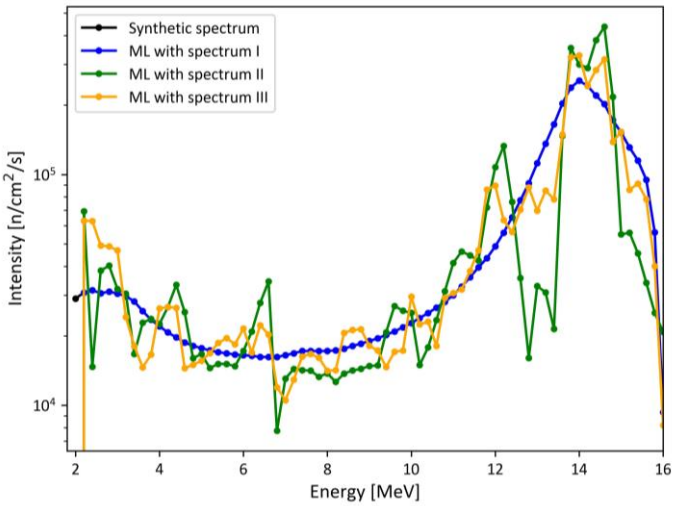

Figure 10.18. The spectra (71 bins) reconstructed by the ML method using the synthetic data simulated for Gradel-Fusion NSD 35 2-DT-C-W.

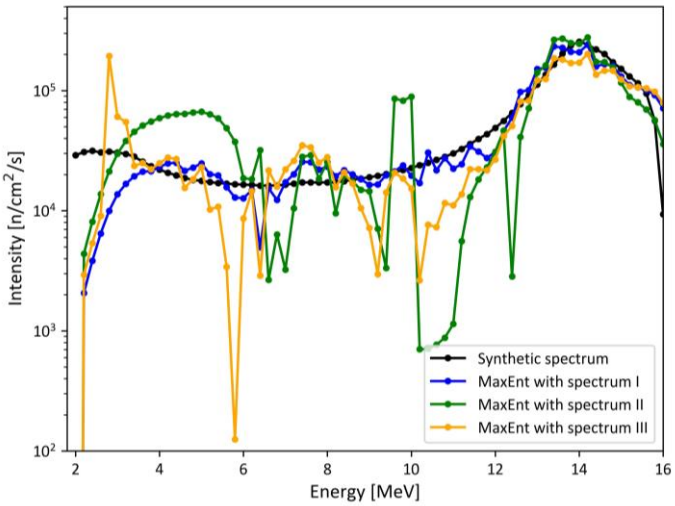

Figure 10.19. The spectra (71 bins) reconstructed by the MaxEnt method using the synthetic data simulated for Gradel-Fusion NSD 35 2-DT-C-W.

Table 10.7. The accuracies$_s$, accuracies$_a$, and C_R obtained for the synthetic data simulated for Gradel-Fusion NSD 35 2-DT-C-W and 71 bin structure by different methods.

Method	Mean accuracy$_s$ [%]	Mean accuracy$_a$ [%]	C_R
TR	51	40	1.3
MFI with spectrum I	35	7	5.0
MFI with spectrum II	65	16	4.1
MFI with spectrum III	61	1	61.0
ML with spectrum I	0	1	1.0
ML with spectrum II	40	5	8.0
ML with spectrum III	57	12	4.8
MaxEnt with spectrum I	34	13	2.6
MaxEnt with spectrum II	86	7	12.3
MaxEnt with spectrum III	57	9	6.3
Mean	24	18	1.3

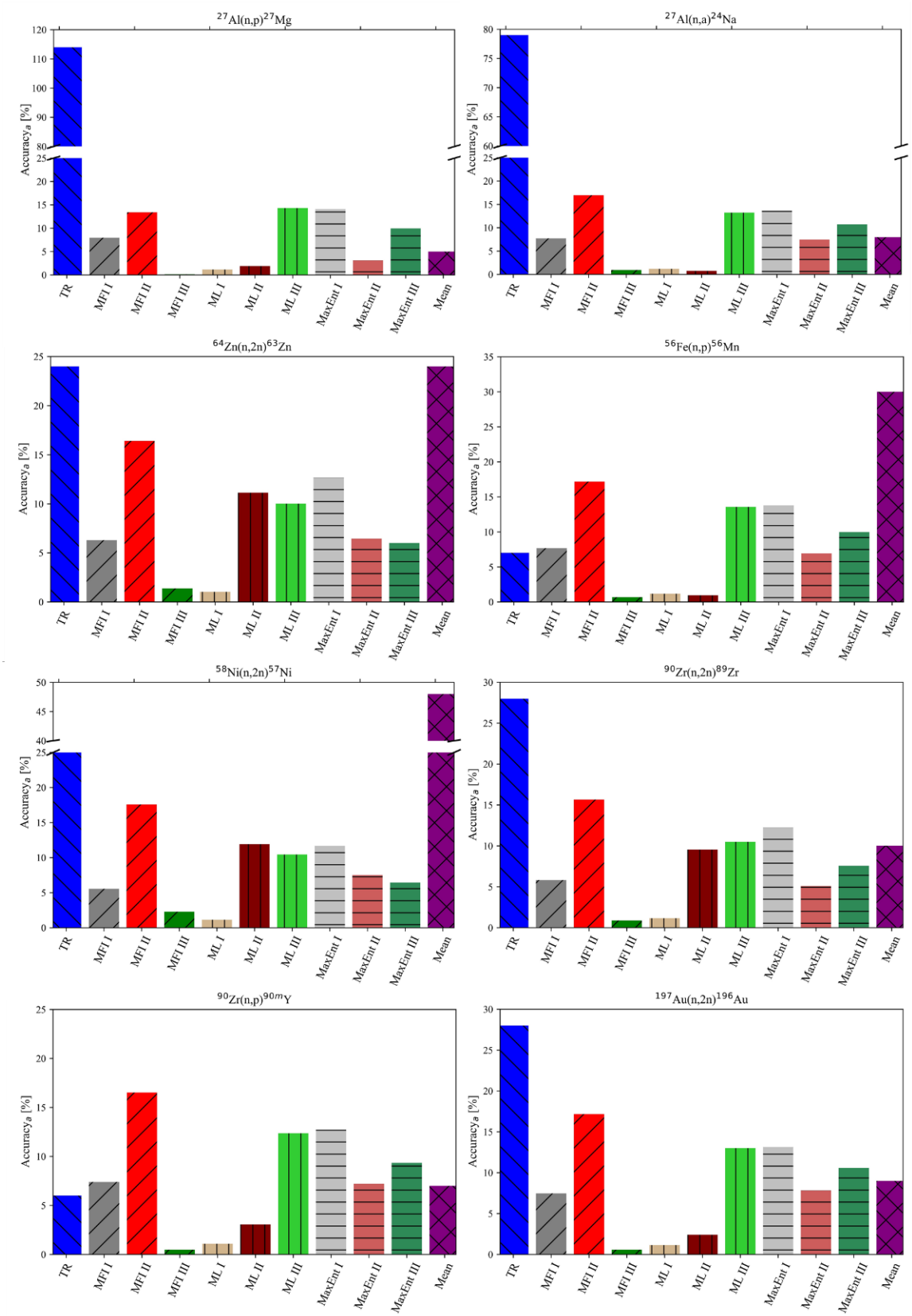

Figure 10.20. Accuracy$_a$ for the reconstruction results obtained by different methods with the synthetic activity originated from spectrum I (71 bins) simulated for Gradel-Fusion NSD 35 2-DT-C-W.

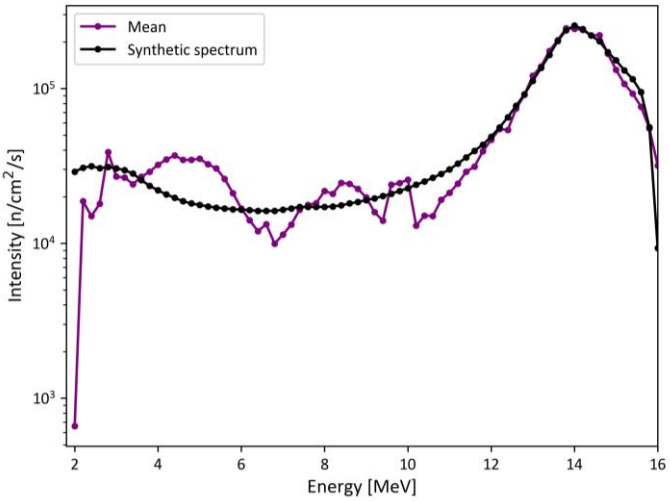

Figure 10.21. The average spectrum (71 bins) from the MFI, ML, and MaxEnt results obtained using the synthetic data simulated for Gradel-Fusion NSD 35 2-DT-C-W.

Four spectra with different energy resolutions were analysed. The smallest considered number of bins, 9, is characterised by a very high activity reconstruction error because of the cross-section distribution averaging. Therefore, this bin structure has not been considered in the experimental data analysis, where activity reconstruction error is the basis of the reliability evaluation. An increase in the bins number makes the reconstruction more complex from a mathematical point of view. The mean $accuracy_s$ for 16 bins are from 17% to 62%, and the $accuracies_a$ are 2 – 3 times lower. The MFI method gave the worst results. In this algorithm, the automatic method of the regularisation parameter selection sometimes does not provide the optimal solution. Therefore, the result obtained for one default spectra has a much higher error than others. The MaxEnt algorithm has the lowest sensitivity for selecting the default spectrum because of the strong regularisation. The highest $accuracy_s$ for 51 bins is for MaxEnt and equals 54%. The best mean $accuracy_a$ is about 1% for the ML method. The mean spectrum was calculated to improve the results, and the lowest spectrum reconstruction error, 24%, was obtained. The ratio of the accuracies for spectrum and activity is close to 1 in this case. The average spectrum with 71 bins reconstruction error for different methods varies from 34% to 86%, corresponding to activity accuracy from 1% to 40%. The mean spectrum calculations improve the results. The mean $accuracy_s$ equals 24% and $accuracy_a$ 18%. Due to the smallest uncertainties and standard deviations, the mean spectrum with 51 bins was found as the best result. The correlation between activity and spectrum accuracies has been used to evaluate the uncertainty of the experimental data reconstruction.

10.1.2.2 Experimental data analysis

The experimental data (see table 10.2) obtained by the activation method during irradiation by Gradel-Fusion NSD 35 2-DT-C-W neutron generator have been used to reconstruct the neutron spectrum. The synthetic data analysis was implemented to estimate the uncertainty of the reconstructed results and evaluate the reconstruction reliability. The uncertainty of the reconstructed spectrum is calculated from the following equation:

$$Uncertainty = accuracy_a \cdot C_R \qquad (10.1.2.2.1)$$

The uncertainty of the activation measurement is included in the $accuracy_a$, and all other elements, like the uncertainty of the method itself, in C_R value.

The default spectra presented in figure 10.5 have been used in the reconstructions with the experimental data. Three bin structures were considered: 16, 51, and 71. The spectrum with 9 bins was omitted because of the small activity reconstruction precision and the low amount of information about the spectrum.

The reconstruction results obtained by the TR and MFI methods for the 9 bin structure are presented in figure 10.22. The intensity of neutron emission with energies below 6 MeV for the TR solution is two times smaller than the 14 MeV peak. The differences between spectra obtained by the MFI algorithm with various default spectra are negligible. The number of 14 MeV neutrons is similar to the emission level of the neutrons with energy below 6 MeV. This result is the effect of the application of the second-order derivative as the regularisation matrix and interpolation of the reactions cross-sections. The level of intensity is too high for the background in the low scattering conditions of the experiment. The significant presence of the low-energy neutrons indicates the appearance of the DD and TT reactions in the generator. The reconstruction results obtained by the ML method are presented in figure 10.23. The number of neutrons with energies of about 2 - 3 MeV is two orders of magnitude smaller than the emission intensity for 14 MeV neutrons. The shape of the spectra demonstrates a slight increase of the intensity around 2.5 MeV suggesting the DD reaction presence. The spectra reconstructed by the MaxEnt method are presented in figure 10.24. The difference between results obtained with various default spectra is lower than 5% for energies higher than 11 MeV. The emission level magnitude for the energies below 6 MeV is the same as for 14 MeV neutrons, like in the MFI results. The result is the effect of the regularisation by the matrix based on the entropy defined by equation (5.3.6) for this bin structure. The evaluation of the reconstructed spectra reliability has been done based on the activation simulation by FISPACT-II.

The $accuracy_a$ comparison for the different methods is presented in figure 10.25. In the case of the activity simulated for the TR result, the mean $accuracy_a$ is 39%, with a standard deviation of 22%. The lowest $accuracy_a$, equal to 5%, is for the reaction (n,2n) on Zr. The results are difficult to interpret because the other reactions with threshold energy above 8 MeV are characterised by errors higher than 50%. The high standard deviation of the $accuracies_a$ indicates that the neutron emission distribution is not correctly reconstructed by the TR method. Similar results with the lowest accuracy for $^{90}Zr(n,2n)^{89}Zr$ are obtained by the MFI and MaxEnt methods. The mean $accuracy_a$ for the MFI algorithm is 44%. The errors for each reaction fluctuated from 9% to 73%. The $accuracy_a$ for the MaxEnt method varies from 42% to 46%, with a standard deviation of about 22%. The shape of the spectrum reconstructed by the ML method is different from other algorithms results, and the $accuracies_a$ are the lowest for reaction on Zn. The error for (n,2n) reaction on Zr is also one of the smallest. It indicates that the neutron intensity in high energy bins (>14 MeV) is close to the experimental values. The highest $accuracy_a$ is for Ni, which can be connected with incorrectly reconstructed neutron intensities in the energy range 10 – 14 MeV. The mean $accuracies_a$ for default spectra I, II and III are 37%, 40%, and 35%, respectively. All results are characterised by a standard deviation higher than 20% and cannot be used to interpret the neutron emission from the gas-plasma target neutron generator. The level of the discrepancy between activity simulated by FISPACT-II with the reconstructed spectra and experimental results does not allow for pointing out the proper result.

The average spectrum has been calculated to improve the results (see figure 10.26). The mean $accuracy_a$ is 40%, with a standard deviation of 19%. The conclusions about reactions that took part in the NG contradict each other. The high $accuracies_a$ make it impossible to select the proper solution. It is connected with the interpolation of the reactions cross-sections for wide high-energy bins and algorithms themselves. The results obtained for this bin structure are not satisfying due to high disagreement between reconstructed and experimental activities and the inconsistent results obtained by different methods.

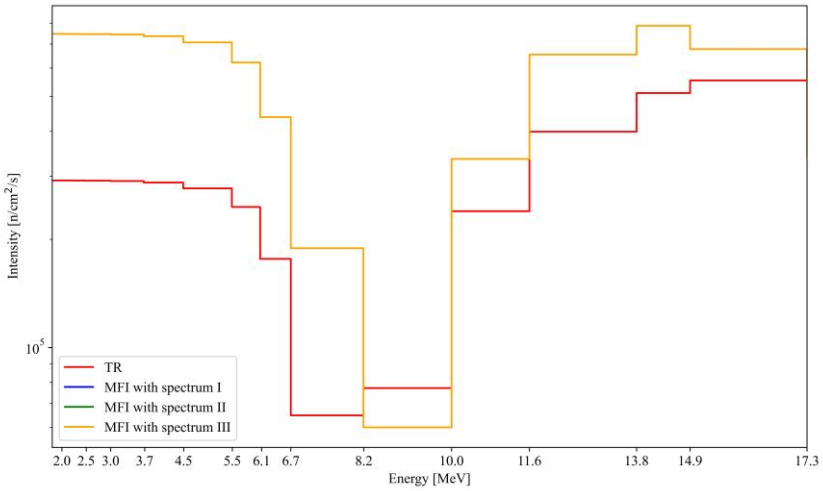

Figure 10.22. The spectra (16 bins) reconstructed by the TR and MFI methods using the experimental results from foils irradiation by Gradel-Fusion NSD 35 2-DT-C-W.

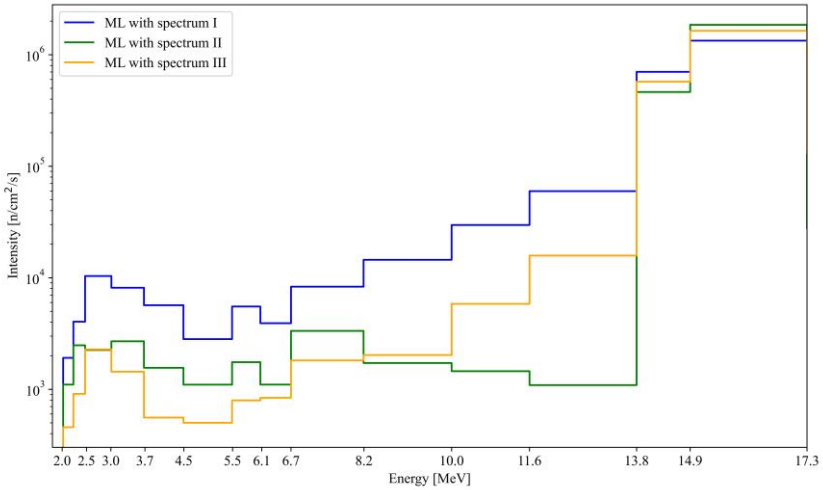

Figure 10.23. The spectra (16 bins) reconstructed by the ML method using the experimental results from foils irradiation by Gradel-Fusion NSD 35 2-DT-C-W.

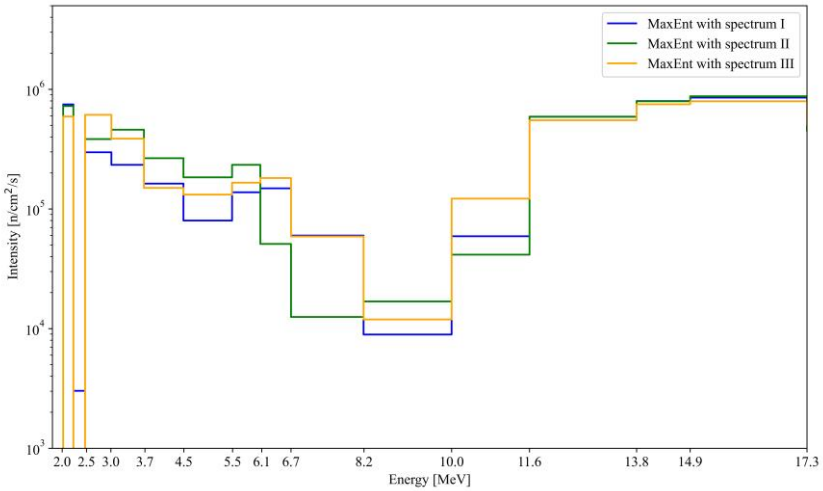

Figure 10.24. The spectra (16 bins) reconstructed by the MaxEnt method using the experimental results from foils irradiation by Gradel-Fusion NSD 35 2-DT-C-W.

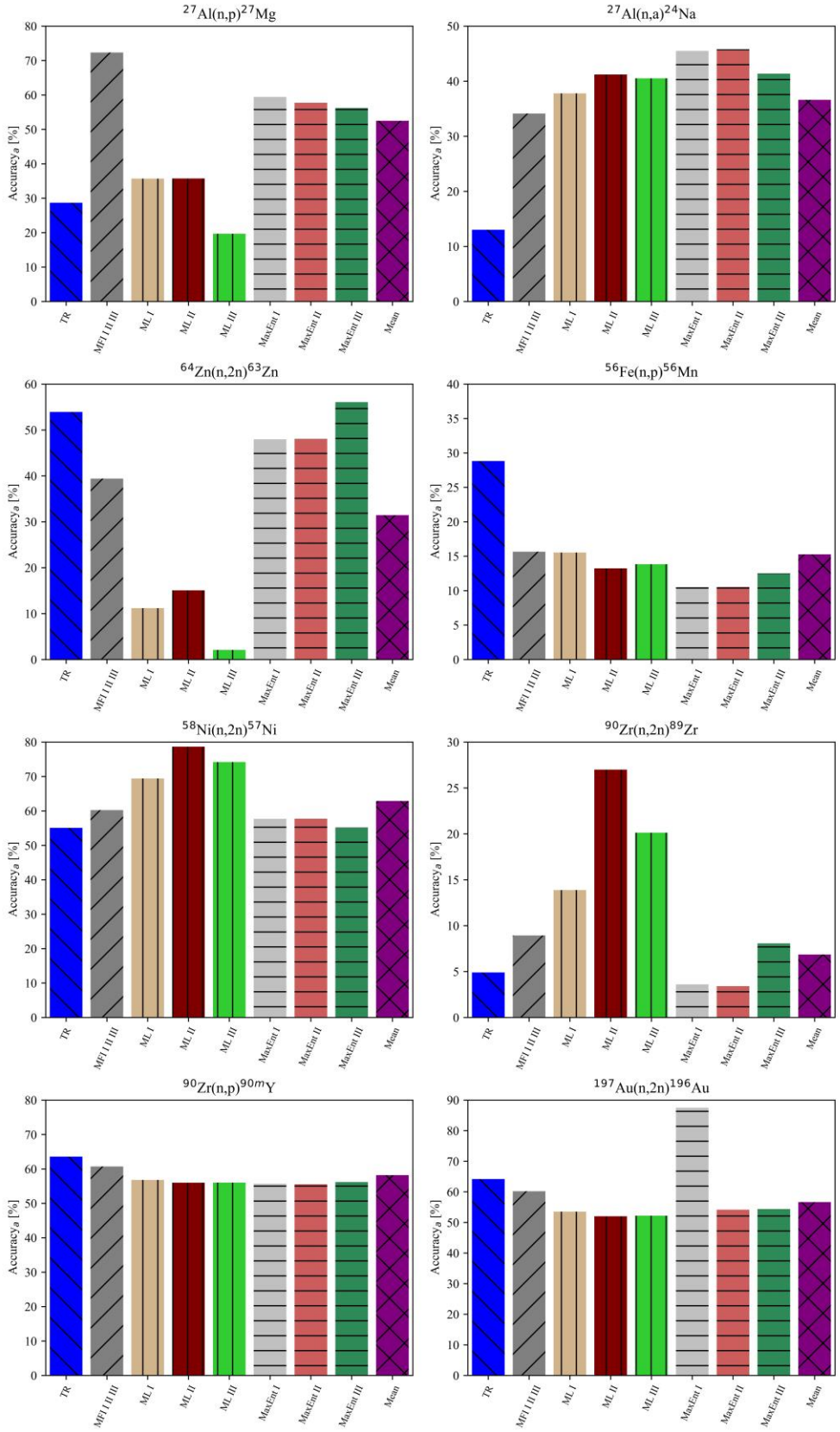

Figure 10.25. Accuracy$_a$ for the reconstructed results obtained by different methods (16 bins) with the experimental data for Gradel-Fusion NSD 35 2-DT-C-W.

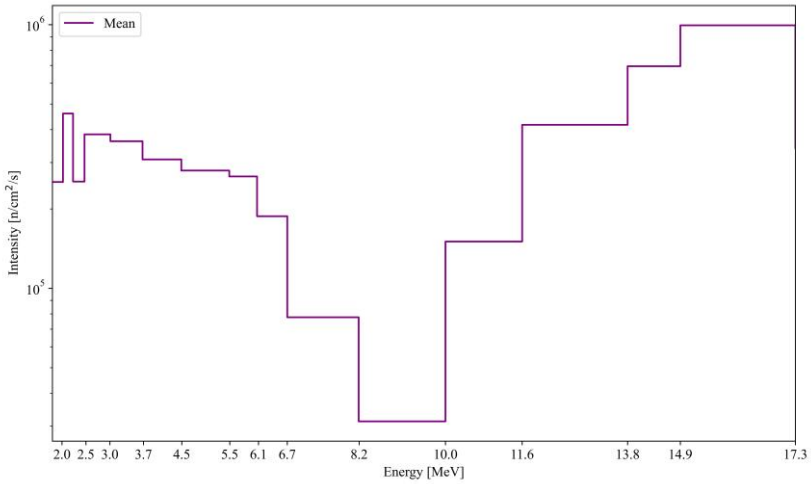

Figure 10.26. The average spectrum (16 bins) from the TR, MFI, ML, and MaxEnt results obtained using the experimental data from foils irradiation by Gradel Fusion NSD 35 2-DT-C-W.

The reconstruction results with 51 energy bins for the experimental data obtained by the TR and MFI methods are presented in figure 10.27. In the neutron spectrum produced by the TR algorithm, the peak around 14 MeV energy is broad from 12 MeV up to 16 MeV. The significant emission is also reconstructed for energies below 7 MeV. The solution obtained by the MFI method has a high energy peak of around 14 MeV with intensity at the level of $10^5 – 10^6$ neutrons/s/cm^2. The width of the peak changes for different default spectra. The part of the spectrum with energy lower than 12 MeV has about 10^5 smaller emission. The results of the reconstruction by the ML method are presented in figure 10.28. The calculations with the default spectrum I gave a spectrum with a narrow 14 MeV peak (from 13 MeV to 16 MeV) and a sudden rise of the intensity around energy 7 MeV that is found as an artefact connected with the cross-sections. The result obtained with spectrum II as default has a much wider 14 MeV peak and artefact in the same position. Spectrum III reconstructs the narrow 14 MeV peak with higher intensity in the energy above 15 MeV. The results from the MaxEnt method are presented in figure 10.29. The shape of the obtained spectra is similar to the MFI solution. The significant neutron intensity is connected only with the DT reaction for all methods apart from TR. The absence of the emission in the low energy range (below 6 MeV) implies that the DD or TT reactions do not occur in the generator. The slow decrease of the neutron emission from 14 MeV to 10 MeV is related to the neutrons scattered in the NG housing. The maximal neutron intensity varies from $5.2 \cdot 10^5$ to $1.5 \cdot 10^6$ neutrons/s/cm^2. There is a problem with the reconstruction of bins with energies higher than 16 MeV connected with the effect of boundary conditions on algorithms and default spectra influence on the results.

The discrepancy between reconstructed spectra and actual neutron intensity emitted by Gradel-Fusion NSD 35 2-DT-C-W has been evaluated by comparing the experimental activity with values simulated by FISPACT-II. The accuracies$_a$ are presented in figure 10.30. The mean accuracy$_a$ for the TR method equals 22%. The worst accurcay$_a$, 39%, is for reaction on Ni, which has the highest energy threshold. It indicates the problems with reconstructing the shape of the 14 MeV peak. The mean accuracy$_a$ for the spectra obtained by the MFI method varies between 21% and 22%. The lowest accuracies$_a$ have reactions Al(n,α), Fe(n,p), and Zr(n,2n). The main difference between solutions obtained with various default spectra is the level of emission neutrons with energies below 12 MeV. The highest intensity in this range is observed for result calculated with spectrum III as default. In this case, the accuracy$_a$ for Al(n,p) is also 2%. The relative difference between intensity in the 14 MeV peak and lower energies seem to be not correctly reconstructed due to the inconsistency in the accuracy$_a$ obtained for all reactions. The mean accuracy$_a$ for results obtained with the ML method varies from 20% to 22%. The highest error, 59%, is for reaction on Ni and was obtained for the default spectrum III. The intensity of neutron

emission in the bins with energy above 15 MeV was overestimated. The reaction with threshold energies below 7 MeV is reconstructed with the best accuracy (2% - 15%). Only the $accuracy_a$ for Al(n,α) reaction for spectrum I as default is higher. It is connected with the rapid intensity rise of around 7 MeV. The mean $accuracy_a$ obtained for the MaxEnt method varies from 20% to 23%. Reactions Fe(n,p) and Zr(n,2n) are characterised by $accuracy_a$ lower than 1%. Again, the reactions with threshold energies above 10 MeV have up to 50% of accuracy.

The mean spectrum has been calculated to improve the reliability of the reconstruction results (see figure 10.31). The negligible intensity of low-energy neutrons indicates the absence of the DD and TT reactions in the NG. The widening of the 14-MeV peak on the left side is related to a significant amount of scattered neutrons. The $accuracy_a$ worse than 30% for reactions with threshold energies above 8 MeV implies that the number of neutrons scattered in the NG elements is slightly overestimated. The $accuracies_a$ for the TR method are lower in the case of reactions on Au, Zr, and Ni due to the problem with the reconstruction of the boundary bins in other algorithms. The last energy bin should be characterised by negligible neutron emission. The intensity of the neutron emission in the last considered bin depends on the influence of the boundary conditions on the specific algorithm and used default spectrum. The artefact in the energy of about 7 MeV is reproduced from the ML solution. The overall uncertainty of the neutron spectrum emitted by Gradel-Fusion NSD 35 2-DT-C-W was determined as 18%.

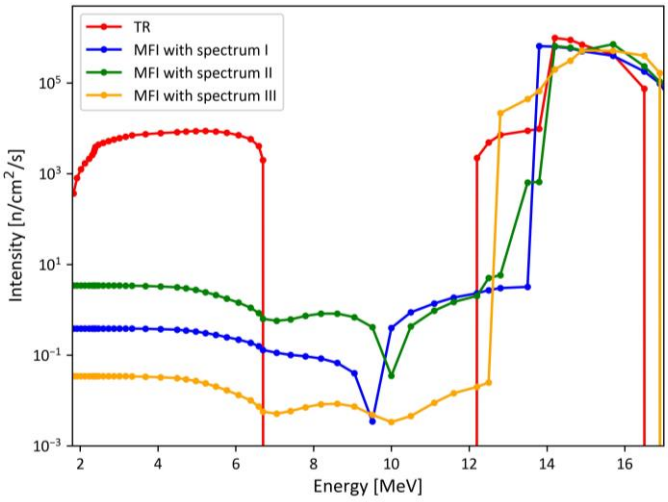

Figure 10.27. The spectra (51 bins) reconstructed by the TR and MFI methods using the experimental results from foils irradiation by Gradel-Fusion NSD 35 2-DT-C-W.

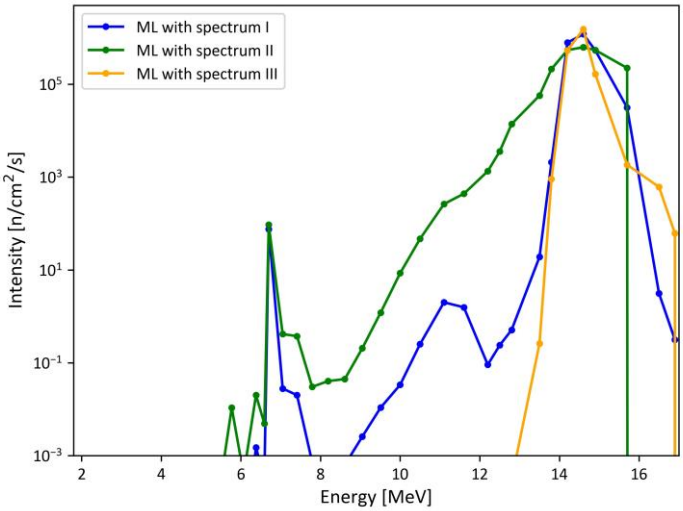

Figure 10.28. The spectra (51 bins) reconstructed by the ML method using the experimental results from foils irradiation by Gradel-Fusion NSD 35 2-DT-C-W.

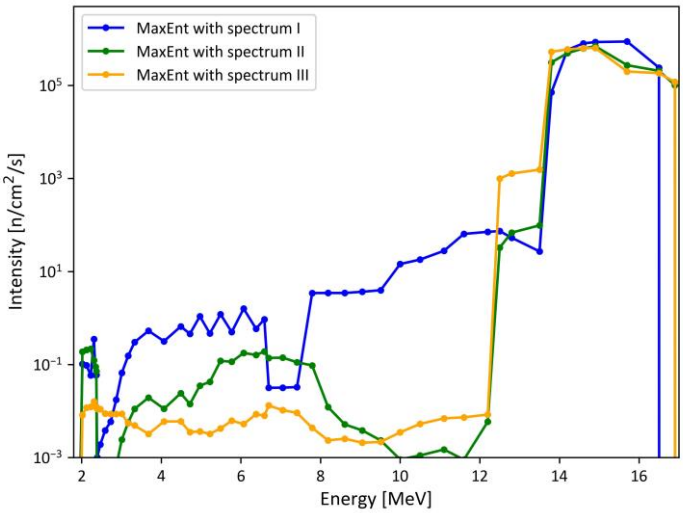

Figure 10.29. The spectra (51 bins) reconstructed by the MaxEnt method using the experimental results from foils irradiation by Gradel-Fusion NSD 35 2-DT-C-W.

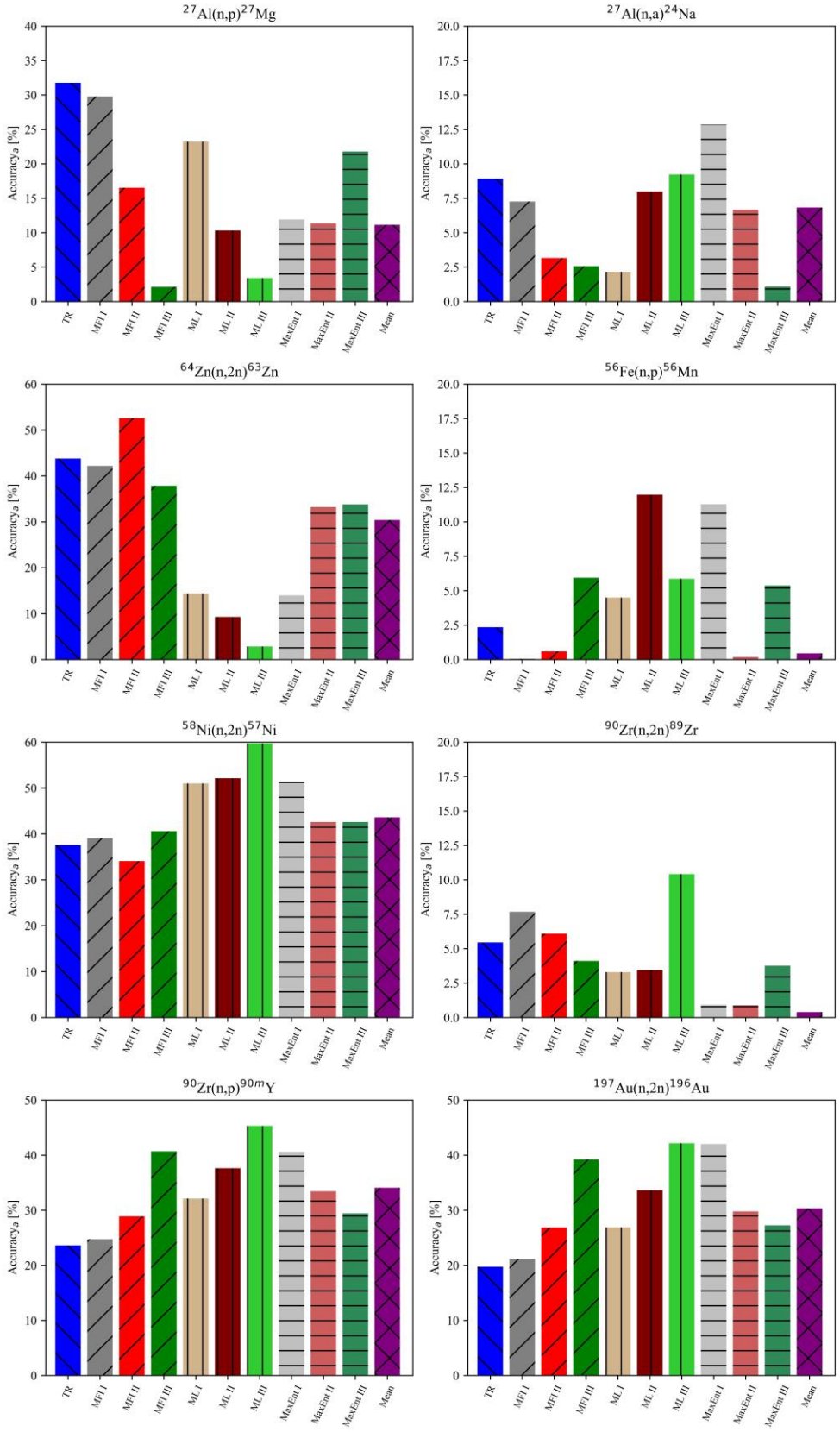

Figure 10.30. Accuracy$_a$ for the reconstructed results obtained by different methods (51 bins) with the experimental data for Gradel-Fusion NSD 35 2-DT-C-W.

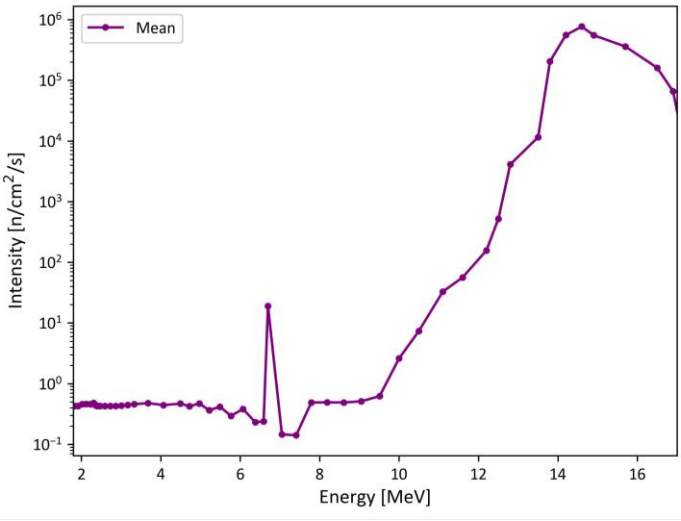

Figure 10.31. The average spectrum (51 bins) from the TR, MFI, ML, and MaxEnt results obtained using the experimental data from foils irradiation by Gradel Fusion NSD 35 2-DT-C-W.

The last analysed was 71 bin structure, with a regular energy spacing not compatible with FISPACT-II. Therefore, the accuracy$_a$ is expected to be higher than in the case of 51 bins. In this case, the level of ill-posedness is the highest due to many unknown elements of the solution. The neutron spectrum reconstructions by the TR and MFI methods are presented in figure 10.32. Both methods provide the 14 MeV peak with an intensity of $10^5 – 10^6$ neutrons/s/cm^2. The strong regularisation makes the peak smooth even for the TR algorithm. Neutron intensity higher than 1 n/s/cm^2 is reconstructed for energies below 7 MeV. The number of neutrons in this part of the spectrum is higher than in the results for 51 bins. The solutions obtained by the ML method are presented in figure 10.33. The differences between neutron emission intensity values reconstructed with various default spectra are at the level of 15%. The 14 MeV peak is shifted to the 16 MeV energy. It is connected with the interpolation of the cross-sections and the strong impact of reactions with high energy thresholds on the result with regular bin structure. The significant neutron emission is reconstructed between 9 – 10 MeV and 2 – 4 MeV. The artefact produced by the ML algorithm is shifted to the higher energy (9 MeV) compared to the result with 51 bins. The effect is connected with the interpolation of the cross-sections and maximum observed for Al(n,p) reaction. The neutrons with energy around 3 MeV might be related to the DD reaction or background. The results obtained by the MaxEnt algorithm are presented in figure 10.34. The spectra were over-smoothed by the entropy matrix (see equation (5.3.6)). Therefore, the 14 MeV peak is wide from 10 MeV to 16 MeV. There is no intensity drop to zero in the last energy bin. The emission of the neutrons with energy below 10 MeV is only 100 times smaller than the peak, indicating the TT reaction's occurrence and scattered neutrons in the generator housing. Additionally, a small emission peak occurs for energy around 2 MeV, which implies the significant presence of the DD reaction in the generator.

The reconstructed spectra were used to simulate the activity by FISPACT-II. The accuracies$_a$ for all methods and reactions are presented in figure 10.35. The mean error of reconstructed activity for the TR algorithm is 40%, with a 35% standard deviation. The accuracies$_a$ related to the reactions on Al are equal to 114% and 79%. Despite the additional uncertainty connected with the bin structure modification required before simulation, the neutron spectrum cannot be estimated by the TR result. The activity error for the MFI method varies from 21% to 44% for different default spectra. The result obtained with default spectrum I provide an accuracy$_a$ smaller than 15% for all reactions with low threshold energies. The reactions Zr(n,p) and Au(n,2n) are connected with the highest accuracy$_a$. It indicates a problem with the reconstruction of the spectrum energy range from 8 to 12 MeV, where the neutron emission intensity is negligible. The rest of the MFI results have two times higher accuracies$_a$, making the spectrum interpretation

impossible. The discrepancy between experimental data and simulation results for the ML method varies from 2% to 55%. The reconstructed 14 MeV peak reproduces the reactions activities with a low energy threshold, but the rest of the errors are higher than 20%. The mean $accuracy_a$ for the MaxEnt result obtained with default spectrum I is 47%. The reconstruction with spectrum III provides the best result with a mean $accuracy_a$ equal to 20%. The high $accuracies_a$ for the Ni and Zr indicate the neutron emission intensity overestimation above 15 MeV. The problem with the boundary conditions and termination of the spectrum is stronger in the case of regular spacing between bins.

The mean spectrum obtained from values provided by the MFI, ML and MaxEnt methods is presented in figure 10.36. The TR result was omitted in the calculation due to the $accuracy_a$ being higher than 100%. The mean $accuracy_a$ for averaged spectrum is 18%. The errors higher than 10% are for Ni, Fe, and Zn reactions. It is connected with the absence of the intensity drop for energies above 15 MeV. The uncertainty of the spectrum reconstruction was estimated as 29% (18%·C_R+5% connected with the spectrum modification before simulation estimated based on the analysis of multiple spectra).

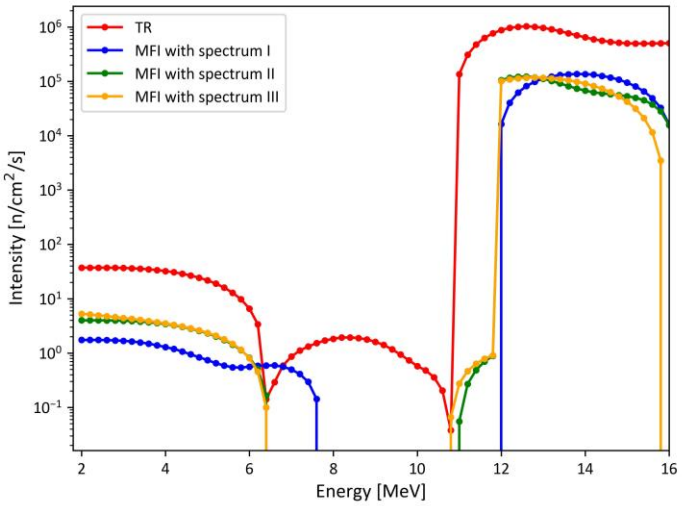

Figure 10.32. The spectra (71 bins) reconstructed by the TR and MFI methods using the experimental results from foils irradiation by Gradel-Fusion NSD 35 2-DT-C-W.

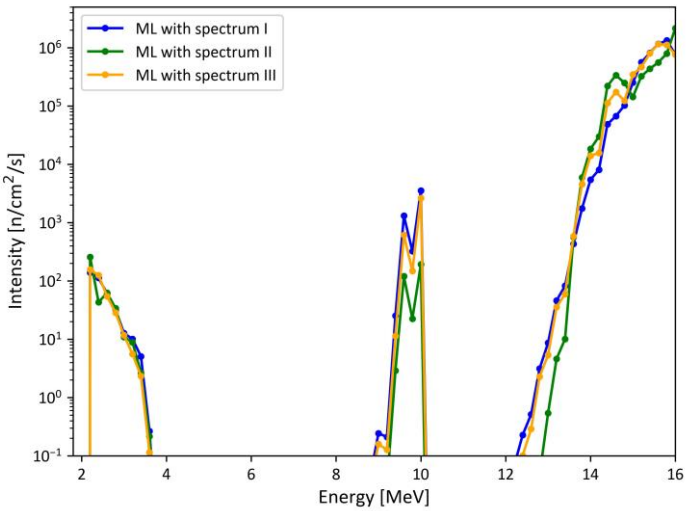

Figure 10.33. The spectra (71 bins) reconstructed by the ML method using the experimental results from foils irradiation by Gradel-Fusion NSD 35 2-DT-C-W.

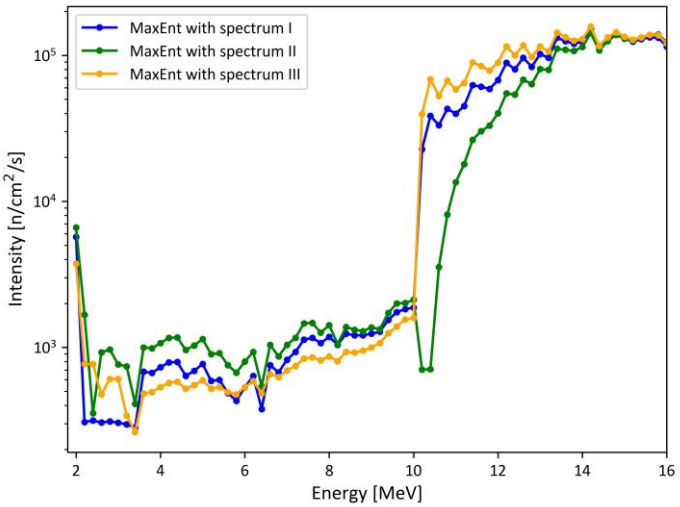

Figure 10.34. The spectra (71 bins) reconstructed by the MaxEnt method using the experimental results from foils irradiation by Gradel-Fusion NSD 35 2-DT-C-W.

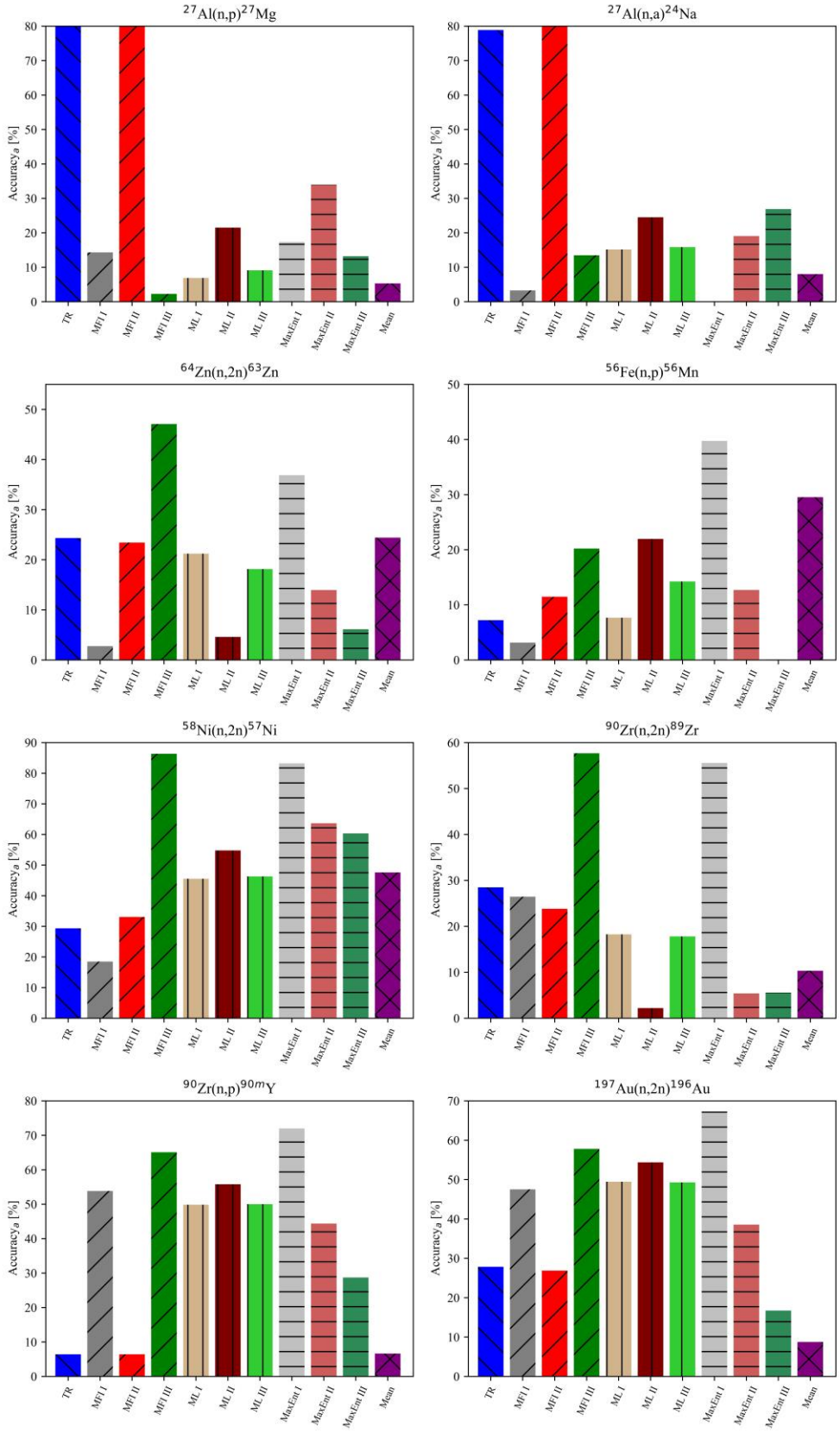

Figure 10.35. Accuracy$_a$ for reconstructed results obtained by different methods (71 bins) with the experimental data for Gradel-Fusion NSD 35 2-DT-C-W.

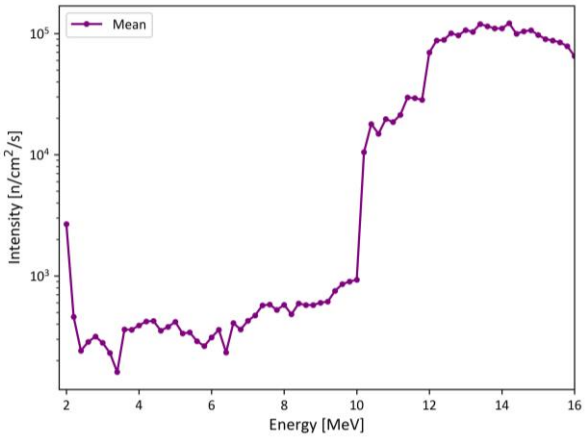

Figure 10.36. The average spectrum (71 bins) from the MFI, ML, and MaxEnt results obtained using the experimental data from foils irradiation by Gradel Fusion NSD 35 2-DT-C-W.

The reconstruction results for the set of the activity presented in table 10.2 obtained by the BrilLanCe 380 scintillator are not fully satisfactory. The $accuracy_a$ for 16 bin spectra vary from 50% to 71%. Therefore, the obtained spectra cannot be used to evaluate which fusion reactions took place in the NG. The 51 bins reconstruction results are characterised by a 20% - 23% $accuracy_a$. The lowest uncertainty was obtained by the ML and MaxEnt methods. The results for 71 bins are worse because the matrix describing the problem is more ill-conditioned, and $accuracy_a$ varies between 18% - 47%. In the spectrum structure with a high number of energy bins, averaging through all results improves the reconstruction. The $accuracy_a$ for the mean spectrum with 71 bins is 18%; therefore, the reconstruction uncertainty equals 29%. The lowest $accuracy_s$ was obtained for 51 bins and equal 18%. The main difference between the spectra with the two structures is the number of neutrons below 10 MeV energy. The broad peak around 14 MeV connected with the reaction kinetics is reconstructed in both cases. The regular structure (71 bins) implies the significant presence of the DD and TT reactions and the neutrons scattered in the generator elements. The intensity in this part of the spectrum with 51 bins is negligible. Due to the decrease of the tritium amount in the NG, the meaningful impact might have the neutron emission related to the DD reaction, but the results obtained for 71 bins are less probable because of the uncertainty value.

The neutron spectrum reconstruction's uncertainty makes interpretation of the occurrence of the fusion reactions, scattering and molecular effects difficult. The improvement of the calculation can be achieved by applying the activity measurement method that provides better uncertainty. It can be accomplished using an HPGe detector with numerical characterisation, which allows for precise efficiency calibration. The analysis analogous to that presented above with another type of generator is described in the following subchapter.

10.2 Neutron generator Sodern Genie 16C

A seal-tube neutron generator Genie 16C manufactured by Sodern (described in subchapter 2.3.1) was used in the experiment carried out in NCBJ. The experiment aimed to measure neutron source characteristics by the activation method [Las2020]. The main difference between Sodern Genie 16C and Gradel-Fusion NSD 35 2-DT-C-W is the reaction kinetics. The seal-tube neutron generator is based on the beam-target DT reaction. The activity of used foils has been registered by an HPGe spectrometer that allows for obtaining experimental results with the high precision. The activation measurement was used to reconstruct the neutron spectrum. The interpretation of the neutron spectrum allows investigation of the changes in the NG connected with the long-term operation, e.g., beam particles deposition on the target.

10.2.1 Neutron activation measurement

In the experiment with NG Sodern Genie 16C, the set of used foils was slightly different than in the case of the gas-plasma target generator. The cylindrical samples with 18 mm diameter of Al, Fe, Ni, Zr, Nb, and Au with 1 mm thickness and a 0.5 mm thick Mg foil were used. The properties of the reactions with neutrons in selected materials, crucial for the activation method, are shown in table 10.1. In this experiment, (n,p) reaction on the Zr was not measured. The cross-sections dependence on the energy for the considered reactions is presented in figure 10.2.

NG was placed inside a large hall far from the walls to reduce the impact of the backscattered neutrons. The foils were placed 21 cm from the generator tube in the plastic capsule (see figure 10.37). They were irradiated by continuous neutron flux of $2 \cdot 10^8$ n/s in 4π by 3h. After irradiation, the foils were manually transported to the gamma spectrometry laboratory. The activation products in the foils were measured by the HPGe detector. The spectrometer is characterised by 30% of relative efficiency and 1.8 keV resolution for 1332 keV energy. The foils were measured separately by putting them directly on the detector endcap in the optimal measurement sequence. The efficiency calibration was made with numerical characterisation and Canberra Laboratory Calibration Software (LabSOCS) [Bro2003]. The specific activities have been corrected to the value corresponding to the end of irradiation. The measurement results are presented in table 10.8. Owing to the use of the more precise spectrometer and efficiency calibration, the maximal uncertainty of the calculated activity is 12%. The more regular distribution of the reaction cross-section can also improve the neutron spectrum reconstruction.

Figure 10.37. The location of the Sodern Genie 16C during the experiment (left) and capsule with dosimetry foils (right) [Las2017].

Table 10.8. Results of the neutron activation measurement of Sodern Genie 16C measured by the HPGe detector.

Sample	Reaction	Specific activity [Bq/g]	Uncertainty [%]
Al	$^{27}Al(n,p)^{27}Mg$	25.94	11
	$^{27}Al(n,\alpha)^{24}Na$	4.58	6
Fe	$^{56}Fe(n,p)^{56}Mn$	9.10	7
Ni	$^{58}Ni(n,2n)^{57}Ni$	0.19	8
Zr	$^{90}Zr(n,2n)^{89}Zr$	0.90	7
Au	$^{197}Au(n,2n)^{196}Au$	0.69	12
Mg	$^{24}Mg(n,p)^{24}Na$	6.98	6
Nb	$^{93}Nb(n,2n)^{92m}Nb$	0.35	5

10.2.2 Neutron spectrum reconstruction

An analysis analogous to the one described in chapter 10.2.1 has been made for Sodern Genie 16C neutron generator. The next subchapter (10.2.2.1) contains an analysis of the synthetic data. Two types of accuracies connected with the spectrum and activity reconstruction were calculated. Their ratio (C_R) was used to estimate the spectrum reconstruction uncertainty from the experimental data, which is described in detail in subchapter 10.2.2.2.

10.2.2.1 Synthetic data analysis

The reconstruction of the neutron spectrum has been considered in the energy range of 1.8 - 17 MeV. The lower limit is connected to the smallest threshold energy of the analysed reactions. The highest energy was shifted in comparison to the analysis of Gradel Fusion NSD 35 2-DT-C-W due to the high intensity reconstructed in the last energy bins. The considered spectrum structures are 51 bins compatible with FISPACT-II and 76 bins with 200 keV spacing. The spectra with lower resolution (9 and 16 bins) are excluded from the analysis because the simulated activity has a very low agreement with the experimental results. Three default spectra with a dominant neutron emission intensity peak around 14-MeV have been prepared (see figure 10.38). The first spectrum originates from [Las2020] and the results of the calculation made using codes Gravel [Mat1994] and Maxed [Reg1999] for the 175 bin structure. Spectrum II is the same as in the previous analysis originating from the Monte Carlo simulation for the sealed-tube NG [Cuf2017]. The last spectrum (III) is the mean value of the two described above with added random noise. The intensity in the 14 MeV peak varies in $3.4 - 4.4 \cdot 10^3$ n/s/cm^2. The neutron emission above 10 MeV increases from about 10 up to 10^3 n/s/cm^2. The significant impact of the scattered neutrons is considered.

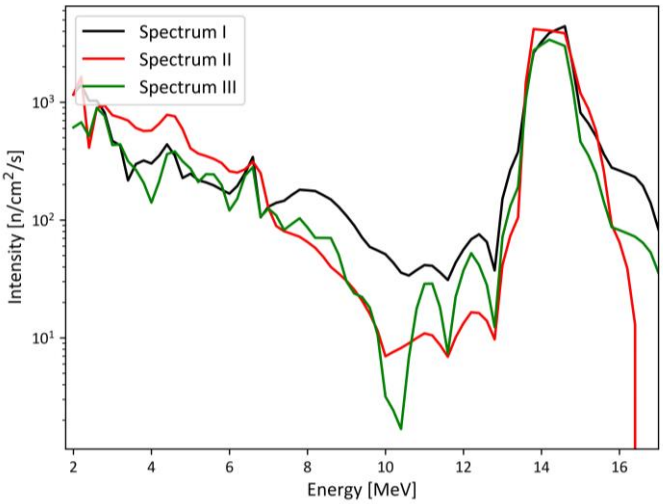

Figure 10.38. The default spectra (76 bin structure) for reconstruction of the neutron spectrum emitted by Sodern Genie 16C.

The synthetic activation data obtained by the FISPACT-II inventory code with spectrum I was used as an input in the analysis of the neutron spectrum reconstruction capability. The synthetic values and their comparison with the experimental data are presented in table 10.9. The disagreement with the experimental results is lower than in the case of Gradel Fusion NSD 35 2-DT-C-W. The reaction on Au causes a problem because of the high experimental uncertainty compared to other samples. The accuracy$_a$ improvement was achieved by applying the TR, MFI, ML, and MaxEnt methods.

Table 10.9. Synthetic specific activity obtained by the FISPACT-II inventory code with spectrum I for Sodern Genie 16C analysis.

Sample	Reaction	Specific activity [Bq/g]	Simulation uncertainty [%]	Disagreement with experimental results [%]
Al	$^{27}Al(n,p)^{27}Mg$	25.45	9.6	2
	$^{27}Al(n,\alpha)^{24}Na$	5.96	9.7	30
Fe	$^{56}Fe(n,p)^{56}Mn$	8.06	9.3	11
Ni	$^{58}Ni(n,2n)^{57}Ni$	0.17	12.8	13
Zr	$^{90}Zr(n,2n)^{89}Zr$	0.92	7.2	3
Au	$^{197}Au(n,2n)^{196}Au$	1.51	10.7	118
Mg	$^{24}Mg(n,p)^{24}Na$	8.43	10.8	21
Nb	$^{93}Nb(n,2n)^{92m}Nb$	0.46	16.0	30

The neutron spectra with 51 energy bins reconstructed by the TR and MFI methods are presented in figure 10.39. The solution from the TR algorithm has a mean $accuracy_s$ equal to 157%. The regularisation based only on the derivative matrix does not provide a result similar to spectrum I. The 14 MeV peak is wider, and the neutron intensity below 4 MeV is lower than the default. The difference between spectra obtained by the MFI method with spectra I and II is negligible, and its mean $accuracy_s$ is 38%. Spectrum III allows obtaining a mean $accuracy_s$ of 48%. The shape of the peak with an energy of around 14 MeV is reconstructed as well as the intensity rise of about 2 MeV. Application of the weigh matrix improves the regularisation results significantly. The spectra reconstructed by the ML method are presented in figure 10.40. The calculation with spectrum I does not implement changes. The mean $accurcay_s$ for the rest of the default spectra varies from 32% to 51%. In general, the spectrum shape is reproduced. The results of the reconstruction by the MaxEnt method are presented in figure 10.41. The mean $accuracies_s$ are 29%, 39%, and 32% for spectra I, II, and III, respectively. The MaxEnt method provides the results with the lowest errors. The shape of the neutron spectrum is well reconstructed by the MFI, ML, and MaxEnt methods for all considered default spectra, indicating properly selected regularisation parameters.

The $accuracies_a$ for all methods and reactions are presented in figure 10.42. The ratios C_R are shown in table 10.10. The main issue with ill-conditioned problems is the existence of an infinite number of solutions. The different neutron spectra can provide the same irradiation activities. Therefore, evaluating the spectrum reliability based only on the activity comparison does not provide a trustworthy analysis. The mean $accuracy_a$ obtained by the TR algorithm is 7%, for the MFI method varies from 6% to 9%. In both cases, the $accuracy_a$ higher than 11% is only for (n,p) reaction on Al. It is connected with over or underestimating the energy bins below 3 MeV. The result obtained by the MFI method with spectrum III is characterised by the lowest standard deviation of 2%. The absolute values might be reproduced imprecisely, but the shape of the spectrum is the closest to the synthetic one used in the simulation. The mean $accurcay_a$ for the ML method is 1% for two default spectra. The reconstruction result identical to the synthetic spectrum was not presented in the figure. The highest $accuracy_a$, 5%, is for reaction on Mg. It is connected with the discrepancy between the synthetic and reconstructed spectrum for energy between 10 MeV and 13 MeV, where the reaction cross-section is dominant. The mean $accuracies_a$ for results obtained by the MaxEnt method vary from 3% to 29%. The standard deviations for these results are below 3%.

The mean spectrum from the MFI, ML, and MaxEnt methods has been calculated to improve the reconstruction error. The TR result was excluded from the calculations due to a significant difference between its shape and all other solutions for energies below 4 MeV. The average neutron spectrum is presented in figure 10.43. The mean $accurcay_s$ is 21%, and $accurcay_a$ is 7% [Mik2022b].

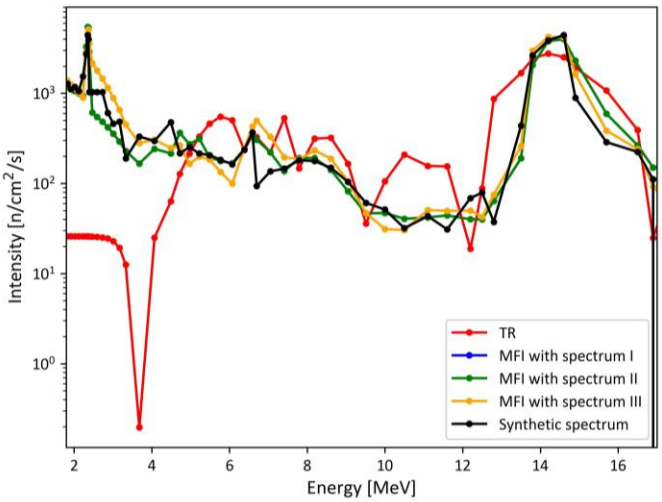

Figure 10.39. The spectra (51 bins) reconstructed by the TR and MFI methods using the synthetic data simulated for Sodern Genie 16C.

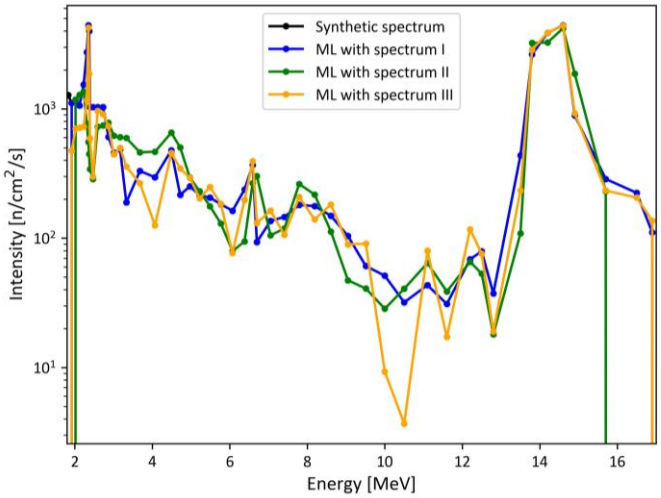

Figure 10.40. The spectra (51 bins) reconstructed by the ML method using the synthetic data simulated for Sodern Genie 16C.

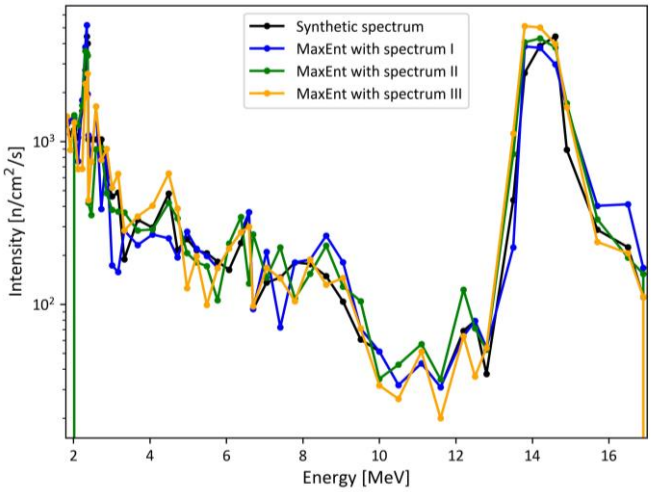

Figure 10.41. The spectra (51 bins) reconstructed by the MaxEnt method using the synthetic data simulated for Sodern Genie 16C.

Table 10.10. The accuracies$_s$, accuracies$_a$, and C_R obtained for the synthetic data simulated for Sodern Genie 16C and 51 bin structure by different methods.

Method	Mean accuracy$_s$ [%]	Mean accuracy$_a$ [%]	C_R
TR	157	7	22.4
MFI with spectrum I	38	6	6.3
MFI with spectrum II	38	6	6.3
MFI with spectrum III	48	9	5.3
ML with spectrum I	0	0	0.0
ML with spectrum II	51	1	51.0
ML with spectrum III	32	1	32.0
MaxEnt with spectrum I	29	3	9.7
MaxEnt with spectrum II	39	17	2.3
MaxEnt with spectrum III	32	29	1.1
Mean	21	7	3.0

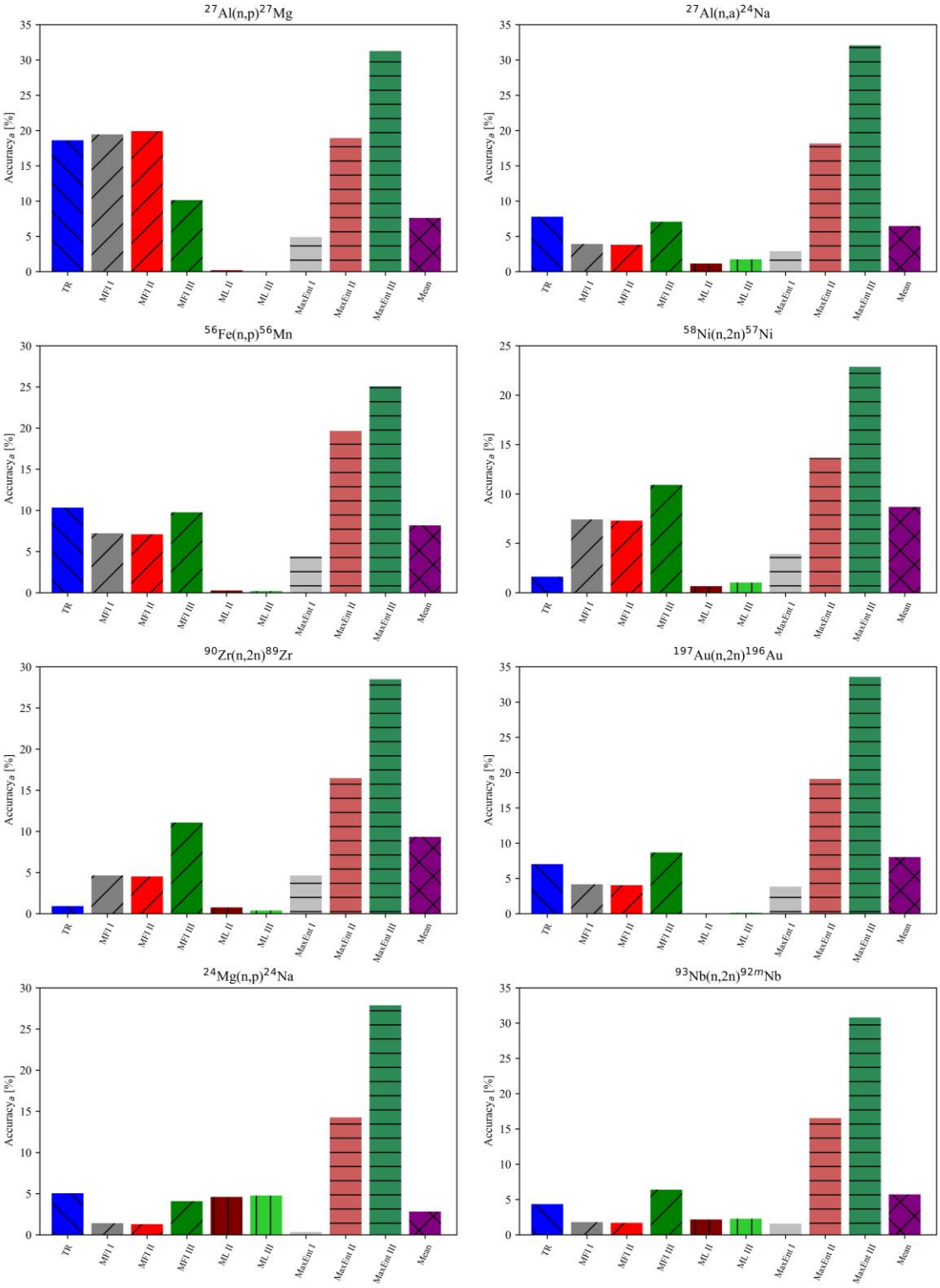

Figure 10.42. Accuracy$_a$ for reconstructed results obtained by different methods with the synthetic activity originated from spectrum I (51 bins) simulated for Sodern Genie 16C.

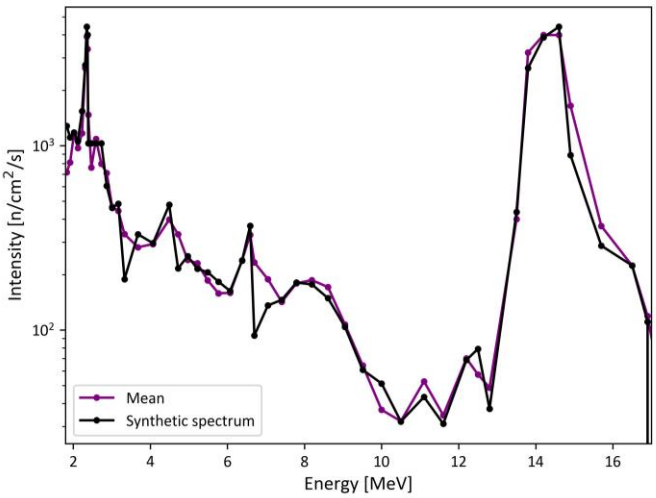

Figure 10.43. The average spectrum (51 bins) from the MFI, ML, and MaxEnt results obtained using the synthetic data simulated for Sodern Genie 16C.

The neutron spectra with 76 bins obtained by the TR and MFI methods are presented in figure 10.44. The TR algorithm provides the solution with strong oscillations of the neutron emission values, which makes its shape different from spectrum I. The mean $accuracy_s$ for the MFI method varies from 25% to 28%. The shape of the spectrum with regular energy bins is fully reconstructed. The results obtained by the ML algorithm are presented in figure 10.45. The code did not modify the spectrum I used as default. The spectrum reconstructed with the default spectrum II differs from the synthetic one used in the simulation by about 42%. The highest discrepancy is observed for energy bins above 16 MeV. Strong fluctuations in the neutron emission characterize the result obtained by the ML method with spectrum III, but its mean $accuracy_s$ is 25%. The results obtained by the MaxEnt algorithm are presented in figure 10.46. Due to the strong regularisation, the differences between reconstruction solutions for various default spectra are small. The mean $accuracy_s$ varies from 18% to 19%, which is the best result. The neutron spectra with the regular structure are reconstructed with the better precision than in the case of 51 bins. It is connected with the irregular energy ranges in the bins in the structure compatible with FISPACT-II and interpolating the cross-sections in the contribution matrix. The 51 bin spectrum has better resolution in the low energy part, where neutrons impact on the measurement is weak due to the threshold energies. The broad energy bins around 14 MeV make reconstruction more difficult. The changes in the cross-section above 8 MeV are rapid and smaller bins better reflect these effects.

The spectra obtained by different methods have been used in FISPACT-II to simulate the induced activities. The discrepancy between the reconstructed and synthetic data is presented in figure 10.47. The mean $accuracy_a$ for the TR method is 4%. The same problem occurs for 51 bins, the activities are reconstructed with good precision, but the spectrum error is almost 100%. The comparison of the results obtained by different methods allows for the selection of the neutron spectra that are inconsistent. Despite the low $accuracy_a$, it should be acknowledged as not reliable. The highest $accuracy_a$ is equal to 24% for Fe foil and the MFI method with spectrum I as default. The small $accuracy_s$ in the energy range from 3 MeV to 17 MeV influence the Mn activity induced in Fe. The mean $accuracy_a$ for other default spectra used in the MFI algorithm equals 8%. The standard deviation for these results is lower than 2%. The highest discrepancy between reconstructed and experimental activity obtained by the ML method was observed for the reaction on Au. It is connected with the low neutron emission intensity in the bins with energy above 16 MeV. The mean $accuracies_a$ are 5% and 7% for spectrum II and III as default. Due to the high precision of the bins around 14 MeV, the lowest discrepancy between activities is characterized by the reaction on Mg, which has a maximum cross-section in this area. The mean

activity accuracies for the MaxEnt method vary from 2% to 3%. The highest $accuracy_a$, in this case, characterise (n,p) reaction on Al which has the lowest energy threshold. The spectrum part with energy below 3 MeV is reconstructed with the highest discrepancy.

The mean spectrum (see figure 10.48) was calculated to improve the $accuracy_s$. The mean $accuracy_s$ is 11%, which is the best result. The mean $accuracy_a$ is equal to 6%. The highest error resulted for (n,p) reaction on Al which influences discrepancies of the reconstruction in the full spectrum energy range. Table 10.11 shows C_R [Mik2022b].

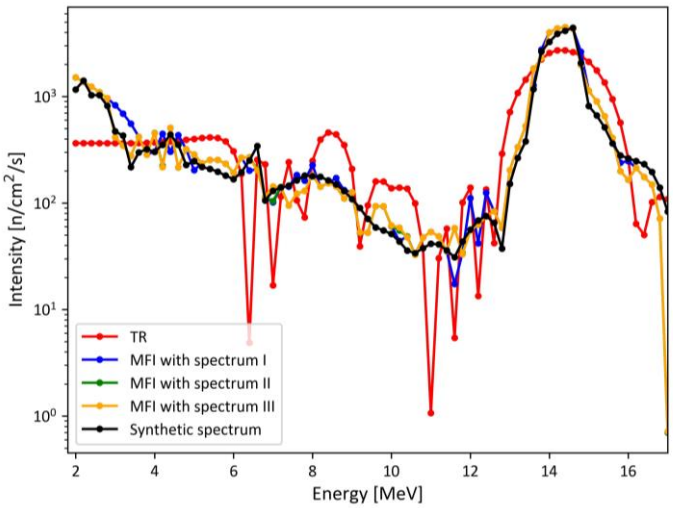

Figure 10.44. The spectra (76 bins) reconstructed by the TR and MFI methods using the synthetic data simulated for Sodern Genie 16C.

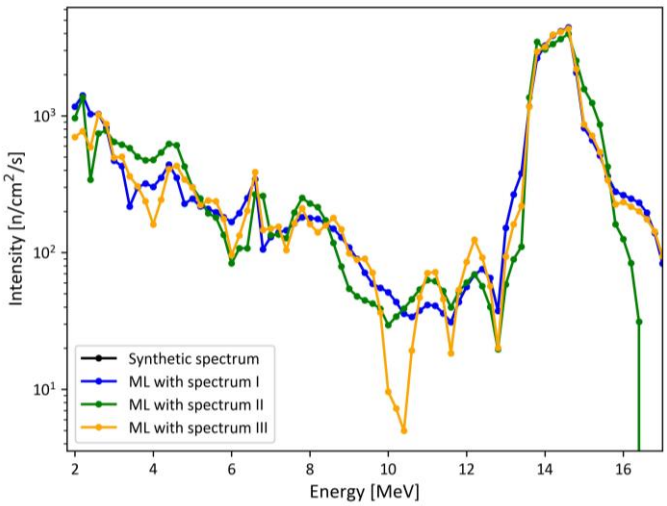

Figure 10.45. The spectra (76 bins) reconstructed by the ML method using the synthetic data simulated for Sodern Genie 16C.

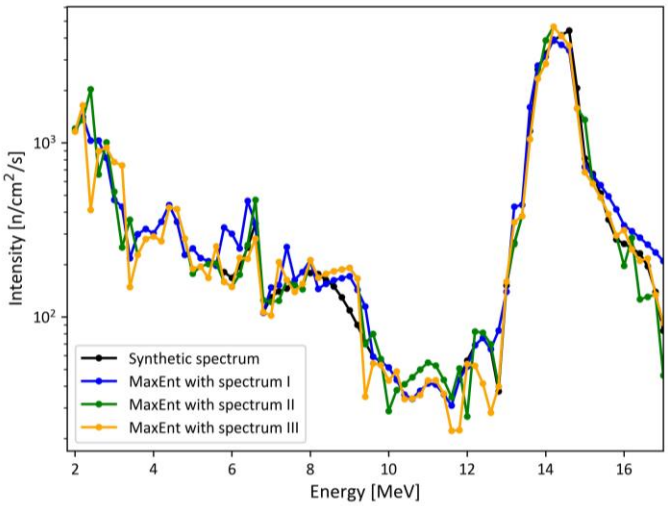

Figure 10.46. The spectra (76 bins) reconstructed by the MaxEnt method using the synthetic data simulated for Sodern Genie 16C.

Table 10.11. The accuracies$_s$, accuracies$_a$, and C_R obtained for the synthetic data simulated for Sodern Genie 16C and 76 bin structure by different methods.

Method	Mean accuracy$_s$ [%]	Mean accuracy$_a$ [%]	C_R
TR	97	4	24.3
MFI with spectrum I	28	14	2.0
MFI with spectrum II	25	8	3.1
MFI with spectrum III	25	8	3.1
ML with spectrum I	0	0	0.0
ML with spectrum II	42	5	8.4
ML with spectrum III	25	7	3.6
MaxEnt with spectrum I	18	2	9.0
MaxEnt with spectrum II	21	3	7.0
MaxEnt with spectrum III	19	2	9.5
Mean	11	6	1.8

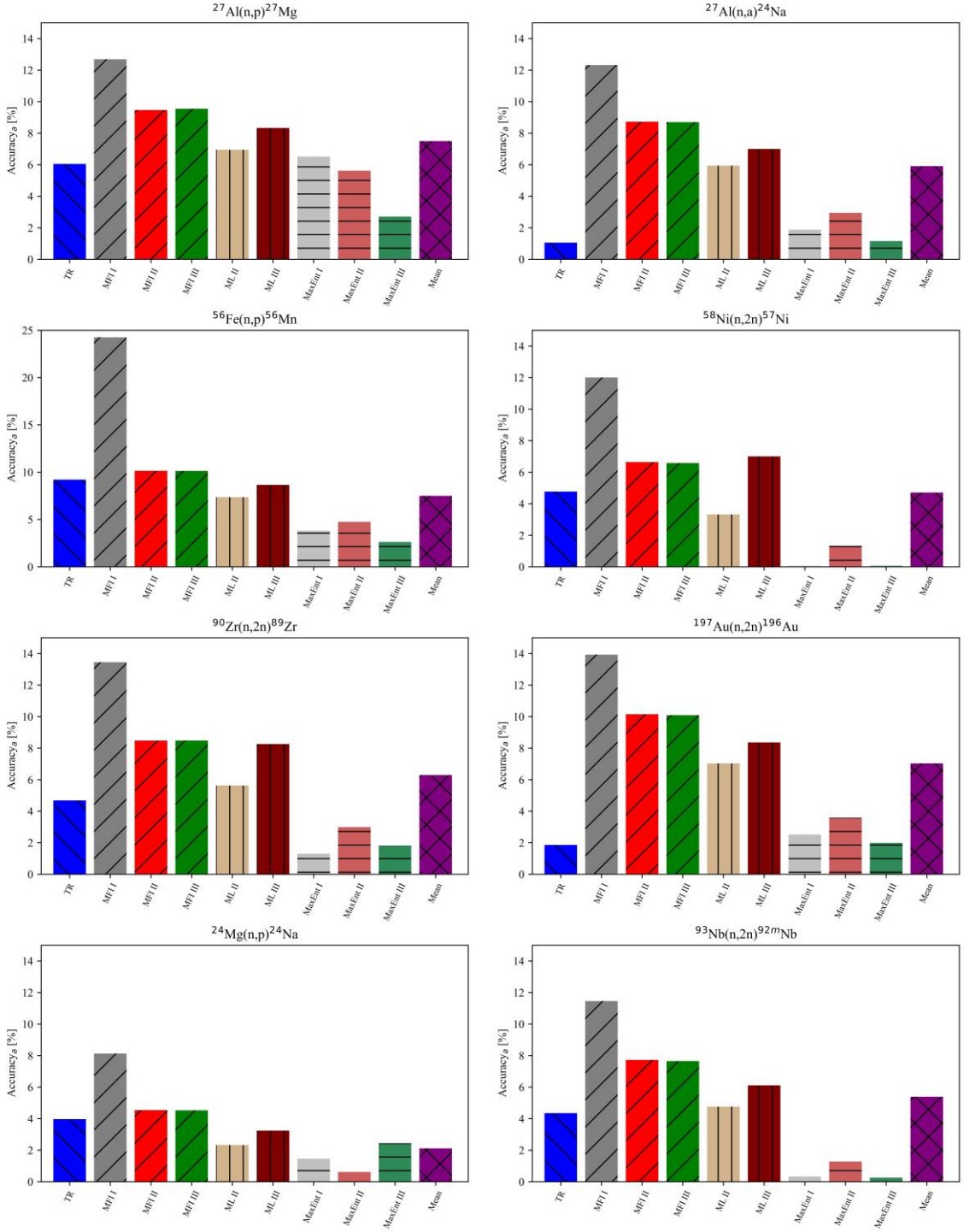

Figure 10.47. Accuracy$_a$ for reconstructed results obtained by different methods with the synthetic activity originated from spectrum I (76 bins) simulated for Sodern Genie 16C.

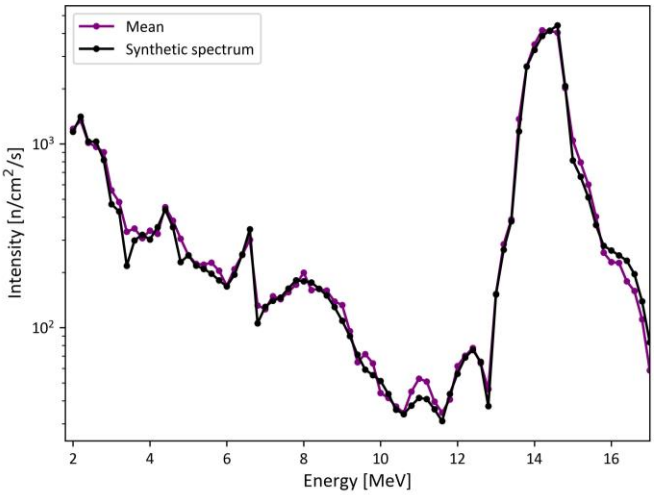

Figure 10.48. The average spectrum (76 bins) from the TR, MFI, ML, and MaxEnt results obtained using the synthetic data simulated for Sodern Genie 16C.

10.2.2.2 Experimental data analysis

The ratio of activity and spectrum accuracies established in the synthetic data analysis was used to calculate the uncertainty of the neutron spectrum reconstruction from the experimental results. In the synthetic data analysis, the activity induced in Au was two times higher than the measured value. This reaction has the highest uncertainty, but it was used in the calculations to avoid reducing the number of data points. The default spectra used in the reconstruction of the experimental data are the same as for the synthetic analysis (see figure 10.38).

The results of the neutron spectrum reconstruction with 51 bins obtained for the experimental data by the TR and MFI methods are presented in figure 10.49. The 14 MeV peak reconstructed by the TR algorithm is broad. The intensity below 12 MeV is significant, up to $2.2 \cdot 10^3$ n/s/cm^2. The results obtained by the MFI method with various default spectra have a similar shape of the 14 MeV peak with a maximum of around $3.8 \cdot 10^3$ n/s/cm^2. There is an intensity decrease between 8 and 12 MeV. For spectrum I, as default, the number of neutrons with an energy of about 2 MeV is higher than 14 MeV. In the results obtained with spectra II and III, the emission level for energies below 8 MeV is up to $2.3 \cdot 10^3$ n/s/cm^2. The shape of the reconstructed spectra indicates a strong influence of the scattered neutrons on the measurement. The results obtained by the ML method are presented in figure 10.50. For all default spectra, two peaks with the maximum with the same order of magnitude occur around 6 – 9 MeV and 13 – 17 MeV energies. The presence of the peak with lower energy can be connected to the thresholds of the reactions on Au and Mg. A similar problem with the ML algorithm was observed in the analysis of the experimental data for the Gradel-Fusion NSD 35 2-DT-C-W neutron generator. The code does not include the regularisation that acts like smoothing, which is necessary for these calculations. The results of the reconstruction by the MaxEnt method are presented in figure 10.51. The shape of the spectra is similar to that obtained by the MFI algorithm. The maximal intensity is shifted from 14.1 MeV to 14.6 MeV. It is connected with the kinematics of the beam-target reaction. The number of neutrons below 8 MeV is about 40% of the maximal value. All methods provide the neutron spectra with explicit peak originating from the DT reaction and meaningful contribution from the scattered neutrons. The DD reaction related to the presence of deuterium ions in the target cannot be distinguished.

The accuracies$_a$ for activity simulated by FISPACT-II with all obtained spectra are presented in figure 10.52. The accuracy for the Au activity obtained by the MFI, ML, and MaxEnt methods is about two times lower than for spectrum I, which was obtained by Gravel and Maxed codes. The errors for the TR result are very high; the mean value equals 79%. It is connected with the high

intensity reconstructed for energy range 8 – 12 MeV. The TR method is the simplest and provides the neutron spectrum that cannot be interpreted as emitted by Sodern Genie 16C NG. The mean accuracies$_a$ for the MFI method vary from 10% to 13%. The best result is obtained with spectrum III as default. Despite the reaction on Au, only accuracy$_a$ for Fe is higher than 5%. The mean accuracy$_a$ for the ML method is about 13%. The reaction on Mg was reconstructed with the lowest error, which proved the strong impact of its cross-section on the solution. In this algorithm, the absolute values of the cross-sections with comparable uncertainty play a crucial role. The mean accuracy$_a$ for the MaxEnt method is 10%. An accuracy$_a$ higher than 7% is observed only for the reaction on the Au. The MaxEnt algorithm reconstructed the neutron spectrum with the lowest uncertainty.

The mean spectrum from results obtained by the MFI, ML, and MaxEnt methods is presented in figure 10.53. The TR result was excluded from averaging because the accuracy$_a$ was much higher than that obtained for other methods. The mean accuracy$_a$ is 10%, and since C_R equals 3, the uncertainty of the spectrum reconstruction is 30%. If Au reaction is excluded from the calculation, the uncertainty is 15%. The 14 MeV peak is slightly shifted to the higher energies, which is connected with the beam-target mechanism of the reaction. The high intensity with energies below 8 MeV indicates the surprisingly strong impact from scattered neutrons that makes examination of the impact of the DD reactions impossible.

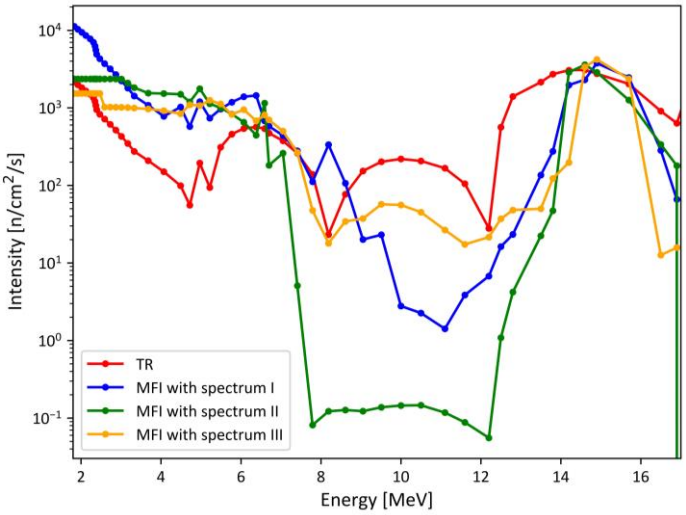

Figure 10.49. The spectra (51 bins) reconstructed by the TR and MFI methods using the experimental results from foils irradiation by Sodern Genie 16C.

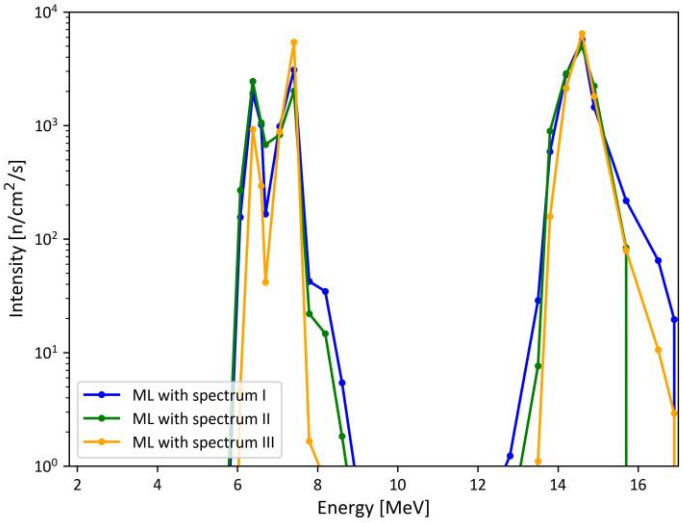

Figure 10.50. The spectra (51 bins) reconstructed by the ML method using the experimental results from foils irradiation by Sodern Genie 16C.

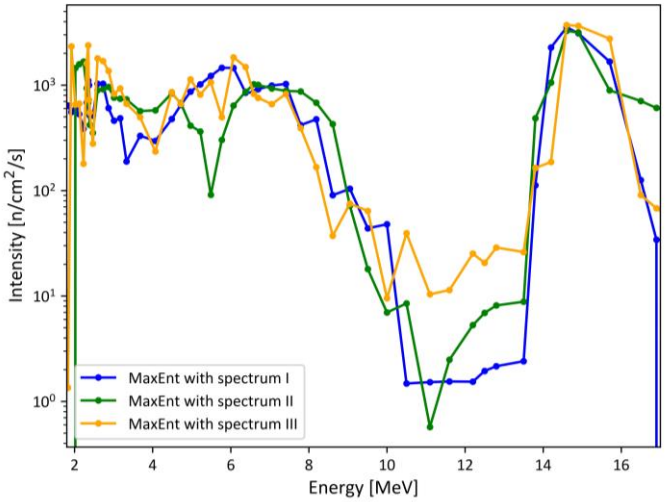

Figure 10.51. The spectra (51 bins) reconstructed by the MaxEnt method using the experimental results from foils irradiation by Sodern Genie 16C.

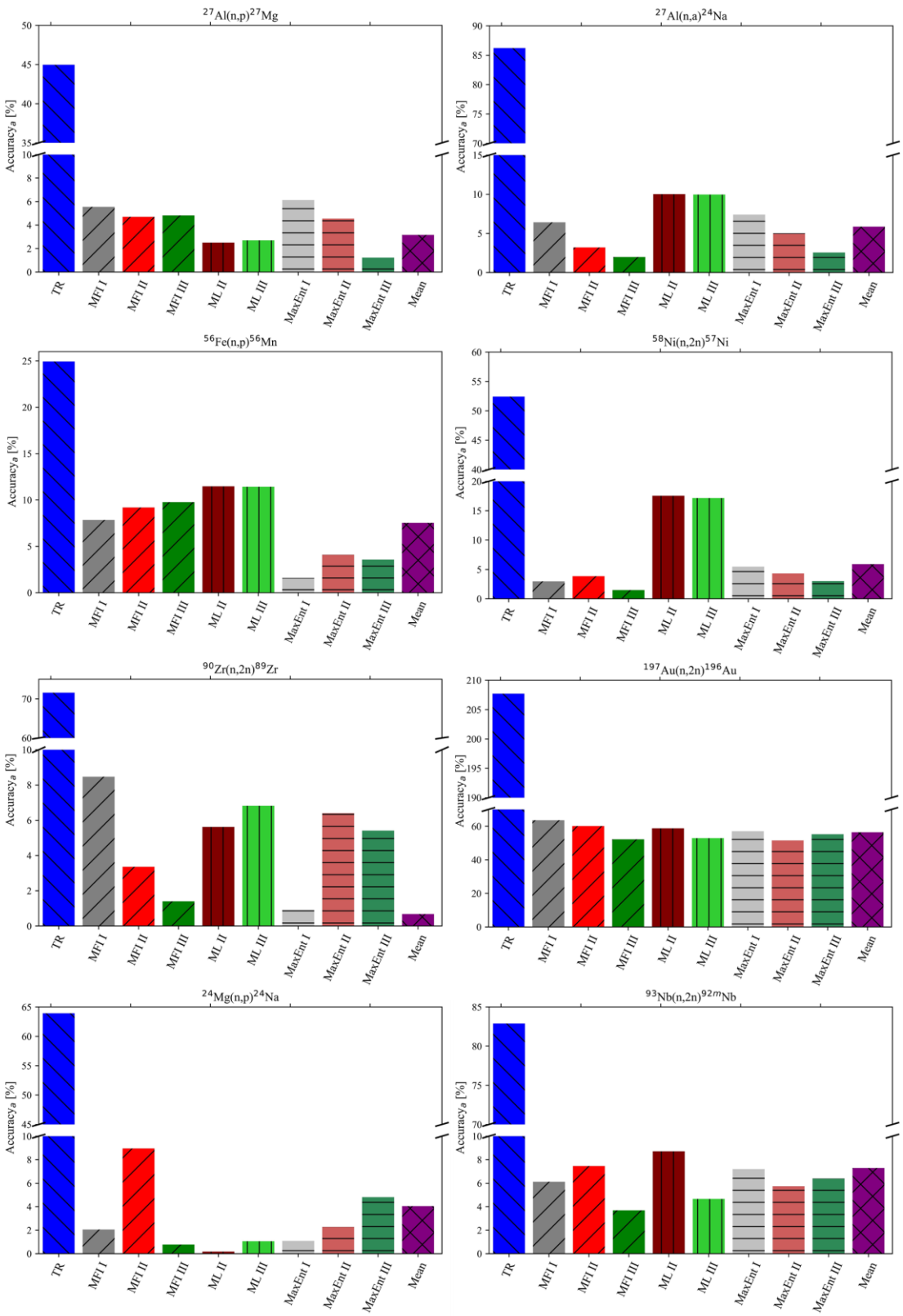

Figure 10.52. Accuracy$_a$ for reconstructed results obtained by different methods (51 bins) with the experimental data for Sodern Genie 16C.

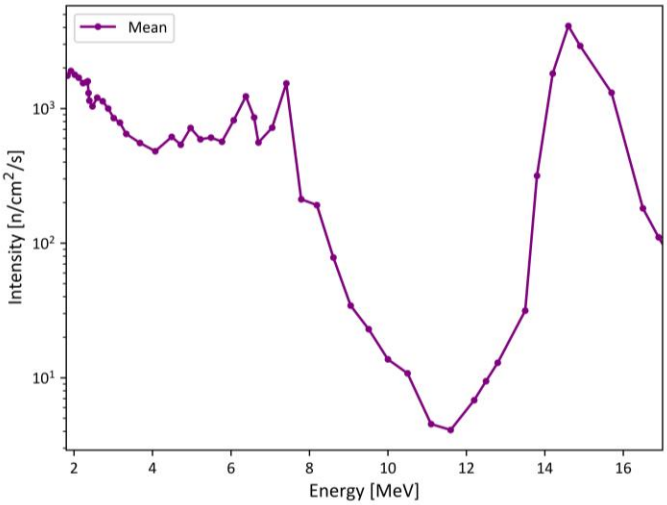

Figure 10.53. The average spectrum (51 bins) from the MFI, ML, and MaxEnt results obtained using the experimental data from foils irradiation by Sodern Genie 16C.

The reconstructed spectra with 76 bins by the TR and MFI methods are presented in figure 10.54. The neutron intensity from the TR algorithm fluctuates strongly from 1 to $2.7 \cdot 10^3$ n/s/cm^2. The simple regularisation does not provide the smooth solution in this case. The maximal emission obtained by the MFI code corresponds to 14.6 MeV. The same shift in the 14 MeV peak is observed for the 51 bin structure. The lowest number of neutrons is emitted with energy between 8 and 12 MeV. The significant impact on the spectrum have bins with energy below 8 MeV that correspond to the scattered neutrons. The results of the reconstruction by the ML method are presented in figure 10.55. The same problem as for the 51 bin structure occurs in this calculation. The structure with neutron intensity below 10 MeV is identified as artefacts. The neutron spectra obtained by the MaxEnt method are shown in figure 10.56. The 14 MeV peak reconstructed from spectrum I is broad from 10 MeV up to 17 MeV. The regularisation matrix calculated based on this default input oversmoothed high energy part of the spectrum. All results introduce domination of the direct DT neutrons and a significant number of scattered particles. The impact of the DD reaction is not visible. The reconstructed spectra are similar to the results with 51 energy bins.

The accuracies$_a$ for all methods and reactions are presented in figure 10.57. Again, the accuracy calculated for Au foils which is higher than 50%, increases the spectrum reconstruction uncertainty. The mean accuracy$_a$ for the TR algorithm is 18%. Except for Au, the (n,α) reaction on Al is characterised by the highest discrepancy between simulation and experimental data. It is related to the sudden intensity drops for energies between 6 and 12 MeV, where its cross-section increases. The mean accuracy$_a$ for the MFI method varies from 11% to 13%. For the default spectrum I, an accuracy$_a$ above 10% is observed for Fe foil, which has a non-zero cross-section in a wide energy range. The worse accuracy for reaction (n,p) on Al for spectrum II as default is connected with underestimating the emission below 3 MeV. Spectrum III as input provides the result with an accuracy$_a$ higher than 10% for Fe(n,p) and Al(n,p). It indicates that the neutron intensity below 8 MeV is slightly overestimated. The boundary conditions in connection with the default spectra are the reason for the reconstruction of a too high contribution of the scattered neutrons. The mean accuracy$_a$ for the ML method varies from 14% to 15%. The highest accuracy$_a$ (except Au) characterises the Al foil due to the low threshold energies for both observed reactions and the absence of the neutron intensity in the part of the spectrum with energy below 6 MeV. The lowest accuracies$_a$ are observed for Mg, Fe, and Nb, which have threshold energies between 3 MeV and 9 MeV. The artefacts in the spectrum originate from fitting the result to these reactions. The mean accuracy$_a$ for MaxEnt varies from 12% to 15%. Ni foil is characterised by the highest error obtained for the default spectra I and II, which is

connected with overestimating the intensity in energy bins above 16 MeV. In the calculations with spectrum III, the worst $accuracy_a$ is obtained for Fe and Ni. The Ni(n,2n) cross-section values has one of the highest uncertainties in the FISPACT-II calculations.

The average spectrum from all results is presented in figure 10.58. The mean activity accuracy is 10%. All reactions (after Au exclusion) have errors below 5%. The spectrum reconstruction uncertainty is estimated as 18%. The result is very similar to the spectrum obtained in the calculation with the 51 bin structure. The dominant 14 MeV peak is shifted by about 0.5 MeV, which is related to the DT reaction kinematics. The significant impact of the scattered neutrons does not allow for the interpretation of the DD reaction presence and additional deposition of the beam ions in the target. The $accuracy_a$ implies an overestimation of the lower energy part of the spectrum.

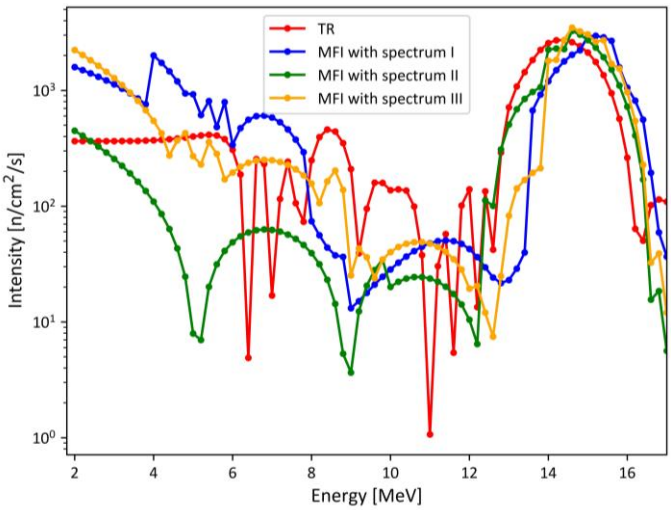

Figure 10.54. The spectra (76 bins) reconstructed by the TR and MFI methods using the experimental results from foils irradiation by Sodern Genie 16C.

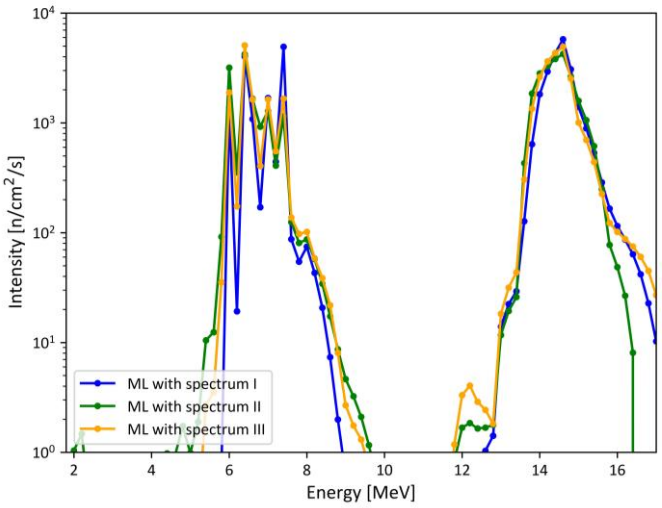

Figure 10.55. The spectra (76 bins) reconstructed by the ML method using the experimental results from foils irradiation by Sodern Genie 16C.

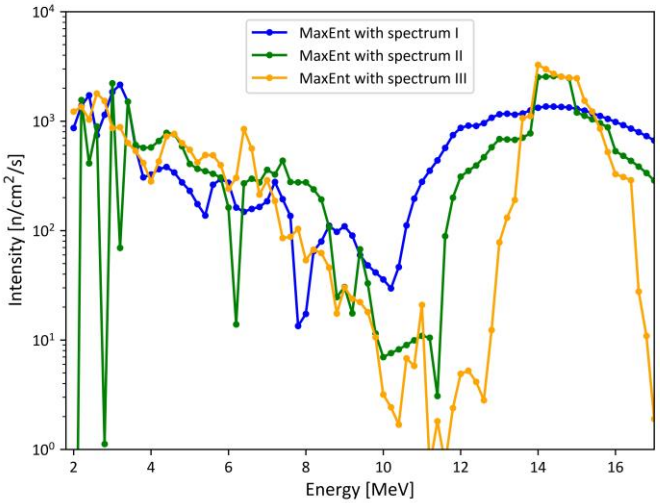

Figure 10.56. The spectra (76 bins) reconstructed by the MaxEnt method using the experimental results from foils irradiation by Sodern Genie 16C.

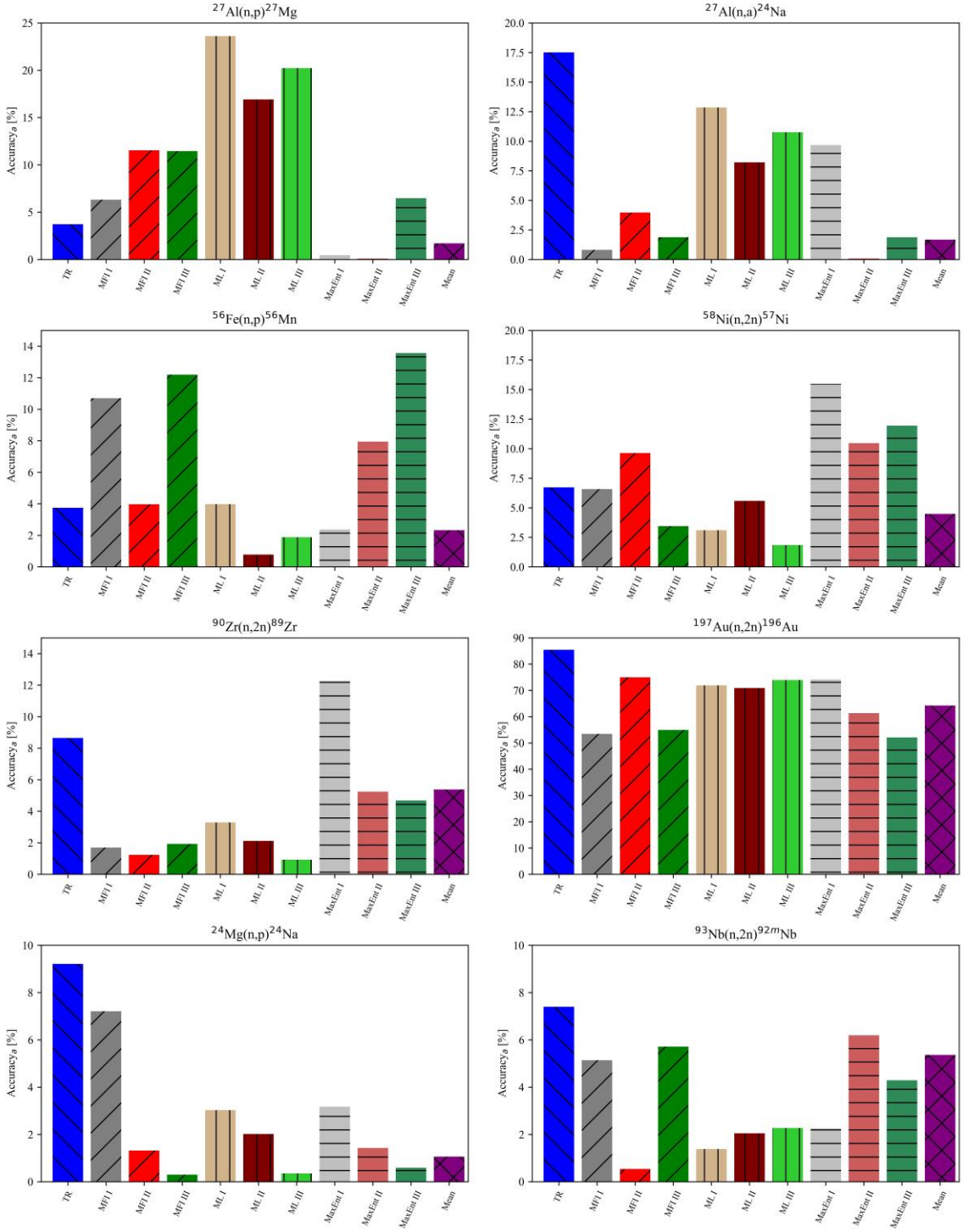

Figure 10.57. Accuracy$_a$ for reconstructed results obtained by different methods (76 bins) with the experimental data for Sodern Genie 16C.

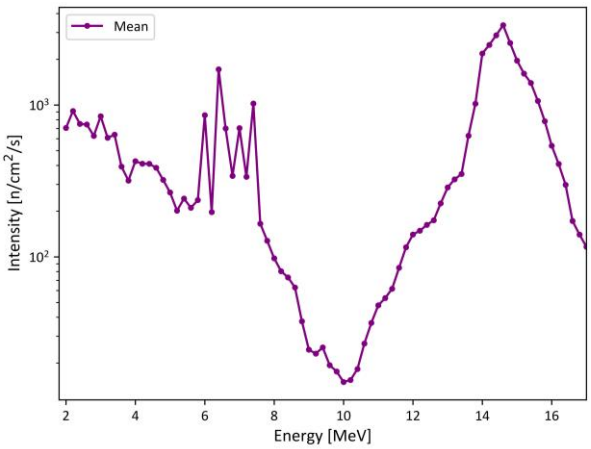

Figure 10.58. The average spectrum (76 bins) from the MFI, ML, and MaxEnt results obtained using the experimental data from foils irradiation by Sodern Genie 16C.

The neutron spectrum reconstruction based on the activity measured by the HPGe detector was characterised by lower errors than the calculation with the measurement done by BrilLanCe 380 scintillator. In this case, two energy bins structures were considered due to the lowest uncertainty of the simulation by FISPACT-II and cross-section interpolation. The results obtained by the TR method were inconsistent with other algorithms. Therefore, it was not considered in the interpretation of the neutron spectrum emitted by Sodern Genie 16C. The 51 bins spectra have mean $accuracy_a$ for the MFI, ML, and MaxEnt codes between 10% and 14%. The best result was produced by the MaxEnt method. The mean result has an $accuracy_a$ equalled 10%, and the uncertainty of the spectrum reconstruction was 30%, or if the reaction on Au is excluded from analysis, 15%. The $accuracy_a$ for 76 bins varies from 11% to 15%. The lowest uncertainty of the spectrum reconstruction was for the MFI algorithm. The mean spectrum improves the results. The $accuracy_a$ is 10%, and spectrum reconstruction uncertainty equals 18% (11% in case of omission of the Au reaction). The mean spectra with 51 and 76 bins structures have similar shapes. The 14 MeV peak is slightly moved to higher energies, about 0.5 MeV, due to the kinematics of the beam-target mechanism of the DT reaction. The scattered neutrons with energies below 8 MeV are overestimated and are the significant background that makes evaluation of the DD reaction presence impossible. The impact from 2.5 MeV neutrons can increase if deuterium from the beam is additionally deposited on the tritium target during the operation; the effect is too small to be distinguished from the background.

The high uncertainty and disruptions in the measurement of Au foil increase the spectrum reconstruction uncertainty. After excluding this sample from the analysis, the best spectrum reconstruction uncertainty was improved from 18% to 11%. Applying the HPGe detector to the activation measurement improved the precision of the neutron spectrum calculations. Another approach that can amend the reconstruction's precision is expanding the irradiation foil list. It increases the input information and makes calculations easier. The achieved uncertainty allows for the interpretation of the neutron spectra emitted by two kinds of portable generators. The NGs differ in the basics of operation and the relative position of the activation foils. The placement of the irradiation foils directly on the Gradel-Fusion NSD 35 2-DT-C-W allows for reducing the impact of the scattered neutrons and observing a negligible impact from DD and TT reactions in the gas-plasma target generator. The localisation of the foils further from the source in the Sodern Genie 16C NG measurement provides the spectrum with the domination of the 14.5 MeV peak and significant intensity of the scattered neutrons. The background limits the possibility of interpreting the spectrum below 8 MeV. The analysis proved that the presented methodology could be applied to the neutron spectrum reconstruction from large fusion devices like tokamaks. Its interpretation is aimed at the ion temperature estimation and study of the fuel behaviour.

Part IV: Conclusions and future plans

The inverse problems are common in analysing the data from plasma diagnostics, and various methods are applied to find the approximate solution. The reconstruction of the one- or two-dimensional physical quantity distributions is relevant for plasma physics studies based on the main products of the fusion reactions, neutrons. Neutron measurements are crucial for fusion power determination. The local neutron emissivity in the tokamak poloidal cross-section provides information about the fast ion behaviour, the presence of the MHD effects and the temperature and density distributions. Therefore, neutron tomography helps in studies of plasma stability and confinement. The neutron energy spectrum is used to determine the ion temperature, fuel ratio, and presence of the different reactions. Broad neutron parameters analysis is the key to fusion reaction studies and fulfilment of the ignition condition in future thermonuclear reactors.

The Minimum Fisher Information Regularisation algorithm developed in IPP CAS [Ods2012] for soft X-ray and bolometric tomography has been implemented by the thesis author to analyse the neutron data from the Radial Neutron Camera for ITER and the neutron camera on JET. The main change in the code concerns the determination of the geometry matrix describing the plasma seen by the neutron detectors through collimators. The version of the MFI algorithm prepared by the thesis author introduces the field of views with truncated cone shapes, including solid angles, instead of simple lines used in the previous version. The novel approach is the application of the total neutron yield measured by an independent monitor as the additional constraint.

The analysis of the synthetic data for RNC performed by the thesis author shows that the changes in the camera architecture connected with the space requirements will have a negligible influence on the reconstruction results. The neutron emissivity in ITER tokamak is expected to be reproduced with an uncertainty below 10% in the plasma core, which is the requirement for RNC operation established by ITER Organisation. A comparison of the results obtained for the ex-port part of RNC equipped with different types of detectors shows that the lowest reconstruction error is obtained when the plastic scintillators are used. The discrepancies between accuracy obtained with plastic and gas scintillators are insignificant, and the final decision about detectors will be made based on the test of the prototypes. The influence of the noise levels has been compared with the detector exclusion from the input data. In case of the noise rise above 5% for only one of the detectors it is better to eliminate it from the analysis. The resolution of the plasma magnetic field configuration strongly affects the results obtained by the MFR method due to smoothing along its lines in the regularisation. Therefore, the impact of the magnetic field displacements has been analysed. The limits of the position shift that allow obtaining the neutron emissivity distribution with an accuracy of at least 10% were established at 5 cm. If the magnetic field configuration diverges slightly from the actual structure, the tomography calculation still fulfils the requirement. The analysis shows that the total neutron yield constraint improves the precision of the solution. The calculations performed with the synthetic data demonstrate that RNC can be used during ITER operation for neutron emissivity distribution studies and ion temperature estimation. The TR, MFI, and ML codes are considered for real-time data processing. Further analysis of the calculation time is required to find the optimal algorithm that allows for online data processing with a time resolution of 10 ms. The application of two different methods allows for results benchmarking and increase in the precision of the neutron emissivity profile reconstruction. It improves the safety of the device due to the implementation of RNC as a diagnostic for burn control. The MFR code will be used in the offline analysis for plasma physics studies due to the extended time of calculation. The analysis shows that limitations of the method, which need to be considered during the experiment are connected with the measurement uncertainty, camera positioning, and magnetic field determination. The reconstructed neutron emissivity will be used to investigate the distribution of fusion power production in the tokamak and the influence of

the operation parameters like plasma current or magnetic field strength on plasma stability. It is also possible to add a vertical camera to the tomographic calculations. Therefore, asymmetry in neutron emissivity distribution can be investigated.

The thesis author validated the MFR code during the deuterium-tritium campaign on JET tokamak in 2021. The results of the measurement of 14.1 MeV neutrons by plastic scintillators Bicron BC418 were used to reconstruct the neutron emissivity distribution in the plasma. Two operation scenarios developed for ITER were considered. The results collected for the hybrid scenario discharges were analysed to investigate the influence of the tritium amount on neutron production stability. The comparison of the neutron emissivity profiles shows that in the tritium-rich discharges, asymmetries or hollowness occur less frequently. The hydrogen isotope ratio of 50% or higher supplies more stable plasma than lower amounts of tritium. The presented analysis shows the importance of the maintenance of tritium content on a high level for plasma stability. The knowledge about fusion power production with different fuel ratios helps to extend plasma confinement time by optimisation of this parameter. In the baseline scenario, the sawtooth crash appears frequently. It causes a sudden drop in the neutron rate and shortens the discharge duration. The influence of this MHD activity on the neutron emissivity distribution was analysed. Before and during the sawtooth crash, neutron profiles were always symmetric, with maximum emission in the core centre. After the neutron rate drop, hollowness in the distribution occurs frequently. The same effect was observed for the discharges where the total neutron yield decrease was connected with the NBI heating system problems. No connection between the sawtooth activity with the disruption in the neutron emissivity distribution was found. The effects might be faster than the time resolution of the camera. In this case, the analysis does not allow to confirm or deny the hypothesis about the hydrogen ions precession in deuterium-tritium plasma. The problem needs to be analysed further, but detailed studies of sawtooth crash phenomena require a camera with a higher time resolution. The analysis of the total neutron yield constraint influence on JET tomography calculation indicates no improvement in the absolute neutron intensity reconstructed by the MFR code. This effect can be connected with the differences between the energy thresholds used in the measurement by the neutron monitor and the camera detectors. The plastic scintillators Bicron BC418 measure only neutrons with energies higher than 13 MeV. The fission chambers register neutrons from DT and DD reactions. Additional constraint application into the analysis of the neutron emissivity profiles from plasma with the domination of the beam-target reactions does not improve the tomography calculation result like in the case of thermal plasma. The auxiliary heating systems can cause a toroidal asymmetry in the ion temperature distribution. Therefore, the neutron yields might vary with the position of the measurement. The continuation of the analysis of the deuterium-tritium discharges during the next JET campaign is planned. The code application to neutron tomography on other tokamaks is also proposed. The first results of the analysis of experimental data collected on MAST-U by the MFR code were obtained in 2021.

The neutron energy spectrum reconstruction is another example of the inverse problem in plasma physics. The activation method was used for the determination of the neutron spectrum emitted by two kinds of portable neutron generators. The author of the thesis prepared the codes based on the Tikhonov Regularisation, Minimum Fisher Information, Maximum Likelihood, and Maximum Entropy methods. The synthetic spectrum reconstruction preceded the analysis of the experimental data to determine the ratio of the error of the spectrum reconstruction ($accuracy_s$) and the discrepancy between activity simulated by the FISPACT-II inventory code for the calculation results and data used as input ($accuracy_a$). At first, the neutron spectrum emitted by plasma generator Gradel-Fusion NSD 35 2 DT-C-W was analysed. The synthetic data analysis was made for spectra with different energy resolutions (9, 16, 51, and 71 bins). The 9 bin structure was excluded from the experimental data analysis due to the high uncertainty of the activity simulation connected with the low energy resolution. The activities of irradiated foils (Al, Zn, Fe, Ni, Zr, Au) were measured by BrilLanCe 380 scintillator. The specific activity at the end of

the irradiation varies from 0.17 kBq/g to 2.99 kBq/g. The minimal uncertainty of the experimental data equals 10%. The mean $accuracy_a$ for the 16 bin structure is higher than 50%, which precludes the interpretation of the neutron spectrum. The best results were obtained for the 51 bin spectrum. The mean $accuracy_a$ varies from 20% to 23%. The lowest reconstruction uncertainty, 18%, was obtained for the average spectrum from all methods. The obtained neutron spectrum contains significant intensity only for the 14 MeV peak. The mean $accuracy_a$ for 71 bins varies from 18% to 47%. The results improvement was achieved by calculating the mean spectrum with the exclusion of the TR and ML methods that provide non-physical results in this case. Due to the required spectrum modification before the simulation, the reconstruction uncertainty was estimated at 29%. The significant neutron emission below 10 MeV and small peak around 2 MeV indicates the presence of the DD and TT reactions in the generator. This observation is less probable, the result has higher uncertainty, but possible due to the decreased tritium content. The settlement of the best result is complex because of the uncertainties and differences in the neutron spectrum shape. All calculations done by the thesis author confirm the hypothesis that the combination of the different methods allows for a more precise reconstruction of neutron spectrum based on activation technique than the application of a single algorithm. The analysis shows that the most suitable bin structures are 51 and 76 because they are characterised by the lowest uncertainties connected with the cross-section interpolation and the FISPCAT-II simulation. In the second analysis, the HPGe detector with numerical characteristics was used to measure the activities of foils irradiated in the neutron flux emitted by Sodern Genie 16C portable generator. The specific activities induced in Al, Fe, Ni, Zr, Au, Mg, and Nb vary from 0.19 Bq/g to 25.94 Bq/g with uncertainties below 12%. The synthetic and experimental data were used to analyse two bin structures. The $accuracy_s$ in the synthetic data analysis was lower for the 76 bins structure. The regular distribution of the energy provides better reconstruction results due to better resolution in the high-energy part of the spectrum, where all reactions have non-zero cross-sections and lower errors in the cross-section interpolation. The mean $accuracy_a$ obtained for the experimental data varies from 12% to 18%. The lowest errors were obtained by the MFI and MaxEnt algorithms. The average spectra for both bin structures have a similar shape, indicating a significant impact from the scattered neutrons. The background level can be overestimated by the MFI and MaxEnt codes, which is connected with the impact of the boundary conditions. The values in the border bins were high due to the filtering character of the regularisation and cutting of the neutron energies. The uncertainties equal 15% and 11% for 51 and 76 bins, respectively (in the case of Au reaction exclusion from the analysis). The domination of the DT reaction is clearly visible in the reconstruction results. However, it is not possible to distinguish the impact from the DD reaction due to the background level below 8 MeV. The verification of the theory that beam ions are adsorbed on the target requires repeating the experiment with a different location of the dosimetry foils, e.g. on the neutron generator housing. Valuable will be cross-checking the results with neutron spectrometers, for example, plastic scintillators. The codes developed by the thesis author can be applied to investigate the neutron spectrum emitted by large fusion devices like tokamaks. It is planned to use all possible foils in the measurement on JT60-SA tokamak and reconstruct the spectrum by described methods. Only the reactions on Al, Ni, Zn, Y, Cd, In, Au, Si, Fe, Co, Cu, Zr, and Nb can be used in the analysis of DD and DT neutrons. During the described experiments, not all mentioned materials were available. The increase of the number of used dosimetry foils decreases the ill-posedness of the problem. The synthetic data analysis allows for estimating the precision of the reconstruction and selection of the most suitable bin structure for the selected set of activation reactions. The application of FISPACT-II inventory code provides information about the disagreement of the reconstruction results with the emitted spectrum and the uncertainty of the calculations. The analysis shows that the uncertainty required from neutron activation measurement is at least 10% to provide consistent results for various bin structures.

References

[Ada1993] Adams, J. M., Jarvis, O. N., Sadler, G. J., Syme, D. B., & Watkins, N. (1993). The JET neutron emission profile monitor. Nuclear Instruments and Methods in Physics Research Section A: Accelerators, Spectrometers, Detectors and Associated Equipment, 329(1-2), 277-290.

[Ang2011] Angelone, M., Pillon, M., Prestopino, G., Marinelli, M., Milani, E., Verona, C., ... & Esposito, A. (2011). Thermal and fast neutron dosimetry using artificial single crystal diamond detectors. Radiation Measurements, 46(12), 1686-1689.

[Ang2014] Angioni, C., Mantica, P., Pütterich, T., Valisa, M., Baruzzo, M., Belli, E. A., ... & Contributors, J. E. (2014). Tungsten transport in JET H-mode plasmas in a hybrid scenario, experimental observations and modelling. Nuclear Fusion, 54(8), 083028.

[Ant1996] Anton, M., Weisen, H., Dutch, M. J., Von der Linden, W., Buhlmann, F., Chavan, R., ... & Paris, P. (1996). X-ray tomography on the TCV tokamak. Plasma physics and controlled fusion, 38(11), 1849.

[Arf1999] Arfken, G. B., & Weber, H. J. (1999). Mathematical methods for physicists.

[Ast2018] Aster, R. C., Borchers, B., & Thurber, C. H. (2018). Parameter estimation and inverse problems. Elsevier.

[Atz2004] Atzeni, S., & Meyer-ter-Vehn, J. (2004). The physics of inertial fusion: beam plasma interaction, hydrodynamics, hot dense matter (Vol. 125). OUP Oxford.

[Ave1954] Aves, R., Barnes, D., & Mackenzie, R. B. (1954). Fission chambers for neutron detection. Journal of Nuclear Energy (1954), 1(1-2), 110–116.

[Bat2011] Batenburg, K. J., & Sijbers, J. (2011). DART: a practical reconstruction algorithm for discrete tomography. IEEE Transactions on Image Processing, 20(9), 2542-2553.

[Bat2018] Batistoni, P., Popovichev, S., Ghani, Z., Cufar, A., Giacomelli, L., Hawkins, P., ... & Krasilnikov, V. (2018). 14 MeV calibration of JET neutron detectors—phase 2: in-vessel calibration. Nuclear Fusion, 58(10), 106016.

[Bei1990] Beidler, C., Grieger, G., Herrnegger, F., Harmeyer, E., Kisslinger, J., Lotz, W., ... & Wobig, H. (1990). Physics and engineering design for Wendelstein VII-X. Fusion Technology, 17(1), 148-168.

[Ber1988] Berger, J. O., & Wolpert, R. L. (1988). The likelihood principle. IMS.

[Ber1990] Bertolini, E. (1990). JET design, construction and performance. Nuclear Energy, 29(1), 31-45.

[Ber2012] Bertalot, L., Barnsley, R., Direz, M. F., Drevon, J. M., Encheva, A., Jakhar, S., ... & Walsh, M. (2012). Fusion neutron diagnostics on ITER tokamak. Journal of Instrumentation, 7(04), C04012.

[Ber2019] Bertalot, L., Krasilnikov, V., Core, L., Saxena, A., Yukhnov, N., Barnsley, R., & Walsh, M. (2019). Present status of ITER neutron diagnostics development. Journal of Fusion Energy, 38(3), 283-290.

[Beu2012] Beurskens, M. N. A., Frassinetti, L., Osborne, T., Snyder, P. B., Alper, B., Angioni, C., ... & Zarzoso, D. (2012). Hybrid compared to baseline ELMy H-Mode confinement in JET. to be submitted to Nuclear Fusion.

[Bie2015] Bielecki, J., Giacomelli, L., Kiptily, V., Scholz, M., Drozdowicz, K., Conroy, S., ... & JET EFDA Contributors. (2015). Phillips-Tikhonov regularization with a priori information for neutron emission tomographic reconstruction on Joint European Torus. Review of Scientific Instruments, 86(9), 093505.

[Bie2019] Bielecki, J., & Kurowski, A. (2019). Neutron Diagnostics for Tokamak Plasma: From a Plasma Diagnostician Perspective. Journal of Fusion Energy, 38(3), 386-393.

[Bin2017] Binda, F., Ericsson, G., Conroy, S., Sunden, E. A., & Contributors, J. E. T. (2017). Calculation of the profile-dependent neutron backscatter matrix for the JET neutron camera system. Fusion engineering and design, 123, 865-868.

[Bin2018] Binda, F. (2018). Absolute calibration of the JET neutron profile monitor. Review of Scientific Instruments.

[Bit2013] Bittencourt, J. A. (2013). Fundamentals of plasma physics. Springer Science & Business Media.

[Ble2015] Bleyer, I. R., & Leitão, A. (2015). Novel regularization methods for ill-posed problems in Hilbert and Banach spaces. Publicações matemáticas do IMPA.

[Bon2006] Bonheure, G., Popovichev, S., Bertalot, L., Murari, A., Conroy, S., Mlynar, J., ... & JET-EFDA contributors. (2006). Neutron profiles and fuel ratio nT/nD measurements in JET ELMy H-mode plasmas with tritium puff. Nuclear fusion, 46(7), 725.

[Bos1992] Bosch, H. S., & Hale, G. M. (1992). Improved formulas for fusion cross-sections and thermal reactivities. Nuclear fusion, 32(4), 611.

[Bos2013] Bosch, H. S., Wolf, R. C., Andreeva, T., Baldzuhn, J., Birus, D., Bluhm, T., ... & Jenzsch, H. (2013). Technical challenges in the construction of the steady-state stellarator Wendelstein 7-X. Nuclear Fusion, 53(12), 126001.

[Boy2003] Boyd, T. J., Boyd, T. J. M., & Sanderson, J. J. (2003). The physics of plasmas. Cambridge University Press.

[Bri2008] Brix, M., Hawkes, N. C., Boboc, A., Drozdov, V., Sharapov, S. E., & Jet-Efda Contributors. (2008). Accuracy of EFIT equilibrium reconstruction with internal diagnostic information at JET. Review of Scientific Instruments, 79(10), 10F701.

[Bri2009] Scintillation Products Technical Note: BrilLanCeTM Scintillators Performance Summary (Revision: January, 2009). https://www.crystals.saint-gobain.com/

[Bro2003] Bronson, F. (2003). Validation of the accuracy of the LabSOCS software for mathematical efficiency calibration of Ge detectors for typical laboratory samples. Journal of Radioanalytical and Nuclear Chemistry, 255(1), 137-141.

[Car1975] Carter, L. L., & Cashwell, E. D. (1975). Particle-transport simulation with the Monte Carlo method (No. TID-26607). Los Alamos Scientific Lab., N. Mex.(USA).

[Cas2002] Casella, G., & Berger, R. L. (2021). Statistical inference. Cengage Learning.

[Cec2018] Cecconello, M., Sperduti, A., Fitzgerald, I., Conroy, S., Holm, S. J., & Weiszflog, M. (2018). The neutron camera upgrade for MAST Upgrade. Review of Scientific Instruments, 89(10), 10I110.

[Ces2014] Cester, D., Nebbia, G., Stevanato, L., Pino, F., & Viesti, G. (2014). Experimental tests of the new plastic scintillator with pulse shape discrimination capabilities EJ-299-33. Nuclear Instruments and Methods in Physics Research Section A: Accelerators, Spectrometers, Detectors and Associated Equipment, 735, 202-206.

[CHAIN2] https://users.euro-fusion.org/pages/codes-data/chain2/www/chain2.pdf

[Cho2004] Chong, E. K., & Zak, S. H. (2004). An introduction to optimization. John Wiley & Sons.

[Cob2016] Coburn, J., Luker, S. M., Parma, E. J., & DePriest, K. R. (2016). Modeling, calibration, and verification of a fission chamber for ACRR experimenters. In EPJ Web of Conferences (Vol. 106, p. 05001). EDP Sciences.

[Coo1966] Cooper, J. (1966). Plasma spectroscopy. Reports on Progress in Physics, 29(1), 35.

[Cra1991] Crane, T. W., & Baker, M. P. (1991). Neutron detectors. Passive Nondestructive Assay of Nuclear Materials, (13), 1-28.

[Cra2016] Craciunescu, T., Murari, A., Kiptily, V., Lupelli, I., Fernandes, A., Sharapov, S., ... & JET Contributors. (2016). Evaluation of reconstruction errors and identification of artefacts for JET gamma and neutron tomography. Review of Scientific Instruments, 87(1), 013502.

[Cuf2017] Cufar, A., Batistoni, P., Conroy, S., Ghani, Z., Lengar, I., Milocco, A., ... & Contributors, J. E. T. (2017). Calculations to support JET neutron yield calibration: Modelling of neutron emission from a compact DT neutron generator. Nuclear Instruments and Methods in Physics Research Section A: Accelerators, Spectrometers, Detectors and Associated Equipment, 847, 199-204.

[DDD2017] Esposito B. (2017) DA Design Description Document System Design Description (DDD) 55.B1_RNC received from the DA. IDM UID T24H9T. 29 Jun 2017 / 1.0

[DDD2020] Marocco D. (2020) DA Design Description Document System Design Description (DDD) 5.B1_RNC received from the DA. IDM UID T24H9T 19 Feb 2020 / 2.0

[Deb2011] Dębicki, Z., Jędrzejczak, K., Karczmarczyk, J., Kasztelan, M., Lewandowski, R., Orzechowski, J., ... & Wibig, T. (2011). Helium counters for low neutron flux measurements. Astrophysics and Space Sciences Transactions, 7(4), 511-514.

[Del2020] Esposito B. (2020). Deliverable D3.1-01 Baseline definition of ex-port RNC detector module: trade-off studies to select best detector options, idm@F4E UID / VERSION 2N54PT. 02 July 2020 / 1.0

[Den1998] Denisova, N. V. (1998). Maximum-entropy-based tomography for gas and plasma diagnostics. Journal of Physics D: Applied Physics, 31(15), 1888.

[Dha2012] D'haeseleer, W. D., Hitchon, W. N., Callen, J. D., & Shohet, J. L. (2012). Flux coordinates and magnetic field structure: a guide to a fundamental tool of plasma theory. Springer Science & Business Media.

[Don2007] Donné, A. J. H., Costley, A. E., Barnsley, R., Bindslev, H., Boivin, R., Conway, G., ... & Young, K. (2007). Diagnostics. Nuclear Fusion, 47(6), S337.

[Dur1987] Durrani, S. A., & Bull, R. K. (2013). Solid state nuclear track detection: principles, methods and applications (Vol. 111). Elsevier.

[EFwiki] https://users.euro-fusion.org/tfwiki, Accessed: 6th January 2021

[End1982] Endo, Y., Ito, T., & Seki, E. (1982). A counting-campbelling neutron measurement system and its experimental results by test reactor. IEEE Transactions on Nuclear Science, 29(1), 714-717.

[Ert1996] Ertl, K., Von der Linden, W., Dose, V., & Weller, A. (1996). Maximum entropy based reconstruction of soft X-ray emissivity profiles in W7-AS. Nuclear Fusion, 36(11), 1477.

[Equ1978] Equipe, T. F. R. (1978). Tokamak plasma diagnostics. Nuclear Fusion, 18(5), 647.

[Fan2012] Fantidis, J. G., Dimitrios, B. V., Constantinos, P., & Nick, V. (2012). Fast and thermal neutron radiographies based on a compact neutron generator. Journal of Theoretical and Applied Physics, 6(1), 1-8.

[Fie2021] Field, A. R., Aleiferis, S., Belonohy, É., Carvalho, P., Coffey, I., Frigione, D., ... & Contributors, J. E. T. (2021). The impact of fuelling and W radiation on the performance of high-power, ITER-baseline scenario plasmas in JET-ILW. Plasma Physics and Controlled Fusion, 63(9), 095013.

[Fou2002] Foulon, F., Bergonzo, P., Amosov, V. N., Kaschuck, Y., Frunze, V., Tromson, D., & Brambilla, A. (2002). Characterisation of CVD diamond detectors used for fast neutron flux monitoring. Nuclear Instruments and Methods in Physics Research Section A: Accelerators, Spectrometers, Detectors and Associated Equipment, 476(1-2), 495-499.

[Fre2010] Freidberg, J. P. (2010). Plasma physics and fusion energy. Cambridge university press.

[Fri1988] Frieden, B. R. (1988). Applications to optics and wave mechanics of the criterion of maximum Cramer-Rao bound. Journal of Modern Optics, 35(8), 1297-1316.

[Fri2000] Frieden, B. R. (2000). Physics from Fisher information: a unification.

[Fri2004] Fridman, A., & Kennedy, L. A. (2021). Plasma physics and engineering. CRC press.

[Fri2007] Frieden, B. R. (2007). Exploratory data analysis using Fisher information (p. 363). R. A. Gatenby (Ed.). London:: Springer.

[Fro2006] Froula, D. H., Ross, J. S., Divol, L., & Glenzer, S. H. (2006). Thomson-scattering techniques to diagnose local electron and ion temperatures, density, and plasma wave amplitudes in laser produced plasmas. Review of scientific instruments, 77(10), 10E522.

[Gar2011] Garofalo, A. M., Solomon, W. M., Park, J. K., Burrell, K. H., DeBoo, J. C., Lanctot, M. J., ... & Snyder, P. B. (2011). Advances towards QH-mode viability for ELM-stable operation in ITER. Nuclear Fusion, 51(8), 083018.

[Gar2019] Garzotti, L., Challis, C., Dumont, R., Frigione, D., Graves, J., Lerche, E., ... & Contributors, J. E. T. (2019). Scenario development for D–T operation at JET. Nuclear Fusion, 59(7), 076037.

[Gia2005] Giacomelli, L., Hjalmarsson, A., Sjöstrand, H., Glasser, W., Källne, J., Conroy, S., ... & Weiszflog, M. (2005). Advanced neutron diagnostics for JET and ITER fusion experiments. Nuclear Fusion, 45(9), 1191.

[Gib1990] Gibson, A., & Smeulders, P. (1990). The JET Project: A Review of Progress. JET-P(90)12

[Gol1979] Golub, G. H., Heath, M., & Wahba, G. (1979). Generalized cross-validation as a method for choosing a good ridge parameter. Technometrics, 21(2), 215-223.

[Gra] http://www.nsd-fusion.com

[Gra2010] NSD-Gradel-Fusion Tech. (2010) Note NSD188 Issue 1 Version C 812010 for Christian Regenfus, University of Zurich / CERN

[Gra2015] NSD-Gradel-Fusion User Manual (2015) UM-002 for NSD-35-2-DT-C-W Issue 1 Version B 8-05-2015 for NCNR

[Gre2000] Greenwald, M., Boivin, R., Bonoli, P., Fiore, C., Goetz, J., Granetz, R., ... & Wukitch, S. (2000). Studies of EDA H-mode in Alcator C-Mod. Plasma Physics and Controlled Fusion, 42(5A), A263.

[Gre2011] Greenberg, R. R., Bode, P., & Fernandes, E. A. D. N. (2011). Neutron activation analysis: a primary method of measurement. Spectrochimica Acta Part B: Atomic Spectroscopy, 66(3-4), 193-241.

[Gri2018] Grierson, B. A., Yuan, X., Gorelenkova, M., Kaye, S., Logan, N. C., Meneghini, O., ... & Poli, F. M. (2018). Orchestrating TRANSP simulations for interpretative and predictive tokamak modeling with OMFIT. Fusion Science and Technology, 74(1-2), 101-115.

[Gul1989] Gull, S. F. (1989). Developments in maximum entropy data analysis. In Maximum entropy and Bayesian methods (pp. 53-71). Springer, Dordrecht.

[Gul1994] Gullberg, G. T., & Zeng, G. L. (1994). A reconstruction algorithm using singular value decomposition of a discrete representation of the exponential radon transform using natural pixels. IEEE transactions on nuclear science, 41(6), 2812-2819.

[Han1993] Hansen, P. C., & O'Leary, D. P. (1993). The use of the L-curve in the regularization of discrete ill-posed problems. SIAM journal on scientific computing, 14(6), 1487-1503.

[Han1994] Hansen, P. C. (1994). Regularization tools: a Matlab package for analysis and solution of discrete ill-posed problems. Numerical algorithms, 6(1), 1-35.

[Hen2007] Hender, T. C., Wesley, J. C., Bialek, J., Bondeson, A., Boozer, A. H., Buttery, R. J., ... & Zohm, H. (2007). MHD stability, operational limits and disruptions. Nuclear fusion, 47(6), S128.

[Her1985] Hertel, N. E., & Davidson, J. W. (1985). The response of Bonner spheres to neutrons from thermal energies to 17.3 MeV. Nuclear Instruments and Methods in Physics Research Section A: Accelerators, Spectrometers, Detectors and Associated Equipment, 238(2-3), 509-516.

[Hig2009] Higham, N. J. (2009). Cholesky factorization. Wiley Interdisciplinary Reviews: Computational Statistics, 1(2), 251-254.

[Hja2003] Hjalmarsson, A., Conroy, S., Ericsson, G., Giacomelli, L., Gorini, G., Henriksson, H., ... & Weiszflog, M. (2003). The TOFOR spectrometer for 2.5 MeV neutron measurements at JET. Review of scientific instruments, 74(3), 1750-1752.

[Hor2015] Horton Jr, C. W., & Benkadda, S. (2015). Iter Physics. World Scientific.

[Hut2002] Hutchinson, I. H. (2002). Principles of plasma diagnostics. Plasma Physics and Controlled Fusion, 44(12), 2603.

[Ing1998] Ingesson, L. C., Alper, B., Chen, H., Edwards, A. W., Fehmers, G. C., Fuchs, J. C., ... & Romanelli, M. (1998). Soft X ray tomography during ELMs and impurity injection in JET. Nuclear fusion, 38(11), 1675.

[Ing2008] Ingesson, L. C., Alper, B., Peterson, B. J., & Vallet, J. C. (2008). Chapter 7: Tomography diagnostics: Bolometry and soft-x-ray detection. Fusion Science and Technology, 53(2), 528-576.

[IPA] ITER_D_YWK2VW v.1.3: 5.5.P1.EU.15 Appendix 2 Technical Requirements Annex

[Isl1984] Isler, R. C. (1984). Impurities in tokamaks. Nuclear Fusion, 24(12), 1599.

[Jac2016] Jacobsen, A. S., Stagner, L., Salewski, M., Geiger, B., Heidbrink, W. W., Korsholm, S. B., ... & Weiland, M. (2016). Inversion methods for fast-ion velocity-space tomography in fusion plasmas. Plasma Physics and Controlled Fusion, 58(4), 045016.

[Jar1994] Jarvis, O. N. (1994). Neutron measurement techniques for tokamak plasmas. Plasma physics and controlled fusion, 36(2), 209.

[Jar2016] Jardin, A., Mazon, D., O'Mullane, M., Mlynar, J., Loffelmann, V., Imrisek, M., ... & Malard, P. (2016). Tomographic capabilities of the new GEM based SXR diagnostic of WEST. Journal of Instrumentation, 11(07), C07006.

[Jar2019] Jardin, A., Bielecki, J., Mazon, D., Dankowski, J., Król, K., Peysson, Y., & Scholz, M. (2019). Neural networks: from image recognition to tokamak plasma tomography. Laser and Particle Beams, 37(2), 171-175.

[Jay1957] Jaynes, E. T. (1957). Information theory and statistical mechanics. Physical review, 106(4), 620.

[Jin2008] Jinwei, Y., Qingwei, Y., Gongshan, X., Wei, Z., Xianying, S., & Xu, L. (2008). Fusion neutron flux monitor for ITER. Plasma Science and technology, 10(2), 141.

[Jo2018] Jo, J., Cheon, M., Chung, K. J., & Hwang, Y. S. (2018). Initial result of neutron energy spectrum reconstruction using multi-foil activation method in KSTAR. Fusion Engineering and Design, 136, 793-796.

[Joh2008] Johnson, M. G., Giacomelli, L., Hjalmarsson, A., Källne, J., Weiszflog, M., Sundén, E. A., ... & Jet-Efda Contributors. (2008). The 2.5-MeV neutron time-of-flight spectrometer TOFOR for experiments at JET. Nuclear Instruments and Methods in Physics Research Section A: Accelerators, Spectrometers, Detectors and Associated Equipment, 591(2), 417-430.

[Kak2001] Kak, A. C., & Slaney, M. (2001). Principles of computerized tomographic imaging. Society for Industrial and Applied Mathematics.

[Kar2006] Karpushov, A. N., Duval, B. P., Schlatter, C., Afanasyev, V. I., & Chernyshev, F. V. (2006). Neutral particle analyzer diagnostics on the TCV tokamak. Review of Scientific Instruments, 77(3), 033504.

[Kas2002] Kaschuck, Y. A., Esposito, B., Trykov, L. A., & Semenov, V. P. (2002). Fast neutron spectrometry with organic scintillators applied to magnetic fusion experiments. Nuclear Instruments and Methods in Physics Research Section A: Accelerators, Spectrometers, Detectors and Associated Equipment, 476(1-2), 511-515.

[Kas2014] Kashin, K. (2014). Statistical inference: Maximum likelihood estimation. Notes Statistics, Spring.

[Kee2012] Keen, B. E., Huguet, M., & Hemsworth, R. M. (Eds.). (2012). Fusion Technology 1990. Elsevier.

[Kik2012] Kikuchi, M., Lackner, K., & Tran, M. Q. (2012). Fusion physics. International Atomic Energy Agency.

[Kim2012] Kim, Y., Mack, J. M., Herrmann, H. W., Young, C. S., Hale, G. M., Caldwell, S., ... & Sangster, T. C. (2012). DT gamma-to-neutron branching ratio determined from inertial confinement fusion plasmas. Physics of Plasmas, 19(5), 056313.

[Kno2010] Knoll, G. F. (2010). Radiation detection and measurement. John Wiley & Sons.

[Kol1996] Kolesnichenko, Y. I., & Yakovenko, Y. V. (1996). Theory of fast ion transport during sawtooth crashes in tokamaks. Nuclear fusion, 36(2), 159.

[Kon2012] Koning, A. J., & Rochman, D. (2012). Modern nuclear data evaluation with the TALYS code system. Nuclear data sheets, 113(12), 2841-2934.

[Kra1988] Krane, K. S., & Halliday, D. (1987). Introductory nuclear physics. John Wiley & Sons, Inc.

[Kra2007] Krawczyk-Stando, D., & Rudnicki, M. (2007). Regularization parameter selection in discrete ill-posed problems--The use of the U-Curve. International Journal of Applied Mathematics and Computer Science, 17(2), 157.

[Kru2001] Kruse, P. W. (2001). Uncooled thermal imaging: arrays, systems, and applications (Vol. 51). SPIE press.

[Kwi2019] Kwiatkowski, R., Malinowska, A., Gierlik, M., Rzadkiewicz, J., Szydłowski, A., Urban, A., & Mikszuta, K. (2019). Assessment of 14 MeV DT neutron generator emission with activation and particle track methods. Fusion Engineering and Design, 146, 1060-1063.

[Lao1990] Lao, L. L., Ferron, J. R., Groebner, R. J., Howl, W., John, H. S., Strait, E. J., & Taylor, T. S. (1990). Equilibrium analysis of current profiles in tokamaks. Nuclear Fusion, 30(6), 1035.

[Las2017] Laszynska, E., Mikszuta, K., Jednorog, S., Bienkowska, B., Gierlik, M., Malinowska, A., Rzadkiewicz, J., Szydłowski, A. (2017, May) Shaping of neutron spectra emitted from 14-MeV neutron generator, Poster presented at Neutron and Ion Dosimetry Symposium, Cracow

[Las2020] Laszynska, E., & Mikszuta-Michalik, K. (2020). Deconvolution of neutron spectrum for a DT neutron generator based on a combination of activation method, unfolding processes and numerical simulations. Fusion Engineering and Design, 156, 111593.

[Lin1995] Von der Linden, W. (1995). Maximum-entropy data analysis. Applied Physics A, 60(2), 155-165.

[Liu2021] Liu, B., Lv, H., Li, L., Yang, B., Zhang, F., & Chen, H. (2021). Study on iterative regularization method and application to neutron spectrum unfolding of multi-sphere spectrometer measurement. Nuclear Instruments and Methods in Physics Research Section A: Accelerators, Spectrometers, Detectors and Associated Equipment, 992, 165027.

[Loa2013] Loarer, T., Brezinsek, S., Philipps, V., Bucalossi, J., Douai, D., Esser, H. G., ... & JET-EFDA Contributors. (2013). Comparison of long term fuel retention in JET between carbon and the ITER-like wall. Journal of Nuclear Materials, 438, S108-S113.

[Mae2013] Maeda, S., & Iguchi, T. (2013). A new unfolding code combining maximum entropy and maximum likelihood for neutron spectrum measurement. Journal of Nuclear Science and Technology, 50(4), 381-386.

[Mar2011] Marocco, D., Esposito, B., & Moro, F. (2011). Combined unfolding and spatial inversion of neutron camera measurements for ion temperature profile determination in ITER. Nuclear Fusion, 51(5), 053011.

[Mar2012] Marocco, D., Esposito, B., & Moro, F. (2012). Neutron measurements in ITER using the radial neutron camera. Journal of Instrumentation, 7(03), C03033.

[Mar2016] Marocco, D. (2016, October). System level design and performances of the ITER radial neutron camera. In Proceedings of 26th IAEA Fusion Energy Conference, Kyoto, FIP/P4-16.

[Mat1994] Matzke, M. (1994). Unfolding of pulse height spectra: the HEPRO program system (No. PTB-N-19). SCAN-9501291.

[Mat2007] Matthews, G. F., Edwards, P., Hirai, T., Kear, M., Lioure, A., Lomas, P., ... & Way, M. (2007). Overview of the ITER-like wall project. Physica Scripta, 2007(T128), 137.

[Mat2017] Matos, F. A., Ferreira, D. R., Carvalho, P. J., & Contributors, J. E. T. (2017). Deep learning for plasma tomography using the bolometer system at JET. Fusion engineering and design, 114, 18-25.

[May2014] Mayoral, M. L., Bobkov, V., Czarnecka, A., Day, I., Ekedahl, A., Jacquet, P., ... & Contributors, J. E. (2014). On the challenge of plasma heating with the JET metallic wall. Nuclear Fusion, 54(3), 033002.

[MCNP] Los Alamos Scientific Laboratory. Group X-6. (1979) MCNP : a General Monte Carlo Code for Neutron and Photon Transport. Los Alamos, N.M. : [Springfield, Va.] :Dept. of Energy, Los Alamos Scientific Laboratory.

[Men2003] Mendel Jr, C. W., & Schamiloglu, E. (2003). Plasma Diagnostic Techniques.

[Mer2019] Mertens, P. (2019). The core-plasma CXRS diagnostic for ITER: An introduction to the current design. Journal of fusion energy, 38(3), 264-282.

[Mer2010] Mertens, C., De Lellis, C., & Tondeur, F. (2010). Neutron–photon discrimination and spectrum unfolding with a stilbene detector. Applied Radiation and Isotopes, 68(4-5), 957-960.

[Mik2018] Mikszuta, K. (2018, June). Comparison of the criterions of selection the regularization parameter, implemented to deconvolution methods application in plasma diagnostics. Speech presented on 14th Kudowa Summer School “Toward Fusion Energy”. Kudowa-Zdrój, Poland

[Mik2018b] Mikszuta, K., Gierlik, M., Kwiatkowski, R., Rzadkiewicz J., Szydłowski A. (2018) A comparative study of different deconvolution methods used for reconstruction of neutron spectrum. Poster presented at: Symposium on Fusion Technology 16-21 Sept 2018, Giardini Naxos, Italy.

[Mik2020] Mikszuta-Michalik, K., Imrisek, M., Esposito, B., Marocco, D., Mlynar, J., & Ficker, O. (2020). A total neutron yield constraint implemented to the RNC emissivity reconstruction on ITER tokamak. Fusion Engineering and Design, 160, 111840.

[Mik2021] Mikszuta-Michalik, K., Imríšek, M., Svoboda, J., Weinzettl, V., Bílková, P., Hron, M., ... & Team, C. U. (2021). Concept of the bolometry diagnostics design for COMPASS-Upgrade. Fusion Engineering and Design, 168, 112421.

[Mik2021b] Mikszuta-Michalik, K., Miklaszewski, R., Gierlik, M., Kwiatkowski, R., Rzadkiewicz, J., & Szydłowski, A. (2021). Application of the different deconvolution methods to the neutron spectrum reconstruction from activation measurement. Fusion Engineering and Design, 173, 112934.

[Mik2021R] Mikszuta-Michalik K. (2021). NT- F4E FPA327 07- 04 ENEA.7030550: 2nd System Performance Assessment Update (analysis)

[Mik2022] Mikszuta-Michalik, K., Marocco, D., & Esposito, B. (2022). Comparison of deconvolution techniques for 1D neutron emission profile reconstruction using ITER Radial Neutron Camera synthetic measurements [Manuscript submitted for publication].

[Mik2022b] Mikszuta-Michalik, K., & Miklaszewski, R. (2022) Reconstruction of neutron spectrum emitted by portable 14 MeV neutron generator by a combination of different methods [Manuscript submitted for publication].

[Miy2006] Miyamoto, K. (2005). Plasma physics and controlled nuclear fusion (Vol. 38). Springer Science & Business Media.

[Mly1995] Mlynář, J. (1995). Pixels method computer tomography in polar coordinates. Czechoslovak Journal of Physics, 45(10), 799-816.

[Mly2007] Mlynar, J., Bonheure, G., Murari, A., Popovichev, S., & Svoboda, V. (2007). Abelisation of the Neutron Profile Data at JET using Minimum Fisher Regularisation. In 34th EPS Conference on Plasma Physics,(Warsaw, Poland 2nd-6th July 2007).

[Mly2010] Mlynar, J., Weinzettl, V., Bonheure, G., Murari, A., & JET-EFDA CONTRIBUTORS. (2010). Inversion techniques in the soft-X-ray tomography of fusion plasmas: toward real-time applications. Fusion Science and Technology, 58(3), 733-741.

[Mly2012] Mlynar, J., Imrisek, M., Weinzettl, V., Odstrcil, M., Havlicek, J., Janky, F., ... & JET-EFDA Contributors. (2012). Introducing minimum Fisher regularisation tomography to AXUV and soft x-ray diagnostic systems of the COMPASS tokamak. Review of Scientific Instruments, 83(10), 10E531.

[Mly2013] Mlynar, J., Bonheure, G., Ficker, O., Bauer, K., Popovichev, S., Murari, A., & JET EFDA Contributors Collaboration. (2013, October). Unfolding of energies of fusion products from the nuclear activation data at JET. In APS Division of Plasma Physics Meeting Abstracts (Vol. 2013, pp. UP8-003).

[Mly2015] Mlynar, J., Tomes, M., Imrisek, M., Alper, B., O'Mullane, M., Odstrcil, T., & Puetterich, T. (2015). Soft X-ray tomographic reconstruction of JET ILW plasmas with tungsten impurity and different spectral response of detectors. Fusion Engineering and Design, 96, 869-872.

[Mor2009] Moro, F., Petrizzi, L., Brolatti, G., Esposito, B., Marocco, D., & Villari, R. (2009). The ITER radial neutron camera: An updated neutronic analysis. Fusion engineering and design, 84(7-11), 1351-1356.

[Mun2016] Munro, D. H. (2016). Interpreting inertial fusion neutron spectra. Nuclear Fusion, 56(3), 036001.

[Mur2005] Murari, A., Bertalot, L., Conroy, S., Ericsson, G., Kiptily, V., Popovichev, S., ... & JET-EFDA Contributors. (2005). New developments in JET neutron, γ-ray and particle diagnostics with relevance to ITER. Nuclear fusion, 45(10), S195.

[Mut1998] Mutihac, R. C., Stanciulescu, C., Cicuttin, A., & Cerdeira, H. A. (1998). Topics in Bayesian statistics and maximum entropy (No. IC-98-137). SCAN-0001057.

[NDS] https://www-nds.iaea.org/exfor/exfor.htm

[Neg2006] Negus, C. R., Giroud, C., Meigs, A. G., Zastrow, K. D., Hillis, D. L., & JET-EFDA Contributors. (2006). Enhanced core charge exchange recombination spectroscopy system on Joint European Torus. Review of scientific instruments, 77(10), 10F102.

[Nis2013] Nishikawa, K., & Wakatani, M. (2013). Plasma Physics: basic theory with fusion applications (Vol. 8). Springer Science & Business Media.

[Ods2012] Odstrcil, M., Mlynar, J., Odstrcil, T., Alper, B., Murari, A., & Contributors, J. E. (2012). Modern numerical methods for plasma tomography optimisation. Nuclear Instruments and Methods in Physics Research Section A: Accelerators, Spectrometers, Detectors and Associated Equipment, 686, 156-161.

[Ods2016] Odstrčil, T., Pütterich, T., Odstrčil, M., Gude, A., Igochine, V., Stroth, U., & ASDEX Upgrade Team. (2016). Optimized tomography methods for plasma emissivity reconstruction at the ASDEX Upgrade tokamak. Review of Scientific Instruments, 87(12), 123505.

[Orl1988] Orlinskij, D. V., & Magyar, G. (1988). Plasma diagnostics on large tokamaks. Nuclear fusion, 28(4), 611.

[Pam2003] Pamela, J., Solano, E. R., & Contributors, J. E. (2003). Overview of JET results. Nuclear fusion, 43(12), 1540.

[Pam2007] Paméla, J., Matthews, G. F., Philipps, V., Kamendje, R., & JET-EFDA Contributors. (2007). An ITER-like wall for JET. Journal of nuclear materials, 363, 1-11.

[Pas2004] Pasqualotto, R., Nielsen, P., Gowers, C., Beurskens, M., Kempenaars, M., Carlstrom, T., ... & JET-EFDA Contributors. (2004). High resolution thomson scattering for joint european torus (JET). Review of Scientific Instruments, 75(10), 3891-3893.

[Peh2013] Pehlivanovic, B., Avdic, S., Marinkovic, P., Pozzi, S. A., & Flaska, M. (2013). Comparison of unfolding approaches for monoenergetic and continuous fast-neutron energy spectra. Radiation measurements, 49, 109-114.

[Pie2010] Piel, A. (2017). Plasma physics: an introduction to laboratory, space, and fusion plasmas. Springer Science & Business Media.

[Pil2011] Pillon, M., Angelone, M., Krása, A., Plompen, A. J. M., Schillebeeckx, P., & Sergi, M. L. (2011). Experimental response functions of a single-crystal diamond detector for 5–20.5 MeV neutrons. Nuclear Instruments and Methods in Physics Research Section A: Accelerators, Spectrometers, Detectors and Associated Equipment, 640(1), 185-191.

[Pol2002] Polevoi, A. R., Mukhovatov, V. S., Shimada, M., Medvedev, S. Y., Ivanov, A. A., Kukushkin, A. S., & Murakami, Y. (2003). ITER confinement and stability modelling. In Proceedings of joint conference of ITC-12 and APFA'01: Frontiers in plasma confinement and related engineering/plasma science.

[Pre2007] Press, W. H., William, H., Teukolsky, S. A., Saul, A., Vetterling, W. T., & Flannery, B. P. (2007). Numerical recipes 3rd edition: The art of scientific computing. Cambridge university press.

[Pre2013] Pressé, S., Ghosh, K., Lee, J., & Dill, K. A. (2013). Principles of maximum entropy and maximum caliber in statistical physics. Reviews of Modern Physics, 85(3), 1115.

[Pro2011] Prokopowicz, R., Bienkowska, B., Drozdowicz, K., Jednorog, S., Kowalska-Strzeciwilk, E., Murari, A., ... & JET-EFDA Contributors. (2011). Measurements of neutrons at JET by means of the activation methods. Nuclear Instruments and Methods in Physics Research Section A: Accelerators, Spectrometers, Detectors and Associated Equipment, 637(1), 119-127.

[Reg1999] Reginatto, M., & Goldhagen, P. (1999). MAXED, a computer code for maximum entropy deconvolution of multisphere neutron spectrometer data. Health Physics, 77(5), 579-583.

[Reg2008] Reginatto, M., & Zimbal, A. (2008). Bayesian and maximum entropy methods for fusion diagnostic measurements with compact neutron spectrometers. Review of Scientific Instruments, 79(2), 023505.

[Rin1991] Rinard, P. (1991). Neutron interactions with matter. Passive nondestructive assay of nuclear materials, (375-377).

[Riv2014] Riva, M., & Belli, F. (2014). Neutron emission profiles and energy spectra measurements at JET. In International Conference on Fusion Reactor Diagnostics (Vol. 1612).

[Riv2017] Riva, M., Marocco, D., Belli, F., Esposito, B., Pollastrone, F., Bielecki, J., ... & Popovichev, S. (2017). Hardware architecture of the data acquisition and processing system for the JET Neutron Camera Upgrade (NCU) project. Fusion engineering and design, 123, 873-876.

[Rol1988] Rolfs, C. E., Rodney, W. S., & Rodney, W. S. (1988). Cauldrons in the cosmos: Nuclear astrophysics. University of Chicago press.

[Rom2011] Romodanov, V. L., Sakharov, V. K., Chernikova, D. N., Ryzhkov, V. I., Khasaev, T. O., & Sladkov, A. A. (2011). Properties of radiation from portable pulsed neutron generators. Atomic energy, 111(1), 42-47.

[Ron2010] Ronchi, E., Conroy, S., Sunden, E. A., Ericsson, G., Johnson, M. G., Hellesen, C., ... & JET-EFDA Contributors. (2010). A parametric model for fusion neutron emissivity tomography for the KN3 neutron camera at JET. Nuclear fusion, 50(3), 035008.

[Ros2009] Rosenstock, W., Koble, T., Risse, M., & Berky, W. (2009). Detection of concealed fissionable material by delayed neutron counting (No. INIS-XA--09N0647). IAEA-SM/EN-09, Fraunhofer-INT, Euskirchen, Germany.

[Rps1995] Van Rossum, G., & Drake Jr, F. L. (1995). Python tutorial (Vol. 620). Amsterdam: Centrum voor Wiskunde en Informatica.

[Sam2008] Samarskii, A. A., & Vabishchevich, P. N. (2008). Numerical methods for solving inverse problems of mathematical physics. de Gruyter.

[Sas2008] Sasao, M., Nishitani, T., Krasilnilov, A., Popovichev, S., Kiptily, V., & Kallne, J. (2008). Chapter 9: Fusion product diagnostics. Fusion science and technology, 53(2), 604-639.

[Sas2010] Sasao, M., Bertalot, L., Ishikawa, M., & Popovichev, S. (2010). Strategy for the absolute neutron emission measurement on ITER. Review of Scientific Instruments, 81(10), 10D329.

[Sat2013] Sato, T., Niita, K., Matsuda, N., Hashimoto, S., Iwamoto, Y., Noda, S., ... & Sihver, L. (2013). Particle and heavy ion transport code system, PHITS, version 2.52. Journal of Nuclear Science and Technology, 50(9), 913-923.

[SG03-15A] Report on deliverable D15a for specific grant 03 (TR-F4E 327 SG03-15a): Simulation Tools and Procedures.

[She1982] Shepp, L. A., & Vardi, Y. (1982). Maximum likelihood reconstruction for emission tomography. IEEE transactions on medical imaging, 1(2), 113-122.

[Sim2007] Shimada, M., Campbell, D. J., Mukhovatov, V., Fujiwara, M., Kirneva, N., Lackner, K., ... & Sipps, A. C. C. (2007). Progress in the ITER physics basis-Chapter 1: overview and summary. Nuclear Fusion, 47, S1-S17.

[Sin2014] Singh, A., Kumar, A., & Topkar, A. (2014). Performance study of polycrystalline CVD diamond detectors for fast neutron monitoring. In AIP Conference Proceedings (Vol. 1591, No. 1, pp. 611-613). American Institute of Physics.

[Sip2005] Sips, A. C. (2005). Advanced scenarios for ITER operation. Plasma physics and controlled fusion, 47(5A), A19.

[Sip2016] Sips, A., Schweinzer, J., Luce, T. C., Wolfe, S. M., Urano, H., Hobirk, J., ... & Stober, J. (2016). Assessment of the Baseline Scenario at q95~ 3 for ITER. In 26th IAEA Fusion Energy Conference (FEC 2016).

[Ski1984] Skilling, J., & Bryan, R. K. (1984). Maximum entropy image reconstruction-general algorithm. Monthly notices of the royal astronomical society, 211, 111.

[Sod] http://www.sodern.com/website/en/ref/home.html

[Sodman] SODERN, E. (2008). GENIE 16C/D user manual, ver. July 2008. Eads Sodern Inc.

[Sta1981] Stacey Jr, W. M. (1981). Fusion plasma analysis. Wiley.

[Sta1999] Start, D. F. H., Jacquinot, J., Bergeaud, V., Bhatnagar, V. P., Conroy, S. W., Cottrell, G. A., ... & van Belle, P. (1999). Bulk ion heating with ICRH in JET DT plasmas. Nuclear Fusion, 39(3), 321.

[Str2008] Stratton, B. C., Bitter, M., Hill, K. W., Hillis, D. L., & Hogan, J. T. (2008). Chapter 5: Passive spectroscopic diagnostics for magnetically confined fusion plasmas. Fusion Science and Technology, 53(2), 431-486.

[Sub2015] Sublet, J. C., Eastwood, J. W., Morgan, J. G., Fleming, M., & Gilbert, M. R. (2015). The FISPACT-II user manual. CCFER (11), 11.

[Sub2017] Sublet, J. C., Eastwood, J. W., Morgan, J. G., Gilbert, M. R., Fleming, M., & Arter, W. (2017). FISPACT-II: an advanced simulation system for activation, transmutation and material modelling. Nuclear Data Sheets, 139, 77-137.

[Sun2013] Sundén, E. A., Ballabio, L., Cecconello, M., Conroy, S., Ericsson, G., Johnson, M. G., ... & Weiszflog, M. (2013). Evaluation of neutron spectrometer techniques for ITER using synthetic data. Nuclear Instruments and Methods in Physics Research Section A: Accelerators, Spectrometers, Detectors and Associated Equipment, 701, 62-71.

[Svo2021] Svoboda, J., Cavalier, J., Ficker, O., Imríšek, M., Mlynář, J., & Hron, M. (2021). Tomotok: python package for tomography of tokamak plasma radiation. Journal of Instrumentation, 16(12), C12015.

[Sym2014] Syme, D. B., Popovichev, S., Conroy, S., Lengar, I., Snoj, L., Sowden, C., ... & Contributors, J. E. (2014). Fusion yield measurements on JET and their calibration. Fusion Engineering and Design, 89(11), 2766-2775.

[Tel1981] Teller, E. (Ed.). (2012). Fusion Part A: Magnetic Confinement. Elsevier.

[Tri2007] Tripathy, S. P., Sunil, C., Nandy, M., Sarkar, P. K., Sharma, D. N., & Mukherjee, B. (2007). Activation foils unfolding for neutron spectrometry: Comparison of different deconvolution methods. Nuclear Instruments and Methods in Physics Research Section A: Accelerators, Spectrometers, Detectors and Associated Equipment, 583(2-3), 421-425.

[Tukan] http://tukan.ncbj.gov.pl/?tukan8k,1

[Val2015] Valkovic, V. (2015). 14 MeV neutrons: Physics and applications. CRC press.

[Vil2007] Villone, F., Joffrin, E., Albanese, R., Ambrosino, G., Ariola, M., Arnoux, G., ... & Piccolo, F. (2007, July). Development of 20s long hybrid scenarios on JET. 34th EPS Conference on Plasma Phys. Warsaw

[Wei2014] Weisen, H., Sips, A. C. C., Challis, C. D., Eriksson, L. G., Sharapov, S. E., Batistoni, P., ... & Contributors, E. J. (2014, August). The scientific case for a JET DT experiment. In AIP Conference Proceedings (Vol. 1612, No. 1, pp. 77-86). American Institute of Physics.

[Wei2015] Weiland, M., Gude, A., Igochine, V., Maraschek, M., Zohm, H., Bohle, R., ... & Pütterich, T. (2015). Investigation of 3D tungsten distributions in (1, 1) kink modes induced by toroidal plasma rotation. Plasma Physics and Controlled Fusion, 57(8), 085002.

[Wes2000] Wesson, J. (2000). The science of JET. Abingdon, Oxon, OX14 3EA, UK.

[Wes2004] Wesson, J., & Campbell, D. J. (2004). Tokamaks. Oxford university press.

[Why2010] Whyte, D. G., Hubbard, A. E., Hughes, J. W., Lipschultz, B., Rice, J. E., Marmar, E. S., ... & Alcator C-Mod Team. (2010). I-mode: an H-mode energy confinement regime with L-mode particle transport in Alcator C-Mod. Nuclear Fusion, 50(10), 105005.

[Wol1999] Wolle, B. (1999). Tokamak plasma diagnostics based on measured neutron signals. Physics Reports, 312(1-2), 1-86.

[Zim2010] Zimbal, A., Giacomelli, L., Nolte, R., & Schuhmacher, H. (2010). Characterization of monoenergetic neutron reference fields with a high resolution diamond detector. Radiation measurements, 45(10), 1313-1317.

[Zoh2017] Zohuri, B. (2017). Inertial confinement fusion driven thermonuclear energy. Springer International Publishing.